

# Theory of screening in the multi-channel multi-impurity Kondo box

Dissertation with the aim of achieving a doctoral degree  
at the Faculty of Mathematics, Informatics  
and Natural Sciences

Department of Physics  
of Universität Hamburg

submitted by  
Mirek Hänsel, M.Sc.  
born March 28, 1986 in Berlin, Germany

Hamburg  
2017



Gutachter/innen der Dissertation:	Prof. Dr. Michael Potthoff Prof. Dr. Peter Schmelcher
Zusammensetzung der Prüfungskommission:	Prof. Dr. Michael Potthoff Prof. Dr. Peter Schmelcher Prof. Dr. Alexander Lichtenstein PD Dr. Elena Vedmedenko Prof. Dr. Michael Rübhausen
Vorsitzende/r der Prüfungskommission:	Prof. Dr. Michael Rübhausen
Datum der Disputation:	12.07.2017
Vorsitzender Fach-Promotionsausschuss Physik:	Prof. Dr. Wolfgang Hansen
Leiter des Fachbereichs Physik:	Prof. Dr. Michael Potthoff
Dekan der Fakultät MIN:	Prof. Dr. Heinrich Graener



# Kurzfassung

Eine allgemeine Theorie bzgl. der Abschirmung von magnetischen Spin-1/2-Störstellen, welche an unmagnetische, metallische Nanostrukturen angekoppelt sind (sog. Kondo-Boxen), wird entwickelt, numerisch implementiert und für einige paradigmatische Modellsysteme im Detail diskutiert. Das aus der räumlichen Beschränkung dieser Nanostrukturen resultierende Ein-Teilchen-Energiespektrum des Nanosubstrats weist endliche Lücken zwischen den Energieniveaus auf, sodass ausschließlich Fermi-Elektronen einen Kanal zur Abschirmung der Störstellen zur Verfügung stellen. Dieser sog. "finite-size Kondo-Effekt" tritt unterhalb einer kritischen Temperatur, der Kondo-Temperatur  $T_K$ , auf. Es entstehen drei mögliche Abschirmungsszenarien, wobei der Spin einer Störstelle entweder unterkompensiert, ganzheitlich, oder überkompensiert abgeschirmt wird. In früheren Arbeiten wurden die Ein-Teilchen-Energiespektren als nicht-entartet angenommen, wodurch maximal ein Abschirmungskanal entsteht, sofern das Fermi-Energieniveau partiell besetzt ist. In der vorliegenden Arbeit wird die Einschränkung auf nicht-entartete Energieniveaus aufgehoben, wodurch Zugang zur Physik von Störstellenabschirmung in Nanosystemen mit entarteten Ein-Teilchen-Energiespektren erlangt wird. Letztgenannte findet man typischerweise in Systemen mit intrinsischen Symmetrien, wie z.B. bei Ringen oder Quadratgittern. Im Grenzfall  $T \rightarrow 0$  wird durch erste Ordnung Störungstheorie in der lokalen Austauschkopplung ein effektiver Hamilton-Operator hergeleitet, der die Ankopplung von Störstellenspins an Sätze delokalisierte Fermiorbitale beschreibt. Es wird gezeigt, dass diese Orbitalsätze von der Störstellenposition, sowie von der elektronischen Füllung und der Geometrie des Nanosubstrats abhängen. In vielen Fällen können die Orbitalsätze in einen koppelnden und einen nicht-koppelnden Anteil zerlegt werden. Die Verteilung der Fermi-Elektronen auf diesen Orbitalen wird analysiert und es wird gezeigt, dass ungekoppelte Orbitale zwar nicht zum Abschirmungsprozess, jedoch zur Grundzustandsentartung beitragen. Die Störstellenspins werden somit durch Fermi-Elektronen auf ankoppelnden Orbitalen abgeschirmt, welche wiederum in unterschiedlichen Relationen zueinander stehen können, z.B. indem sie vollständig, teilweise, oder gar nicht überlappen. Je nach Art des Überlapps entstehen unterschiedliche Abschirmungsarten, welche die Grundzustandseigenschaften beeinflussen. Für Kondo-Boxen, bei denen die Störstellen lokal angekoppelt sind, werden Grundzustandsentartung und Abschirmungsmechanismen für bis zu drei Störstellen untersucht. Während in den meisten Fällen das zu erwartende Verhalten eines Zentralspinmodells gefunden wird, treten jedoch auch Situationen mit einem überraschenden indirekten Austausch zwischen den Störstellen auf. Ein Zusammenhang zum obengenannten Orbitalüberlapp wird ausgearbeitet. Weiter wird gezeigt, dass die lokale Ankopplung von Störstellen nicht ausreicht, um mit dem verwendeten Modell Situationen mit überkompensiertem Spin zu finden. Das Modell wird deshalb durch das Einbeziehen nichtlokaler Störstellenkopplung erweitert. Dadurch wird die Anzahl koppelnder Fermiorbitale pro Störstelle größer eins, wodurch eine Überkompensation einer einzelnen Störstelle durch das metallische Nanosubstrat möglich wird. Die obengenannte Physik wird für eine Vielzahl an Parametern, wie z.B. der Geometrie und Füllung des Nanosubstrats, der Fermi-Elektronenanzahl, der Störstellenanzahl und -position und der effektiven Kopplungsstärke untersucht. Die Theorie wird an einigen exemplarischen Systemen (Ringe und Quadratgitter) getestet, wobei die Ergebnisse leicht auf beliebige Systeme übertragbar sind. Weiter wird gezeigt, dass die vorgestellten Theorien auch auf Systeme mit kleineren kristallographischen Defekten, oder bei denen andere physikalische Effekte zu einer Quasientartung der Energiespektren führen, angewendet werden können.



# Abstract

A general theory of screening magnetic spin-1/2 impurities coupled to nonmagnetic, metallic nanostructures, so-called Kondo boxes, is developed, implemented numerically, and discussed in detail for several paradigmatic model systems. The spatial confinement of these nanostructures results in a gapped one-particle energy spectrum of the host, where only electrons at the Fermi level provide channels to screen the impurity spins. This so-called "finite-size Kondo effect" occurs below a critical temperature  $T_K$ , called the Kondo temperature. Three possible screening scenarios arise, where an impurity spin is either under-, fully, or overscreened. Earlier works on this topic assumed the one-particle energy spectra to be nondegenerate, which thus provide at most one screening channel, if the Fermi energy level is partially occupied. In the present work, the restriction to nondegenerate energy levels is dropped, providing access to the physics of impurity screening in nanosystems with degenerate energy spectra. The latter are typically found in systems with intrinsic symmetries, such as rings or square lattices. By means of first order perturbation theory in the local exchange coupling, an effective Hamiltonian is derived, which describes impurity spins coupled to sets of delocalized Fermi orbitals in the limit of  $T \rightarrow 0$ . It is shown, that these sets are dependent on the impurity positions, as well as on the electronic filling and the geometry of the nanosubstrate. In many cases, the sets can be subdivided into a coupled and an uncoupled part. The distribution of Fermi electrons over these orbitals is analyzed, showing that uncoupled orbitals do not contribute to the screening process, but influence the ground state degeneracy. Thus, the impurity spins are screened by Fermi electrons occupying the coupling Fermi orbitals. The latter can be in different relations to one another, such as fully, partially, or not overlapping. Dependent on this overlap, different forms of screening arise, which affect the ground state properties. For Kondo box models where impurities are coupled locally, ground state degeneracy and screening mechanisms are examined for up to three impurities. While in most cases the expected central-spin model behavior is found, situations with a surprising indirect impurity exchange also occur. A connection to the aforementioned overlap is elaborated. Apart from this, it is shown that coupling impurities locally to the substrate is not sufficient to find overscreening within the presented model. To this end, the model is modified by inclusion of nonlocal impurity coupling. This increases the number of coupling Fermi orbitals per impurity to more than just a single one, which allows to find overscreening with only a single impurity coupled to the metallic host. All of the above listed physics are examined under variation of a plethora of parameters, such as geometry and filling of the host, Fermi electron number, impurity amount and placement, or effective coupling strengths. The theory is tested on several exemplary systems (rings and square lattices), but results are easily transferable to arbitrary systems. Moreover it is shown, that the theories presented are also applicable to systems containing minor crystallographic defects, or where other physical effects result in quasi-degenerate energy spectra.





# Contents

<b>1. Introduction</b>	<b>1</b>
1.1. The Kondo effect - a brief historical overview . . . . .	1
1.2. Kondo cloud and screening . . . . .	3
1.2.1. What is a Kondo cloud? . . . . .	3
1.2.2. Different manifestations of screening . . . . .	4
1.3. Aim and structure of the work . . . . .	6
<b>2. Physics of the Kondo box</b>	<b>9</b>
2.1. The Kondo box with a single impurity . . . . .	9
2.2. Two impurities in a Kondo box . . . . .	11
2.3. Quantum localization of conduction electrons . . . . .	13
<b>3. Screening in nanosystems with degenerate one-particle energy spectrum</b>	<b>17</b>
3.1. First results . . . . .	17
3.2. Hamiltonian and effective low-energy model . . . . .	22
3.2.1. The multi-impurity Kondo box Hamiltonian . . . . .	22
3.2.2. Effective low-energy model . . . . .	24
3.3. General statements on important parameters . . . . .	29
3.4. The single impurity case . . . . .	31
3.5. Nanosystems with two impurities . . . . .	31
3.5.1. Case A) - Fully overlapping coupling Fermi orbitals . . . . .	32
3.5.2. Case B) - Partially overlapping coupling Fermi orbitals . . . . .	33
3.5.3. Case C) - No overlap between coupling Fermi orbitals . . . . .	35
3.5.4. Examination of two impurities on a square-lattice . . . . .	36
3.5.5. Generalizing the results for two-impurity systems . . . . .	40
3.6. Nanosystems with three impurities . . . . .	45
3.6.1. Classification of overlap scenarios . . . . .	45
3.6.2. Toy model for three impurities . . . . .	46
3.6.3. Summary of the nine scenarios . . . . .	67
3.6.4. Transferring the results to exemplary systems . . . . .	69
3.7. Short summary of results for two and three impurities . . . . .	74
3.8. Generalization to more than three impurities . . . . .	75
<b>4. Overscreening</b>	<b>79</b>
4.1. A brief introduction to overscreening . . . . .	79
4.2. Modified Hamiltonian . . . . .	80
4.3. Effective coupling strengths . . . . .	81
4.3.1. Concept and interplay of local and nonlocal coupling . . . . .	81
4.3.2. Testing of the effective coupling-concept . . . . .	83
4.4. Examples of overscreened impurities . . . . .	89
4.4.1. Overscreening in a ring . . . . .	89
4.4.2. Overscreening in square lattices . . . . .	91
<b>5. Applicability to quasi-degenerate systems</b>	<b>97</b>
<b>6. Summary and outlook</b>	<b>101</b>
6.1. Summary of the work . . . . .	101

6.2. Outlook . . . . .	103
<b>Appendix A. Brillouin–Wigner perturbation theory for degenerate systems</b>	<b>105</b>
<b>Appendix B. Hilbert space dimension</b>	<b>107</b>
<b>References</b>	<b>109</b>
<b>List of publications and author contributions</b>	<b>115</b>
<b>Eidesstattliche Erklärung</b>	<b>117</b>
<b>Danksagung</b>	<b>119</b>

# 1. Introduction

## 1.1. The Kondo effect - a brief historical overview

The historical roots of the discovery of magnetism stretch back to the ancient Greece, where roughly 2600 years ago Thales of Miletus reported attractions between lodestones and iron [1]. Aside from rather descriptive results on magnetism, the progress in understanding its origins lasted long, and still continues.

One of the milestones in this progress was the identification of magnetism in solids as a quantum mechanical effect in 1919, nowadays known as the Bohr–van Leeuwen theorem [2]. However, even decades later not every experiment connected to magnetism was understood in detail. A prime example is the work of de Haas, de Boer, and van den Berg [3], published in 1934, where an increase of the electrical resistivity of gold for temperatures  $T \rightarrow 0$  had been reported. This result (which became years later known as the Kondo effect) was unexpected, because in most metals the resistivity decreases monotonically due to decrease of phonon scattering processes with decreasing  $T$ . Years passed by, until the findings were associated with magnetic impurities. This marked the beginning of a new era in condensed matter physics: Magnetic impurities in nonmagnetic host systems stepped into the limelight, and are still subject of intense research.

J. Friedel et al were the first to theoretically investigate magnetic impurities in metals [4–6], while experiments of B.T. Matthias et al showed that the transition temperature of superconductors is affected by the presence of small amounts of atoms carrying magnetic moments [7–11]. Using the theoretical achievements of Friedel and associates, P.W. Anderson addressed himself to the task of explaining the results, proposing a model which schematized the electronic structure of a metal with an embedded impurity [12]. Introduced in 1961, this model became famous as the Anderson impurity model, which has still not forfeited its popularity. However, the minimum in electrical resistivity of *Au*, found by de Haas et al [3], was explained by J. Kondo in 1964 [13]. Honoring his theoretical achievement, the effect was named the Kondo effect.

Studying experimental work on dilute alloys of *Fe* in a series of *Nb-Mo* alloys, presented by Sarachik et al [14], J. Kondo concluded that the resistivity minimum originates from the interaction between the spins of impurity and conduction electrons, and not from other impurity characteristics such as its charge, or even crystal field effects. Moreover, the Kondo effect occurred even for very low impurity concentrations, thus excluding interimpurity correlations as the origin of the effect. To this end, J. Kondo introduced a model which consists of an interaction-free conduction electron part and a Hamiltonian (proposed by C. Zener in 1951 [15] and known in literature as *s-d* model) that describes interactions of the impurity with electronic spins. These two parts build up a Hamiltonian which nowadays is known as the Kondo model. J. Kondo applied perturbation theory up to third order of  $J$  to this model, showing that a  $\ln T$  term appears that contributes to the electrical resistivity, and that the electron-impurity interaction leads to a singular scattering of the conduction electrons near the Fermi level. Together with the contribution of phonon scattering, the  $\ln T$  term finally explained the increase of resistivity [11].

Kondo's solution, however, suffered from a divergence for  $T \rightarrow 0$ , making the theory invalid in the low temperature regime, i.e. where the temperature  $T$  is below the so-called Kondo temperature  $T_K$ . The search for a solution to this deficit became known as the "Kondo problem". It was P.W. Anderson and associates, who introduced a scaling approach in 1970 [16], explaining the finite resistivity for  $T < T_K$ . The key idea was to eliminate higher order energy excitations, which do not contribute to the low energy physics. Although this ansatz broke down for  $T \ll T_K$  due to an infinite increase of the effective coupling strength, the qualitative behavior was predicted correctly. Several years later, K.G. Wilson confirmed Andersons approach by application of his "numerical renormalization group" ("NRG") to the Kondo model [17]. An analytical solution to the Kondo problem was later given by the so-called Bethe ansatz [18] for Kondo [19, 20] and Anderson model [21, 22]. Nowadays, both NRG and Bethe ansatz are methods of enormous popularity, belonging to the standard tools in condensed matter theory (see, for example, [23, 24] and references therein).

Although the origins of Kondo physics have been found and understood in some limiting cases, the topic is still up to date and of great interest. The extension from only few to an entire lattice of impurities (a so-called Kondo lattice) marked the beginning of heavy fermion physics, i.e. systems where conduction electrons have an effective mass of up to 1000 times that of free electrons due to the Kondo effect. Such heavy fermion systems show similarities to high temperature superconductors, making them a hot topic in modern physics [11, 25–35]. Closely related is the research on Kondo insulators (also referred to as Kondo semiconductors) such as  $SrB_6$  [36], which are either metallic or insulating due to the Kondo effect [37]. In the recent past, it was discovered that some insulators have topologically protected states, which lead to a whole new research field of the so-called topological Kondo physics [36, 38–44].

Positioning single atoms with a scanning tunneling microscope (STM) [45–47] was an experimental breakthrough, making it possible to observe the Kondo effect not only via resistivity and susceptibility measurements, but also to resolve the atomic positions beforehand [25, 48–51]. In this context, the zero bias anomaly, which is the spectroscopic manifestation of the Kondo effect, was understood. The insights helped D. Goldhaber-Gordon and associates to detect the Kondo effect in single-electron transistors [52], which can be seen as the birth of quantum dot physics [25]. Quantum dots, which are small semiconducting boxes containing a reservoir of few electrons, are easy to tune, therefore attracting ongoing interest of physicists [53–61]. As such devices are promising candidates for modern chip technology [25], the research on quantum dots has not forfeited its popularity. As a matter of fact, an increasing interest in quantum dots even led to inclusion of Majorana fermions into solid state theory, for example in describing quantum dots coupled to semiconductors or superconductors [62–66].

The reader may already guess, that besides the above named research fields and applications, "Kondo effects" are nowadays found in many different contexts, far apart from its origin as a single metallic impurity on a nonmagnetic host. To name only few examples, a sort of Kondo effect appears in alkali-earth atomic gases [67], and even in quark matter, where heavy quarks act as impurities and light quark matter represents the host [68, 69].

Moreover, in the recent past the Kondo effect became subject of quantum field theories, such as the conformal field theory [70–72], with the purpose of describing for example Weyl and Dirac semimetals [73–75]. Especially impurities in graphene [76], but also in other Dirac materials, as well as unconventional superconductors [77] attract the interest of physicists today. With this tremendous increase of possible applications, the number of different models increased alike. They range from pseudogap Kondo models for unconventional superconductors [77] to models of Majorana fermions, such as Kitaev models [78,

79]. The latter can be brought into relation with the multi-channel Kondo model [80, 81], where especially the two-channel case is examined to describe novel materials (like mass-imbalanced superconductors [82]) by means of a "charge" Kondo effect [80–83].

The reason why the Kondo effect manifests itself in so many different theories and models is, that only few is needed: In a most general formulation, one needs a set of delocalized states (typically the host) which is connected by some sort of exchange interaction to degenerate, usually localized states (i.e. the impurity states). If particles from the host material (typically conduction electrons) can switch their state due to scattering from the impurity, a Kondo effect occurs. That such a scenario is indeed realizable in various ways can be seen by the numerous work connected to Kondo effects. The examples above only give a small overview and are not meant to provide a complete list, as this would go beyond the scope of this introduction. However, the reader may imagine, that the various Kondo effect(s) answer many questions in physics, but also raise a lot of new ones. Not always is a Kondo model an appropriate description of what is believed to be a Kondo system (see, for example, [84]), or the competition between a Kondo effect and other effects gives many contradicting results as stated by Wong et al in the case of Rashba spin-orbit coupling [85].

Although intense research associated with Kondo physics is ongoing, there are still many open questions, especially concerning impurities embedded in nanostructures. For example, magnetic impurities coupled to open chains of finite length have shown a fascinating "finite-size Kondo effect" [86, 87]. Its further investigation is in the focus of the present work. This requires to take a closer look at physical details, presented in the next section.

## 1.2. Kondo cloud and screening

### 1.2.1. What is a Kondo cloud?

In his early works, J. Friedel found out, that spin and charge density of substrate electrons are being distorted by the bare presence of a single magnetic atom, leading to results nowadays known as Friedel oscillations and the Friedel sum rule [4–6]. It was the first quantum mechanical description of screening processes, thus being fundamental to the Kondo effect, which is a collective screening phenomenon: A spin corresponding to an impurity (for example, an adatom) can be screened by electrons (or comparable particles in field theories) due to an exchange interaction. As was found out, it is the electrons around the Fermi energy level that participate in the screening process, which can be seen in the rise of the so-called Kondo peak (also known as Abrikosov–Suhl resonance), i.e. a resonance in the electronic density of states around the Fermi energy [11]. It is therefore not surprising, that a vanishing of the density of states at the Fermi energy may quench the Kondo effect. This usually happens, if the Kondo effect competes with other effects, such as cooper pairing, in combination with Hund’s coupling [88, 89], or in gapped and pseudogapped Fermi systems [69, 77], resulting in quantum phase transitions between screened and unscreened magnetic moments [90].

In the pristine Kondo effect with a magnetic impurity embedded in a nonmagnetic host metal, the screening leads to formation of a spin singlet [13]. It occurs below a temperature  $T_K$ , the Kondo temperature, which characterizes the energy scale where this screening is found. Associated to the Kondo temperature is a length scale  $\xi_K$ ,

$$\xi_K = \hbar v_F / (k_B T_K) , \quad (1.1)$$

where  $v_F$  is the Fermi velocity (in the following,  $\hbar = k_B = 1$ ). The quantity  $\xi_K$  can be interpreted as the size of the so-called Kondo screening cloud, see Fig. 1.1 [87, 91]. Conduction electrons within a range of length  $\xi_K$  around the impurity site in real space participate in the screening process, while electrons outside of the cloud form a Fermi liquid according to Landau's Fermi liquid theory [87, 92–94].

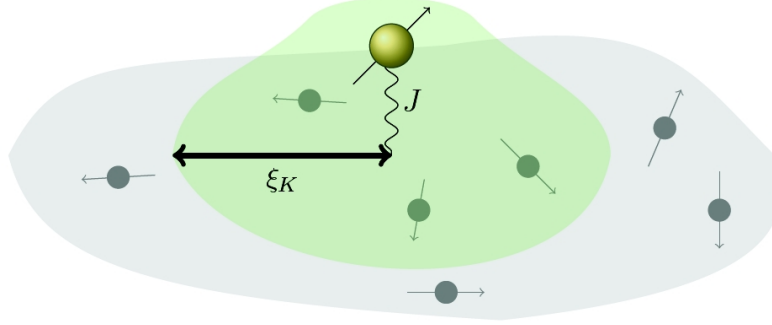


Figure 1.1.: Coupling of an impurity (yellow sphere) to conduction electrons (grey spheres) with coupling strength  $J$ . The Kondo cloud is highlighted with a green background, its extension is given by  $\xi_K$ . Figure adapted from Ref. [87].

Associating the Kondo temperature with the energy needed to break a Kondo singlet, one finds that strong (antiferromagnetic) impurity–electron coupling  $J$  leads to higher Kondo temperatures than weak coupling. In the weak coupling realm, this relation can be expressed by

$$T_K \propto \exp\left(-\frac{1}{\rho_0 J}\right), \quad (1.2)$$

which is a result from the scaling theories' solutions of the Kondo problem [91], where  $\rho_0$  is the host's free density of states at the Fermi energy. Since a high Kondo temperature  $T_K$  corresponds to a small Kondo cloud extension according to Eq. (1.1), strong  $J$  leads to formation of a shortly extended (or even localized) cloud, while the Kondo cloud becomes larger for decreasing  $J$ . Consequently, interesting physics are to be expected if the Kondo cloud size exceeded the system's extension, i.e. if it became mesoscopically large. This aspect is fundamental to the present work, as systems of small spatial extension are in the focus. For comparison, a Kondo temperature of some tens of Kelvins roughly corresponds to an extension of the Kondo cloud in the nanometer regime [95], thus competing with the spatial extension of confined nanostructures.

### 1.2.2. Different manifestations of screening

Screening is a rather general name used in many contexts, such as the screening of charge, or spin. In the context of spins, P. Nozières and A. Blandin have subdivided screening into categories underscreening, full screening, and overscreening [82, 96]. The key idea is, that each singly occupied atomic orbital of the host provides a screening channel, and the number of such channels  $n_c$  is compared to the magnitude of the spin in order to distinguish between the scenarios. In other words, given an impurity with total spin  $S$ , this spin can either be underscreened, if the number of screening channels  $n_c < 2S$ , or fully screened ( $n_c = 2S$ ), or overscreened, if  $n_c > 2S$ . For spin-1/2 impurities, the three cases are shown exemplary in Fig. 1.2.

The original Kondo model describes a single impurity coupled locally (in real-space) to a substrate. In order to screen the impurity's spin, the coupling must be antiferromagnetic, i.e. the spin components of the impurity and the conduction electrons must be of opposite

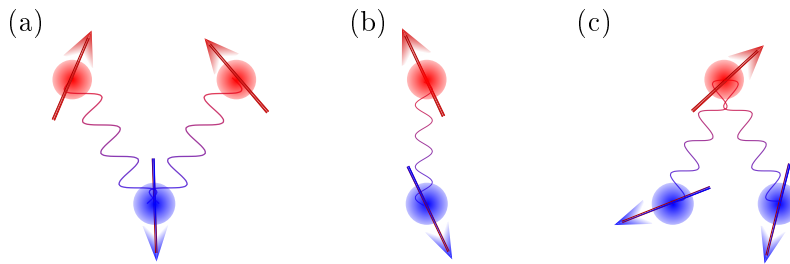


Figure 1.2.: Spin-1/2 impurities (red spheres with arrows) coupled to singly occupied atomic orbitals (blue spheres with arrows) can lead to (a) underscreening, (b) full screening, or (c) overscreening.

sign. If the system is large in its spatial extensions, enough conduction electrons are available for screening the impurity's spin, or possibly even to overscreen it (if the conduction electrons have a spin  $s > 1/2$  [97, 98]).

In confined nanosystems, the screening mechanism is different than in bulk substrates, for the Kondo cloud exceeds the system size if the coupling strength is weak. In combination with the size-induced discretization of the nanosubstrate's energy level spectrum, the impurity spin could be screened by a single Fermi electron only, rather than by several conduction electrons [86, 94, 95]. This extreme case is the so-called "finite-size Kondo effect". The screening channels  $n_c$  are then obtained by the Fermi electrons only. Note, that the number of these channels is not necessarily identical to the number of available Fermi electrons, because screening requires an antiparallel alignment of spins. For example, the spin of an impurity coupled to a single orbital, occupied by two Fermi electrons with opposing  $z$ -spin quantum number, is unscreened. In such a case, there is no screening channel since the orbital carries no total magnetic moment. It thus has to be kept in mind, that screening in confined systems is a filling-dependent effect.

Within nanosystems, the three types of screening become vivid: One gets underscreening, if multiple impurities couple to the same Fermi electron (Fig. 1.2(a)), or if a single impurity with spin greater than  $1/2$  is coupled to the Fermi electron. Full screening is found, for example, when a single spin-1/2 impurity couples to the Fermi electron, thus forming a spin-singlet (Fig. 1.2(b)). In order to find overscreening, several Fermi electrons are required to couple to the impurity, while the spin of the latter must be smaller than the total spin of the coupling Fermi electrons (Fig. 1.2(c)).

The physics of systems with screened impurities differ in many ways from systems with unscreened impurities. In experiments, the former usually manifests in the increase (substrates with magnetic adatoms, such as found by de Haas, de Boer, and van den Berg [3]) or, oppositely, in the decrease (quantum dots, for example [52, 53]) of electrical resistivity. Furthermore, the density of states (which is experimentally easily accessible) shows a characteristic (Abrikosov-Suhl, or Kondo) resonance at the Fermi level, and the total spin of a system decreases due to screening of the magnetic impurity. Especially overscreening is believed to be connected to the so-called non-Fermi-liquid behavior, which is characterized by yielding unusual logarithmic or power-law temperature dependencies of electronic and magnetic properties, as found in a number of actinide and rare-earth systems [99].

### 1.3. Aim and structure of the work

In the recent past, the possibility of using the electron's spin-degree of freedom in addition to its charge has attracted enormous interest in both research and industrial applications. The use of magnetic atoms or molecules in magnetic information storage devices [100], or as building blocks for spintronic devices [101, 102] are just few examples of current hot topics.

Despite of intense research in the field of Kondo physics, the influences of impurities in systems of finite size are yet not fully understood. However, there are many experimental realizations, such as in individual grains [103, 104], in metallocene molecules [105], or when impurities are coupled to nanodiamonds, where they are promising candidates as quantum markers for biomedical applications [106]. Carbon nanotubes, doped with  $C_60$ -clusters [107], or coupled to a localized electron [108], attract great interest as quantum dots, and yield as nanowires a perfect playground for the research on finite-size systems. Furthermore, mesoscopic rings with in-line quantum dots attract the researchers' interest, because ground state properties and changes in the persistent current of the ring are affected by the quantum dot (see Ref. [109] and references therein).

At low temperatures, a theoretical treatment by means of conventional models fails in all of the above mentioned examples, because the size of the Kondo cloud - fundamental for the screening of an impurity - would exceed the extension of the host material. Since the Kondo cloud is spatially confined, relevant length scales are being cut off, leading to a competition between Kondo effect (characterized by  $T_K$ ) and an energy scale  $\Delta$  arising from the geometrical confinement of the system. In order to account for this finite-size aspect, the standard theories must be modified [110–116]. A prominent example is the Kondo box model [86, 110], which is the nanosystem analogue to the Kondo model, and thus tailored for studying a single impurity coupled to a spatially confined host.

The physics within the Kondo box model become even more complex if not only one, but multiple impurities are connected to the finite-sized nanosubstrate, allowing for another competition, namely between Kondo screening and interimpurity exchange [86, 117, 118]. Intense studies on one-dimensional systems (for example impurity-doped nanowires [86, 87, 95, 119]) have shown, that the complex interplay of these effects leads to fascinating physical behavior, such as an unconventional reentrance of the Kondo effect in the weak coupling regime. This so-called "finite-size Kondo effect" is characterized by singlet formation between an impurity spin and a single Fermi electron, so that the impurity spin becomes (fully) screened [95].

The results in the above named references define the starting point of the present work. Multiple impurities coupled to systems of finite size, while in the low-temperature regime, are in the focus. The aim of this thesis is to extend the previous work on Kondo box systems, especially of Ref. [86, 87], by inclusion of degeneracy and quasi-degeneracy within the one-particle energy spectra. As the origin of (quasi-)degeneracy typically comes from symmetries in the nanostructures, this opens the opportunity to describe higher dimensional nanosystems (such as 2- or 3-dimensional materials). Due to the degeneracy of energy levels, basically an unlimited amount of Fermi electrons is available. A question to answer is, how these electrons participate in the fundamental processes of underscreening, full screening, and overscreening in confined nanostructures. The answer to this question is very complex, as it strongly depends on the amount, the location, and the coupling of magnetic impurities to the nanosystems. Therefore, a main aspect of the work is to categorize and to understand the different physical situations leading to these screening processes. To this end, perturbation theory in first order of the coupling parameter  $J$  is applied to the Kondo box model. Possible experimental realizations are impurities coupled



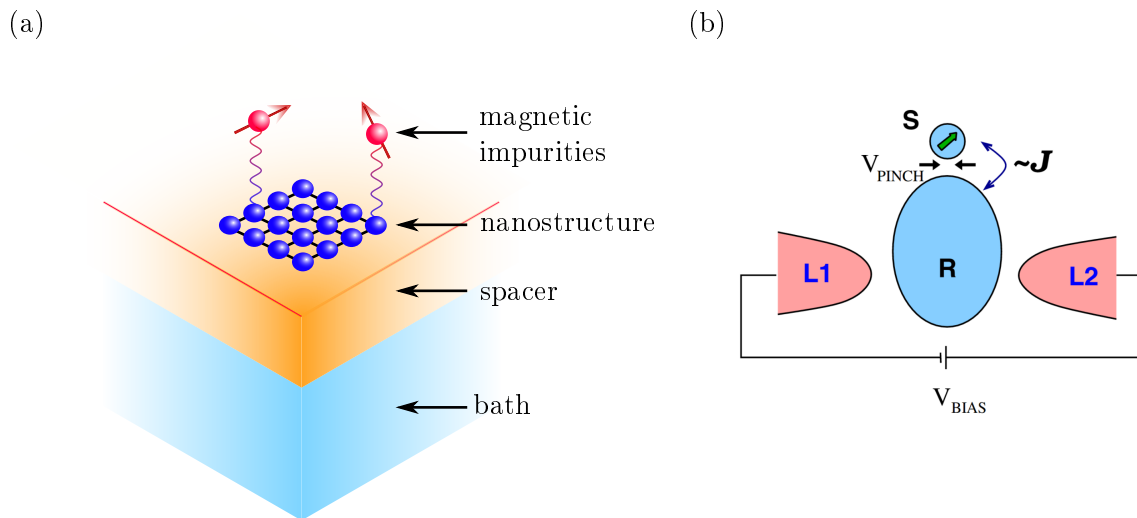


Figure 1.3.: Possible experimental realizations of the nanostructures examined in this work. (a) Magnetic impurities coupled to a two-dimensional nanostructure. The spacer is an insulating layer, separating the nanostructure from a bath. (b) A double quantum dot system, consisting of a small dot "S" that behaves as a single impurity spin in the Coulomb blockade regime, and a finite reservoir dot "R". The small dot S is exchange coupled with strength  $J$  to R. The coupling of  $R$  to the leads  $L1$ , and  $L2$  is not regarded in the present work. Figure adapted from Ref. [111].

to a finite-size substrate, which itself is separated by a spacer from a bulk material (see Fig. 1.3(a)), or (so-called T-shaped) double quantum dots as described by Refs. [111, 120], see Fig. 1.3(b). The generalization to clusters of quantum dots, where a lead-coupled central quantum dot can be seen as an impurity, while the surrounding quantum dots (if coupled to one another) build a nanosubstrate (similar to the setup in Refs. [121, 122]), is another possible application.

The work is structured as follows: In Chap. 2, the reader is introduced to the physics of the Kondo box, where previous results, especially of Refs. [86, 87, 95, 110, 119] are collected and analyzed. First results connected to degenerate energy levels are discussed in Sec. 3.1. The theory for higher-dimensional nanosystems, i.e. systems with possibly degenerate one-particle energy spectra, is presented in the following section. In Secs. 3.3 to 3.7, the ground state of the nanostructures for up to three impurities is examined with respect to the influence of different model parameters, such as geometric aspects (lattice size and dimension, impurity locations) and its direct consequences (degeneracy of the one-particle energy spectrum, effective coupling strengths), or influences of the total electron number. "Golden rules" for a generalization of the results to more than three impurities are found in Sec. 3.8. All results are analyzed with respect to the different screening types. As the model presented in Chap. 3 excludes any kind of overscreening, slight modifications to the theory must be done. Specifically, overscreening, which is in the focus of Chap. 4, can be found by inclusion of nonlocal coupling. The corresponding theory is presented in Sec. 4.2. The sections thereafter give insights into the concept of multi-channel coupling, which is subsequently tested on several exemplary systems. Chap. 5 is dedicated to check the applicability of the former presented theories to systems with quasi-degenerate energy spectra, which is relevant for a more realistic description of the nanosystems presented in this work. A summary of the results, as well as an outlook are given in Secs. 6.1 and 6.2, respectively.



## 2. Physics of the Kondo box

Nanosystems aroused the interest of physicists with the experimental breakthrough of surface spectroscopy using scanning tunneling microscopy (STM) [48, 123]. Motivated by further experimental work, such as the spectroscopy of discrete electronic states in single *Al* particles [103], the experimental realization of trapped conducting nanoparticles [124], electron transistors made from nanocrystals [125], and studies of band gap influences on superconductivity [104], W.B. Thimm et al introduced a theoretical model representing a magnetic impurity embedded in a spatially confined system, which is ever since known as the Kondo box model [110].

The main difference to vastly extended systems is, that the one-particle energy spectrum of nanosystems is not continuous, but discrete, and therefore gapped. The energy gap around the Fermi energy, hereafter named  $\Delta$ , is an important energy scale for the low-temperature physics, yielding physics contrary to that of bulk systems [86, 87, 112–114, 116, 126–132]. A competition between the level spacing  $\Delta$  and the Kondo temperature  $T_K$  arises, if these energy scales become comparable, which is the case for nanostructures of nanometer size [110]. In other words, the extension of the Kondo cloud would exceed the system size, which leads to a cutoff of relevant correlation lengths. On the one hand, this cutoff makes common approaches such as standard numerical renormalization group (NRG) unavailable, on the other hand, logarithmic divergences of the Kondo temperature are removed, thus yielding the opportunity to treat the physics within perturbation theory [87].

In the following, a short overview of Kondo box physics is given, so that the reader gains insight into relevant research results, which help to understand the present work. The following sections can be seen as brief summaries of Refs. [86, 87, 110, 131].

### 2.1. The Kondo box with a single impurity

The model Thimm et al proposed in their publication [110] is a single impurity Anderson model with discrete conduction electron spectrum, which reads in slave-boson representation

$$\mathcal{H} = \mathcal{H}_0 + \varepsilon_d \sum_{\sigma} f_{\sigma}^{\dagger} f_{\sigma} + \nu \sum_{j,\sigma} \left( c_{j\sigma}^{\dagger} b^{\dagger} f_{\sigma} + H.c. \right) . \quad (2.1)$$

The first term,

$$\mathcal{H}_0 = \sum_{j,\sigma} \varepsilon_j c_{j\sigma}^{\dagger} c_{j\sigma} , \quad (2.2)$$

describes the "free" system, where  $c_{j\sigma}^{\dagger}$  ( $c_{j\sigma}$ ) create (annihilate) conduction electrons at discrete energy levels  $\varepsilon_j \propto j\Delta$ . Note, that this choice of  $\varepsilon_j$  gives a nondegenerate eigenenergy spectrum, as found in open one-dimensional chains (as depicted in Fig. 2.1).

The second term in Eq. (2.1) is associated with the (only) impurity, and describes the occupation of a specific energy level  $\varepsilon_d$ , which lies well below the Fermi energy level  $\varepsilon_F$ .

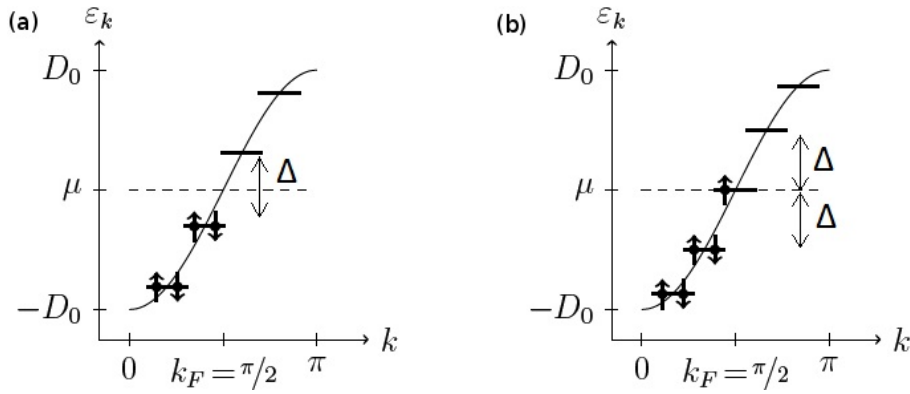


Figure 2.1.: Energy dispersions of a one-dimensional chain (open boundaries) without any impurities. (a) The chemical potential  $\mu$  lies between two energy levels (later denoted as "off-resonant" case), and (b) the "on-resonant" case, where  $\mu$  falls together with the highest occupied energy level, i.e. the Fermi energy level. Arrows represent electrons. The finite-size gap is denoted by  $\Delta$ , and the band edges by  $\pm D_0$ . Figure adapted from Ref. [87].

For  $\varepsilon_d$ , the constraint  $\sum_{\sigma} f_{\sigma}^{\dagger} f_{\sigma} + b^{\dagger} b = 1$  accounts for the limit of infinite Coulomb repulsion between two electrons on the  $d$ -level, ensuring  $\varepsilon_d$  to be singly occupied.

Electronic fluctuations between conduction electron levels  $\varepsilon_j$  and impurity level  $\varepsilon_d$  are taken into account by the third term of Eq. (2.1), with  $\nu$  being the transfer matrix element.

With this model, Thimm et al found out (amongst other results), that for temperatures  $T \gg \Delta$  the shape of the Kondo resonances are indistinguishable from the bulk case ( $\Delta \rightarrow 0$ ) [110]. In the realm of  $T \lesssim \Delta$ , however, the Kondo resonance splits up into a series of subpeaks, which correspond to the discrete energy levels of the box. Furthermore, results are different for odd and even total electron numbers.

The latter aspect is fundamental: For  $T \ll \Delta$  and an even total electron number, the highest occupied energy level of the free conduction electron system, as well as the  $d$ -level, are singly occupied each, while all other nondegenerate energy levels are doubly occupied. This scenario will be referred to as the "on-resonant" case in the following. The inner energy can be lowered by forming a singlet between the conduction electrons and the single  $d$ -electron. The singly occupied conduction electron level (i.e. the topmost one) carries the largest spectral weight, which results in the (single) Kondo resonance at around the Fermi energy. With decreasing temperature, the resonance becomes sharper, indicating that the screening occurs with only the (single) Fermi electron, which is the finite-size Kondo effect.

On the other hand, an odd total number of electrons implies that all one-particle energies of the free conduction system are doubly occupied, which is what is called an "off-resonant" case from now on. Thimm et al found a two-peak structure in the impurity spectral function for  $T \ll \Delta$ . The explanation is, that transitions between the highest occupied energy level and the impurity level are blocked due to full occupation of the former. For an energy penalty of order  $\Delta$ , the two topmost electrons can be redistributed equally between their original energy level, and the next highest. Then, an exchange with the  $d$ -level becomes possible, which is the reason two Kondo resonances are found in this case. The spectral weight of the peaks is lower than in the on-resonant case, as the energy penalty weakens the Kondo correlations.

These results were the first to provide theoretical predictions of Kondo physics in a nanostructure, and moreover showed that the confined geometry yields physics very different

from the ones known from bulk systems. Thimm et al's work [110] opened up the field of Kondo box physics, and marked the starting point for further research. One extension, namely the inclusion of a second impurity, will be presented in the next section.

## 2.2. Two impurities in a Kondo box

The physics of the Kondo box as presented by Thimm et al [110] gave fascinating insights into Kondo screening of a single impurity in nanostructures. What happens, however, if not only one, but multiple impurities are coupled to the finite-size host, which is almost exclusively the case in real materials [133–135]? Aside from Kondo physics, an indirect interaction between impurities, mediated by the itinerant conduction electrons of the (not necessarily confined) host, comes into play. Found by Ruderman, Kittel, Kasuya, and Yosida, this coupling mechanism is known as RKKY interaction [136–138]. Its corresponding coupling strength, i.e. the interimpurity coupling  $J_{\text{RKKY}}$ , can be derived perturbatively, yielding  $J_{\text{RKKY}} \propto J^2$ , if  $J$  is the coupling strength of a single impurity to the substrate. The coupling with strength  $J_{\text{RKKY}}$  between two impurities can either be ferro- or antiferromagnetic, depending on the distance between them. For antiferromagnetic RKKY exchange, the impurities form a singlet state, which is weakly coupled to the bath. In the other regime, given by ferromagnetic interimpurity coupling, the impurity spins tend to form Kondo singlets with the host.

It was Doniach who pointed out, that there is a competition between Kondo effect and RKKY interaction [139, 140]. For strong  $J$ , Kondo singlets suppress magnetism, but with decreasing coupling strength the singlets break up and magnetic order increases [139, 141, 142]. At very small coupling strength, the RKKY exchange eventually dominates. The crossover between these regimes is given by the Doniach point  $J_D$ , i.e. a coupling strength, where  $J_{\text{RKKY}} = T_K$  (realm 3 in Fig. 2.2).

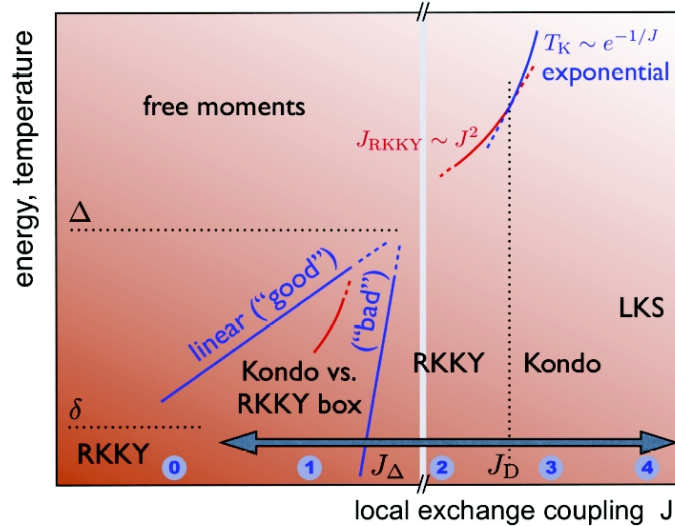


Figure 2.2.: Phase diagram showing different coupling regimes dependent on energy scales and coupling strength  $J$  in the on-resonant case. Figure adapted from Ref. [87]. See text for explanation.

It is in the nature of things, that the competition between Kondo physics and RKKY exchange may also occur in systems of finite size [86, 117, 118]. A necessary requirement for such gapped systems, however, is a partially filled Fermi energy level, as the finite-size Kondo effect is the screening of an impurity spin by Fermi electrons only (review

Sec. 1.2, or Refs. [86, 87, 94]). If the chemical potential lies within the finite-size gap  $\Delta$  (see Fig. 2.1(a)), i.e. the "off-resonant" case, then no Fermi electrons are available for screening: The screening channels cancel out due to full occupation of the Fermi energy level. Impurities may interact indirectly via the RKKY mechanism, but Kondo screening cannot be observed.

If, on the other hand, the Fermi energy level is partially occupied, i.e. in the "on-resonant" case (depicted in Fig. 2.1(b)), then finite-size Kondo screening is possible. The competition between finite-size Kondo effect and RKKY interaction is therefore only present in such on-resonant cases, which are discussed in the following.

An exemplary system of two impurities, located at neighboring sites of a (finite) open metallic chain of length  $L$ , and coupled locally with strength  $J$  to the latter, is in the focus of Ref. [86]. Unlike Thimm et al [110], the authors of Ref. [86] modeled the Kondo box by means of a Kondo model with a finite number of sites ( $i, j = 1, \dots, L$ ):

$$\mathcal{H} = -t \sum_{\langle i,j \rangle, \sigma} c_{i\sigma}^\dagger c_{j\sigma} + J \sum_{r=1}^{R=2} \mathbf{s}_{i_r} \mathbf{S}_r . \quad (2.3)$$

In the equation above,  $t$  denotes the hopping between neighboring sites  $\langle i, j \rangle$ , and  $c_{i\sigma}^\dagger$  ( $c_{i\sigma}$ ) are creation (annihilation) operators of conduction electrons with spin  $\sigma$  in the metallic chain. The second term describes the local coupling of  $R$  impurities, modeled as spins, to the conduction electron spin  $\mathbf{s}_{i_r}$ , at the lattice site of the  $r$ th impurity. Note, that the Kondo model can be derived from the Anderson model, if the latter is in the so-called "Kondo regime" (details follow in Subsec. 3.2.1), which has been shown by J.R. Schrieffer and P.A. Wolff [143] in 1966. This legitimates the usage of the Kondo model, which is somehow simpler because a local magnetic moment of the impurity exists permanently, avoiding assumptions of infinite Coulomb repulsion on a certain energy level.

In case of two impurities, Fig. 2.2 shows the corresponding phase diagram. For very strong couplings  $J$ , the impurities form local Kondo singlets ("LKS", regime 4). This singlet formation is in competition with the system's temperature. If the latter dominates the energy scale, the impurity spins remain as free moments, thus not being coupled to the host.

With decreasing coupling strength  $J$ , (local) Kondo singlets break up more easily (since  $T_K \propto \exp(-1/\rho_0 J)$ ), and eventually RKKY interaction competes with the (conventional) Kondo effect, if  $J \approx J_D$ , with  $J_D$  being the Doniach point (regime 3). Below this point (regime 2), the RKKY interaction dominates.

If the Kondo temperature becomes comparable to the finite-size gap  $\Delta$ , the influences of the Kondo box size become relevant (regime 2, with corresponding coupling strength  $J_\Delta$ ). Note, that  $J_\Delta < J_D$  (as shown in Fig. 2.2) is achieved, if the host system is still sufficiently large, because  $\Delta$  is antiproportional to the system size.

Regime 1, completely dominated by finite-size effects, requires some more explanation. The blue curve, which represents the Kondo screening, splits up into a "good" and a "bad" part. This notation corresponds to lattice sites, where the effective coupling of impurities exists ("good") or vanishes ("bad"). The effective coupling is a renormalization of the initial coupling strength  $J$  with the spectral weight of the one-particle eigenstate at the Fermi edge. Due to construction of the chains, the spectral weight might happen to be zero at certain lattice sites. If an impurity is placed on such a site, the effective coupling vanishes, which then gives the "bad" site scenario. In this case, the impurity is effectively not coupled to the nanosubstrate, making RKKY the preferred exchange mechanism. On

the other hand, impurity placement on "good" sites yields a situation, where the energy for Kondo singlet formation is linear in  $J$  and thus preferred over RKKY exchange coupling, which is of order  $J^2$ . This reentrant (finite-size) Kondo effect is the thrilling prove of influences originating from the confined lattice geometry.

The energy scale denoted with  $\delta$  (regime 0) belongs to a very weak coupling of the Kondo box to an environment (for example, to leads). In this case, the Kondo cloud may extent to sites belonging to the bath, and the reentrant Kondo effect breaks down.

Some remarks on the above listed results shall be made: Firstly, similar to the results of Thimm et al [110], "odd-even effects" were found, meaning that the physics of an even number of electrons differs strikingly from physics with odd electron number. This is not surprising, because the one-particle energy spectrum has the same structure as the one used in Ref. [110]. Therefore, the total number of electrons fixes the amount of Fermi electrons, and therewith the occupation (partial or full) of the highest occupied energy level. A partially occupied energy level ("on-resonant" case), which corresponds to an even electron number in Ref. [110], and an odd electron number in Ref. [86], yields a Fermi electron which can be used for screening, while contrary in "off-resonant" cases the impurities are much weaker coupled to the nanosubstrate (and possibly even screen themselves, as in the work of Schwabe et al [86]).

The authors of Ref. [86] have used the density matrix renormalization group (DMRG) method [144, 145], which gives basically exact results for one-dimensional systems, especially in the regime of strong coupling  $J$ . Moreover, a perturbative treatment of the Kondo box model is used to govern the low-energy physics. Since this theory is fundamental to the present work, it will be discussed in detail in Sec. 3.2. The perturbative approach in Ref. [86] was performed up to second order in  $J$  to cover off-resonant cases in the weak- $J$  regime. According to the results presented in the aforementioned reference, the impurity spins either couple to one another due to RKKY interaction, or they are screened by conduction electrons. In the weak- $J$  regime, a combination of both is found. Following the nomenclature of Sec. 1.2.2, the screening found can be classified as full screening in cases of both very strong and very weak  $J$ , and as underscreening in the intermediate regime, where  $J \approx t$ . It might be due to the modeled system, that no signs of overscreening have been found.

## 2.3. Quantum localization of conduction electrons

The insights gained from the two-impurity Kondo box analysis discussed in the last section helped to construct an interesting physical situation [131]: In the regime of strong coupling, i.e.  $J \gg t$  (where  $J$  is the local coupling strength and  $t$  is the hopping between neighboring sites), the formation of local Kondo singlets can be used to localize electronic states. On an open chain of length  $L$ , two impurities are placed at sites 2 and  $L - 1$ , thus localizing the electrons at sites 1 and  $L$  (see Fig. 2.3(a)). Due to this quantum localization, conduction electrons at the edge sites can be regarded as separate spins, which are weakly coupled (with coupling strength  $\alpha \ll t \ll J$ ) to the middle region of the chain (see Fig. 2.3(b)). This mechanism is called inverse indirect magnetic exchange (IIME), as proposed in Ref. [119]. Depending on the effective chain length ( $d' + 1$ ) in the middle region, two regimes have to be distinguished: The case of either odd, or even distances, see Fig. 2.3(c).

If the distance  $d'$  is odd, then the "center chain" is of even length, which corresponds to an off-resonant case where no Fermi electrons are available for screening of the effective edge spins ( $\mathbf{s}_1, \mathbf{s}_L$ ). Despite of the strong impurity-host coupling  $J$ , an effective RKKY model

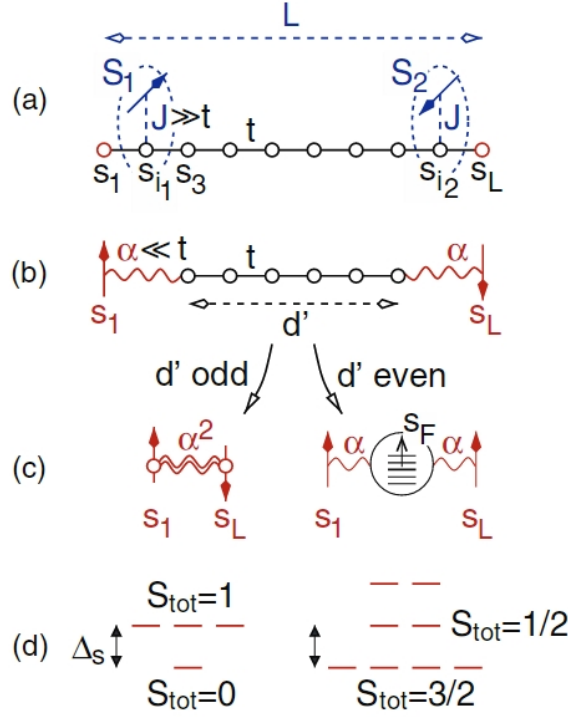


Figure 2.3.: (a) Strong coupling of specifically located impurity spins  $S_{1,2}$  (blue arrows) leads to localized edge states, which (b) form localized spins that are weakly coupled to the "center region" of the one-dimensional chain. (c) Depending on the chain length of this center region ( $d' + 1$ ), two scenarios are found: an effective RKKY model (left column) for an off-resonant center chain, and a central spin model (right column) for on-resonant center chains. The low-energy spectrum of both scenarios is shown in (d), with  $\Delta_s$  being the singlet-triplet excitation energy. Figure adapted from Ref. [131].

$\mathcal{H}_{\text{RKKY}}^{\text{eff}}$  can be used to describe this scenario, as  $\alpha \ll J$ . Analogous to the conventional two-spin RKKY model, which can be derived by second order perturbation theory,

$$\mathcal{H}_{\text{RKKY}} = J_{\text{RKKY}} \mathbf{S}_1 \mathbf{S}_2, \quad (2.4)$$

the effective model  $\mathcal{H}_{\text{RKKY}}^{\text{eff}}$  reads

$$\mathcal{H}_{\text{RKKY}}^{\text{eff}} = J' \mathbf{s}_1 \mathbf{s}_L. \quad (2.5)$$

Here,  $J' \propto \alpha^2$ . As shown in Fig. 2.3(d) (left column), the ground state is a singlet, which is due to the antiferromagnetic spin-spin coupling.

If, on the other hand, the central chain has odd length ( $d'$  is even), one gets an on-resonant scenario. The single Fermi electron spin ( $\mathbf{s}_F$ ) acts as a central spin model, to which the localized spins  $\mathbf{s}_1$  and  $\mathbf{s}_L$  are coupled with strength  $\alpha$  (see right column of Fig. 2.3(c)). The (ferromagnetic) linear-in- $\alpha$  coupling dominates over RKKY exchange, giving a quartet ground state (right column of Fig. 2.3(d)). DMRG calculations show, that this quartet is degenerate with a doublet ground state, but the origin of the latter is not fully clear.

Summarizing the above listed results, one again sees great differences between on- and off-resonant situations. Moreover, the finite size of the system, combined with a very specific placement of impurities, provides the option of localizing electrons, as done at the chain edge sites 1 and  $L$ . An indirect coupling between these electrons occurs, which, however, is strongly dependent on the extension (and therefore, on the geometry) of the center



region. The coupling of the quantum localized states to the substrate can be mapped to low-energy models, which for their part are perfectly described by perturbation theory. DMRG calculations show great agreement with the perturbatively derived results, proving that fundamental insights can already be obtained by perturbative treatment. In addition, this specific example of impurity spins coupled to a chain of noninteracting electrons shows a strong dependence of impurity placement, since a different positioning of the impurities would lead to a breakdown of the localized electron states.

All of the above examples, be it the pioneering work of Thimm et al [110], or the two-impurity Kondo box models [86, 131] have in common, that the discrete one-particle energy spectrum is nondegenerate. Although this is clearly the case in many physical systems, the overall picture is not complete, for symmetries within the nanostructures may lead to degeneracies of the nanosubstrate's energy spectrum. The focus of the next chapter lies on such degenerate one-particle energies, showing enormous differences to the nondegenerate cases discussed above.



### 3. Screening in nanosystems with degenerate one-particle energy spectrum

For the models discussed in the preceding chapter, a nondegenerate one-particle energy spectrum of noninteracting conduction electrons was used, which is the correct description for many systems such as one-dimensional chains with open boundary conditions, quasi-degenerate systems at zero temperature, or generally most systems without lattice geometries. The Fermi energy level is trivially also nondegenerate, and, depending on the filling, "on-resonant" cases (i.e. odd filling, resulting in one Fermi electron,  $n_F = 1$ ), or "off-resonant" cases (even total number of electrons) are realized. However, for systems with intrinsic symmetries, such as one-dimensional chains with periodic boundary conditions (so-called rings), or higher-dimensional systems (such as square lattices), the electronic one-particle energies may become degenerate. A direct consequence is, that electrons may occupy more than one single-particle state with the same energy. Therefore, situations with a plethora of Fermi electrons are possible, opening up opportunities to find under-, full, and overscreening.

A first remark shall be made on the "odd-even effects" found in systems with nondegenerate energy spectra, where "odd" and "even" denoted the filling of the Fermi energy level, leading to on- and off-resonant cases. For systems with degenerate one-particle spectra, however, "odd" and "even" are rather misleading names, as both even and odd electron numbers can lead to on-resonant scenarios, i.e. where the Fermi energy levels are partially occupied. Therefore, in the following only the names "on-" and "off-resonant" will be kept and used for distinction.

Before tackling the overall problem of degenerate energy levels, an exemplary system is presented in the next section, introducing the reader to the topic, and to commonly used notation.

#### 3.1. First results

In a pioneering work [95], a periodic chain has been used to obtain a degenerate one-particle energy spectrum. Depending on the length  $L$  of this ring, either off-resonant cases ( $L = 4m + 2$ ,  $m \in \mathbb{N}$ ), or on-resonant cases ( $L = 4m$ ) were found under assumption of half-filling ( $n = L$ ). Two impurities with spins  $\mathcal{S}_{1,2}$  are coupled with strength  $J$  at neighboring sites  $i_1$  and  $i_2$  to the ring structure (see Fig. 3.1(a)).

The method of choice to treat one-dimensional systems accurately for moderate chain lengths up to  $L \approx 100$  and intermediate coupling strength  $J$  is the density-matrix renormalization group (DMRG) [144], but modifications to standard DMRG are required due to the periodicity of the system. Folding an (open) chain of length  $L$  in the middle, and connecting its ends by hopping terms  $t_{1,L}$  and  $t_{L,1}$  yields the wanted periodic structure, which can then be treated by means of standard DMRG operating on the new sites of the

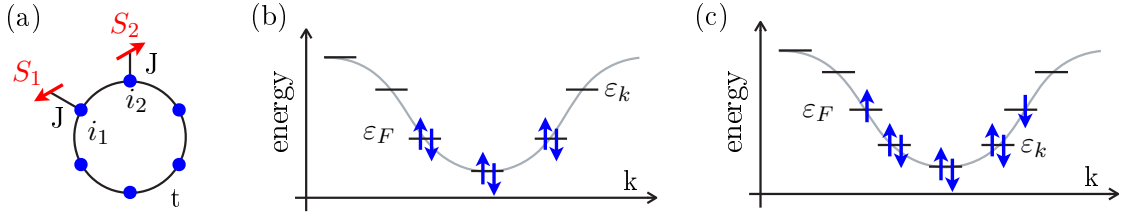


Figure 3.1.: (a) One-dimensional chain with periodic boundary conditions and  $L$  lattice sites. The hopping of electrons between neighboring sites occurs with energy  $t$ . At sites  $i_{1,2}$ , impurities with spin  $\mathbf{S}_{1,2}$  are coupled locally with strength  $J$ . The corresponding discrete energy spectra of conduction electrons shown at half-filling for (b) off-resonant ( $L = 6$ ) and (c) on-resonant ( $L = 8$ ) cases. The gray cosine shaped line shows the continuum ( $L \rightarrow \infty$ ). Figures adapted from Ref. [95].

half-length chain. This folding procedure helps to avoid long-range hopping terms in the Hamiltonian, which are known to hamper the scaling properties of the DMRG algorithm. However, the local Hilbert space increases due to the folding, restricting the application of DMRG to larger systems [95]. In especially this case of large chain lengths, particularly for systems in the thermodynamic limit ( $L \rightarrow \infty$ ), the numerical renormalization group (NRG) [17] becomes the preferable tool to analyze the physics. However, the combination of weak coupling and small system size is hardly accessible with both DMRG and NRG, but is predestined for perturbative approaches as done in Ref. [86]. Such a perturbative treatment of nanosystems is in the focus of this work, and will be presented in detail in Subsec. 3.2.2.

Before elaborating the theoretical details, an overview of the specific ring system with two impurities on neighboring lattice sites is shown for different coupling strengths  $J$  and chain lengths  $L$ , for both on- and off-resonant cases.

The first topic of interest is the variation of  $J$ , as competitions between RKKY exchange and Kondo effect are expected to arise, especially in the weak coupling regime. Similar to what has been presented in Sec. 2.2, local Kondo singlets are expected for strong couplings, and influences of the RKKY mechanism should be found for decreasing  $J$ . Further decrease of the coupling strength drives the system into the Kondo box regime, where the energy gap  $\Delta$  comes into play as a new energy scale.

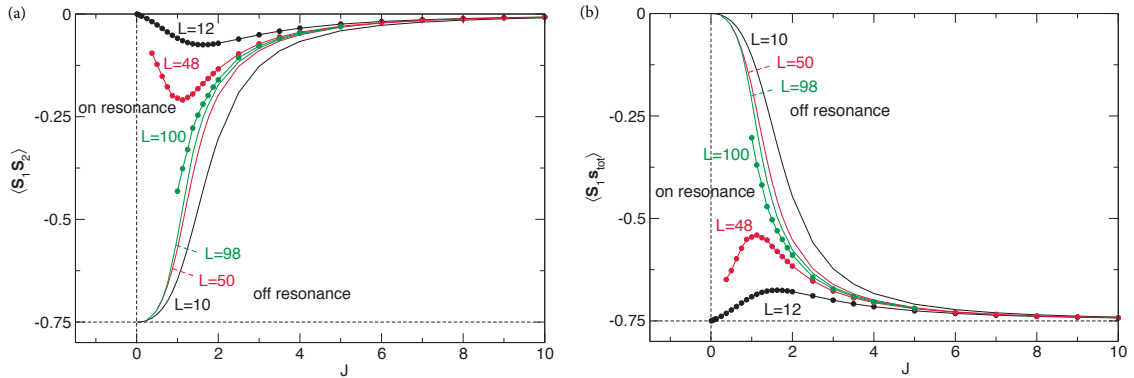


Figure 3.2.: Interimpurity correlations  $\langle \mathbf{S}_1 \mathbf{S}_2 \rangle$  (a), and impurity-substrate correlations  $\langle \mathbf{S}_1 \mathbf{s}_{\text{tot}} \rangle$  (b) for two impurity spins coupled to a ring structure as depicted in Fig. 3.1(a). Lines for off-resonant cases and dots for on-resonant configurations as calculated by DMRG. Figures adapted from Ref. [95].

For various chain lengths  $L$  (covering both on- and off-resonant situations), Fig. 3.2 shows the interimpurity correlations as well as the correlations of a single impurity spin with the

substrate (the total conduction electron spin  $\mathbf{s}_{\text{tot}}$ ),  $\langle \mathbf{S}_1 \mathbf{s}_{\text{tot}} \rangle$ . Note, that reflection symmetry implies  $\langle \mathbf{S}_1 \mathbf{s}_{\text{tot}} \rangle = \langle \mathbf{S}_2 \mathbf{s}_{\text{tot}} \rangle$ . As expected, the strong- $J$  regime is clearly dominated by local Kondo singlets, because the interimpurity correlation vanishes and the impurity spin is coupled perfectly antiferromagnetically to the substrate, i.e.  $\langle \mathbf{S}_1 \mathbf{s}_{\text{tot}} \rangle = -3/4$ . This result is certainly identical for both on- and off-resonant configurations, because this distinction becomes only relevant in the Kondo box regime, which requires a Kondo screening cloud comparable to the size of the system. As the Kondo cloud is localized for strong  $J$ , it does not exceed the system's dimension, thus the Kondo box regime is not entered.

With decreasing  $J$ , the RKKY regime sets in. Local Kondo singlets are broken up, which can be seen in the (absolute) decrease of  $\langle \mathbf{S}_1 \mathbf{s}_{\text{tot}} \rangle$ . Simultaneously, interimpurity correlations set in, leading to  $\langle \mathbf{S}_1 \mathbf{S}_2 \rangle < 0$ . The negative sign of the latter correlation indicates an antiferromagnetic coupling between the impurities, which fits perfectly to the RKKY mechanism, where  $J_{\text{RKKY}}$  is negative for neighboring impurities, thus aligning them antiparallel. Again, these trends of the correlation functions are equivalent for both on- and off-resonant situations, showing that the Kondo box regime has not set in yet.

At roughly  $J \lesssim 3$ , the first signs of the Kondo box regime are found. Decrease of  $J$  leads to a turnaround of the correlation functions in on-resonant cases, recovering the characteristics of impurity screening by the host system: The interimpurity correlation vanishes, proving that Kondo singlet formation dominates over the RKKY interaction. Correspondingly,  $\langle \mathbf{S}_1 \mathbf{s}_{\text{tot}} \rangle \rightarrow -3/4$ , which proves that the impurity spins are coupled (and thus screened) by the substrate. For off-resonant scenarios, however, no Fermi electrons are available for screening, making RKKY the dominant exchange mechanism. In the extreme limit of  $J \rightarrow 0$ , both impurities are eventually not coupled to the host anymore, and the interimpurity correlation takes its minimum value of  $-3/4$ .

These results are in great agreement with the phase diagram presented in Fig. 2.2, where a reentry of the Kondo effect sets in for weak  $J$  in on-resonant cases. Note, that in the analysis above, impurities are placed on "good sites" of the ring. "Bad sites", according to the notation within Fig. 2.2 and Sec. 2.2, are not found in periodic chains.

Another aspect of interest is the thermodynamic limit,  $L \rightarrow \infty$ . In this case, the conduction electron system becomes gapless, i.e.  $\Delta \propto 1/L \rightarrow 0$ , and, correspondingly,  $J_\Delta \rightarrow 0$ . For coupling strengths  $J \gg J_\Delta$ , the occupation of states at the Fermi energy thus becomes irrelevant, and differences between on- and off-resonant scenarios are not expected to be found. While DMRG algorithms struggle with large systems due to an tremendous increase of the Hilbert space dimension, the numerical renormalization group (NRG) is tailored to treat such systems [146]. Finite systems, however, are not treatable with standard NRG, since the heart of NRG is a logarithmic discretization of the (continuous) energy spectrum, whereas the energy spectra of spatially confined systems consist of discrete poles. Moreover, in on-resonant cases a pole exists at the Fermi energy level, which cannot be resolved on the logarithmic scale. Despite these limitations, A.K. Mitchell was able to overcome these difficulties, implementing the above described ring structure with two impurities (see Ref. [95]). The results are shown in Fig. 3.3.

The NRG calculations prove, that chain lengths  $L \approx 10^5$  perfectly match to results obtained for the thermodynamic limit (red crosses in the lower right panel of Fig. 3.3). Moreover, the data obtained by the modified NRG matches well with DMRG results (shown as circles in Fig. 3.3), which is nontrivial due to the rediscrretization of the conduction electron spectrum. Only for  $L = 100$ , DMRG results deviate from the ones obtained by modified NRG, which is exactly due to the discretization problem of NRG for finite systems. By reduction of NRG's discretization parameter  $\Lambda$  to  $\Lambda \rightarrow 1$ , which represents the bare model, the discrepancies between DMRG and NRG vanish.

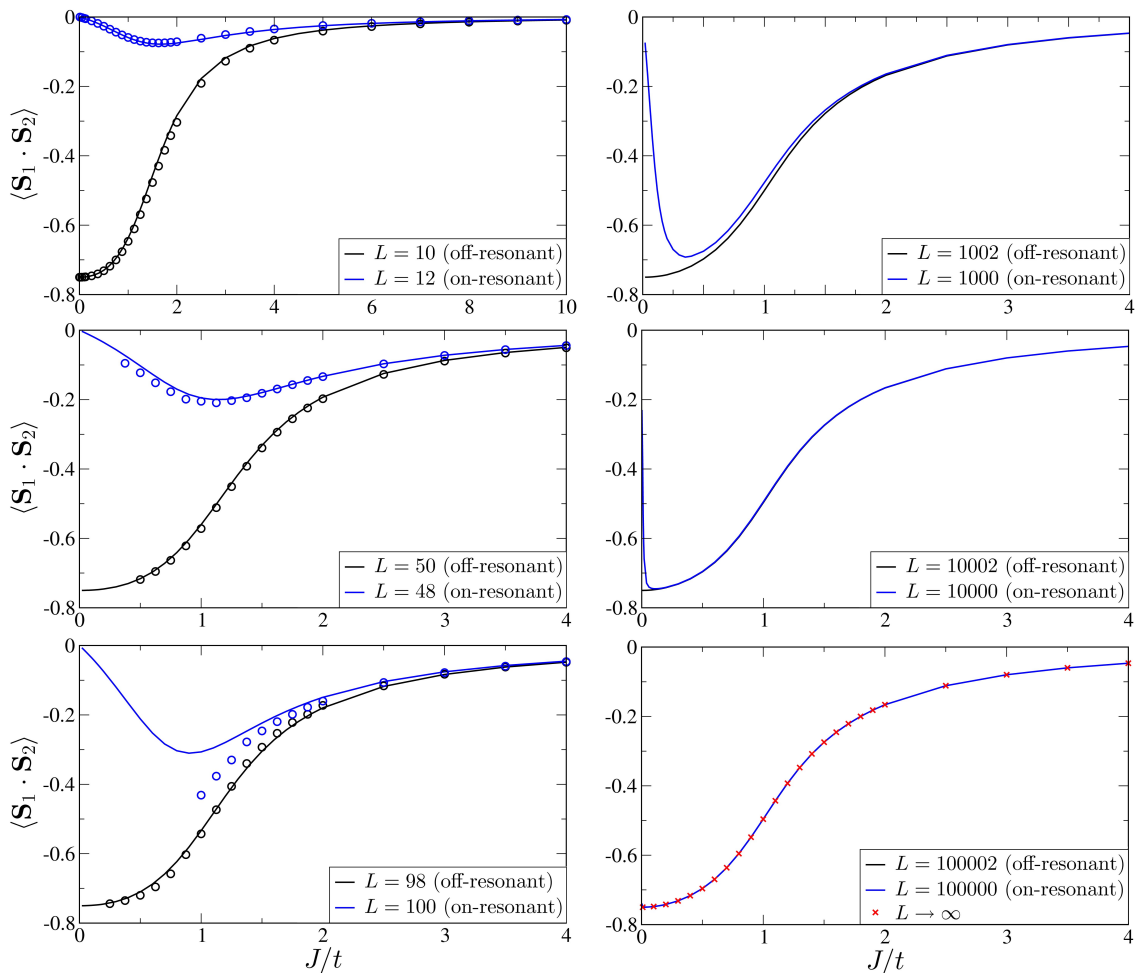


Figure 3.3.: Interimpurity correlation  $\langle \mathbf{S}_1 \mathbf{S}_2 \rangle$  for two impurity spins coupled to a ring structure as depicted in Fig. 3.1(a), with focus on increasing system size to examine the transition to the thermodynamic limit. Blue lines show on-resonant, black lines off-resonant cases as calculated by NRG. For comparison, DMRG results (see also Fig. 3.2(a)) are included as circles. The red crosses (lower right panel) show standard NRG calculations for the continuum ( $L \rightarrow \infty$ ). Figures adapted from Ref. [95].

In all off-resonant cases, the interimpurity correlation  $\langle \mathbf{S}_1 \mathbf{S}_2 \rangle \rightarrow -3/4$  for weak coupling, proving the RKKY mechanism being dominant. The crossover from the local Kondo singlet regime occurs uniformly with increasing chain length  $L$ . In on-resonant cases and chain lengths  $L = 1000$  and  $L = 10000$ , a clear RKKY regime is found for intermediate coupling strengths  $J$ . For weak  $J$ , the competition between finite-size Kondo effect and RKKY mechanism sets in.

As expected, the reentrant Kondo physics behavior can more easily be seen when the chain length is smaller. Using  $J_\Delta \propto 1/\ln L$ , which marks the crossover to the finite sized system, one finds that this transition region is shifted to very weak coupling strengths  $J$  for large lattices. Therefore, unless  $J \gtrsim J_\Delta$ , finite-size effects are usually not observed for large chain lengths. It is in the nature of things, that this situation changes with decreasing  $L$ , making finite-size effects visible for a greater range of  $J$ . For system sizes below  $L = 100$ ,  $J_\Delta \approx J_D$ , impeding a  $J$ -regime where only RKKY interaction is found. This explains, why on-resonant spin-spin correlations do not reach the value of  $-3/4$  for smaller systems: The local Kondo singlet realm (strong  $J$ ), and the finite-size regime (weak  $J \lesssim J_\Delta$ ) have a continuous transition, competing with  $J_{\text{RKKY}}$  which is of the same order. In the extreme case of very small lattices, the RKKY regime is almost entirely suppressed.

The weak coupling realm can be further examined. Naming  $T_s$  the low-energy scale, which is needed to break Kondo singlets, the following behavior is expected due to the analysis above:

$$\begin{aligned} T_s &\stackrel{J \rightarrow 0}{\propto} J^2 && \text{off-resonant} , \\ T_s &\stackrel{J \rightarrow 0}{\propto} J && \text{on-resonant} . \end{aligned} \quad (3.1)$$

The upper line of Eq. (3.1) represents off-resonant scenarios, which have clearly been found to be dominated by RKKY interactions. The effective low-energy RKKY model (see Eq. (2.4)) scales with  $J_{\text{RKKY}} \propto J^2$ , making  $T_s \propto J^2$  a plausible expectation. In on-resonant cases,  $T_s \propto J$  can be assumed due to the work of Schwabe et al [86] (see Sec. 2.2), where perturbation theory in  $J$  has successfully been applied to finite-size systems, showing the linear-in- $J$  dependence of on-resonant configurations. With the theory presented in Sec. 3.2, this will become clearer to the reader.

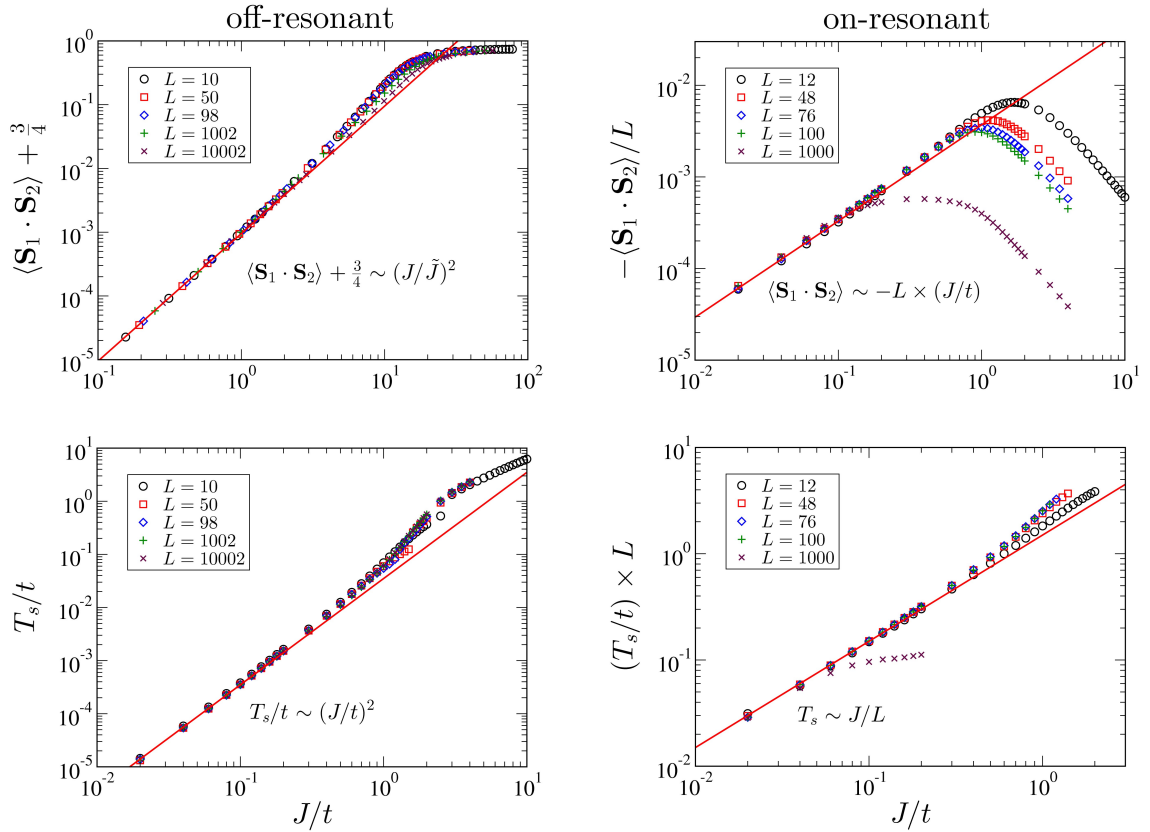


Figure 3.4.: Upper panels: Interimpurity correlations  $\langle \mathbf{S}_1 \mathbf{S}_2 \rangle$  dependent on  $J$ , plotted for various system sizes  $L$ . Quadratic (off-resonant) and linear (on-resonant)  $J$ -dependencies as given by the inserted formulae belong to higher order corrections of the correlation functions (see Ref. [95] for more details). Lower panels:  $J$ -dependence of  $T_s$ , which represents a low-energy scale for singlet formation. The scaling behavior is shown for off-resonant (left panels) and on-resonant cases (right panels). The calculations were performed with modified NRG. Figures extracted from Ref. [95].

To prove the applicability of Eq. (3.1), Fig. 3.4 shows NRG calculations of the  $J$  dependence of  $T_s$  in both on- and off-resonant cases (lower panel). The red line represents the asymptotic behavior as given in Eq. (3.1). Combined with the interimpurity correlations (upper panel), the RKKY regime (characterized by  $\langle \mathbf{S}_1 \mathbf{S}_2 \rangle \rightarrow -3/4$ ) is indeed found for  $J \rightarrow 0$  in off-resonant cases of any chain length, while the vanishing of  $\langle \mathbf{S}_1 \mathbf{S}_2 \rangle$  proves the Kondo singlet formation for  $J \rightarrow 0$  in all on-resonant cases.

All these results show, that the weak coupling regime exhibits fascinating physics, driven by a competition between coupling strength, system size and different interaction mechanisms (Kondo singlet formation and RKKY exchange). Moreover, the results are sensitive on the geometry (i.e. size of the system, impurity placement), and on intrinsic parameters such as the filling, leading to on- and off-resonant scenarios with contrary physical behavior.

In conclusion, many effects, such as differences between on- and off-resonant cases, as well as the finite-size Kondo effect, are lost in the limit of large lattice sizes  $L$ . On the other hand, the weak coupling regime, and likewise the intermediate coupling regime in nanostructures, show amazing finite-size physics as described above. However, many questions have not been answered yet. A simple example are chains of odd length, but also higher dimensional systems are of great interest. Moreover, up to now there is basically nothing known about geometric influences, both of the substrate shape and of impurity placement onto a given nanostructure. In addition, the total electron number (i.e. the filling  $n$ ), as well as the number and location of impurity spins are parameters, which should also be examined in more detail.

As one can see, the opportunities to investigate finite-size systems are not at all used up. It is the aim of the present work to examine missing aspects and to get a more general view on finite-size systems. In the next section, a theoretical framework will be established by means of first order perturbation theory in  $J$ , covering the interesting low-energy physics of on-resonant configurations, where the finite-size Kondo effect occurs. The theory has already been presented in Ref. [95], and successfully confirmed the weak-coupling behavior presented above. Nevertheless, more general insights can be gained with this theory, which requires a detailed description.

## 3.2. Hamiltonian and effective low-energy model

### 3.2.1. The multi-impurity Kondo box Hamiltonian

Modeling a multi-impurity Kondo box, i.e. a spatially confined nanosubstrate system with  $R$  impurities coupled to the former, is possible in several ways. W.B. Thimm et al's proposal of a Kondo box [110] by means of an Anderson impurity model is a very good starting point, but likewise a Kondo model can be used. The latter models impurities as spins, which are locally exchange coupled with coupling strength  $J$  to the substrate, which here is metallic and of finite size. Both models are applicable, but for describing impurities with permanent magnetic moments, the Anderson model has to be in the so-called "Kondo regime". Following the notation of Ref. [110] (see also Sec. 2.1), a singly occupied electronic impurity level  $\varepsilon_d$  is required, which can be realized by a strong on-site Coulomb repulsion  $U$ . Moreover, charge fluctuations on this level must be completely suppressed, so that only a super-exchange-like mechanism connects impurity and conduction electron states. Since these constraints are automatically fulfilled in the simpler Kondo model, the latter seems more appropriate. Following the theoretical work of Schwabe et al (see Secs. 2.2, 2.3, and 3.1, as well as Refs. [86, 87, 95, 131]), such a multi-impurity Kondo model is used as the basis for the present work.

As already presented in Eq. (2.3), the Hamiltonian of the multi-impurity Kondo box model consists of two parts, i.e. the nanosubstrate of itinerant conduction electrons,  $\mathcal{H}_0$ , and a term describing the coupling of impurity spins,  $\mathcal{H}_1$ :

$$\mathcal{H} = \mathcal{H}_0 + \mathcal{H}_1 . \quad (3.2)$$



The first term models a single  $s$ -band of noninteracting conduction electrons,

$$\mathcal{H}_0 = \sum_{\langle i,j \rangle, \sigma} t_{ij} c_{i\sigma}^\dagger c_{j\sigma} , \quad (3.3)$$

where  $t_{ij}$  are the hopping matrix elements for electrons moving between lattice sites  $i$  and  $j$ . In the following, hoppings between neighboring sites are taken into account, which is denoted by  $\langle i, j \rangle$  below the sum, resulting in a tight-binding band. Note, however, that  $\mathcal{H}_0$  is not restricted to this constraint. In order to account for the spatial confinement of the geometry,  $i, j = 1, \dots, L \ll \infty$ , with  $L$  being the total number of lattice sites. The difference between Kondo model and Kondo box model thus only lies within the number of present sites  $L$ . Electrons with spin projection  $\sigma = \uparrow, \downarrow$  are created (annihilated) by operators  $c_{i\sigma}^\dagger$  ( $c_{i\sigma}$ ) at site  $i$ , to which the corresponding orbital  $|i, \sigma\rangle$  belongs. Note, moreover, that the system's geometry is encoded in the hopping matrix, and the energy spectrum of the (nano)substrate is completely defined by  $H_0$ .

It is helpful to transform the tight-binding Hamiltonian  $\mathcal{H}_0$  into momentum space using the following transformation:

$$\begin{aligned} c_{i\sigma}^\dagger &= \sum_{k,g} U_{kg,i} c_{kg\sigma}^\dagger , \\ c_{i\sigma} &= \sum_{k,g} U_{i,kg}^* c_{kg\sigma} . \end{aligned} \quad (3.4)$$

In the above equations,  $U_{kg,i}$  and its adjunct counterpart are the matrix elements of a unitary matrix  $\mathbf{U}$  that diagonalizes the (spin-independent) hopping matrix  $t_{ij} = t_{ji}$ :

$$\sum_{\langle i,j \rangle} U_{kg,i} t_{ij} U_{j,k'g'}^* = \varepsilon_{kg} \delta_{kk'} \delta_{gg'} , \quad (3.5)$$

whereby the index  $g = 1, \dots, G(k)$  accounts for a possible degeneracy of the Hamiltonian's one-particle eigenenergies  $\varepsilon_{kg}$ . With the eigenbasis  $|k, g, \sigma\rangle$  of the transformed Hamiltonian, the spin-independent  $U$ -matrix elements can be written as

$$U_{kg,i} = \langle k, g, \sigma | i, \sigma \rangle . \quad (3.6)$$

As will be seen in the upcoming sections, these matrix elements play a fundamental role for different screening mechanisms and ground state properties of the systems.

The conduction electrons are locally exchange coupled to magnetic impurities. The corresponding Hamiltonian,  $\mathcal{H}_1$ , reads

$$\mathcal{H}_1 = J \sum_{r=1}^R \mathbf{s}_{i_r} \mathbf{S}_r , \quad (3.7)$$

whereby the impurities are modeled as spins  $\mathbf{S}$ . For the present work, the spin quantum number of the latter is set to  $S^{\text{imp}} = 1/2$ , although the model is not restricted to this specific value. Impurities are enumerated with index  $r = 1, \dots, R$ , and are located at sites  $i_r$  on the lattice. At site  $i_r$ , the  $r$ th impurity spin  $\mathbf{S}_r$  couples locally antiferromagnetic with constant coupling strength  $J > 0$  to the electrons' spin density  $\mathbf{s}_{i_r}$ ,

$$\mathbf{s}_{i_r} = \frac{1}{2} \sum_{\sigma, \sigma'} c_{i_r\sigma}^\dagger \boldsymbol{\sigma}_{\sigma\sigma'} c_{i_r\sigma'} . \quad (3.8)$$

In the above equation,  $\boldsymbol{\sigma}_{\sigma\sigma'}$  stands for the vector of Pauli matrices.

### 3.2.2. Effective low-energy model

The multi-impurity Kondo box Hamiltonian, as given above, withstands exact analytical solutions. Several very successful approaches have been established in the past, such as the density-matrix renormalization group (DMRG) [144], or the numerical renormalization group (NRG) [17]. While DMRG works accurately for one-dimensional systems, the NRG is tailored for impurity models with a continuous host energy spectrum. Systems with more than one spatial extension, which are moreover of finite size, are therefore not adequately represented by these powerful tools. For the low-energy regime, however, the finite-size attribute can be turned into an advantage, as perturbation theory becomes applicable. While the Kondo temperature  $T_K \propto \exp(-1/\rho_0 J)$  bears a singularity for extended systems in the weak coupling regime, the confinement of the Kondo cloud cuts off relevant energy scales, making perturbation theory in  $J$  accessible for nanosystems (see e.g. Ref. [87] for details).

The validity of the perturbation theory depends on the relevant energy scales, which are conduction electron hopping  $t$ , temperature  $T$ , coupling strength  $J$ , and energy level spacing  $\Delta = T_K(J_\Delta)$ .

For the sake of clarity, the discrete energy levels belonging to the same energy in the one-particle spectrum are called multiplets due to their degeneracy. Since energy levels (and/or multiplets) are not necessarily distributed equally within the spectrum, a measure for the energy difference cannot be quantified easily. However, the energy level (or multiplet) of interest is the highest occupied one, i.e. the Fermi energy level  $\varepsilon_F$ . Therefore,  $\Delta$  can be defined as the energy difference between the multiplets around the Fermi energy (see, for example, Fig. 2.1). For the first order perturbation theory in  $J$ , which is the one applied in the present work, the temperature must then be smaller than the finite-size gap  $\Delta$  in order to avoid thermal excitations between different multiplets, which are not covered by the first order of the theory. The band width scales with hopping  $t$ , thus  $\Delta \propto t$  for constant system size. As the coupling strength  $J$  is the perturbation parameter,  $J$  must necessarily be much smaller than  $t$ .

The first order perturbation theory cannot account for RKKY exchange (which is an effect of order  $J^2$ ), thus  $J$  should be much weaker than  $J_D$ , which is the Doniach point (i.e. the crossover between local Kondo singlet formation and RKKY exchange, see Fig. 2.2). Moreover, to enter the regime of finite-size physics, the condition  $J \lesssim J_\Delta$  must be fulfilled, where  $J_\Delta$  is defined by  $\Delta = T_K(J_\Delta)$ . Summing this up, the following conditions for a trustworthy application of first order perturbation theory in  $J$  can be gathered:

$$\begin{aligned} T &\ll \Delta, \\ J &\ll t, \\ J &\lesssim J_\Delta \ll J_D. \end{aligned} \tag{3.9}$$

Using the above relations, as well as

$$\Delta = T_K(J_\Delta) = D_0 \exp\left(-\frac{1}{\rho_0 J_\Delta}\right), \tag{3.10}$$

where  $D_0$  is half the bandwidth of the host and  $\rho_0$  its density of states at the Fermi energy, one gets

$$J \lesssim J_\Delta = \frac{1}{\rho_0 \ln \frac{D_0}{\Delta}} \tag{3.11}$$

as an easy-to-check condition. To ensure the validity, the temperature is fixed at absolute zero throughout the entire work.

Now that the parameter regime is set, perturbation theory can be applied to the full Hamiltonian (3.2). This requires the knowledge of the unperturbed Hamiltonian's ( $\mathcal{H}_0$ 's) many-body ground state. The latter is built up by the Fermi sea (FS), that is the conduction electrons occupying all one-particle energy levels  $\varepsilon_{kg}$  below the Fermi energy level  $\varepsilon_F$ , i.e.  $\varepsilon_{kg} \leq \varepsilon_{k_Fg} \equiv \varepsilon_F$ . Since degeneracy of the Fermi energy level is possible, the ground state may be degenerate as well. Index  $\gamma = 1, \dots, \Gamma$  accounts for this degeneracy, so that the  $\Gamma$ -fold degenerate  $N$ -electron ground state can be written as  $|\text{FS}, \gamma\rangle$ .

Two physically different situations are possible, depending on the degree of degeneracy  $\Gamma$ . The first case are "off-resonant" scenarios, where  $\Gamma = 1$ . This case is realized, if the Fermi energy level (or multiplet) is fully occupied. Terms of linear-in- $J$  order vanish for  $\Gamma = 1$ , since all doubly occupied energy levels are magnetically inert, which is why there is no linear-in- $J$  Kondo effect. Therefore, the leading order for off-resonant configurations is  $J^2$ , which has exemplarily been shown in Sec. 3.1. Consequently, such off-resonant cases cannot be treated with first order perturbation theory.

As for the present work, the focus lies on the  $\Gamma > 1$  cases, where the finite-size Kondo effect can be found in linear order of  $J$ . A characteristic feature of these so-called "on-resonant" cases are incompletely filled one-particle Fermi energy levels at energy  $\varepsilon_F$ .

The perturbation theory presented below is in fact not restricted to certain values of  $\Gamma$ . For on-resonant cases with  $\Gamma > 1$ , first order perturbation theory is sufficient, while second order is required for off-resonant cases. As the latter is not of interest in this work, the theory is only presented up to first order.

In a first step, a projector  $P_0$  onto the space of ground states (of the unperturbed Hamiltonian,  $J = 0$ ) is defined:

$$P_0 = \sum_{\gamma=1}^{\Gamma} |\text{FS}, \gamma\rangle \langle \text{FS}, \gamma| . \quad (3.12)$$

This projector can be used to apply Brillouin-Wigner perturbation theory (see Appendix A for more details). Up to linear order in  $J$ , one then obtains the following effective low-energy model:

$$\mathcal{H}_{\text{eff}} = E^{\text{FS}} + P_0 H_1 P_0 . \quad (3.13)$$

The first term,  $E^{\text{FS}}$ , is the energy of the Fermi sea which results from 0th order perturbation theory. As this summand only gives a constant energy shift, it can be neglected in all further considerations. However, the second term is adequate to describe the low-energy physics, and is in the focus of interest of the present work.

In order to explore and understand the physics modeled by the effective Hamiltonian, some algebra must be done. In a first step,  $\mathbf{s}_{i_r}$  from Eq. (3.8) is being transformed into momentum space using Eq. (3.4):

$$\mathbf{s}_{i_r} = \frac{1}{2} \sum_{\substack{k, k' \\ g, g'}} \sum_{\sigma, \sigma'} U_{kg, i_r} c_{kg\sigma}^\dagger \boldsymbol{\sigma}_{\sigma\sigma'} U_{i_r, k'g'}^* c_{k'g'\sigma'} . \quad (3.14)$$

The calculation of  $P_0 \mathbf{s}_{i_r} P_0$  returns non-zero results only if the electronic operators annihilate and create electrons at the same energy level, thus  $k = k'$ . Terms with  $k \neq k'$  represent electronic excitations, which must vanish due to the projection onto the ground state by  $P_0$ . Also, electrons above the Fermi edge  $\varepsilon_F$  cannot be annihilated (since there are none), so that terms with  $k' > k_F$  do not contribute either. If  $k = k' < k_F$ , the annihilated electron with spin  $\sigma'$  and orbital index  $g'$  must be recreated by  $c_{kg\sigma}^\dagger$  in order to maintain a ground state configuration. Therefore,  $g = g'$  and  $\sigma = \sigma'$ , which moreover leads to  $\boldsymbol{\sigma}_{\sigma\sigma}$ , if

$k = k' < k_F$ . Since all Pauli matrices are traceless, the sum over  $\sigma$  kills all contributions of terms with  $k = k' < k_F$ . As a result, terms only contribute if  $k = k' = k_F$ , leading to

$$P_0 \mathbf{s}_{i_r} P_0 = \frac{1}{2} \sum_{g,g'} \sum_{\sigma,\sigma'} U_{k_F g, i_r} U_{i_r, k_F g'}^* \boldsymbol{\sigma}_{\sigma\sigma'} c_{k_F g \sigma}^\dagger c_{k_F g' \sigma'} P_0 . \quad (3.15)$$

The effective Hamiltonian can now be rewritten as follows:

$$\mathcal{H}_{\text{eff}} = \frac{J}{2} \sum_{r=1}^R \sum_{g,g'} \sum_{\sigma,\sigma'} U_{k_F g, i_r} U_{i_r, k_F g'}^* \boldsymbol{\sigma}_{\sigma\sigma'} c_{k_F g \sigma}^\dagger c_{k_F g' \sigma'} P_0 \mathbf{S}_r . \quad (3.16)$$

It is helpful to already note some important aspects of this Hamiltonian. First off, the low-energy physics of this model are determined by electrons occupying the Fermi energy levels at energy  $\varepsilon_{k_F g} = \varepsilon_F$ . As discussed above, electrons below the Fermi level do not contribute, which means they can be neglected. This is a great advantage for the numerics, because calculation expense (i.e. memory and time) is here not proportional to the number of electrons the system is filled up with. Moreover, the system size and even its dimension are not crucial parameters for numerical calculations, since only  $G(k_F) = G_F$  orbitals must be taken into account for the electronic system. A brief discussion about the Hilbert space dimension, which is the limiting factor for numerical calculations, as well as a comparison to the exact diagonalization method (ED) is given in Appendix B.

Secondly, one should note, that  $\mathbf{s}_{i_r}$  (Eq. (3.15)) is usually a nonlocal quantity in momentum space, because  $g$  and  $g'$  are not necessarily equal. This makes a vivid interpretation of the model difficult, because impurity spins then couple to a delocalized electron spin with spin quantum number  $1/2$ . The full consequences of this result will become clear when discussing the results (see especially Subsec. 3.5.2).

As so often in physics, reformulation of the problem helps to gain deeper insights. To this end, the aforementioned issue of delocalized electron spins is attacked now in order to obtain a spin-only model. Similar to Eq. (3.4), the following transformations are introduced:

$$\begin{aligned} c_{k_F g \sigma}^\dagger &= \sum_h V_{hg}(i_r) c_{k_F h \sigma}^\dagger(i_r) , \\ c_{k_F g \sigma} &= \sum_h V_{gh}^*(i_r) c_{k_F h \sigma}(i_r) . \end{aligned} \quad (3.17)$$

The idea behind this step is to diagonalize the dyadic product  $U_{k_F g, i_r} U_{i_r, k_F g'}^* = u_{gg'}(i_r)$ . As  $u_{gg'}$  is dependent on the lattice site  $i_r$ , the diagonalization matrix  $\mathbf{V}$  of dimension  $G_F \times G_F$ , as well as construction and annihilation operators  $c_{k_F h \sigma}^\dagger$  and  $c_{k_F h \sigma}$  inherit this dependence. This implies, that this second transformation is in general different for each impurity site  $i_r$  with  $r = 1, \dots, R$ . Performing the diagonalization one gets:

$$\sum_{g,g'} V_{gh'}^*(i_r) U_{k_F g, i_r} U_{i_r, k_F g'}^* V_{hg}(i_r) = x_h(i_r) \delta_{hh'} , \quad (3.18)$$

where

$$x_{h=1}(i_r) = \sum_g |U_{k_F g, i_r}|^2 \quad (3.19)$$

is the only non-zero eigenvalue. To this eigenvalue belongs an eigenvector, which, due to the dyadic (and thus hermitian) form of  $u_{gg'}$ , is simply  $U_{k_F g, i_r}$ :

$$\sum_{g'} u_{gg'} \cdot U_{k_F g', i_r} = U_{k_F g, i_r} \sum_{g'} U_{i_r, k_F g'}^* U_{k_F g', i_r} = U_{k_F g, i_r} |U_{i_r, k_F g}|^2 . \quad (3.20)$$

To prove that there is only one non-zero eigenvalue, one introduces an arbitrary vector  $W_{k_F g', i_r}$ , which is chosen orthogonal to  $U_{k_F g, i_r}$ :

$$\sum_{g'} u_{gg'} \cdot W_{k_F g', i_r} = U_{k_F g, i_r} \sum_{g'} U_{i_r, k_F g'}^* W_{k_F g', i_r} = 0 . \quad (3.21)$$

In a  $G_F$ -dimensional space, one can find  $G_F - 1$  vectors of form  $W$ , which are all orthogonal to  $U$ . Diagonalizing matrix  $u_{gg'}$  therefore leads to a matrix with only one non-zero entry. The corresponding normalized eigenvector  $V_{h=1g}$  to this non-zero eigenvalue is thus

$$V_{h=1g}(i_r) = \frac{U_{i_r, k_F g}^*}{\sqrt{\sum_g |U_{k_F g, i_r}|^2}} . \quad (3.22)$$

Returning to the delocalized electron spins as given by Eq. (3.15), and applying the transformation (3.17), one gets the following result:

$$P_0 \mathbf{s}_{i_r} P_0 = \sum_g |U_{k_F g, i_r}|^2 \mathbf{s}_F(i_r) , \quad (3.23)$$

where

$$\mathbf{s}_F(i_r) = \frac{1}{2} \sum_{\sigma, \sigma'} c_{k_F h \sigma}^\dagger(i_r) \boldsymbol{\sigma}_{\sigma \sigma'} c_{k_F h \sigma'}(i_r) \Big|_{h=1} \quad (3.24)$$

is the electron spin on the spin-degenerate Fermi orbital  $|F_{h=1}, i_r, \sigma\rangle$ :

$$\begin{aligned} |F_{h=1}, i_r, \sigma\rangle &= c_{k_F h=1 \sigma}^\dagger(i_r) |\text{vac}\rangle \\ &= \frac{1}{\sqrt{\sum_g |U_{k_F g, i_r}|^2}} \sum_g U_{k_F g, i_r} \sum_i U_{i, k_F g}^* |i, \sigma\rangle . \end{aligned} \quad (3.25)$$

In the last step, the inverses of Eqs. (3.4),

$$c_{k_F g \sigma}^\dagger = \sum_i U_{i, k_F g}^* c_{i \sigma}^\dagger , \quad (3.26)$$

and (3.17),

$$c_{k_F h \sigma}^\dagger(i_r) = \sum_g V_{gh}^*(i_r) c_{k_F g \sigma}^\dagger , \quad (3.27)$$

have been used. The orbitals defined by Eq. (3.25) are degenerate one-particle eigenstates of  $\mathcal{H}_0$  belonging to the Fermi energy  $\varepsilon_F$ . They are delocalized over the entire lattice, and, in general, different for each impurity spin  $\mathbf{S}_r$ . This entails great complexity, because not only the number of impurities, but also their geometric positions lead to a great variety of physically different situations.

Using Eqs. (3.16) and (3.23), an effective Hamiltonian in spin-only form can be written as

$$\mathcal{H}_{\text{eff}} = P_0 \sum_{r=1}^R J_{\text{eff}}(h=1, i_r) \mathbf{s}_F(i_r) \cdot \mathbf{S}_r , \quad (3.28)$$

with

$$J_{\text{eff}}(h=1, i_r) = J x_{h=1}(i_r) = J \sum_g |U_{k_F g, i_r}|^2 \quad (3.29)$$

being the effective coupling between impurity spin  $\mathbf{S}_r$  and electrons in the first ( $h = 1$ ) delocalized Fermi orbital. The Hamiltonian (3.28) has formally the structure of a central-spin model, where the conduction electrons at the Fermi level form the "central" degrees of freedom.

Fig. 3.5(a) shows a simple manifestation of the effective Hamiltonian: Given the system of Sec. 3.1, i.e. an open one-dimensional chain, to which two impurities are coupled at sites  $i_{1,2}$ , the effective low-energy model describes the respective impurity spins coupled to a single central spin  $\mathbf{s}_F$ , which arises from a single Fermi electron occupying a Fermi orbital. Note, that there is no degeneracy of the Fermi energy level  $\varepsilon_F$ , so that only a single Fermi orbital is present, i.e. the Fermi orbitals as defined in Eq. (3.25) are identical for both impurities. In this form, the effective low-energy model is equivalent to a regular central-spin model.

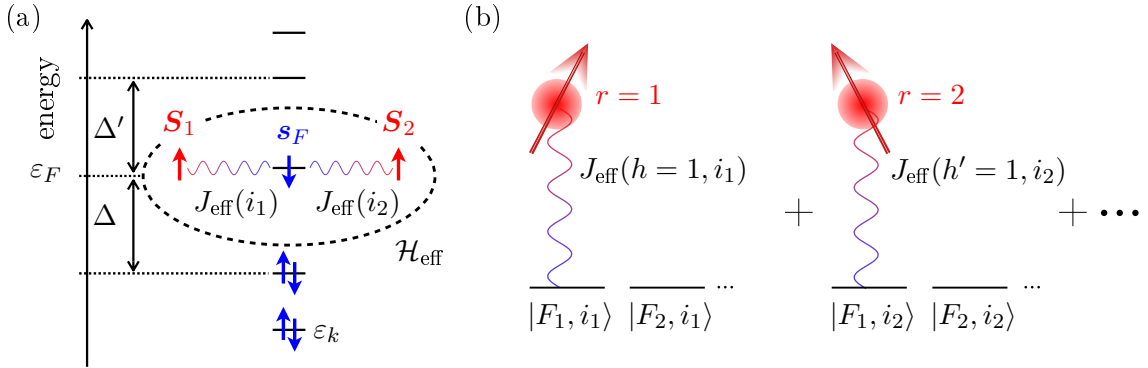


Figure 3.5.: (a) One-particle energy spectrum with a nondegenerate ( $G_F = 1$ ) Fermi level  $\varepsilon_F$  at  $J = 0$ . For  $0 < J \ll t$ , the dashed region represents the effective low-energy model of the system discussed in Sec. 3.1: Two impurities with spins  $\mathbf{S}_{1,2}$  are coupled to a "central" spin degree of freedom ( $\mathbf{s}_F$ ) which originates from a single Fermi electron ( $n_F = 1$ ) at the delocalized one-particle state with energy  $\varepsilon_F$ . Dependent on the impurities' locations  $i_{1,2}$  on the lattice in real-space, possibly different effective couplings  $J_{\text{eff}}(i_{1,2})$  arise. As only one screening channel is available ( $n_F = n_c = 1$ ), this situation corresponds to underscreening according to Sec. 1.2.2. The gaps  $\Delta$  and  $\Delta'$  in the energy spectrum are assumed to be of same order. Figure adapted from Ref. [95]. (b) Schematic picture of the effective Hamiltonian given by Eq. (3.28). Each impurity  $r$  couples to one specific Fermi orbital  $|F_{h=1}, i_r, \sigma\rangle$  (index  $\sigma$  has been dropped in the figure) with an impurity-dependent effective coupling constant  $J_{\text{eff}}(h, h' = 1, i_r)$ . There is no coupling to orbitals  $|F_{h \neq 1}, i_r, \sigma\rangle$  because  $J_{\text{eff}}(h \neq 1, i_r) = 0$ . The orbitals which belong to a given impurity  $r$  are not necessarily identical to those of another impurity ( $\neq r$ ), as each orbital set has its own,  $r$ -dependent basis. For the scenario shown in (a),  $|F_1, i_1\rangle = |F_1, i_2\rangle$ , and orbitals  $F_{2,3,\dots}$  do not exist.

However, one must not forget that the electronic "central" spin is a site-dependent construct, which is in general different for each impurity spin. The model given by Eq. (3.28) is thus a rather unconventional central-spin model, where each impurity spin couples to its own, customized central region. It must be emphasized, that the effective Hamiltonian given in Eq. (3.28) consequently acts in general on non-orthogonal orbitals.

In order to call attention to the complexity of the physics, a schematic picture of the general effective low-energy Hamiltonian is illustrated in Fig. 3.5(b). For each impurity  $r$ , a specific set of  $G_F$  spin-degenerate Fermi orbitals  $|F_h, i_r, \sigma\rangle$  exists. Orbitals belonging to a given impurity are pairwise orthogonal to one another, i.e.  $\langle F_{h_1}, i_r, \sigma | F_{h_2}, i_r, \sigma \rangle = \delta_{h_1 h_2}$ . Regarding orbitals belonging to different impurities, i.e.  $\langle F_h, i_r, \sigma | F_{h'}, i_{r'}, \sigma \rangle$  with  $r \neq r'$ ,

one cannot generally say how these orbitals are related to each other. Full, partial or no overlap are possible options, depending on where the corresponding impurities are located on the lattice. Therefore, the physics of the problem are sensitive to the amount of orbital sets (i.e. the number of impurities), as well as to the number of orbitals in each set (i.e. the degeneracy of the one-particle Fermi energy levels  $G_F$ ).

With the explanations above, one can get an idea of how the effective Hamiltonian can be understood as a central-spin model. Although each spin couples to a customized set of Fermi orbitals, these orbitals may overlap, forming a central region to which several impurities couple. If orbitals fully overlap, one can get a common central-spin model. On the other hand, a vanishing orbital overlap leads to a sum of several independent central-spin models, where each "central spin" consists of one Fermi orbital only. If several impurities are present, one usually gets a mixture of the above mentioned cases.

It remains the question, how the filling, more precisely the number of  $k_F$ -electrons, hereafter referred to as  $n_F$ , fits into Fig. 3.5(b). The  $n_F$  Fermi electrons are distributed over each set of Fermi orbitals corresponding to a fixed impurity, i.e. the occupation numbers of all  $G_F$  orbitals corresponding to the  $r$ th impurity sum up to  $n_F$ :

$$\sum_{\sigma}^{\uparrow, \downarrow} \sum_{h=1}^{G_F} n_{|F_h, i_r, \sigma\rangle} = n_F . \quad (3.30)$$

This relation holds true for each  $r = 1, \dots, R$ . Regarding Fig. 3.5(b), one therefore must place  $R \cdot n_F$  conduction electrons onto the  $R \cdot G_F$  Fermi orbitals, which is indeed confusing as only  $n_F$  Fermi electrons are present. However, this is the correct way to include the Fermi electrons into Fig. 3.5(b). It might help to clarify, that there are only  $G_F$  Fermi orbitals, which are formulated in  $R$  (in general) different basis systems. The "+"-sign in Fig. 3.5(b) comes from the sum over  $R$  impurities in the effective Hamiltonian, Eq. (3.28), but (in general) cannot be carried out due to different basis states, in which the  $R$  summands of the effective Hamiltonian are formulated. The crucial point is, that these different basis states (almost always) have a non-vanishing overlap, which determines the physics.

In the next sections, all possible overlap scenarios and their influences on ground state properties are examined. The theory is used to demonstrate characteristic situations for multiple impurities, including the geometric dependence of impurity placement.

### 3.3. General statements on important parameters

A very specific situation (two neighboring impurities coupled to a ring in one dimension) has already been discussed in Sec. 3.1. However, the model presented in Eq. (3.28) is strongly dependent on the number and the placement of impurities, yielding a plethora of so far uncharted geometries. In the next sections, general results obtained by first order perturbation theory calculations are presented and classified. In order to comply with the parameter restrictions defined in Eq. (3.9), throughout the entire work the temperature is fixed at absolute zero, the hopping is set to  $t = 1$ , and the coupling strength is fixed well below at  $J/t = 0.1$ . As presented in the theory, the latter is chosen isotropic in the spatial dimensions. Furthermore, the total spin of each impurity is set to  $1/2$ , although the theory is not restricted to this specific value.

A fundamental quantity of the theory is  $G$ , which is the number of degenerate one-particle energy levels at given energy  $E$ . It is dependent on geometric parameters of the conduction electron system, i.e. its lattice size and dimension, and is furthermore influenced

by the number of neighboring sites used for conduction electron hopping. As such one-particle energy degeneracy results from the system's symmetries, one has to distinguish between systems with open and periodic boundaries. Fig. 3.6 exemplarily shows the energy-dependent degeneracy  $G$  of two different systems, i.e. a one-dimensional ring (a) and a two-dimensional square lattice (b). For particle-hole symmetric Hamiltonians  $\mathcal{H}_0$ , the degeneracy distribution  $G$  is symmetric as well.

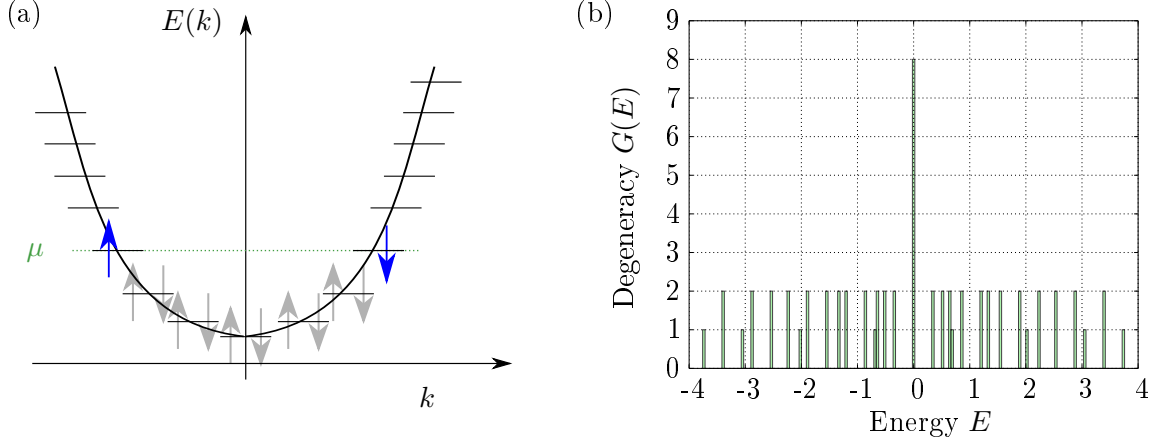


Figure 3.6.: (a) Energy dispersion of a one-dimensional chain of 16 lattice sites with periodic boundary conditions (i.e. a ring). The chemical potential is denoted by  $\mu$ , which is equivalent to the Fermi energy  $\varepsilon_F$  for  $T = 0$  K. Gray arrows represent the conduction electrons' spins in fully occupied orbitals, while the blue ones stand for Fermi electrons. For the depicted filling, the degeneracy of the Fermi energy level is  $G_F = 2$ . The histogram in (b) shows the degeneracy of energy levels for a two-dimensional square lattice of  $8 \times 8$  sites with open boundary conditions.

Since only Fermi electrons contribute to the Hamiltonian (3.28), the focus lies on the degeneracy of one-particle energy levels at the Fermi energy  $\varepsilon_F$ , which is denoted by  $G_F$  in the following. It goes without saying, that  $G_F$  varies with the filling. As can be seen at the ring structure's energy dispersion depicted in Fig. 3.6(a), for fillings  $n = 1, 2$  and  $n = 31, 32$  one gets the nondegenerate case with  $G_F = 1$ , while for all other fillings  $G_F = 2$ . For higher-dimensional systems, such as the exemplary  $8 \times 8$ -square lattice analyzed in Fig. 3.6(b), the degeneracy distribution generally becomes more complex. Note, that it is not the filling  $n$ , but rather the number of Fermi electrons  $n_F$  that is a limiting parameter for numerical calculations. For the ring system from Fig. 3.6(a),  $n_F = 3$  is the maximum number of Fermi electrons, while  $n_F = 15$  is the maximum amount (in case the filling is  $56 < n < 72$ ) for the square lattice corresponding to Fig. 3.6(b). Except for very low fillings, one thus usually has  $n_F \ll n$ . Especially for higher-dimensional systems, this yields great advantages for the numerical treatment (see Appendix B for details).

Note, moreover, that if  $\mathcal{H}_0$  is chosen particle-hole symmetric (as is done throughout the entire work), the one-particle energy spectrum is symmetric with respect to  $E = 0$ . It is therefore sufficient, to focus on systems with half-filling or less.

Now that the connection between electron filling  $n$ , Fermi electron number  $n_F$ , and degree of Fermi energy level degeneracy  $G_F$  is clear, one can tackle the fundamental aspect of nanosystems with degenerate energy spectra: Examining the relation of Fermi orbitals, given by Eq. (3.25), of which there are as many as  $G_F$ . It will be shown below, how the total ground state spin is influenced by different overlap scenarios. This is of great interest, as the ground state spin is directly related to the ground state degeneracy, fixing the experimentally accessible entropy.



Since each impurity has its own set of  $G_F$  Fermi orbitals, physics get more complex with increase of impurity spins  $R$ . Fortunately, it is possible to understand the basic system properties by analysis of systems with few spins only. The next pages lead the reader from the single impurity case (Sec. 3.4) to systems with up to three impurities (Sec. 3.6). Although a general classification of systems with more than three impurities goes beyond the scope of this work, some results and "golden rules" can be transferred. The latter are presented in Sec. 3.8. All numerical results presented below were obtained using exact diagonalization of the effective Hamiltonian (3.16).

### 3.4. The single impurity case

Starting with the simple case of one impurity only ( $R = 1$ ), just one set of Fermi orbitals  $|F_h, i_1, \sigma\rangle$ ,  $h = 1, \dots, G_F$ , is needed. All  $G_F$  Fermi orbitals are pairwise orthogonal to each other and the impurity spin couples to only one of these orbitals. In the following, the first orbital ( $h = 1$ ) is chosen as this coupling orbital.

For a system with given conduction electron filling  $n$ , the number of Fermi orbitals  $G_F$ , and the amount of Fermi electrons  $n_F$  are fixed parameters. The question of interest is now, how these  $n_F$  conduction electrons distribute over the available Fermi orbitals.

As for minimizing the internal energy, the formation of a singlet between impurity spin and a conduction Fermi electron is favorable. Therefore, the first Fermi orbital tends to be singly occupied, which is the only option to screen the impurity spin. The remaining  $n_F - 1$  Fermi electrons distribute over  $G_F - 1$  spin-degenerate Fermi orbitals, leading to a ground state degeneracy (GSD) of

$$\text{GSD} = \binom{2(G_F - 1)}{n_F - 1}. \quad (3.31)$$

### 3.5. Nanosystems with two impurities

Systems with two impurities ( $R = 2$ ) can be perfectly used to study simple Fermi orbital relations between orbitals of different sets. Such a set consists of  $G_F$  pairwise orthogonal Fermi orbitals, all of them belonging to the  $r$ th impurity. For  $R = 2$ , there are thus two sets of orbitals. Several different options arise, how Fermi orbitals of the first set are related to the ones of the second set. As will be shown below, the physics crucially depend on these relations.

What is considered in the following, is the scalar product  $\Omega_{r_1 r_2}$  of the Fermi orbitals belonging to different impurities ( $r_1 = 1, r_2 = 2$ ). The specific diagonalization for each impurity, Eq. (3.18), leaves  $G_F - 1$  orbitals undefined, but gives the Fermi orbital ( $h = 1$  for  $r_1$  and  $h' = 1$  for  $r_2$ ) to which the impurity spin couples. Thus, one can evaluate the expression:

$$\Omega_{12} = \langle F_{h=1, i_{r=1}, \sigma} | F_{h'=1, i_{r=2}, \sigma} \rangle. \quad (3.32)$$

Three different situations are possible, depending on how much the orbitals overlap with one another. One thus distinguishes between full (A)), partial (B)) and no overlap (C)) cases (see Fig. 3.7), which are discussed in detail below.

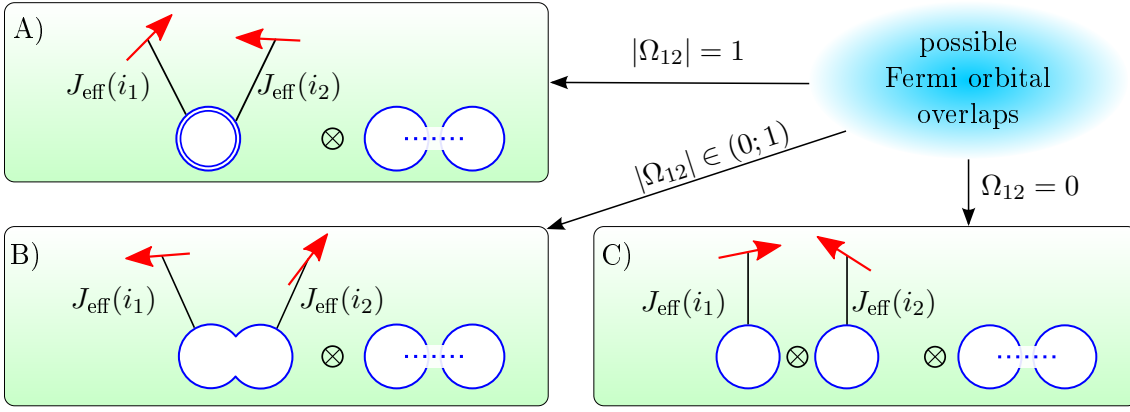


Figure 3.7.: The three possible manifestations of Fermi orbital overlap for systems with two impurities. Impurity spins (red arrows) couple to Fermi orbitals (blue circles) with effective coupling strength  $J_{\text{eff}}(i_r)$ . In case A), the two coupling Fermi orbitals (one from each set) have complete overlap ( $|\Omega_{12}| = 1$ ), thus both impurity spins couple to the same orbital, represented by the blue double circle. Partial overlap,  $|\Omega_{12}| \in (0; 1)$ , is shown in case B), while no overlap ( $\Omega_{12} = 0$ ) is depicted in case C). Blue circles with dots inside show Fermi orbitals to which no impurity spin is coupled. The tensor product symbol has to be understood as a separator between linearly independent orbitals. The indices  $h$  and  $h'$ , corresponding to the coupling Fermi orbital of each set (see Eq. (3.29)) have been dropped for compactness.

### 3.5.1. Case A) - Fully overlapping coupling Fermi orbitals

If the two Fermi orbitals are identical (despite  $r_1 \neq r_2$ ), the scalar product is trivially  $\Omega_{12} = \pm 1$ . The sign is not of importance, as it describes only the orbitals' orientation. In this full overlap case, the diagonalization matrices  $V$  and  $V^*$  from Eq. (3.18) diagonalize not only  $u_{gg'}(i_{r=1}) = U_{k_Fg, i_{r=1}} U_{i_{r=1}, k_Fg'}^*$ , but also  $u_{gg'}(i_{r=2})$ . As a consequence, both impurity spins couple to the same Fermi orbital (see case A) in Fig. 3.7).

Now, the question of interest is, how the  $n_F$  Fermi electrons distribute over these  $G_F$  Fermi orbitals. In all numerical calculations it was found, that the coupled orbital (i.e. the one to which the impurities couple) favors to become singly occupied. In contrary to fully occupied or empty Fermi orbitals, a singly occupied one is magnetic, which allows the impurity spins to align according to  $J_{\text{eff}}$ . As  $J$  and  $J_{\text{eff}}$  always have the same sign, and  $J$  is chosen to be antiferromagnetic, the two impurity spins couple antiferromagnetically to the Fermi electron in that first orbital. The  $k_F$ -electron tries to screen both impurity spins, which is not fully possible as there are two impurity spin channels. This is a textbook example of underscreening, resulting in a doublet, formed by the first Fermi electron and both impurities. Moreover, one can regard this situation as a perfect central-spin model, with the Fermi electron being the center coupled to two impurity spins. For this model, the Lieb-Mattis theorem [147] holds true. The theorem states, that the ground state multiplet has a total spin of  $|S_A - S_B|$ , where  $S_A$  ( $S_B$ ) is the maximum total spin of a bipartite sublattice  $A$  ( $B$ ). The theorem can be applied, if the coupling between spins on the same sublattice is ferromagnetic (or zero), and antiferromagnetic between the sublattices. Note, that the constraint of ferromagnetic coupling within a sublattice is not of relevance here, as the electronic sublattice contains only a single "site" (i.e. coupling Fermi orbital) and the sublattice of impurity spins has no interimpurity coupling. However, the second condition (antiferromagnetic coupling between sublattices) is true here, giving a total spin of one for the impurities and a total spin-1/2 for the Fermi electron. According to the theorem, this gives a ground state doublet, proving the presented results right.

The remaining Fermi electrons distribute over  $G_F - 1$  spin-degenerate Fermi orbitals, so that the total degeneracy of the ground state in case A),  $\text{GSD}(A)$ , can be written as

$$\text{GSD}(A) = 2 \cdot \binom{2(G_F - 1)}{n_F - 1}. \quad (3.33)$$

This formula holds true for on-resonant cases, which is  $0 < n_F < 2G_F$ . The first factor comes from the doublet, while the binomial represents the Fermi orbitals that are not coupled to either impurity spin. It must be emphasized, that the latter are not specified by the unitary transformation  $V$  given by Eq. (3.18). However, these orbitals are by construction pairwise orthogonal, which allows to write down the binomial as done in the equation above.

### 3.5.2. Case B) - Partially overlapping coupling Fermi orbitals

The case of partially overlapping Fermi orbitals (see case B) in Fig. 3.7) is more complicated to understand due to its difficult visualization. Starting again from the theoretical point of view, the transformation matrices  $V$  and  $V^*$ , given in Eq. (3.18), diagonalize by construction  $u_{gg'}(i_{r=1})$ , but do not diagonalize  $u_{gg'}(i_{r=2})$ . Therefore, it is not possible to find a representation, where the impurity spins couple to single Fermi orbitals given in the same basis. In other words, diagonalizing  $u_{gg'}(i_{r=1})$  gives a set of  $G_F$  pairwise orthogonal Fermi orbitals for the first impurity, where its spin couples to one orbital only, while the second impurity spin couples to several Fermi orbitals in the same basis, see Fig. 3.8. This picture has the enormous drawback, that the second impurity spin couples partially to several Fermi orbitals. It is not intuitive, what happens physically if such a partially coupled orbital is occupied by a Fermi electron. It thus seems smarter to mix up the two sets of Fermi orbitals, where each set is constructed in a way, that the corresponding impurity couples to one Fermi orbital only. One then picks out the coupling Fermi orbitals, which gives the left part of case B) in Fig. 3.7 (overlapping blue circles connected to red spins).

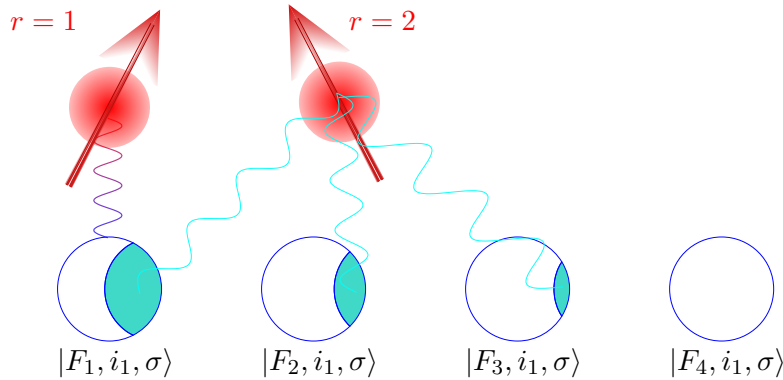


Figure 3.8.: Schematic picture of overlapping Fermi orbitals (case B)) in basis of the first ( $r = 1$ ) impurity. White circles with blue borders represent the orthogonal Fermi orbital set of the first impurity. Within this set, the turquoise areas represent the overlapping part of the second impurity's coupling Fermi orbital ( $h' = 1$ ). Although this is a correct visualization, it is not useful because it would lead to irritating, or even wrong conclusions when talking about Fermi electron occupation.

It has proven useful to introduce the linear span  $\mathcal{L}_{\text{c.o.}}$  of the subspace of coupling orbitals ("c.o."), i.e. the Fermi orbitals that are coupled to impurity spins. For case B),  $\mathcal{L}_{\text{c.o.}} = 2$ , thus up to four Fermi electrons can be found in these orbitals, respecting Pauli's exclusion principle. This information is important in two ways: Firstly, one knows to how many

$k_F$ -electrons the impurity spins may couple and, secondly, how many orbitals remain uncoupled, namely  $G_F - \mathcal{L}_{c.o.}$ .

It is everything but a vivid depiction, how overlapping Fermi orbitals of different sets have to be understood. Indeed, it is possible to find an overlap between the coupling orbital of the first set with uncoupled Fermi orbitals in the representation of the second basis. Even the extreme case, that the coupling orbital of the first set is a linear combination of all Fermi orbitals of the second set, cannot be excluded in any way. All that counts, however, is the number of coupling orbitals defining the linear span. It might be due to the freedom of choosing  $G_F - 1$  arbitrary, uncoupled but pairwise orthogonal vectors for each set, that these uncoupled Fermi orbitals may be separated from the coupled Fermi orbitals. Even if a coupling orbital has unavoidably overlap with an uncoupled one from a different set, the linear span  $\mathcal{L}_{c.o.}$  is not affected. As noted before, there is no intuitive illustration for this fact. Consequently, the bubble of uncoupled Fermi orbitals (right part of Fig. 3.7, case B)) cannot be specified, and must be understood as a construct of  $G_F - \mathcal{L}_{c.o.}$  orbitals. As will be seen later (see Fig. 3.10), numerical results underline this concept.

Filling the Fermi orbitals with  $k_F$ -electrons is qualitatively similar to case A): The coupling Fermi orbitals are preferably singly occupied, as this minimizes the internal energy. If one  $k_F$ -electron is present, the overlapping Fermi orbitals contain an electronic spin-1/2, which couples to both impurity spins (with spin-1/2 each). In total, one impurity spin-1/2 can be screened, and an impurity spin-1/2 remains unscreened. One thus gets a doublet, which is twofold degenerate. Note, however, that the Fermi orbitals overlap, leading to partial screening of both impurities rather than complete screening of one impurity spin. This can be proven by checking the interimpurity correlation function  $\mathbf{S}_1\mathbf{S}_2$ , which is non-zero (see an example in Fig. 3.11). This is clear due to the Fermi orbitals' overlap, which allows an indirect impurity coupling mediated by the Fermi electron.

By adding a second Fermi electron, both coupling Fermi orbitals become singly occupied. Complete screening of the impurity spins is possible, leading to a (nondegenerate) singlet state. Although other configurations, such as triplet states, can generally not be excluded, nothing but singlets have been found in the numerical calculations done for the present work. This is, however, not surprising, because the impurity spins are coupled antiferromagnetically to the Fermi electrons, thus preferring singlet formation rather than triplets or quintuplets.

According to the rule, that coupling Fermi orbitals are preferably singly occupied, further increase of  $k_F$ -electrons results in filling of the uncoupled Fermi orbitals (if present). Not until the uncoupled Fermi orbitals are fully occupied, the coupling Fermi orbitals become doubly occupied (see, for example, Fig. 3.10). This underlines again, that singly occupied coupling Fermi orbitals decrease the internal energy the most.

Summing the discussion above up, one gets the following degeneracy of the ground state for case B):

$$\text{GSD(B)} = \begin{cases} 2 & , \text{ if } n_F = 1 \text{ or } n_F = 2G_F - 1 \\ 1 & , \text{ if } n_F = 2 \text{ or } n_F = 2G_F - 2 \\ \binom{2(G_F-2)}{n_F-2} & , \text{ if } 2 < n_F < 2G_F - 2 \end{cases} . \quad (3.34)$$

Note, moreover, that Eq. (3.34) holds true for both equal and unequal coupling strengths  $J_{\text{eff}}(i_{1,2}) \neq 0$ .

### 3.5.3. Case C) - No overlap between coupling Fermi orbitals

The third and last scenario of how two coupling Fermi orbitals are related to one another is the case of missing overlap (case C), depicted in Fig. 3.7). Mathematically, the transformation matrices  $V$  and  $V^*$ , given in Eq. (3.18), diagonalize both  $u_{gg'}(i_{r=1})$  for the first and  $u_{gg'}(i_{r=2})$  for the second impurity. In contrast to case A), these diagonalizations have a different eigenvalue each, returning two orthogonal and thus linearly independent coupling Fermi orbitals. The linear span is again  $\mathcal{L}_{\text{c.o.}} = 2$ , thus providing  $G_F - \mathcal{L}_{\text{c.o.}}$  uncoupled Fermi orbitals.

Due to complete separation of the two coupling Fermi orbitals, a new aspect comes into play: Assuming there is only one Fermi electron, which Fermi orbital becomes occupied? The answer to this question is dependent on the two effective coupling strengths  $J_{\text{eff}}(h = 1, i_1)$  and  $J_{\text{eff}}(h' = 1, i_2)$ . For reasons of compactness, the coupling Fermi orbital indices  $h$  and  $h'$  are neglected in the following. If  $J_{\text{eff}}(i_1) \neq J_{\text{eff}}(i_2)$ , the Fermi orbital with stronger effective coupling becomes occupied. However, if both effective coupling constants are equal, occupying either Fermi orbital is equally probable. The latter case thus increases the number of possible ground state configurations, i.e. the degeneracy, by a factor of two (see Fig. 3.10 for a specific example). Note, that such a situation does not occur in case B), because the Fermi orbitals have a finite overlap there. Therefore, for scenario B) there is no selection rule to which impurity the Fermi electron should couple as it always couples to both impurity spins.

In the non-overlapping case, however, only one impurity couples (antiferromagnetically) to exactly one Fermi orbital. Thus, each impurity spin is fully screened, if enough  $k_F$ -electrons are present. In case of only one singly occupied coupling Fermi orbital ( $n_F = 1$ , and  $n_F = 2G_F - 1$ ), the second impurity spin is uncoupled, giving an impurity spin degeneracy of two, which is reflected in the twofold ground state degeneracy. For two Fermi electrons (and likewise for  $n_F = 2G_F - 2$  Fermi electrons), both impurity spins form singlets with the  $k_F$ -electrons in their respective Fermi orbitals. Additional Fermi electrons then occupy uncoupled Fermi orbitals up to their complete filling, just as described for the cases A) and B) above.

In total, the degeneracy of the ground state for the non-overlapping case C) reads:

$$\text{GSD(C)} = \begin{cases} 2 & , \text{ if } n_F = 1 \text{ or } n_F = 2G_F - 1, \text{ and } J_{\text{eff}}(i_1) \neq J_{\text{eff}}(i_2) \\ 4 & , \text{ if } n_F = 1 \text{ or } n_F = 2G_F - 1, \text{ and } J_{\text{eff}}(i_1) = J_{\text{eff}}(i_2) \\ 1 & , \text{ if } n_F = 2 \text{ or } n_F = 2G_F - 2 \\ \binom{2(G_F-2)}{n_F-2} & , \text{ if } 2 < n_F < 2G_F - 2 \end{cases} . \quad (3.35)$$

Note, that the analysis of the effective coupling strengths is only relevant if one Fermi orbital is singly occupied. In all other cases, both impurities couple to both coupling Fermi orbitals, disregarding the specific strengths of  $J_{\text{eff}}(i_1)$  and  $J_{\text{eff}}(i_2)$ .

### 3.5.4. Examination of two impurities on a square-lattice

In the following, numerical results are presented to confirm the descriptions above. A square lattice of size  $8 \times 8$  with open boundary conditions is chosen, see Fig. 3.9, where the total filling  $n$  is set to approximately half-filling, resulting in an eightfold degenerate Fermi energy level  $\varepsilon_F$ . The figure shows, which scenario results depending on the location of the two impurities, and if the effective couplings are equal or unequal.

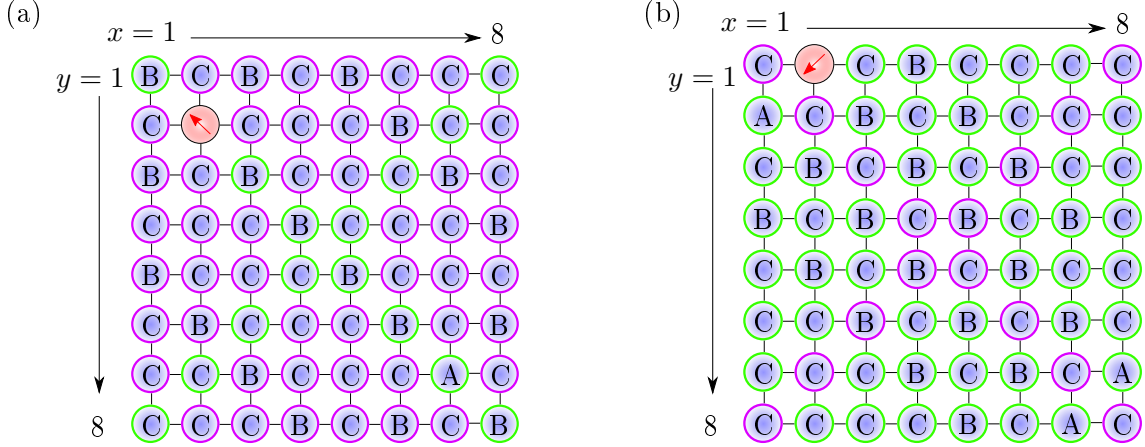


Figure 3.9.: Two impurities located on an  $8 \times 8$ -square lattice with open boundary conditions. The total filling is around half-filling, assuring an eightfold degenerate Fermi energy  $\varepsilon_F$  (see also Fig. 3.6(b)). In (a), the first impurity is fixed at site (2;2), while in (b) an impurity is fixed at site (1;2) (red bubble with red arrow inside). The letters A, B, and C label the physical situation found, if the second impurity is located at the corresponding lattice site. Green borders around the lattice sites represent cases, where both effective coupling strengths are equal, i.e.  $J_{\text{eff}}(i_1) = J_{\text{eff}}(i_2)$ , while violet borders show cases with  $J_{\text{eff}}(i_1) \neq J_{\text{eff}}(i_2)$ .

There is an obvious symmetry along the main diagonal, which is due to the symmetric form of the free Hamiltonian  $\mathcal{H}_0$ . Note, that neither overlap nor effective coupling strengths are influenced by the impurity positions, as these quantities solely depend on the  $U$ -matrices that diagonalize  $\mathcal{H}_0$ . The impurities' positions, however, are important to pick out specific parts of the  $U$ -matrices, giving site-dependent results.

In the following, some specific impurity locations are selected to represent the three possible overlap scenarios, checking the theoretical predictions from Secs. 3.5.1 to 3.5.3.

#### Ground state degeneracy for selected configurations

As a prove of concept, Fig. 3.10 shows representative numerical results for the ground state degeneracy of the three cases A), B), and C). For full overlap of the Fermi orbitals (case A)), the linear span of coupling orbitals is one, thus there is one more uncoupled Fermi orbital than in cases B) and C), where  $\mathcal{L}_{\text{c.o.}} = 2$  (reminder: number of uncoupled orbitals is  $G_F - \mathcal{L}_{\text{c.o.}}$ ). This is reflected in a much greater ground state degeneracy for case A), especially around half-filling of Fermi electrons. In cases B) and C),  $G_F - \mathcal{L}_{\text{c.o.}} = 6$  Fermi orbitals remain uncoupled, leading to the same ground state degeneracy in the range of  $2 < n_F < 14$ .

In all cases, a huge jump in the ground state degeneracy occurs from  $n_F = \mathcal{L}_{\text{c.o.}} \rightarrow \mathcal{L}_{\text{c.o.}} + 1$ , which is a clear indicator, that uncoupled Fermi orbitals are occupied for  $n_F > \mathcal{L}_{\text{c.o.}}$ . For  $n_F \leq \mathcal{L}_{\text{c.o.}}$ , on the other hand, the ground state degeneracy must result from singly

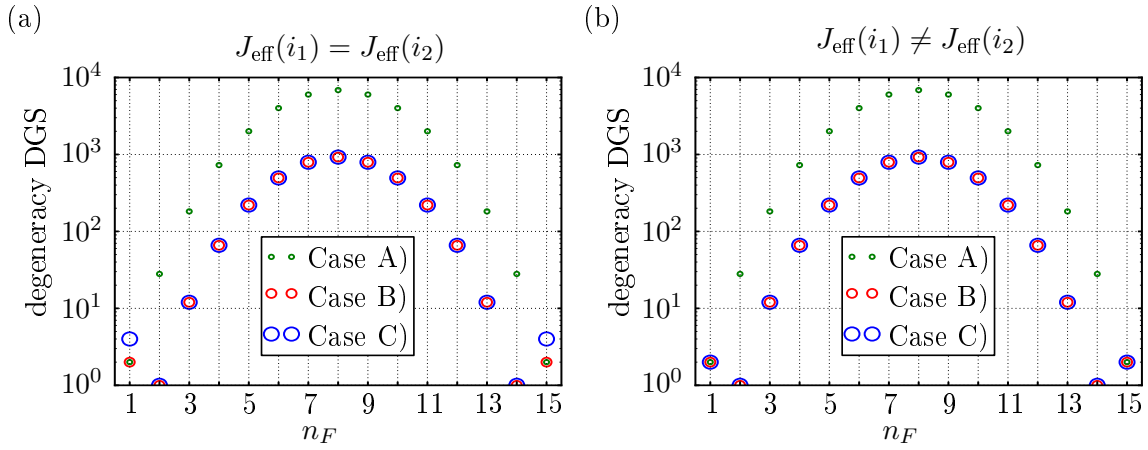


Figure 3.10.: Degeneracy of the ground state plotted semi-logarithmically against the amount of  $k_F$ -electrons for an eightfold degenerate Fermi energy  $\varepsilon_F$ , i.e.  $G_F = 8$  (see also Eqs. (3.33)-(3.35) for specific values). The effective coupling strengths  $J_{\text{eff}}$  between impurity spin and corresponding Fermi orbital are either equal (a) or unequal (b). The original system is an  $8 \times 8$ -square lattice with open boundary conditions, where the first impurity is located at site (2;2). To realize the three cases for equal coupling strengths, the second impurity is located at (7;7) for case A), (4;4) for case B), and (6;3) for case C). In (b), case A) cannot be realized with the given lattice parameters, but theoretically expected data points are given for completeness. While the first impurity is again located at (2;2), the second one is on sites (3;7) for case B), and (8;5) for case C).

occupied coupling Fermi orbitals, since the degeneracy is rather small. If, for example, one Fermi electron occupied an uncoupled orbital, the minimum degeneracy is  $\binom{14}{1} = 14$  for case A), or  $\binom{12}{1} = 12$  for cases B) and C). This exceeds the found values in the  $n_F \leq \mathcal{L}_{\text{c.o.}}$  regime by far. Moreover, the symmetric form of the diagrams in Fig. 3.10 shows, that singly occupied coupling orbitals remain singly occupied, if additional Fermi electrons can occupy uncoupled Fermi orbitals. Not until all of the uncoupled orbitals are doubly occupied, the coupling orbitals become fully occupied. This can be seen at the crossover  $n_F = 2G_F - \mathcal{L}_{\text{c.o.}} \rightarrow 2G_F - \mathcal{L}_{\text{c.o.}} + 1$ , where the degeneracy of ground states decreases dramatically. This behavior is of course expected, because empty orbitals are equivalent to fully occupied ones in particle-hole symmetric models. Therefore, statements made for fillings below half-filling of Fermi orbitals are likewise valid for the case of more than half-filling.

Another aspect to revive is the partial overlap case (i.e. case B)), which is difficult to grasp due to the mixing of different bases of the coupling Fermi orbitals. For this reason, the concept of the linear span of coupling orbitals,  $\mathcal{L}_{\text{c.o.}}$ , has been introduced. The exemplary data in Fig. 3.10, combined with the discussions in the previous paragraphs, shows that this concept seems to be successful. If more than two Fermi orbitals were connected to the impurities, there must be fewer uncoupled Fermi orbitals. This would lead to lower ground state degeneracy than calculated by Eq. (3.34). This is, however, not the case, legitimating the concept of using the linear span.

For determining the ground state degeneracy, the exemplary data points presented in Fig. 3.10 underline, that the specific values of the effective coupling strengths  $J_{\text{eff}}$  are only relevant if the coupling Fermi orbitals do not overlap, which is case C), and if only one coupling Fermi orbital is singly occupied. If these requirements are fulfilled, the relation between  $J_{\text{eff}}(i_1)$  and  $J_{\text{eff}}(i_2)$  determines whether the ground state has an additional degeneracy due to identical physical situations (which is the case if  $J_{\text{eff}}(i_1) = J_{\text{eff}}(i_2)$ ).

### Spin–spin correlations

In order to underpin the results presented before, Fig. 3.11 shows exemplary data points for the impurity–impurity correlations for the three cases. If the Fermi orbitals overlap fully (case A)), and the effective coupling strengths are equal, both impurity spins align perfectly antiferromagnetic to the  $k_F$ -electron in the coupling orbital. Consequently, both impurity spins have the same orientation, giving  $\langle \mathbf{S}_1 \mathbf{S}_2 \rangle = 0.25$ , which is parallel alignment, and thus ferromagnetic coupling. This result matches perfectly to the Lieb–Mattis theorem [147], where each sublattice is assumed to be ferromagnetic (including the case of no intra-sublattice interactions). The case of unequal effective couplings cannot be found in the original  $8 \times 8$ -lattice at around half-filling and will thus be investigated below (see page 39).

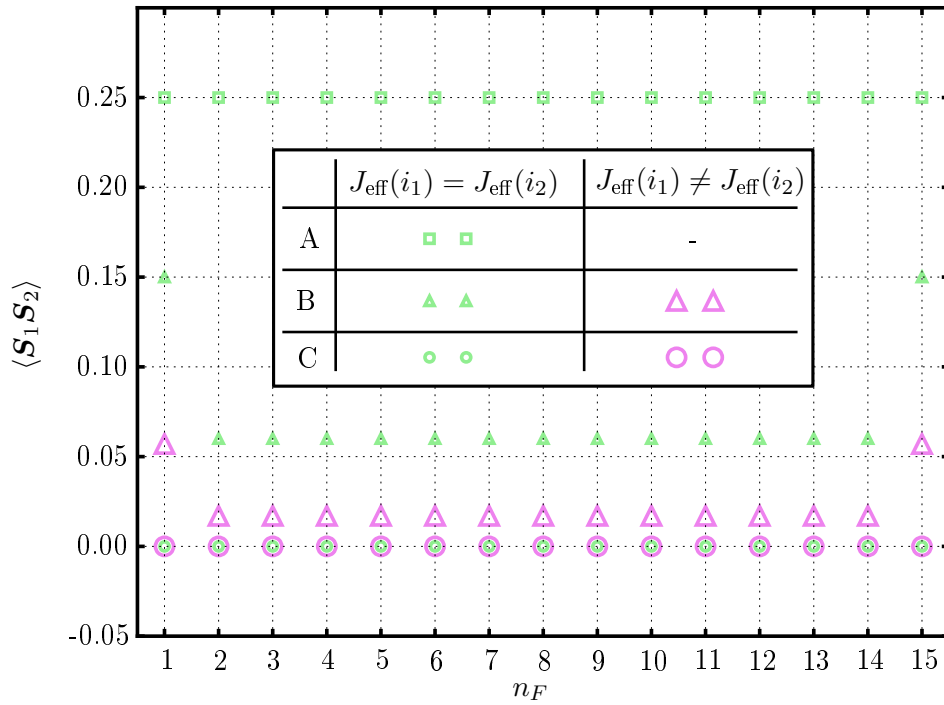


Figure 3.11.: Exemplary interimpurity correlations plotted against the amount of  $k_F$ -electrons for a system with  $G_F = 8$ . The data comes from specific impurity placement, with the first impurity always fixed at site (2;2) and the second at site (7;7) for case A), site (4;4) for case B), and site (6;3) for case C), all of the above for equal effective coupling strengths. If  $J_{\text{eff}}(i_1) \neq J_{\text{eff}}(i_2)$ , the second impurity was placed at sites (3;7) for case B), and (8;5) for case C). Since case A) with unequal  $J_{\text{eff}}$  is not present in the given system (see Fig. 3.9), there is no data.

The data for case B), i.e. partially overlapping Fermi orbitals, are qualitatively representative, but not quantitatively. For different locations of the two impurities, the data points might even overlap, or found at different values. Neither can be said, that equal effective couplings show stronger spin–spin correlations than in case of unequal coupling strengths. However, there is a clear sign of lower spin–spin correlations, if both coupling Fermi orbitals are singly occupied rather than only one is singly occupied. This indicates, that the impurity spins tend to form singlets with  $k_F$ -electrons, which is easier if there is one Fermi electron for each impurity. Since both impurities are connected via the Fermi orbitals, it is however not surprising to find finite values for the correlation function.

One can moreover see, that the correlation functions shown in Fig. 3.11 are either vanishing (case C)), or positive, showing in the latter case that the impurities align parallel and their



correlation is thus ferromagnetic. That the correlation is zero if the coupling Fermi orbitals have no overlap is an expected result, because the impurities are not connected via somehow overlapping Fermi orbitals, and thus there is no medium to mediate a correlation between them.

In all cases, but best seen in case B), the correlation function remains unchanged in between  $2 \leq n_F \leq 14$ . Especially for case A), which has one more uncoupled Fermi orbital than cases B) and C), this holds true for the range  $1 \leq n_F \leq 15$ . It can be concluded, that the construct of spins and Fermi electrons occupying coupling orbitals is not affected by any additional  $k_F$ -electrons, as long as the coupling Fermi orbitals remain singly occupied. This result goes hand in hand with the numerical data shown in Fig. 3.10, where the degeneracy of the ground state indicates that singly occupying coupling Fermi orbitals has highest priority. Since the correlation function does not change after the coupling Fermi orbitals are singly occupied, the idea of the linear span of coupling Fermi orbitals finds again its confirmation. It moreover shows, as said before, that the schematic picture 3.8 is not helpful to understand the underlying physics.

### Completion of missing data from case A)

The analysis above is yet not complete, as it suffers from the lack of data for case A), if the effective coupling strengths are not equal. Staying with the  $8 \times 8$ -square lattice, but changing the total filling to  $n = 43$ , one enters a regime of a nondegenerate Fermi energy level  $\varepsilon_F$  (see the energy level distribution in Fig. 3.6(b)). Consequently, only one Fermi orbital exists, so that both impurities unavoidably couple to this orbital. No matter how the impurities are placed on the lattice, it is always case A) (full Fermi orbital overlap), without any remaining uncoupled Fermi orbitals.

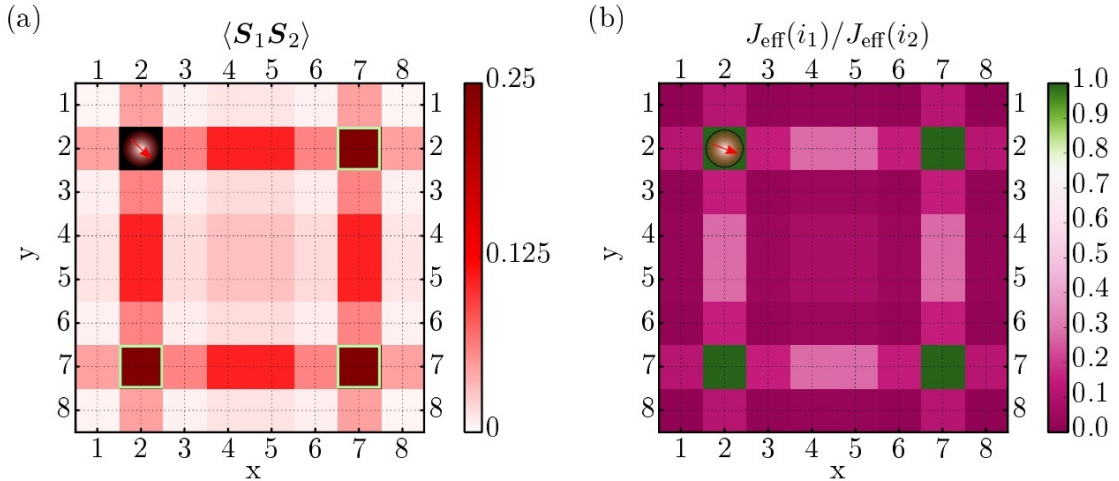


Figure 3.12.: Given an  $8 \times 8$ -square lattice with open boundary conditions and a total filling of  $n = 43$ . Due to this nondegenerate case,  $G_F = 1$  and  $n_F = 1$ . One impurity is fixed at site  $(x; y) = (2; 2)$ , the other one is passed through the entire lattice. (a) Correlations between the impurity spins in the ground state. The green boxes show sites, where the effective coupling strengths are equal. On all other sites,  $J_{\text{eff}}(i_1) \neq J_{\text{eff}}(i_2)$ . (b) Quotient of the effective couplings (normed to a maximum of one).

The question to answer is, whether the interimpurity spin–spin correlation is dependent on the effective coupling strengths. As shown in Fig. 3.12, this is indeed the case. For the given system with  $n = 43$  electrons, one finds situations with equal coupling strengths, i.e. one impurity is located at site  $(2; 2)$ , while the second one is either placed on  $(2; 7)$ ,  $(7; 2)$ , or

(7;7). In these cases, the quotient of the effective couplings is trivially one (see (b) in the above mentioned figure), and the interimpurity spin-spin correlation is  $1/4$ , as previous results for case A) with equal coupling strengths have already shown (see Fig. 3.11,  $n_F = 1$ ). However, if the coupling strengths are not equal, the spin-spin correlation is less than  $1/4$ , meaning that both spins are not aligned perfectly ferromagnetic. Combining the results from Figs. 3.12(a) and (b), it can be seen that the strength of the correlation is directly connected to the quotient of the effective coupling strengths: The weaker one impurity (compared to the other impurity) is coupled to the Fermi orbital, the smaller the spin-spin correlation becomes. This can be understood as follows: Fermi electron and the impurity with stronger effective coupling try to form a singlet, but the impurity with weaker  $J_{\text{eff}}$  also tries to align antiparallel with the  $k_F$ -electron. This competition scales obviously with the coupling strengths. One limiting case is a vanishing effective coupling, which results in a singlet of Fermi electron and the stronger bound impurity spin, while a free impurity remains. Thus, the interimpurity spin-spin correlation must be zero. Another limiting case is the scenario of equal coupling strengths, where no impurity spin can be favored for singlet formation. By aligning both impurity spins alike (thus giving  $\langle \mathbf{S}_1 \mathbf{S}_2 \rangle = 1/4$ ), the screening is most effective, reducing the internal energy the most. The crossover between these limiting cases is fluid.

For selected impurity locations, all numerical results fit well into the theoretical framework established above. It is, however, neither possible nor desired to check every impurity configuration. Moreover, one probably does not want to restrict oneself to a fixed lattice size of  $8 \times 8$ , and maybe not even to a specific lattice geometry. Therefore, the aim of the next subsection is to generalize the results.

### 3.5.5. Generalizing the results for two-impurity systems

Up to this point, three possible scenarios concerning the overlap of Fermi orbitals in systems with two impurities have been identified. Furthermore, a concept to predict the ground state degeneracy just by knowing the Fermi orbital overlap, the number of Fermi electrons, and the effective coupling strengths, was presented. To this end, exemplary data points were given to underpin and to understand the argument. Topic of the next paragraphs is to show, that the discussions and results above hold true not only for specific system configurations, but for every possible lattice geometry.

In order to generalize the results, the most important step is to free oneself from the rather restrictive  $8 \times 8$ -square lattice used for explanations above. For the previous examples, the geometry of the lattice ( $8 \times 8$ -square lattice) and its electron filling has always been stated. This is, in fact, only necessary to determine the degeneracy of the Fermi energy ( $G_F$ ) and the number of Fermi electrons ( $n_F$ ), according to Fig. 3.6. To predict the physical situation, it is unimportant where a  $G_F$ -fold degenerate Fermi energy has its origins, be that a 1-dimensional ring, an  $8 \times 8$ -square lattice with open boundary conditions, or any other lattice with electron filling resulting in  $G_F = 2$ . However, the knowledge of the Fermi orbital sets is required, as they give the overlap of coupling Fermi orbitals on the one, and the effective coupling strengths  $J_{\text{eff}}$  on the other hand. To perform an analysis, a toy model for two impurities is introduced in the next paragraphs.

### Toy model for two impurities

To examine the three cases A), B), and C) for arbitrary lattices, a simple toy model is introduced: It consists of two vectors, each representing a coupling Fermi orbital. The first vector is fixed in one direction, say the  $x$ -axis, while the second vector lies within the  $x$ - $y$ -plane. The angle between both vectors, called  $\phi$ , determines the overlap of the coupling Fermi orbitals, and therewith the physical situation, i.e. case A), B), or C), according to Fig. 3.13.

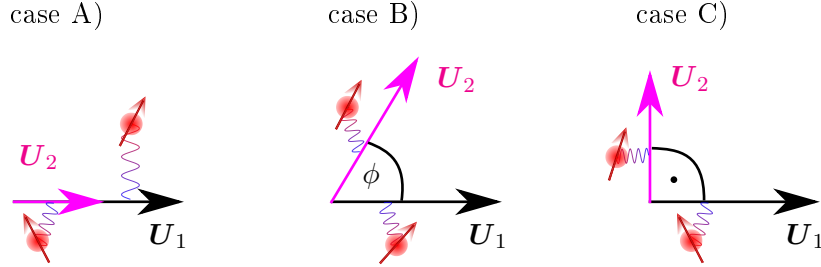


Figure 3.13.: Toy model consisting of two vectors  $U_1$  and  $U_2$ , each representing the coupling Fermi orbital connected to its impurity (red bubble with arrow). Vector  $U_1$  is fixed in size (length = 1), and direction ( $\phi = 0$ ), while  $U_2$  is scalable, and its direction is given by angle  $\phi$ . Dependent on  $\phi$ , one can reproduce either case A) ( $\phi = 0, \pi$ ), case B) ( $0 < \phi < \pi$ ,  $\phi \neq \pi/2$ ), or case C) ( $\phi = \pi/2$ ).

Note, that all Fermi orbitals, both coupling and uncoupled ones, can be represented by vectors living in a  $G_F$ -dimensional Hilbert space, which rises the question, whether the coupling Fermi orbitals can be described by a two-dimensional Hilbert space within the toy model. This is indeed possible, because the linear span of  $r$   $d$ -dimensional vectors is maximally  $r$ , if  $r < d$ . Here,  $r = R = 2$  is the number of impurities and  $d = G_F$  the number of Fermi orbitals, where  $G_F > R$  usually. One can always find a rotation that represents  $R$  vectors in a maximally  $R$ -dimensional Hilbert space. A powerful method of performing such a rotation is the Gram–Schmidt process for orthonormalization of vectors, which is used to iteratively construct orthogonal (and normalized) vectors. For the present work, the Gram–Schmidt process is used to check for linear dependence of the  $R$   $G_F$ -dimensional coupling Fermi orbitals. The first coupling Fermi orbital is used as the starting vector, and one tries to orthonormalize the second against the first vector via the Gram–Schmidt method. If this is not possible, i.e. if the Gram–Schmidt method fails, both vectors are linearly dependent. Contrary, if the process succeeds, both vectors are necessarily linearly independent. This is an important information, especially if more than two impurities are present. The uncoupled Fermi orbitals become irrelevant, because they are orthogonal to the coupling ones by construction. Therefore, performing the Gram–Schmidt process with the uncoupled orbitals produces vectors, which are again orthogonal to the vectors representing the coupling Fermi orbitals. Thus, the Gram–Schmidt process proves, that mapping  $R$  vectors of dimension  $G_F$  to vectors living in  $R$ -dimensional Hilbert space (or even smaller) is mathematically correct, which justifies the usage of the above introduced toy model.

Just for completeness, one can state the following: If the number of impurities (i.e. the number of coupling Fermi orbitals) is greater than the degeneracy of the Fermi energy,  $R > G_F$ , then  $R - G_F$  coupling Fermi orbitals are linearly dependent. For  $R = 2$ , this would be the case for nondegenerate ( $G_F = 1$ ) one-particle energies.

The focus of the presented toy model is to examine a greater range of the Fermi orbital overlap, as well as the weight of the coupling Fermi orbitals (graphically represented by the toy model's vector lengths). As will be shown below, this directly corresponds to

the coupling  $J_{\text{eff}}$  of impurities to the Fermi orbitals, which is therefore a freely selectable parameter.

In general, the transformation matrix elements  $U_{k_F g, i_r}$ , used for the coupling Fermi orbitals (see Eq. (3.25)), have different weights for different impurities  $r$ . This is due to the cutoff of states in momentum space, which reduces the number of momentum states to  $k = k_F$ . The overlap, however, is a normalized quantity, thus disregarding different weights. Therefore, the overlap  $\Omega$  directly corresponds to the angle  $\phi$  in the toy model, because

$$\Omega_{12} = \frac{\mathbf{U}_1 \cdot \mathbf{U}_2}{|\mathbf{U}_1| |\mathbf{U}_2|} = \cos(\phi) . \quad (3.36)$$

Different weights of the  $\mathbf{U}$ -vectors manifest themselves in miscellaneous effective coupling strengths, as can be seen in Eq. (3.29). For whatever kind of system, all coupling Fermi orbitals can be normalized, maybe for the price of different effective coupling strengths for certain impurities. Transferring this to the toy model brings the insight, that different vector lengths of  $\mathbf{U}_2$  ( $\mathbf{U}_1$  has been fixed!) do not change the overlap  $\Omega$ , but certainly the effective coupling strength  $J_{\text{eff}}(2)$ . Note, that this is just a convention. Exchanging  $J_{\text{eff}}(1)$  by  $J_{\text{eff}}(2)$  leads, naturally, to the same results, since only the corresponding orbitals are switched.

### Results obtained with the two-impurity toy model

The overlap  $\Omega_{12}$ , as well as the relation between the two effective coupling strengths,  $J_{\text{eff}}(1)/J_{\text{eff}}(2)$ , are important quantities. In Fig. 3.14, the difference between ground state energy and first excited energy ( $|\Delta E_{0 \leftrightarrow 1}|$ ) is plotted against all possible overlaps and for different effective coupling relations, providing a visualization for changes of the ground state degeneracy. In Fig. 3.14(a), the number of Fermi electrons is fixed to  $n_F = 1$ , but results are the same for  $n_F = 3$  due to particle-hole symmetry.  $\Omega_{12} = 0$  is a symmetry axis, because the sign of  $\Omega_{12}$  only represents the (unimportant) orientation of the coupling Fermi orbitals.

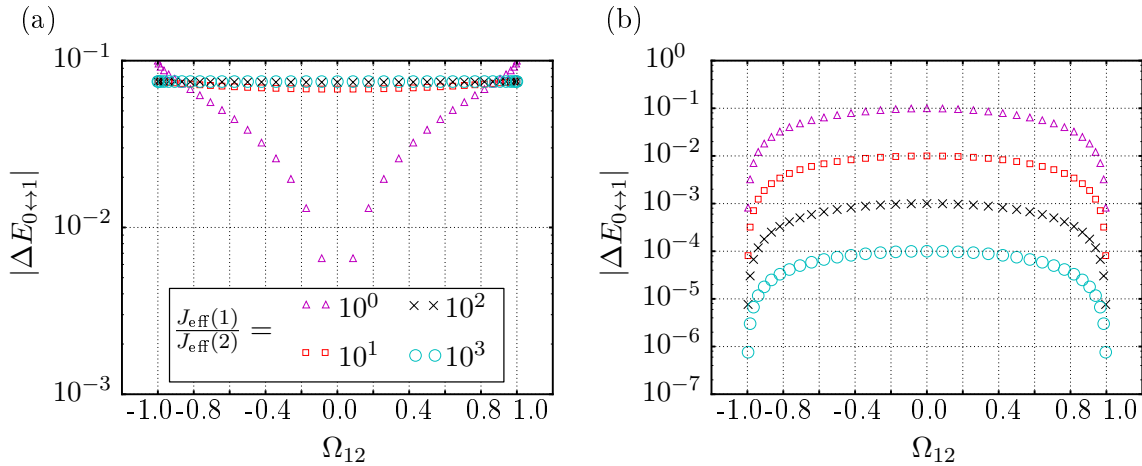


Figure 3.14.: Absolute value of the difference between ground state energy and first excited energy  $|\Delta E_{0 \leftrightarrow 1}|$ , plotted against the overlap  $\Omega_{12}$  between the two coupling Fermi orbitals. Shown are results for several quotients between the effective coupling strengths,  $J_{\text{eff}}(1)/J_{\text{eff}}(2)$ . In (a), the number of Fermi electrons  $n_F$  is fixed to 1 (same results for  $n_F = 3$ ), whereas (b) is for  $n_F = 2$ . The legend given in (a) is also valid for (b).

As can be seen in Fig. 3.14(a), there are qualitatively two different situations: If the effective coupling strengths are equal, then ground state energy and first excited energy

merge in the limit  $|\Omega_{12}| \rightarrow 0$ , which manifests as a divergence in the plot. The merging of energy levels goes hand in hand with an increase of the ground state degeneracy. Indeed, for  $n_F = 1$  the ground state degeneracy was found to be two for cases A) and B), but four in case C), which corresponds to  $\Omega_{12} = 0$ . However, if one effective coupling strength dominates over the other, the ground state remains twofold degenerate for case C), because the single Fermi electron always screens the impurity with greater  $J_{\text{eff}}$ .

For  $n_F = 2$ , both impurities are fully screened in cases B) and C), and the ground state is nondegenerate. The crossover to scenario A), i.e.  $\Omega_{12} = \pm 1$ , shows a divergence, and thus an increase of the system's total spin. This is expected, because in case A) a full screening of both impurities is impossible, since only one coupling Fermi orbital is present and thus just one screening channel is provided. Therewith, Fig. 3.14(b) shows the transition from full screening to underscreening in the limit  $\Omega_{12} \rightarrow \pm 1$ . Moreover, one finds that first excited and ground state energies tend to merge, the more one of the coupling strengths dominates over the other. Although this effect does not manifest as a divergence in the plot, the trend nevertheless indicates a phase transition, which occurs if one impurity decouples due to weak  $J_{\text{eff}}$  and eventually remains as a free spin, increasing the total ground state degeneracy. It is in the eye of the beholder, whether the closely lying energy levels are considered degenerate or nondegenerate, what counts is that such a phase transition can be identified. Note also, that the curves presented in Fig. 3.14(b) show qualitatively the same behavior for both equal and unequal effective coupling strengths. This confirms the theoretical predictions from Subsecs. 3.5.1 to 3.5.3.

One can conclude, that the results obtained with the (more general) toy model are in great agreement with the ground state degeneracy predictions made in Eqs. (3.33) - (3.35). Furthermore, Fig. 3.14 shows that the transitions from cases A) ( $\Omega_{12} = \pm 1$ ) to C) ( $\Omega_{12} = 0$ ) occur continuously, so that deviations from the presented results are highly unexpected.

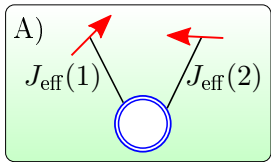
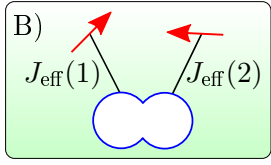
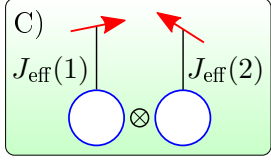
case \ $n_F$	$n_F = 1$	$n_F = 2$
	<p style="text-align: center;"><b>2</b>  <math>\forall G_F</math>  <math>\forall J_{\text{eff}}(1), J_{\text{eff}}(2)</math></p>	<p style="text-align: center;">see Eqs. (3.37)                      and (3.38)</p>
	<p style="text-align: center;"><b>2</b>  <math>\forall G_F (G_F &gt; 1)</math>  <math>\forall J_{\text{eff}}(1), J_{\text{eff}}(2)</math></p>	<p style="text-align: center;"><b>1</b>  <math>\forall G_F (G_F &gt; 1)</math>  <math>\forall J_{\text{eff}}(1), J_{\text{eff}}(2)</math></p>
	<p style="text-align: center;"> <math>\begin{cases} \mathbf{4} &amp; , \text{ if } J_{\text{eff}}(1) = J_{\text{eff}}(2) \\ \mathbf{2} &amp; , \text{ if } J_{\text{eff}}(1) \neq J_{\text{eff}}(2) \end{cases}</math>  <math>\forall G_F (G_F &gt; 1)</math></p>	<p style="text-align: center;"><b>1</b>  <math>\forall G_F (G_F &gt; 1)</math>  <math>\forall J_{\text{eff}}(1), J_{\text{eff}}(2)</math></p>

Table 3.1.: Summary of the ground state's degeneracy for cases A), B), and C), for both one and two Fermi electrons ( $n_F$ ). The bold number represents the part of the ground state degeneracy which is labeled  $\text{GSD}(n_F \leq \mathcal{L}_{\text{c.o.}})$  in the text.  $G_F > 1$  is necessary for cases B) and C). Note, that for all cases  $n_F = 1$  is equivalent to  $n_F = 2G_F - 1$ , and  $n_F = 2$  is equivalent to  $n_F = 2G_F - 2$  for cases B) and C).

Tab. 3.1 summarizes the results found for cases A), B), and C). The systems tend to singly occupy each coupling orbital, as this is the only option to align the connected impurity spins. If more Fermi electrons are available than needed for screening ( $n_F > 1$  in case A),  $n_F > 2$  in cases B) and C)), remaining  $k_F$ -electrons distribute over all uncoupled Fermi orbitals (with a factor of two due to the electronic spin orientation). This information can be put in a general equation: Let  $\text{GSD}(n_F)$  be the total ground state degeneracy for  $n_F$  Fermi electrons, then

$$\text{GSD}(n_F) = \begin{cases} \text{GSD}(n_F \leq \mathcal{L}_{c.o.}) & , \text{ if } n_F \leq \mathcal{L}_{c.o.} \text{ and } n_F \geq 2G_F - \mathcal{L}_{c.o.} \\ \text{GSD}(\mathcal{L}_{c.o.}) \cdot \text{GSD}(U) & , \text{ if } \mathcal{L}_{c.o.} < n_F < 2G_F - \mathcal{L}_{c.o.} \end{cases} \quad (3.37)$$

The reader is reminded, that  $\mathcal{L}_{c.o.}$  is the linear span of coupling Fermi orbitals. For case A),  $\mathcal{L}_{c.o.} = 1$ , while  $\mathcal{L}_{c.o.} = 2$  for cases B) and C). In the regime, where  $n_F \leq \mathcal{L}_{c.o.}$  and  $n_F \geq 2G_F - \mathcal{L}_{c.o.}$ , the total ground state degeneracy arises from the Fermi electrons (singly) occupying the coupling Fermi orbitals, giving a degeneracy called  $\text{GSD}(n_F \leq \mathcal{L}_{c.o.})$ . This value is the one presented in Tab. 3.1. Uncoupled Fermi orbitals simply remain unoccupied, thus they do not affect the total ground state degeneracy, which is why Eq. (3.37) is true for  $G_F \geq \mathcal{L}_{c.o.}$  in this  $n_F$ -regime.

Within the range  $\mathcal{L}_{c.o.} < n_F < 2G_F - \mathcal{L}_{c.o.}$ , the total ground state degeneracy factorizes into a part coming from singly occupied coupling Fermi orbitals, and a factor that comes from the remaining Fermi electrons that occupy uncoupled Fermi orbitals (which requires  $G_F > \mathcal{L}_{c.o.}$ ). The first factor in the corresponding Eq. (3.37),  $\text{GSD}(\mathcal{L}_{c.o.})$ , gives the ground state degeneracy of the "coupled" Fermi orbitals, which are singly occupied by an amount of  $\mathcal{L}_{c.o.}$  Fermi electrons. The value of  $\text{GSD}(\mathcal{L}_{c.o.})$  can be dependent on several parameters, such as effective coupling strengths, and cannot be described by a general formula. The second factor,  $\text{GSD}(U)$ , however, gives the degeneracy of Fermi electrons distributing over  $G_F - \mathcal{L}_{c.o.}$  uncoupled ("U") Fermi orbitals, which can be written as a binomial:

$$\text{GSD}(U) = \binom{2(G_F - \mathcal{L}_{c.o.})}{n_F - \mathcal{L}_{c.o.}}. \quad (3.38)$$

Since the total ground state degeneracy for fillings  $\mathcal{L}_{c.o.} < n_F < 2G_F - \mathcal{L}_{c.o.}$  can easily be calculated with the above formula, and the only "unknown" parameter in Eq. (3.37) is the degeneracy  $\text{GSD}(\mathcal{L}_{c.o.})$ , Tab. 3.1 is restricted to summarize the latter.

As a simple example, case A) for  $n_F = 2$  is briefly discussed: If  $G_F = 1$ , the only Fermi orbital is doubly occupied, giving a fourfold degenerate ground state as the Fermi orbital is magnetically inert. For  $G_F > 1$ , regime  $\mathcal{L}_{c.o.} < n_F < 2G_F - \mathcal{L}_{c.o.}$  of Eq. (3.37) is of interest (since  $\mathcal{L}_{c.o.} = 1$  for this case). From Tab. 3.1, case A),  $n_F = 1$ , one gets  $\text{GSD}(\mathcal{L}_{c.o.} = 1) = \text{GSD}(n_F = 1) = 2$ . This is the degeneracy coming from one Fermi electron singly occupying the coupling Fermi orbital. According to Eq. (3.38), one  $k_F$ -electron remains, distributing over  $G_F - 1$  uncoupled orbitals, thus  $\text{GSD}(U) = \binom{2(G_F - 1)}{2 - 1} = 2(G_F - 1)$ . Following Eq. (3.37),  $\text{GSD}(n_F = 2) = \text{GSD}(\mathcal{L}_{c.o.}) \cdot \text{GSD}(U) = 4(G_F - 1)$ , which is the correct result already known from Eq. (3.33). Note moreover, that  $\text{GSD}(n_F = 2)$  is independent of effective coupling strengths  $J_{\text{eff}}$ , as this property is inherited from  $\text{GSD}(\mathcal{L}_{c.o.} = n_F = 1)$ .

### 3.6. Nanosystems with three impurities

#### 3.6.1. Classification of overlap scenarios

For nanostructures with more than two impurities, the complexity of classification increases enormously. Fig. 3.15 shows in detail, which sorts of (coupling) Fermi orbital overlap are possible, if three impurity spins are present. To avoid confusion with the two-impurity cases, possible overlap scenarios for three impurities are labeled 1), 2a)-d), and 3a)-d), instead. The classification comes from the number of coupling Fermi orbitals (more precisely from their span,  $\mathcal{L}_{c.o.}$ ).

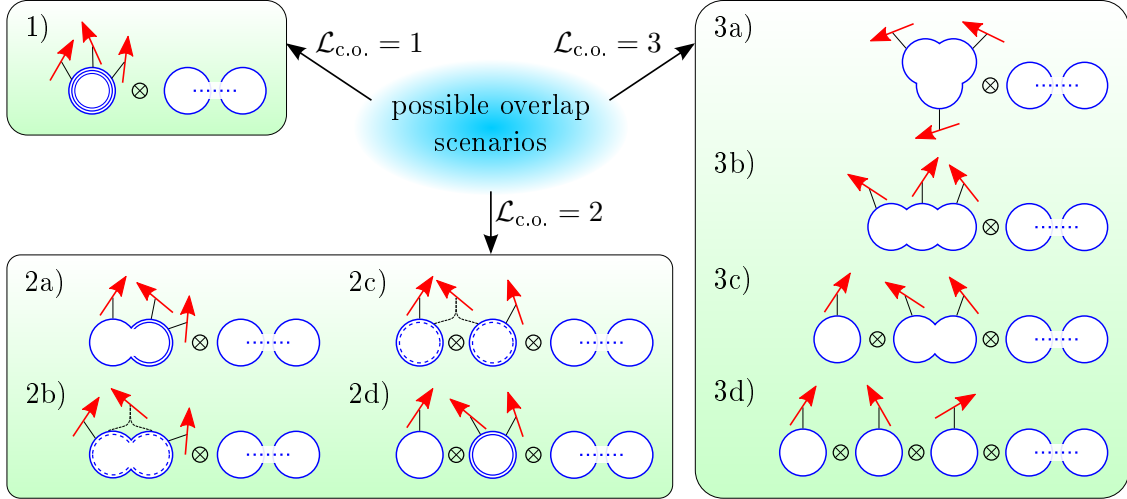


Figure 3.15.: Possible relations between coupling Fermi orbitals for systems with three impurities.  $\mathcal{L}_{c.o.}$  is the span of the subspace constructed by the three coupling orbitals. The triple circle depicted in the upper left box, see 1), represents three identical coupling Fermi orbitals, which consequently overlap fully. Similarly, double circles with solid lines in scenarios 2a) and 2d) stand for two fully overlapping coupling Fermi orbitals. Dashed circles, see cases 2b) and 2c), represent a single coupling Fermi orbital, which is a linear combination of the other two coupling Fermi orbitals (contrary to case 3b), where none of the coupling Fermi orbitals can be written as a linear combination of the others). The tensor product symbol  $\otimes$  indicates orthogonality between Fermi orbitals. Just like in Fig. 3.7, red arrows depict impurities.

To keep the following discussions as simple as possible, the number of Fermi electrons is restricted to a maximum of  $\mathcal{L}_{c.o.}$  for each case. Filling uncoupled Fermi orbitals with electrons simply increases the ground state degeneracy, as has already been shown in the previous sections (see Fig. 3.10, for example). As soon as one Fermi orbital is doubly occupied ( $n_F > G_F$ ), the ground state degeneracy decreases. Empty Fermi orbitals yield the same physics as fully occupied ones, since the orbitals are nonmagnetic in either case. These results apply to all cases, and are therefore not repeated below.

The aim of the next sections is to analyze the nine scenarios by means of a toy model, similar to the one presented in Subsec. 3.5.5.

### 3.6.2. Toy model for three impurities

For all cases depicted in Fig. 3.15, the toy model from Subsec. 3.5.5 can be extended and used for interpretation and discussions. The idea of the toy model is to focus on the coupling Fermi orbitals, where each coupling Fermi orbital is given by a vector. The length of such a vector is proportional to  $J_{\text{eff}}$ , i.e. to the effective coupling strength between impurity spin and its corresponding Fermi orbital. Since three coupling Fermi orbitals are needed, the toy model must consist of three vectors (see Fig. 3.16).

Without loss of generality, the first vector ( $\mathbf{U}_1$ ) can be fixed in  $z$ -direction. The second vector ( $\mathbf{U}_2$ ) always lies within the  $x$ - $z$ -plane. The angle between  $\mathbf{U}_1$  and  $\mathbf{U}_2$  is labeled  $\phi_1$ . The third vector,  $\mathbf{U}_3$ , can point to every coordinate in space, requiring a polar angle (labeled  $\theta_2$ ), and an azimuth angle  $\phi_2$ . Note furthermore, that  $\mathbf{U}_2$  does not require an azimuth angle, since the entire system (all three vectors) can be rotated (around the  $z$ -axis), and angle  $\phi_2$  can be adjusted accordingly. Therefore, the polar angles  $\theta_1$  and  $\theta_2$  lie within the interval  $[0; \pi]$ , while the azimuth angle  $\phi_2$  lies within  $[0; 2\pi]$ . Specific combination of  $\theta_1$ ,  $\theta_2$ , and  $\phi_2$ , gives any scenario depicted in Fig. 3.15.

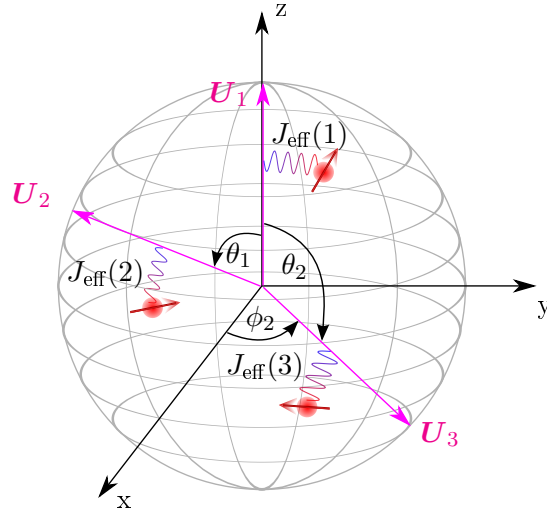


Figure 3.16.: Toy model for three impurities. Magenta vectors  $\mathbf{U}_{1,2,3}$  represent the coupling Fermi orbitals, to which the impurities (red bubbles and arrows) are coupled with strength  $J_{\text{eff}}$ .  $\mathbf{U}_1$  is fixed in  $z$ -direction,  $\mathbf{U}_2$  lies within the  $x$ - $z$ -plane, and  $\mathbf{U}_3$  may point to every direction. The length of the vectors is not necessarily fixed to the sphere radius.

The toy model vectors can be written in the following form:

$$\mathbf{U}_1 = J_{\text{eff}}(1) \begin{pmatrix} 0 \\ 0 \\ 1 \end{pmatrix}, \quad \mathbf{U}_2 = J_{\text{eff}}(2) \begin{pmatrix} \sin \theta_1 \\ 0 \\ \cos \theta_1 \end{pmatrix}, \quad \mathbf{U}_3 = J_{\text{eff}}(3) \begin{pmatrix} \sin \theta_2 \cos \phi_2 \\ \sin \theta_2 \sin \phi_2 \\ \cos \theta_2 \end{pmatrix}. \quad (3.39)$$

One immediately sees, that the overlap  $\Omega$  between two Fermi orbitals (i.e. vectors) is not dependent on  $J_{\text{eff}}$ , as  $\Omega$  is a normalized quantity (recall Eq. (3.36)). The reader is moreover reminded, that the effective coupling strengths  $J_{\text{eff}}$  are (altogether) freely scalable. This is because the toy model does not contain energy scales coming from an underlying lattice geometry, such as a hopping energy  $t$ . Consequently, the toy model is not restricted to weak couplings only. The toy model can rather be understood as a tool to realize all possible coupling Fermi orbitals, and therewith their relations among each other. One can thus examine situations arising from the most exotic lattice geometries, as only their Fermi orbital overlap is relevant to understand their low-energy physics. The next subsections elucidate these physics.



**Case 1) - The analogue to case A)**

Case 1) is very similar to case A) discussed for two-impurity systems. All three coupling Fermi orbitals are identical (i.e.  $\theta_1, \theta_2 \in \{0; \pi\}$ , and  $\phi_2$  arbitrary) giving a span of  $\mathcal{L}_{c.o.} = 1$ , and  $G_F - 1$  uncoupled Fermi orbitals. Several combinations of the number of Fermi electrons ( $n_F$ ), the number of degenerate Fermi levels ( $G_F$ ), and the strength of the effective couplings have to be distinguished.

If possible (dependent on quantities  $n_F$  and  $G_F$ ), the coupling Fermi orbital becomes singly occupied. Under assumption, that all three effective couplings  $J_{\text{eff}}(i = 1, 2, 3) \neq 0$ , this gives a ground state degeneracy of three due to the total spin of  $S = \sum S_{\text{imp}} - \sum S_e = 1$  according to the Lieb–Mattis theorem [147]. Note, that just the Fermi electron which occupies the coupling orbital must be taken into account, as only coupling orbitals form the "central" region of this central-spin model. All other  $k_F$ -electrons are separated from these central-spin model physics, for they distribute over the uncoupled Fermi orbitals. They contribute to the ground state degeneracy according to the binomial from Eq. (3.38) due to their freedom of occupying any uncoupled orbital with either spin orientation. The total ground state degeneracy is then a product of this binomial and the factor three, whereby the latter comes from the central-spin model triplet formed by impurity spins and the  $k_F$ -electron occupying the coupling Fermi orbital.

In some cases, however, the ground state degeneracy is different to the prediction above. This happens, if the coupling orbital becomes magnetically inert due to double occupation ( $n_F = 2G_F$ ), or if one or more effective couplings become very small, technically uncoupling the corresponding impurity spin from the orbital. Each uncoupled impurity contributes to the ground state degeneracy with a factor of two, but also decreases the total spin of the central-spin model.

A numerical prove of these results is found in Fig. 3.17. There, case 1) appears as a limiting case with overlap  $\Omega = 1$ . For one Fermi electron ( $n_F = 1$ , Fig. 3.17(a)) one finds the threefold degenerate ground state, which is independent of the coupling strengths, as explained above. With two Fermi electrons (see Fig. 3.17(b)), the ground state degeneracy depends on the total number of Fermi orbitals  $G_F$ . If  $G_F > 1$ , one  $k_F$ -electron occupies the coupling Fermi orbital (giving the triplet ground state) while the other is in either of  $G_F - 1$  uncoupled Fermi orbitals, increasing the ground state degeneracy by the binomial factor  $\binom{2(G_F-1)}{n_F-1} \stackrel{n_F=2}{=} 2(G_F - 1)$ . Triplet and free  $k_F$ -electron give a total ground state degeneracy of  $6(G_F - 1)$ . On the other hand,  $G_F = 1$  forces both Fermi electrons into the same (and the only present) Fermi orbital, which is therefore nonmagnetic, leaving three uncoupled spins that give a  $2^3 = 8$ -fold degenerate ground state.

**Case 2a) - The analogue to case B)**

If the span of coupling Fermi orbitals ( $\mathcal{L}_{c.o.}$ ) is two, four overlap scenarios are possible (see 2a) - 2d) in Fig. 3.15). Case 2a) is somehow similar to case B) for two-impurity systems, since there are effectively two coupling Fermi orbitals that have neither full, nor vanishing overlap, i.e.  $0 < |\Omega| < 1$ . Contrary to case B), there is an additional impurity spin coupling to either Fermi orbital. Within the toy model, case 2a) occurs, for example, if  $\theta_1 = 0$ , and  $\theta_2 \neq \pi/2$ , while  $\phi_2$  is arbitrary. Of course, different angles may also reproduce this case, but listing them does not bring any further insights.

For investigation of case 2a), the toy model (see Fig. 3.16) consists of two parallel vectors  $\mathbf{U}_2$  and  $\mathbf{U}_3$ , which span an angle  $\theta_1 = \theta_2 = \theta$  (and  $\phi_2 = 0$ ) to vector  $\mathbf{U}_1$ . The overlap is

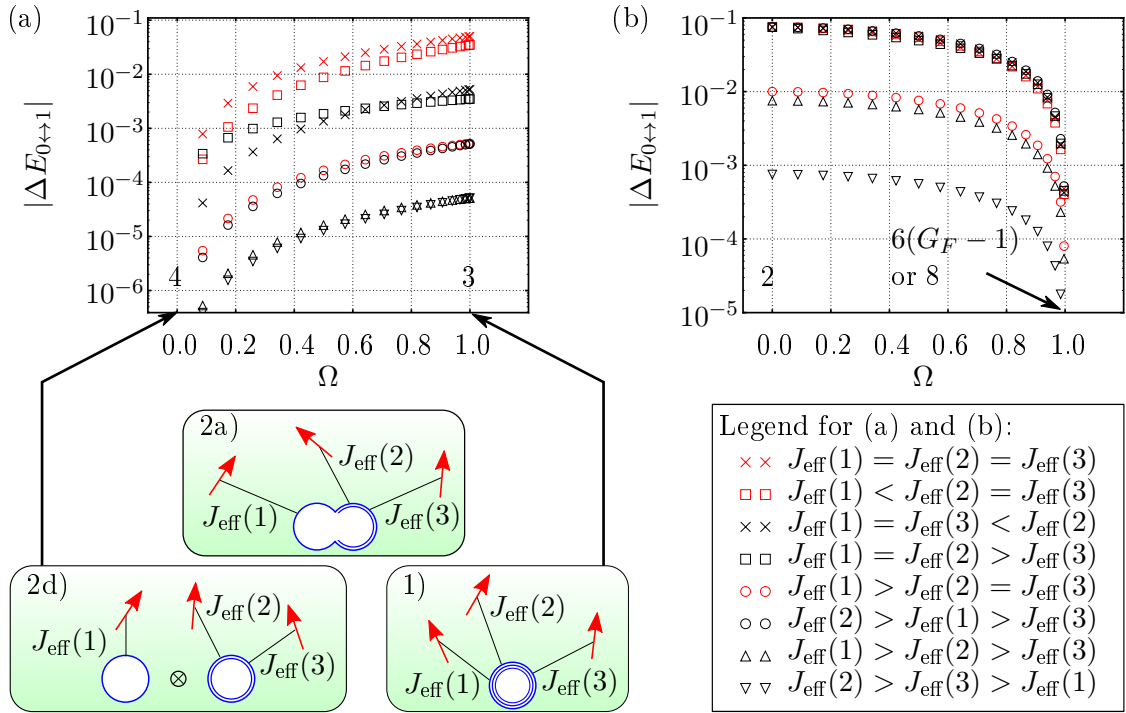


Figure 3.17.: Energy difference  $\Delta E_{0\leftrightarrow 1}$  between ground state and first excited state plotted against various coupling Fermi orbital overlaps  $\Omega$  for (a)  $n_F = 1$  and (b)  $n_F = 2$ . Two coupling orbitals are chosen identical (the ones connected with effective couplings  $J_{\text{eff}}(2)$  and  $J_{\text{eff}}(3)$ ), so that  $0 < \Omega < 1$  gives case 2a). If  $\Omega = 0$ , one coupling Fermi orbital decouples, resulting in case 2d). Likewise,  $\Omega = 1$  is the full overlapping case, i.e. scenario 1), as depicted below the diagram. The numbers and the formula in the diagrams stand for the ground state degeneracy in the limiting cases  $\Omega = 0$  and  $\Omega = 1$ .

thus  $\Omega = \cos(\theta)$ . Case 2a) is found, if  $0 < |\Omega| < 1$ , while  $\Omega = \pm 1$  and  $\Omega = 0$  return cases 1) and 2d), respectively.

Fig. 3.17 shows, dependent on  $\Omega$  and the number of Fermi electrons ( $n_F$ ), how ground state and first excited energy drift apart, or approach one another. This is of interest, since vanishing energy differences  $|\Delta E_{0\leftrightarrow 1}| \rightarrow 0$  imply a possible change in ground state degeneracy, which indeed is found. According to the data presented in Fig. 3.17(a), this happens if  $\Omega \rightarrow 0$  and  $n_F = 1$ , and also if  $\Omega \rightarrow 1$  for  $n_F = 2$ , see Fig. 3.17(b). A main result is, that this behavior can be found for any relation among effective coupling strengths  $J_{\text{eff}}(1)$ ,  $J_{\text{eff}}(2)$ , and  $J_{\text{eff}}(3)$ , no matter if the strengths are equal or differ by several orders in magnitude. Moreover, Fig. 3.17 shows, that transitions between the limiting cases 1) (at  $\Omega = 1$ ) and 2d) (at  $\Omega = 0$ ) are continuous.

If  $n_F = 1$ , system 2a) is closely related to case 1), having the same threefold degenerate ground state. For decreasing overlap, however, a continuous transition from case 2a) to case 2d) occurs. For case 2d), the ground state is always fourfold degenerate, as will be discussed in detail in the corresponding subsection. It remains the question, why case 2a) is rather similar to case 1). A possible reason might be, that coupling all impurity spins to the only Fermi electron is favored for lowering the internal energy. In other words, the favored situation of (partially) screening the impurity spins is only possible, if they are all coupled to the single  $k_F$ -electron. Case 2d), however, always leaves one impurity spin uncoupled, which is therefore an energetically rather unwanted scenario.

Contrary, for  $n_F = 2$  (see Fig. 3.17(b)), cases 2a) and 2d) seem to be closely related, even if the overlap is large. This might be due to the fact, that screening of all impurities

is not only possible, but also easier to achieve as in case 1). Occupying the coupling Fermi orbital of case 1) with two Fermi electrons is not favored, as this does not lower the internal energy (nonmagnetic situation). The other case 1)-scenario, i.e. singly occupying the coupling Fermi orbital with the first, and singly occupying an uncoupled Fermi orbital (if present) with the second Fermi electron, is not favored because only one out of two Fermi electrons can be used for (partially) screening all three impurity spins. In contrast, case 2d) enables both Fermi electrons to (partially) screen the three impurity spins, which is therefore much more favorable than scenario 1). In detail, each of the two coupling Fermi orbitals is then singly occupied. Regardless of  $J_{\text{eff}}(1)$  (but requiring  $J_{\text{eff}}(1) > 0$ ), one  $k_F$ -electron forms a singlet with the corresponding impurity, while the other Fermi electron singly occupies the two-impurity central-spin model, giving a ground state degeneracy of two. However, the transition to case 1) is continuous, but occurs in particular for strong overlap  $\Omega$ . Dependent on the system (precisely on the number of Fermi orbitals  $G_F$ ), a drastic change of the ground state's degeneracy may occur (see discussion of case 1) above for details).

In connection with Fig. 3.17, a final remark should be made on the order of  $\Delta E_{0 \leftrightarrow 1}$ . The presented data is strongly dependent on the choice of the toy model's vector lengths. For example, data points for  $J_{\text{eff}}(1) = 1$ ,  $J_{\text{eff}}(2) = J_{\text{eff}}(3) = 0.1$  are shifted against the data gained by choosing  $J_{\text{eff}}(2) = J_{\text{eff}}(3) = 0.01$ , although both data sets represent the case  $J_{\text{eff}}(1) > J_{\text{eff}}(2) = J_{\text{eff}}(3)$ . The reason is, that the toy model's vectors  $\mathbf{U}$ , which are stretched and shrunk in order to obtain the desired effective coupling strength, are also used to build up the full system's Hamiltonian (which, after diagonalization, gives the energy spectrum). Therefore, the length of the  $\mathbf{U}$ -vectors has direct influence on the energy spectrum, and energy level spacing goes with orders of  $J_{\text{eff}}$ . Thus, the corresponding energy differences  $\Delta E$  are directly affected. In conclusion, Fig. 3.17 helps to qualitatively understand the transition between different orbital overlap scenarios, but is not meant to cover the entire spectrum of effective coupling constants quantitatively. As said before, the fundamental result is to find qualitatively the same crossover behavior, independent of the relation among the three effective coupling strengths.

### Scenario 2b)

The above discussed scenario 2a) differs (together with scenario 2d)) significantly from overlapping cases 2b) and 2c) (review Fig. 3.15), because the latter require three coupling Fermi orbitals, while cases 2a) and 2d) have two coupling orbitals (the third one is identical to either of the other two coupling Fermi orbitals). However, for cases 2b) and 2c), one of the three coupling Fermi orbitals must be linearly dependent on the other two orbitals. This is necessary to get a linear span (of coupling orbitals,  $\mathcal{L}_{\text{c.o.}}$ ) of value two, justifying their classification. One distinguishes between 2b) and 2c) by checking the overlap  $\Omega$  of two linearly independent Fermi orbitals, which is either  $\Omega > 0$ , giving scenario 2b), or  $\Omega = 0$ , which is case 2c).

It might be questionable, if a distinction between cases 2a) and 2b) is useful at all. Regarding the results above, fundamental differences between partially on the one, and fully overlapping orbitals on the other hand have indeed been found. This justifies to take a closer look at these, truly similar looking scenarios. To this end, the toy model (see Fig. 3.16) can again be used. As  $\mathcal{L}_{\text{c.o.}} = 2$ , meaning that one of the coupling Fermi orbitals is linearly dependent on the others, all three coupling orbital vectors  $\mathbf{U}_{1,2,3}$  have to be in one plane (following the notation of the toy model figure, it is the  $x$ - $z$ -plane, with  $\phi_2 = 0$  or  $\phi_2 = \pi$ ). Note, that  $\theta_1 \neq \pi/2$  and  $\theta_2 \neq \pi/2$  must be respected, as this would be scenario 2c).

In Fig. 3.18, the toy models' vectors  $\mathbf{U}_1$  and  $\mathbf{U}_2$  have a fixed overlap of  $\Omega = \cos(80^\circ)$ , and the polar angle  $\theta_2$  of orbital vector  $\mathbf{U}_3$  is varied between  $\mathbf{U}_1$  and  $\mathbf{U}_2$ . Limiting cases are thus  $\theta_2 = 0$ , and  $\theta_2 = 80^\circ$ , where  $\mathbf{U}_3$  has full overlap with either  $\mathbf{U}_1$  or  $\mathbf{U}_2$ , resulting in scenario 2a) as depicted below the diagram. Plotted in Fig. 3.18 are energy differences  $\Delta E_{0\leftrightarrow 1}$  between ground and first excited states, whereby one of the coupling strengths (i.e.  $J_{\text{eff}}(2)$ ) and the number of Fermi electrons  $n_F$  were varied.

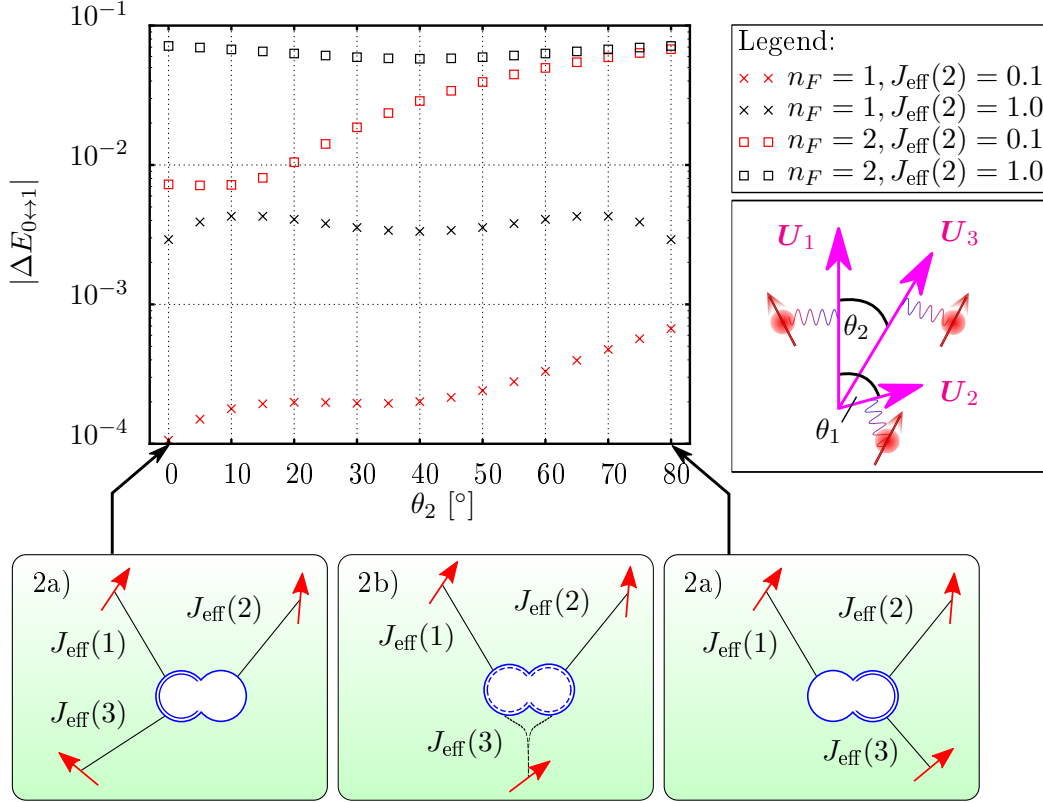


Figure 3.18.: For investigation of scenario 2b), energy differences between ground state and first excited states,  $\Delta E_{0\leftrightarrow 1}$ , are plotted against angle  $\theta_2$  of the toy model (see inset with magenta vectors). Angle  $\theta_1$  between orbitals  $\mathbf{U}_1$  and  $\mathbf{U}_2$  is fixed to  $80^\circ$ . For  $\theta_2 = 0^\circ$  and  $80^\circ$ , two Fermi orbitals are identical, which is case 2a). Red data points stand for a system with an explicitly weak effective coupling  $J_{\text{eff}}(2) = 0.1$ , while black data points represent  $J_{\text{eff}}(2) = 1$ . In all cases,  $J_{\text{eff}}(1) = J_{\text{eff}}(3) = 1$ .

The presented data shows no divergence in  $\Delta E_{0\leftrightarrow 1}$ , therefore the ground state degeneracy is the same as in case 2a). For  $n_F = 1$ , the ground state is thus a triplet (threefold degenerate), while it is a doublet (twofold degenerate) if two Fermi electrons are present.

If all effective coupling strengths are equal (black colored data points in Fig. 3.18), orbital vectors  $\mathbf{U}_1$  and  $\mathbf{U}_2$  are physically equivalent. Concerning orbital vector  $\mathbf{U}_3$ , one expects to find a symmetric point, which should be right in between vectors  $\mathbf{U}_1$  and  $\mathbf{U}_2$ . The figure shows, that this expectation is indeed fulfilled, as data of  $\Delta E_{0\leftrightarrow 1}$  is symmetric to  $\theta_2 = 40^\circ$ .

However, for the exemplary case with  $J_{\text{eff}}(2) < J_{\text{eff}}(1) = J_{\text{eff}}(3)$  (red data points in Fig. 3.18), this symmetry is broken. This is due to the stretching of orbital vector  $\mathbf{U}_2$ , directly influencing the Hamiltonian's energy levels as explained above. For  $\theta_2 \approx \theta_1 = 80^\circ$ , the stretch of  $\mathbf{U}_2$  becomes rather irrelevant, as the Fermi orbitals corresponding to  $\mathbf{U}_1$  and  $\mathbf{U}_3$  are on the same energy scale. Accordingly,  $\Delta E_{0\leftrightarrow 1}$  is of about the same order as in the equal- $J_{\text{eff}}$  case. Decrease of  $\theta_2$  brings orbital vectors  $\mathbf{U}_1$  and  $\mathbf{U}_3$  together, which are of same order (i.e. length), but differ significantly from  $\mathbf{U}_2$ . Since energy level spacing goes with orders of  $J_{\text{eff}}$ , the "almost decoupled" orbital  $\mathbf{U}_2$  significantly changes the energy

spectrum of the Hamiltonian, leading to a decrease in energy differences  $\Delta E$ . This fits to the results presented for case 2a) above.

It goes without saying, that Fig. 3.18 does not cover all possible cases of orbital stretching or shrinking, particularly all relations among effective coupling strengths  $J_{\text{eff}}(1, 2, 3)$ . However, discussions of case 2a) (as the limiting case for  $\theta_2 \rightarrow 0$  and  $\theta_2 \rightarrow \theta_1$ ) have shown, that any combination of  $J_{\text{eff}}(1, 2, 3)$  yields the same qualitative behavior.

While examining different effective coupling strengths seems not promising to bring new insights, the question arises if the results presented above are valid for arbitrary combinations of angles  $\theta_1$  and  $\theta_2$ . For one Fermi electron, Fig. 3.19 shows the entire spectrum of polar angles, where azimuth angle  $\phi_2$  has been set to zero, but simultaneously the range of  $\theta_2$  has been increased from  $180^\circ$  to  $360^\circ$ .

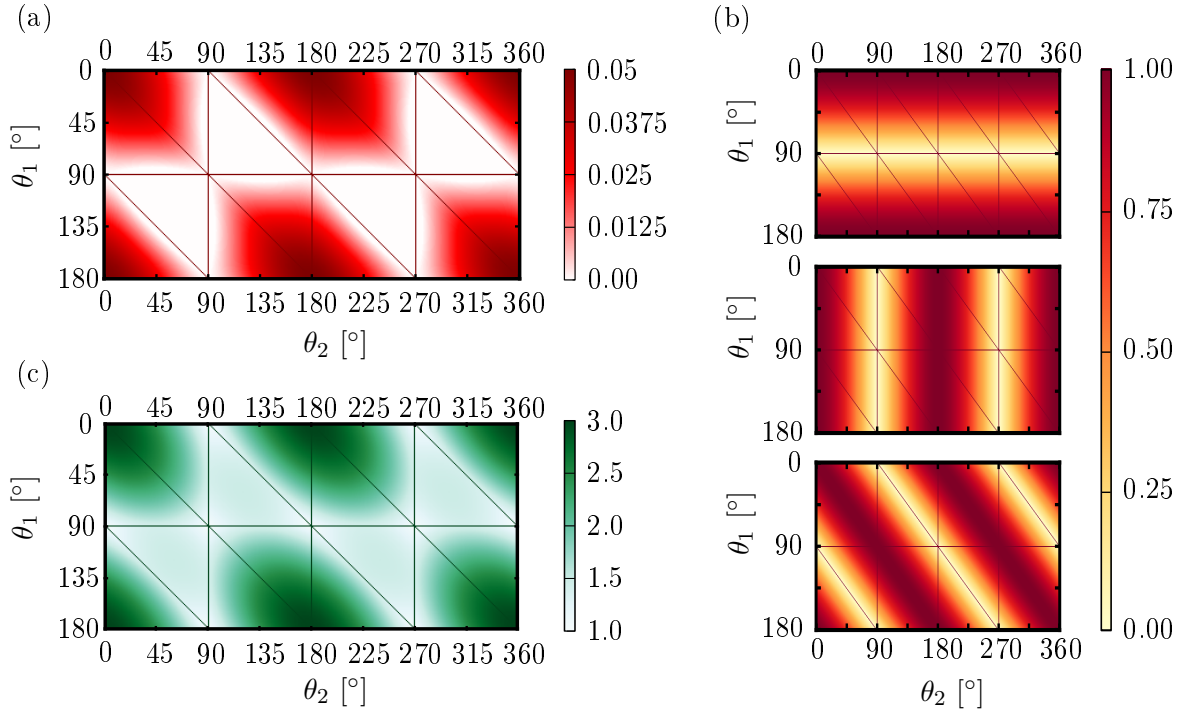


Figure 3.19.: Various quantities for scenario 2b), plotted against polar angles  $\theta_1$  and  $\theta_2$  of the toy model, see Fig. 3.16, with  $\phi_2 = 0$ . In all figures, calculations were performed with a single Fermi electron ( $n_F = 1$ ) and normalized  $\mathbf{U}$ -vectors, resulting in equal effective coupling strengths  $J_{\text{eff}}(1) = J_{\text{eff}}(2) = J_{\text{eff}}(3)$ . Distinctive vertical, horizontal and diagonal lines represent scenarios other than 2b), where data is on purpose not provided to avoid confusion. (a) Energy difference  $\Delta E_{0 \leftrightarrow 1}$  between ground and first excited states. White regions have a nondegenerate ground state, but  $\Delta E_{0 \leftrightarrow 1}$  is strictly not zero. Values have been set to zero, however, to clearly separate singlet (white areas) from triplet (red regions) ground state phases. (b) Plot of absolute overlaps between the toy model's orbital vectors, i.e.  $|\mathbf{U}_1 \cdot \mathbf{U}_2| = |\Omega_{12}|$  (top),  $|\mathbf{U}_1 \cdot \mathbf{U}_3| = |\Omega_{13}|$  (middle), and  $|\mathbf{U}_2 \cdot \mathbf{U}_3| = |\Omega_{23}|$  (bottom). (c) Sum of absolute overlaps  $|\Omega_{\text{tot}}| = |\Omega_{12}| + |\Omega_{13}| + |\Omega_{23}|$ .

Indeed, transitions from the known threefold degenerate ground states to nondegenerate ones occur (see Fig. 3.19(a)), which means there is a transition from triplet to singlet ground state. This is a rather surprising discovery, which proves that physical behavior apart from the central-spin model physics exists in the model presented. Contrary to the latter, where impurity spins try to couple antiferromagnetically to the Fermi electron, a singlet ground state requires antiferromagnetic interimpurity correlations in order to form a nondegenerate state. What makes this aspect so interesting is the fact, that both the

original coupling constant  $J$ , as well as the effective couplings  $J_{\text{eff}}$  are positive parameters, thus favoring an antiparallel alignment between Fermi electron(s) and impurity spins. It is not clear, why in certain parameter regimes singlet formation (nondegenerate ground state, white areas in Fig. 3.19(a)) is preferred over triplet formation (colored areas in Fig. 3.19(a)). A deeper analysis of this phenomenon has shown, that the orbital's overlap is the crucial factor.

In Fig. 3.19(b), absolute values of overlaps  $\Omega_{12}$ ,  $\Omega_{13}$ , and  $\Omega_{23}$  between Fermi orbital vectors  $\mathbf{U}_1$ ,  $\mathbf{U}_2$ , and  $\mathbf{U}_3$  are presented. The overlap vanishes, if two vectors are orthogonal to each other. In the top figure, showing  $|\Omega_{12}| = |\cos(\theta_1)|$ , this happens for  $\theta_1 = 90^\circ$ , which is, according to the notation of the toy model (Fig. 3.16), the polar angle between (in  $z$ -direction fixed) vector  $\mathbf{U}_1$  and orbital vector  $\mathbf{U}_2$ . Trivially, the result is independent of  $\theta_2$ , which is an angle describing vector  $\mathbf{U}_3$ . The subplot in the middle of Fig. 3.19(b) shows  $|\Omega_{13}| = |\mathbf{U}_1 \cdot \mathbf{U}_3| = |\cos(\theta_2)|$ , with  $\theta_2$  being the polar angle between these two vectors. Since  $\theta_2 \in [0^\circ; 360^\circ]$ , there are two angles (at  $90^\circ$  and  $270^\circ$ ) where the overlap vanishes. Trivially, this data is independent of  $\theta_1$ . To understand the subplot at the bottom of Fig. 3.19(b), the involved vectors for case 2b) are given as follows:

$$\mathbf{U}_2 = \begin{pmatrix} \sin \theta_1 \\ \cos \theta_1 \end{pmatrix} \quad \text{and} \quad \mathbf{U}_3 = \begin{pmatrix} \sin \theta_2 \\ \cos \theta_2 \end{pmatrix}. \quad (3.40)$$

Performing the scalar product and taking the absolute value gives  $|\Omega_{23}| = |\cos(\theta_1 - \theta_2)|$ , where an angle addition theorem has been used to shorten the expression. Using the above equation, the spectrum can easily be understood.

Each subplot contains partial structures of the energy difference plot Fig. 3.19(a), indicating a connection between overlap and ground state phase transition. It is thus suggesting to add up the data, defining a total absolute overlap  $|\Omega_{\text{tot}}| = |\Omega_{12}| + |\Omega_{13}| + |\Omega_{32}|$ , which is shown in Fig. 3.19(c). The obvious similarity to Fig. 3.19(a) clearly demonstrates, that ground state degeneracy (and thus the parallel alignment of impurity spins) comes with strong orbital overlap. The already discussed case of complete overlap of all orbitals, which is the central-spin model known from case 1), perfectly fits to this statement. Other limiting cases, i.e. cases with few overlap, are to be discussed below.

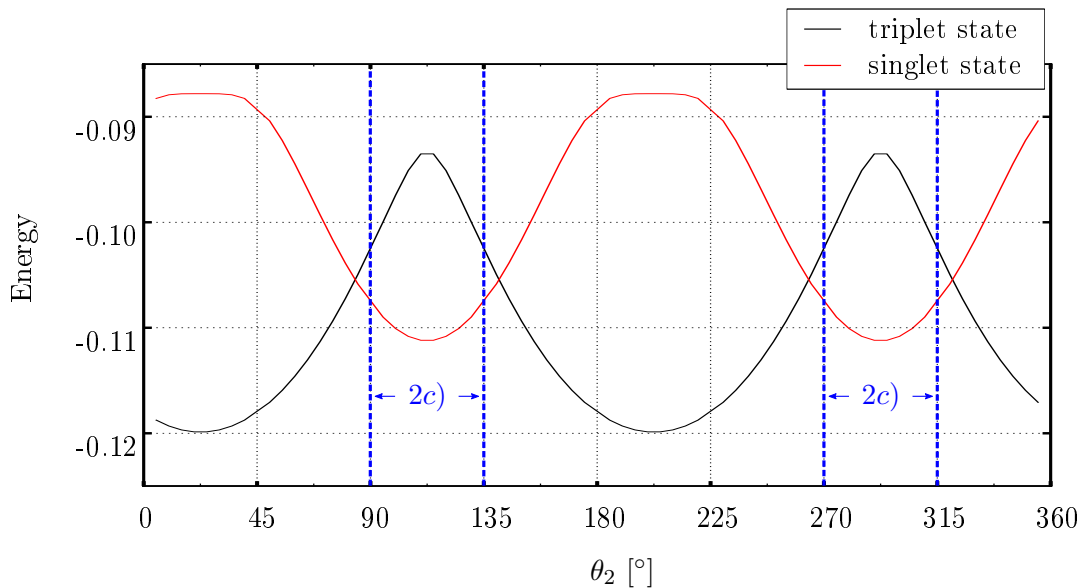


Figure 3.20.: Lowest two energy levels plotted for case 2b) with fixed toy model vectors  $\theta_1 = 45^\circ$ ,  $\phi_2 = 0^\circ$  (see Fig. 3.16 for notation details) and  $n_F = 1$ . Dashed blue lines show data for scenario 2c).

As stated before, energy differences between ground and first excited states depicted in Fig. 3.19(a) are not zero, which can perfectly be seen by exemplary picking data for fixed  $\theta_1 = 45^\circ$ . The two lowest lying energy levels and their degeneracies are shown in Fig. 3.20. The transition from threefold to nondegenerate ground state obviously occurs close to a Fermi orbital overlap situation referred to as case 2c). This scenario will be discussed later in this work.

A question that has not been answered yet is whether ground state phase transitions occur only for one Fermi electron, or maybe even for  $n_F = 2$ . Numerical calculations have shown, that the ground state is always a doublet, if two  $k_F$ -electrons are present. This is central-spin model behavior, where the total spin of the Fermi electron "sublattice" is one and the impurity spin's "sublattice" has a total spin of  $3/2$ , giving a doublet ground state according to the Lieb–Mattis theorem [147]. A possible explanation is, that the two impurity spins each align antiparallel to the  $k_F$ -electrons (as this should be energetically favored). Due to the full overlap of the third Fermi orbital with the other ones, this last orbital is therefore already occupied. It is, however, not a third Fermi electron occupying the third orbital, instead it is the sum of electronic occupation number densities of the two present  $k_F$ -electrons. The last impurity thus couples to these densities and aligns accordingly antiferromagnetically (and thus parallel to the other impurities). With two present Fermi electrons it seems more unlikely for the impurities to flip their spin against the preferred orientation, because the magnetization of the Fermi electron's "sublattice" is greater than it is with only one  $k_F$ -electron. This argumentation assumes, that both Fermi electrons' spins have the same orientation, which can be expected because of the orbital's overlap.

Up to now, case 2b) with  $n_F = 1$  is the first scenario where the physical behavior may deviate from central-spin model physics. The above presented results convey the guess, that case 2c) will surprise analogously.

### Case 2c)

Similar to the cases above, scenario 2c) can be expressed by the toy model (see inset in Fig. 3.21(a)), where two vectors are chosen orthogonally, while the third is a linear combination of the first two vectors. Keeping the notation used before, vectors  $\mathbf{U}_1$  and  $\mathbf{U}_2$  are orthogonal (i.e.  $\theta_1 = 90^\circ$ ) and angle  $\theta_2$  is varied. Fig. 3.21(a) shows the energy difference between ground and first excited states  $\Delta E_{0\leftrightarrow 1}$  in dependence of angle  $\theta_2$ . The data is presented for both one and two Fermi electrons ( $n_F = 1, 2$ ), for both an equal ( $J_{\text{eff}}(1) = J_{\text{eff}}(2) = J_{\text{eff}}(3) = 1$ ) and an unequal ( $J_{\text{eff}}(1) = J_{\text{eff}}(3) = 1, J_{\text{eff}}(2) = 0.1$ ) effective coupling case. Note, that both  $\theta_2 = 0^\circ$  and  $\theta_2 = 90^\circ$  belong to limiting case 2d), which has a fourfold degenerate ground state for  $n_F = 1$ , and gives a doublet ground state if two Fermi electrons are present (see the according discussion of scenario 2d) below for details).

In Fig. 3.21(a), for  $n_F = 1$  a clear transition from case 2d)'s fourfold degenerate ground state to a singlet ground state for case 2c) can be seen, because singlet and triplet states split up, increasing  $|\Delta E_{0\leftrightarrow 1}|$ . That the energy of the singlet is lower than the triplet one's is, as stated above, a rather surprising result. However, such a singlet ground state has already been observed in case 2b) (likewise for  $n_F = 1$ ), if the absolute value of the total orbital overlap  $|\Omega_{\text{tot}}|$  was rather weak (see Figs. 3.19(a) and (b)). One might say, that case 2c) is therefore predestined for a singlet ground state, because one of the three overlaps is by construction zero (in Fig. 3.21 this is  $\Omega_{12}$ ). Moreover, the two remaining overlaps are in a fixed relation of the form

$$|\Omega_{13}| + |\Omega_{23}| = |\cos \theta_2| + |\cos (90^\circ - \theta_2)| \quad , \quad (3.41)$$

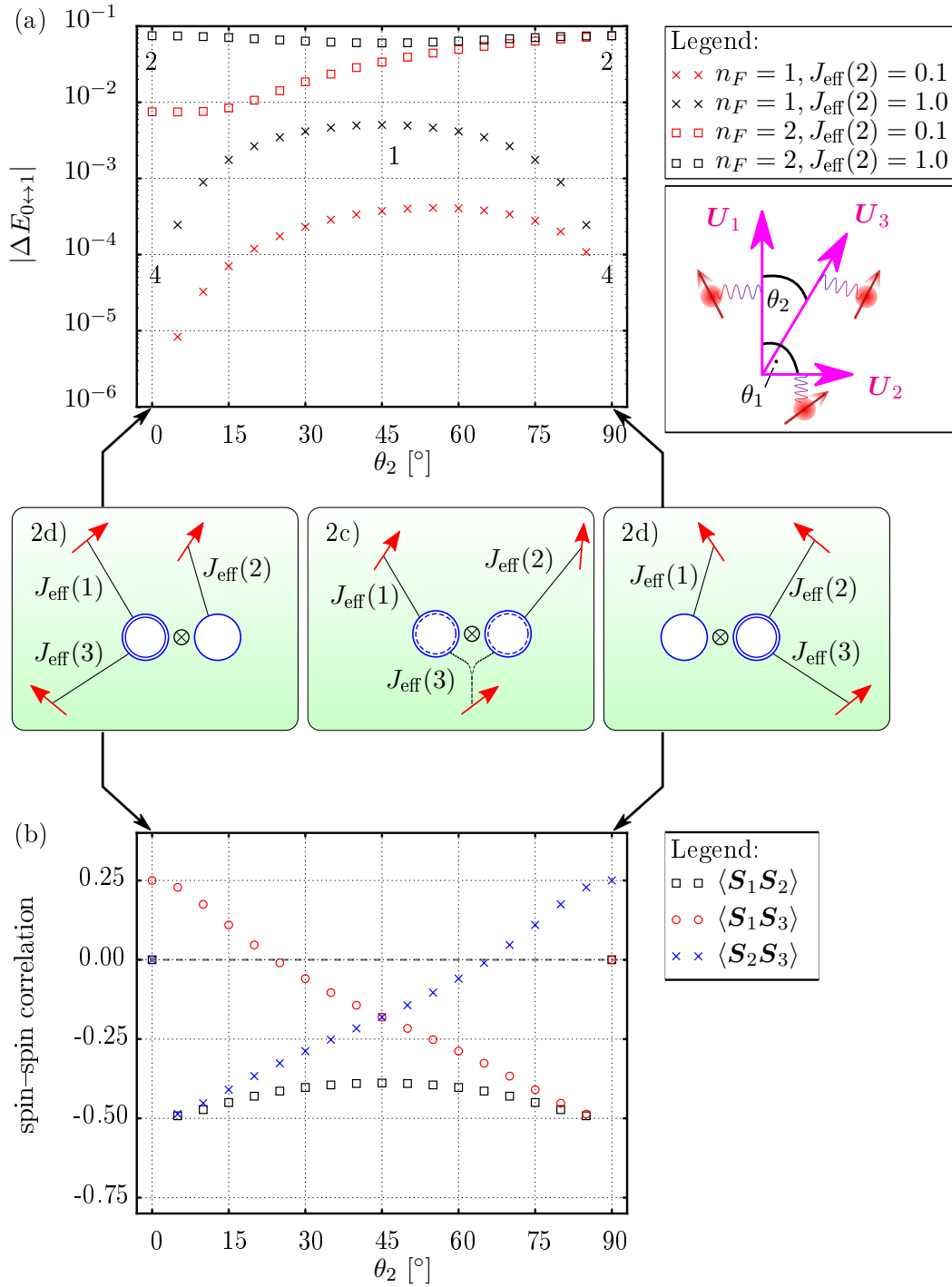


Figure 3.21.: (a) Energy differences between ground and first excited states  $\Delta E_{0\leftrightarrow 1}$ , plotted against angle  $\theta_2$  of the toy model (see inset with magenta vectors). Angle  $\theta_1$  between orbitals  $U_1$  and  $U_2$  is fixed to  $90^\circ$ . For  $\theta_2 = 0^\circ$  and  $90^\circ$ , two Fermi orbitals are identical, which is case 2d). Red data points stand for a system with an explicitly weak effective coupling  $J_{\text{eff}}(2) = 0.1$ , while black data points represent  $J_{\text{eff}}(2) = 1$ . In all cases,  $J_{\text{eff}}(1) = J_{\text{eff}}(3) = 1$ . The numbers inside the diagram show the ground state degeneracy. (b) Interimpurity spin-spin correlations for  $n_F = 1$  and  $J_{\text{eff}}(2) = 1$ . The dashed grey line at zero separates ferromagnetic from antiferromagnetic correlations.



taking a maximum value of  $\sqrt{2}$ , which is thus also the highest value  $|\Omega_{\text{tot}}|$  can take for case 2c). According to the results presented for case 2b) in Fig. 3.19, this has to be considered as a rather weak total overlap. The physics behind the above equation is, that the varied Fermi orbital  $\mathbf{U}_3$  has partial overlap with orbitals  $\mathbf{U}_1$  and  $\mathbf{U}_2$ , where increasing overlap with either orbital goes along with decreasing overlap with the other. The total overlap is thus limited to rather low values. As a consequence, transitions to degenerate ground states within case 2c) are unexpected. This statement has also been verified numerically. In this context it also becomes clear, that varying  $\theta_2$  within the range  $(0^\circ; 90^\circ)$  in Fig. 3.21 is sufficient. Extending the range to  $\theta_2 > 90^\circ$  will not change the maximally achievable total overlap, thus ground state phase transitions are both not expected and not found in numerical calculations.

Although physics of case 2b) smoothly merge with those of case 2c), there is one important difference between both scenarios. In case 2b), all impurity spins couple necessarily to the single Fermi electron, because all three Fermi orbitals have non-vanishing overlap. In contrast, case 2c) provides the opportunity for the Fermi electron to localize in a Fermi orbital, to which just two impurity spins couple (in the middle schematic picture in Fig. 3.21 this would be orbitals  $\mathbf{U}_1$  or  $\mathbf{U}_3$ ). Such a situation, however, excludes singlet formation, because the uncoupled impurity spin contributed with a factor of two to the ground state degeneracy. One can therefore conclude, that the Fermi electron occupies the third Fermi orbital, i.e. the linearly dependent one that connects the orthogonal ones.

The second indispensable prerequisite for singlet formation is ferromagnetic coupling between  $k_F$ -electron and one impurity spin, or likewise antiferromagnetic correlations between the impurities' spins. In order to analyze this aspect, interimpurity spin-spin correlations are shown in Fig. 3.21(b). Again, limiting case 2d) is well understood: For  $\theta_2 = 0^\circ$ , impurities 1 and 2 are not correlated (i.e.  $\langle \mathbf{S}_1 \mathbf{S}_2 \rangle = 0$ ) since their coupling Fermi orbitals are orthogonal. The two spins coupled to the same orbital are perfectly ferromagnetically correlated, i.e.  $\langle \mathbf{S}_1 \mathbf{S}_3 \rangle = 0.25$ , as predicted by former results. For  $\theta_2 = 90^\circ$ , results are analogue. For the region in between, i.e. case 2c), correlation function  $\langle \mathbf{S}_1 \mathbf{S}_2 \rangle$  instantly becomes antiferromagnetic. This is only possible, if the  $k_F$ -electron mediates a coupling between impurities 1 and 2, which accords with the idea, that the Fermi electron is in the linearly dependent orbital. The required condition of antiferromagnetic correlations between impurities is also fulfilled, because at least two correlation functions return negative values in the entire 2c)-regime.

Another detail in Fig. 3.21 to be mentioned is, that  $\theta_2 = 45^\circ$  is a symmetry axis, if effective coupling strengths  $J_{\text{eff}}(1)$  and  $J_{\text{eff}}(2)$  are equal. This is expected, because  $\theta_2 = 45^\circ \pm \theta'$ , with  $\theta'$  being an arbitrary angle  $\in [0^\circ; 45^\circ]$  are physically equivalent situations. Reducing one of the effective coupling strengths, as done with  $J_{\text{eff}}(2)$  in Fig. 3.21(a), certainly breaks this symmetry, but results remain qualitatively the same. As observed in case 2b), Fig. 3.18, where the same parameters for the effective coupling strengths have been used, the energy difference between ground and first excited state  $\Delta E_{0 \leftrightarrow 1}$  is larger for  $\theta_2 \lesssim 90^\circ$  than for  $\theta_2 \gtrsim 0^\circ$ . This is due to the direct influence of  $J_{\text{eff}}(2)$  on the  $\mathbf{U}_2$ -vector, which itself affects the energy spectrum of the full Hamiltonian. For  $\theta_2 \lesssim 90^\circ$ , this influence is rather small, because orbital vector  $\mathbf{U}_3$  dominates the energy scale arising from this orbital (i.e. the corresponding eigenvalue). In contrast, this does not happen for  $\theta_2 \gtrsim 0^\circ$ , where the corresponding eigenvalue of the full Hamilton matrix is only proportional to orbital vector  $\mathbf{U}_2$ , but not to  $\mathbf{U}_3$ .

Contrary to the single Fermi electron case, no dramatic changes of the ground state degeneracy are found if two  $k_F$ -electrons are present (see Fig. 3.21(a)). With two Fermi electrons, each impurity spin is at least partially screened, so that three impurity spins combined with two electron spins have a total spin of  $1/2$ , giving the ground state doublet.

Moreover, numerical calculations show, that the interimpurity spin-spin correlations are always ferromagnetic, indicating that case 2c) has a central-spin model behavior if  $n_F = 2$ .

Summarizing these results, case 2c) is closely related to case 2b). Particularly for a single Fermi electron, both cases deviate from central-spin model behavior as singlet ground states are found. Especially the (by construction) weak total overlap for 2c)-scenarios can be seen as the origin for singlet formation. Calculated interimpurity correlations underpin the results as antiferromagnetic correlations are found. However, a filling of two Fermi electrons leads in cases 2b) and 2c) to central-spin model behavior.

### A try to explain the ground state of case 2c)

Perhaps one could understand the singlet formation within case 2c) by examination of the following effective Hamiltonian:

$$\begin{aligned} \mathcal{H}_{\text{eff}}^{2c)} &= J_{\text{eff}} \sum_{r=1}^{R=3} \mathbf{S}_r \mathbf{s}_r \\ &= \frac{J_{\text{eff}}}{2} \sum_{\sigma, \sigma'} \left( \mathbf{S}_1 c_{1\sigma}^\dagger \boldsymbol{\sigma}_{\sigma\sigma'} c_{1\sigma'} + \mathbf{S}_2 c_{2\sigma}^\dagger \boldsymbol{\sigma}_{\sigma\sigma'} c_{2\sigma'} + \mathbf{S}_3 c_{3\sigma}^\dagger \boldsymbol{\sigma}_{\sigma\sigma'} c_{3\sigma'} \right), \end{aligned} \quad (3.42)$$

where  $\mathbf{S}_r$  is the  $r$ th impurity spin, and the corresponding Fermi orbital is defined via  $c_{r\sigma}^\dagger |0\rangle$ . Since case 2c) is to be modeled, one Fermi orbital (hereafter the third is chosen) must be linearly dependent on the others. This can be realized by setting the creation operator

$$c_{3\sigma}^\dagger = \cos(\alpha) c_{1\sigma}^\dagger + \sin(\alpha) c_{2\sigma}^\dagger, \quad (3.43)$$

and the annihilation operator likewise. Parameter  $\alpha$  thus describes the overlap of the third Fermi orbital with the others, giving limiting case 2d) if  $\alpha = 0$  or  $\alpha = \frac{\pi}{2}$ . Note here, that  $c_{3\sigma}^\dagger$  acts on a nonorthogonal basis. Eq. (3.43) inserted into  $\mathcal{H}_{\text{eff}}^{2c)}$  gives

$$\begin{aligned} \mathcal{H}_{\text{eff}}^{2c)} &= J_{\text{eff}} \left[ \mathbf{s}_1 (\mathbf{S}_1 + \cos^2(\alpha) \mathbf{S}_3) + \mathbf{s}_2 (\mathbf{S}_2 + \sin^2(\alpha) \mathbf{S}_3) \right] + \\ &+ \frac{J_{\text{eff}}}{2} \left( \sum_{\sigma, \sigma'} \left[ c_{1\sigma}^\dagger c_{2\sigma'} + c_{2\sigma}^\dagger c_{1\sigma'} \right] \boldsymbol{\sigma}_{\sigma\sigma'} \cos(\alpha) \sin(\alpha) \right) \mathbf{S}_3. \end{aligned} \quad (3.44)$$

This is a very simplified form of the effective Hamiltonian (3.28), customized for case 2c), where equal effective coupling strengths are assumed and some indices (for example  $k = k_F$ ) are left out to keep the notation simple. Note, that the third addend can have both positive or negative sign due to the product  $\cos(\alpha) \sin(\alpha)$ , which allows for both parallel or, more importantly, antiparallel alignment of spin  $\mathbf{S}_3$  to the other spins. This indicates a possible deviation from central-spin model behavior, where the Lieb-Mattis theorem [147] holds true if the interimpurity correlations (of the spin's sublattice) are either zero or ferromagnetic. As the latter cannot be guaranteed here due to a possibly nonferromagnetic spin-spin coupling, central-spin model physics are not necessarily expected.

The next step is to calculate the internal energy of this Hamiltonian for both a triplet (" $|T\rangle$ ") and a singlet (" $|S\rangle$ ") ground state. Especially for  $\alpha \rightarrow \frac{\pi}{2}$ , the following states could be a good guess:

$$\begin{aligned} |S\rangle &= \frac{1}{\sqrt{2}} \left( |0; 0\rangle_1 |1; 0\rangle_2 |1; -1; -1\rangle_{\text{Imp}} - |0; 0\rangle_1 |0; 1\rangle_2 |-1; 1; 1\rangle_{\text{Imp}} \right), \\ |T\rangle &= \frac{1}{\sqrt{2}} \left( |0; 0\rangle_1 |1; 0\rangle_2 |1; -1; -1\rangle_{\text{Imp}} + |0; 0\rangle_1 |0; 1\rangle_2 |-1; 1; 1\rangle_{\text{Imp}} \right). \end{aligned} \quad (3.45)$$

Here,  $|n_\uparrow; n_\downarrow\rangle_j$  describes the  $j$ th Fermi orbital ( $j = 1, 2$ ), where  $n_\uparrow = 1$  if a Fermi electron with  $z$ -spin projection "up" occupies the orbital, otherwise 0 (analogous for  $n_\downarrow$  with spin projection "down"). The impurity spin states are given by  $|S_1^z; S_2^z; S_3^z\rangle_{\text{Imp}}$ , where values 1 stand for spin-up, and -1 for spin-down. For case 2d) (i.e.  $\alpha \rightarrow \frac{\pi}{2}$ ), the selected states represent a single Fermi electron that occupies the Fermi orbital which has two impurity spins (with indices "2" and "3") coupled.

After some tedious, but straightforward work, one gets

$$\langle S | \mathcal{H}_{\text{eff}}^{2c} | S \rangle > \langle T | \mathcal{H}_{\text{eff}}^{2c} | T \rangle \quad \forall \alpha, \quad (3.46)$$

which is obviously not the result found by numerical calculations. Although the above introduced singlet and triplet states have seemed to be a good choice, especially for the limit  $\alpha \rightarrow \frac{\pi}{2}$ , these states do not represent the physics correctly. Further investigation of the ground states provided by the numerical calculations have shown, that the ground state for case 2c) is not simply one configuration, but a linear combination of almost every possible state from the Hilbert space. This makes analytical calculations basically pointless. What can be learned from the analysis above is, that there is no simple explanation for the singlet ground states found in cases 2b) and 2c). The complex combination of differently weighted states leads to singlet formation, which is nevertheless a thrilling result because this is different from central-spin model physics.

### Case 2d)

If two orbitals are identical and the third one is orthogonal to the former, the overlapping scenario is classified as case 2d) according to Fig. 3.15. Some details have already been mentioned above, since scenario 2d) is often a limiting case of orbital overlap. The following brief discussion of this case is meant to give a short explanation of the ground state's degeneracy, as well as to answer open questions.

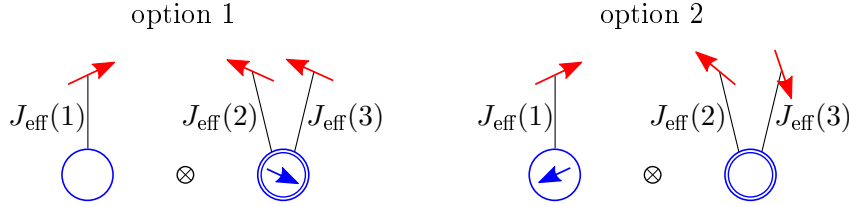


Figure 3.22.: Case 2d): Two possible options, where the single Fermi electron (blue arrow) is located. Each blue ring stands for a coupling Fermi orbital. The single blue ring is the singlet-forming orbital, while the blue double ring represents the full overlap of two orbitals, i.e. the two doublet-forming orbitals. Red arrows depict impurity spins.

Starting with the single Fermi electron case ( $n_F = 1$ ), previous results have shown a fourfold degeneracy of the ground state. The first option is, that the Fermi electron occupies the overlapping Fermi orbitals (hereafter referred to as the "doublet-forming" orbitals), forming an underscreened central-spin model which has a doublet ground state. The third impurity acts as a "free" spin, contributing to the total ground state degeneracy with a factor of two. The second option is, that the  $k_F$ -electron occupies the Fermi orbital that is orthogonal to the doublet-forming orbitals. Since this situation gives a singlet, because the Fermi electron fully screens the impurity spin, the corresponding Fermi orbital will be called the "singlet-forming" orbital. Two impurity spins remain uncoupled and are therefore free, contributing each with a factor of two to the ground state degeneracy. In either case, one obtains the fourfold degenerate ground state. Both options are visualized in Fig. 3.22.

It would be interesting to know, if either option is preferred. To this end, the interimpurity correlation of impurity spins coupling to the doublet-forming orbitals were observed. In case of the first option, the correlation function gives a non-zero value, because the Fermi electron mediates the impurity interaction. If, on the other hand, its value is zero, the impurity spins are not coupled, indicating that the physical situation corresponds to the second option. Note, that correlations between impurity spins of orthogonal Fermi orbitals are not of interest, as those are zero by construction.

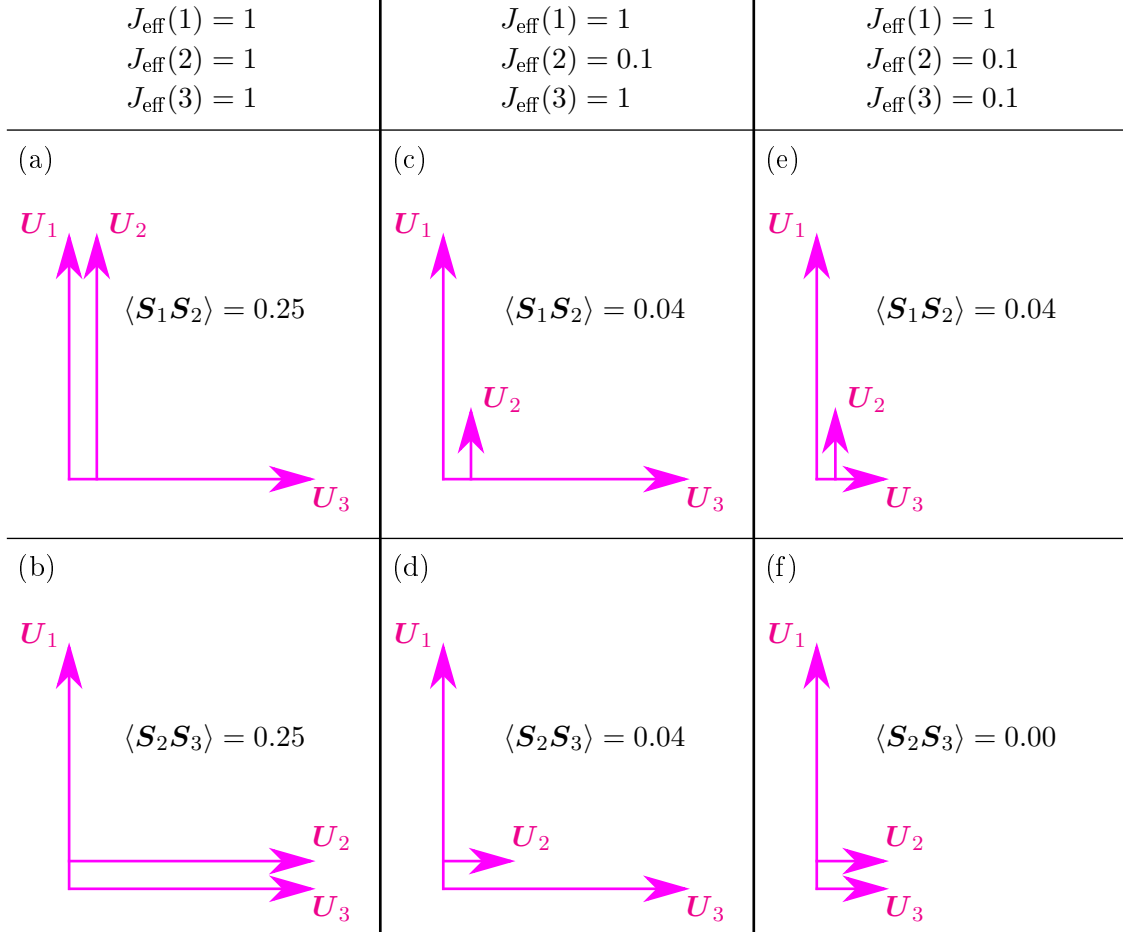


Figure 3.23.: Correlations between the two spins that couple to the fully overlapping (doublet-forming) orbitals in case 2d). The remaining (singlet-forming) orbital is orthogonal to the former ones (depicted with a right angle). Each spin  $\mathbf{S}_i$  couples with an effective coupling strength  $J_{\text{eff}}(i)$  to its corresponding Fermi orbital  $\mathbf{U}_i$ . Values of  $J_{\text{eff}}(i)$  are valid for the entire column. Correlations that are necessarily zero due to orthogonality are left out. In all cases, a single Fermi electron is considered ( $n_F = 1$ ). Note moreover, that the notation from Fig. 3.22 is only consistent with cases (b), (d), and (f).

Fig. 3.23 shows the relevant spin-spin correlation for various coupling strengths  $J_{\text{eff}}$ . In the left column, i.e. Figs. (a) and (b), all coupling strengths are equal. The interimpurity correlation is 0.25, which means the spins are aligned parallel. This clearly shows, that the physical situation corresponds to option 1 as shown in Fig. 3.22. One could say that this is the expected result, because the system favors to have as many impurity spins as possible screened. Due to rotational symmetry of the problem, cases (a) and (b) must be equivalent.

A dependence of the effective coupling strengths  $J_{\text{eff}}$  has in particular been found, if orthogonal orbitals are present (see for example case C) in Fig. 3.10, or the discussion of case 3d) below). Option 2 from Fig. 3.22 might be preferred, if  $J_{\text{eff}}(2)$  (or likewise  $J_{\text{eff}}(3)$ ) is

reduced. Figs. 3.23(c) and (d) show, however, that the interimpurity correlation is again non-zero, indicating that option 1 is still favored. Again, cases (c) and (d) are equivalent because of rotational symmetry.

Reduction of two effective coupling strengths, as shown in Figs. 3.23(e) and (f), leads to different results. In case (e), the singlet-forming orbital  $\mathbf{U}_3$  has its impurity spin much weaker coupled than one of the doublet-forming orbitals (i.e.  $\mathbf{U}_1$ ). Therefore it is clear, that the Fermi electron occupies the doublet-forming orbitals. If, on the other hand, both doublet-forming orbitals are just weakly coupled to their corresponding impurities, option 2 is preferred, since  $\langle \mathbf{S}_2 \mathbf{S}_3 \rangle = 0$  in Fig. 3.23(f).

One can sum up these results with a simple rule: As long as the effective coupling strength corresponding to one of the doublet-forming orbitals is of the same order as the effective coupling strength of the singlet-forming orbital, the Fermi electron is located in the doublet-forming orbitals (option 1 from Fig. 3.22). If, however, the effective coupling strength corresponding to the singlet-forming orbital is significantly greater than the effective coupling strengths corresponding to the doublet-forming Fermi orbitals, option 2 becomes more favorable.

With two Fermi electrons in the 2d)-scenario, a distinction between different effective coupling strengths lapses, because all three impurity spins are coupled to  $k_F$ -electrons. Singlet and doublet are formed, giving a total ground state which is twice degenerate. Since coupling two impurity spins to the same Fermi orbital is a central-spin model, its ground state is known due to the Lieb–Mattis theorem [147]. Placing both Fermi electrons in the same Fermi orbital is in general possible, but energetically inefficient because none of the impurities can be screened then.

### Introducing a stereographic projection

Cases with three coupling orbitals (i.e. cases 3a) - 3d)) cannot be reproduced by a two-dimensional toy model, since all  $\mathbf{U}$ -vectors have to be linearly independent, thus living in a three-dimensional space. A possibility to nevertheless present three-dimensional data are stereographic projections, allowing to map semi-spheres onto (data-filled) circles. In detail, the stereographic projection transforms the spherical coordinates of vector  $\mathbf{U}_3$ , given by  $(|\mathbf{U}_3|, \theta_2, \phi_2)$ , to polar coordinates  $(\rho, \theta_2)$  of vector  $\mathbf{U}'_3$ . Polar coordinate  $\theta_2$  transforms directly. For fixed length of  $\mathbf{U}_3$ , specifically  $|\mathbf{U}_3| = 1$ , a simple trigonometrical calculation returns

$$\rho = 2 \frac{\cos \phi_2}{\sin \phi_2 + 1}, \quad (3.47)$$

where  $\rho$  is the distance from the polar coordinate system's center. Interesting limiting cases are  $\phi_2 = 0^\circ$ , where  $\mathbf{U}_3$  lies within the  $x$ - $z$ -plane (returning  $\rho = 2$  as the maximum value), and  $\phi_2 = 90^\circ$  (giving  $\rho = 0$ ), where  $\mathbf{U}_3$  is orthogonal to both orbitals  $\mathbf{U}_1$  and  $\mathbf{U}_2$ .

Fig. 3.24 shows the projection used in the following. Note, that the orbital vector  $\mathbf{U}_3$  cannot be varied in size, as the projection would lose its uniqueness.

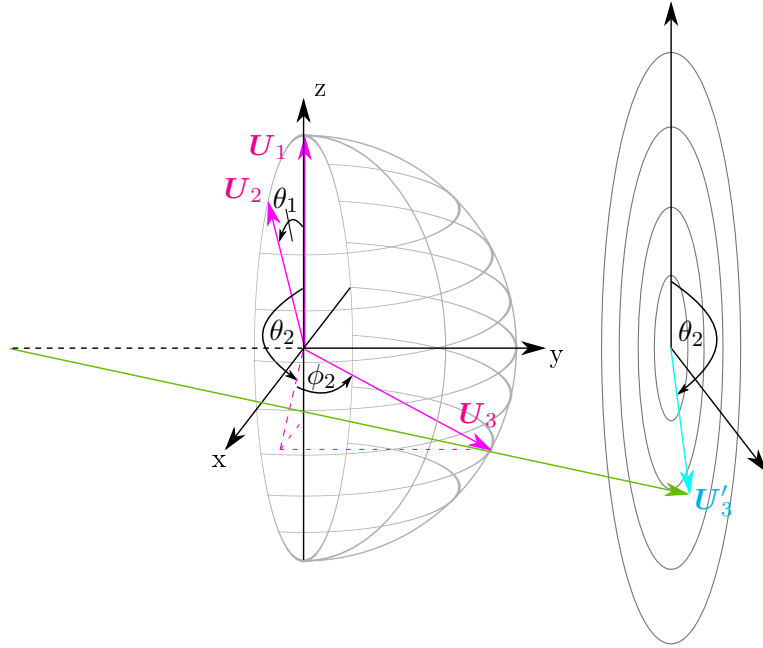


Figure 3.24.: Stereographic projection of the toy model's right semi-sphere to a polar coordinate system. In the toy model (see also Fig. 3.16), Fermi orbital vectors  $\mathbf{U}_1$  and  $\mathbf{U}_2$  lie within the  $x$ - $z$ -plane, while  $\mathbf{U}_3$  has an additional  $y$ -component for scenarios 3a) - 3d). The green vector represents the mapping process for vector  $\mathbf{U}_3$  in the spherical system to  $\mathbf{U}'_3$  in the polar system. While angle  $\theta_2$  remains unchanged,  $\phi_2$  transforms via Eq. (3.47) to  $\rho$ .

### Case 3a)

One of the most widespread scenarios of orbital overlap is case 3a) (see Fig. 3.15). This situation occurs, if all three coupling Fermi orbitals are partially overlapping. However, neither does any of the orbitals have full overlap with another one, nor are two orbitals orthogonal to one another. This definition holds also true for case 2b). The difference is, that all Fermi orbitals in scenario 3a) are linearly independent, thus the linear span of coupling orbitals is  $\mathcal{L}_{c.o.} = 3$ , whereas  $\mathcal{L}_{c.o.} = 2$  for case 2b). As a direct consequence, Fermi orbital vector  $\mathbf{U}_3$  (from the toy model depicted in Fig. 3.16) is now necessarily out of the  $x$ - $z$ -plane, which, unfortunately, makes visualization rather difficult. Using the stereographic projection (see subsection above) remedies this situation.

As remarked above, a close relation to case 2b) is expected, because of the nonvanishing overlap between the Fermi orbitals. It is thus suggesting to examine energy differences between ground and first excited states, i.e.  $|\Delta E_{0\leftrightarrow 1}|$  to see if ground state phase transitions occur. As the absolute total overlap  $|\Omega_{\text{tot}}| = |\Omega_{12}| + |\Omega_{13}| + |\Omega_{32}|$  has been a useful indicator for such phase transitions, it is examined as well.

In the left column of Fig. 3.25, energy differences between ground and first excited states  $|\Delta E_{0\leftrightarrow 1}|$  are shown as a stereographic projection of the toy model's right semi-sphere for systems with one  $k_F$ -electron. While  $\mathbf{U}_1$  is fixed in  $z$ -direction,  $\mathbf{U}_2$  is fixed in the  $x$ - $z$ -plane with  $\theta_1$  as given in the figure, and angles  $\theta_2$  and  $\phi_2$  (giving  $\rho$ ) of  $\mathbf{U}_3$  are varied. Similar to case 2b), both triplet and singlet ground state phases are found for case 3a). To distinguish them, the singlet phases are colored white (even if  $|\Delta E_{0\leftrightarrow 1}| > 0$ ). The fact, that ground state degeneracy transitions occur, even if orbital vectors  $\mathbf{U}_1$  and  $\mathbf{U}_2$  are held constant, is a clear sign that singlet-triplet crossovers can be ascribed to a change in orbital overlaps  $\Omega_{13}$  and  $\Omega_{23}$ .

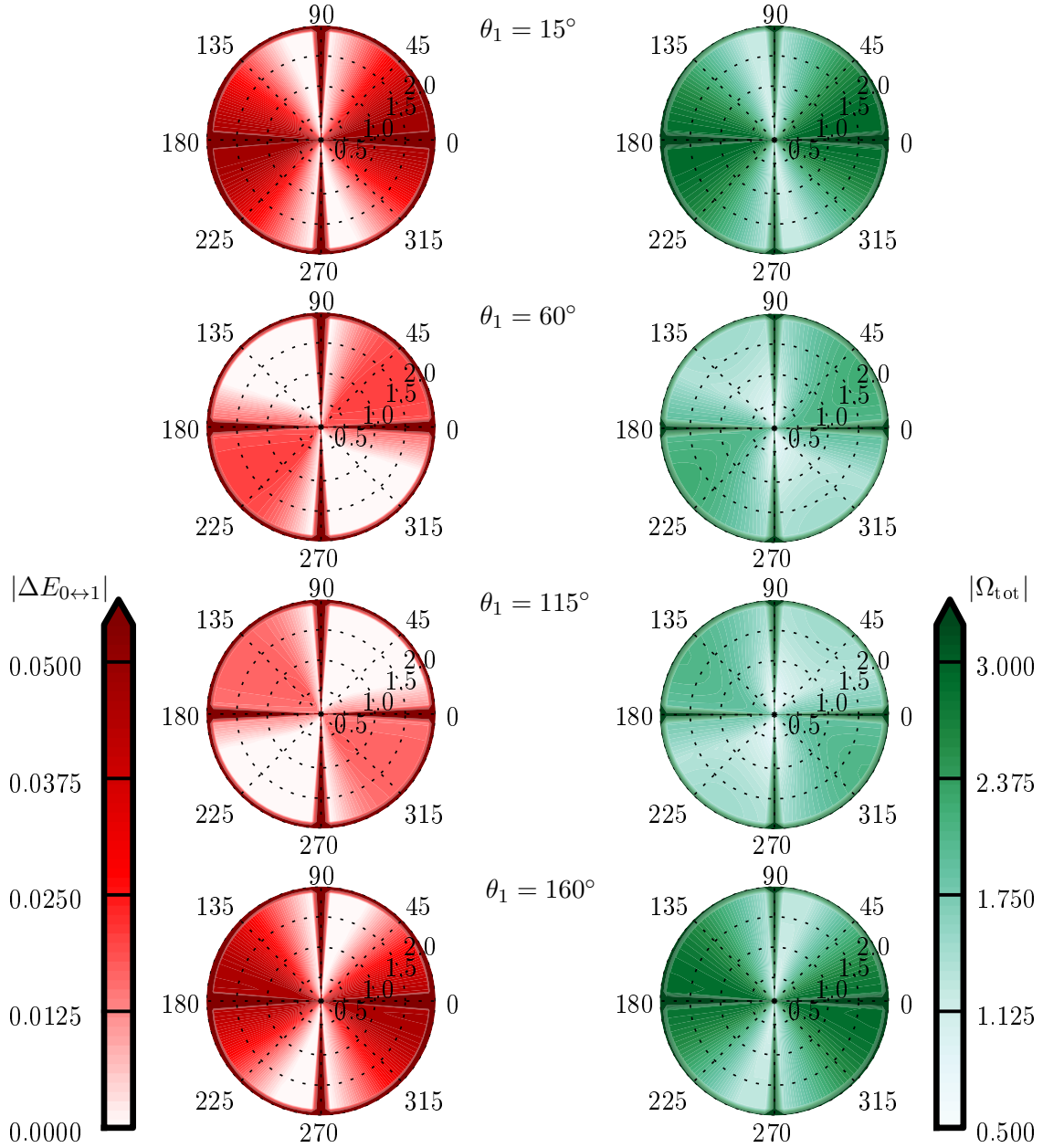


Figure 3.25.: Stereographic projections of the toy model's right semi-sphere, spanned by orbital vector  $\mathbf{U}_3$ , for case 3a). Numbers around the plots are values of  $\theta_2$  in degrees, whereas numbers 0.5 to 2.0 are values of  $\rho$  (see also Fig. 3.24). In the left column,  $|\Delta E_{0\leftrightarrow 1}|$  is shown, where white regions represent singlet ground state configurations. Note, that  $|\Delta E_{0\leftrightarrow 1}|$  is strictly not zero in these realms, but values are manually set to zero for a clear separation of the phases. Colored areas represent triplet ground states. In the right column, the absolute total overlap  $|\Omega_{\text{tot}}|$  is given. Each row is calculated for a fixed polar angle  $\theta_1$  of toy model vector  $\mathbf{U}_2$ . All vectors have the same norm and thus the same effective coupling,  $J_{\text{eff}} = 1$ . The calculations were performed with  $n_F = 1$ . If a combination of angles gives a case other than 3a), the values of  $|\Delta E_{0\leftrightarrow 1}|$  and  $|\Omega_{\text{tot}}|$  are set to exceed the color scales (i.e.  $|\Delta E_{0\leftrightarrow 1}| > 0.05$  and  $|\Omega_{\text{tot}}| > 3$ ) to avoid confusion - for example, the outer ring with  $\rho = 2$  is a case 2)-scenario).

As can be seen in Fig. 3.25, there is also a clear trend, showing that singlet regions are greater the closer  $\theta_1$  is to  $90^\circ$ . This proves, that the ground state regimes also depend on the overlap  $\Omega_{12}$ .

To prove the assumption, that the ground state phases are correlated to the total overlap, its absolute value  $|\Omega_{\text{tot}}| = |\Omega_{12}| + |\Omega_{13}| + |\Omega_{23}|$  is examined. Results are shown in the right column of Fig. 3.25. As expected due to the analysis above, regions of weak total overlap correspond to singlet ground state phases. Moreover, one can see that strong total overlap goes along with a greater separation of ground state and first excited energy levels (compare, for example, diagrams of  $\theta_1 = 15^\circ$  and  $\theta_1 = 115^\circ$ ).

The reader is moreover reminded, that the results shown in Fig. 3.25 are calculated with constant effective couplings  $J_{\text{eff}}$ . As singlet-triplet phase transitions occur nevertheless, the effective coupling strength can be excluded as the reason for the change of ground state phases. If, however, these transitions between singlet and triplet ground state regimes are only dependent on the total overlap, then transitions must occur at the same angle configuration, independent of the effective coupling strengths. The latter are, as explained in context with the introduction of the toy model, basically just a stretch of orbital vectors  $\mathbf{U}$ . The (absolute) total overlap is a normalized quantity, thus independent of  $J_{\text{eff}}$ .

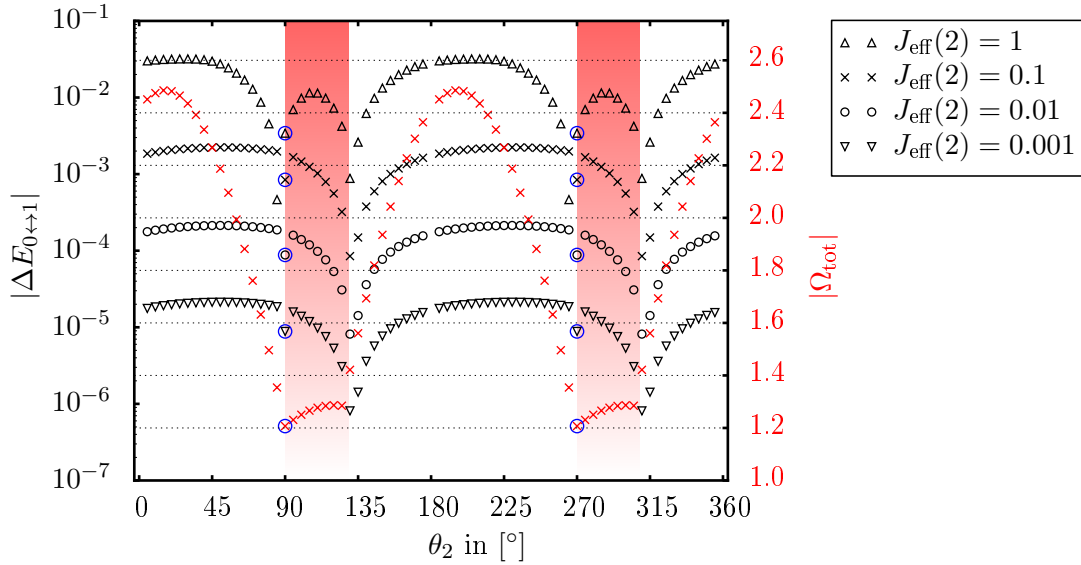


Figure 3.26.: Black colored data: Absolute differences of first excited and ground state energies  $\Delta E_{0\leftrightarrow 1}$  plotted against  $\theta_2$  of toy model's vector  $\mathbf{U}_3$ , where  $\phi_2$  is fixed at  $45^\circ$ . Orbital vector  $\mathbf{U}_2$  is fixed at  $\theta_1 = 45^\circ$ , but its length is varied, leading to different effective coupling strengths  $J_{\text{eff}}(2)$ . The other effective coupling strengths are  $J_{\text{eff}}(1) = J_{\text{eff}}(3) = 1$ . As usual,  $\mathbf{U}_1$  is fixed in  $z$ -direction (see the toy model in Fig. 3.16 for details). Red colored data shows the absolute total overlap  $|\Omega_{\text{tot}}|$ , which is due to its normalization equal for all shown values of  $J_{\text{eff}}(2)$  (using also  $\theta_1 = \phi_2 = 45^\circ$ ). Within the two red bars the ground state is a singlet, outside it is a triplet. Blue circles around data points at  $\theta_2 = 90^\circ, 270^\circ$  belong to scenario 3b), all other data points correspond to case 3a). All results are for one Fermi electron,  $n_F = 1$ .

To underpin this statement, configuration  $\theta_1 = 45^\circ, \phi_2 = 45^\circ$  has been chosen to provide exemplary data (see Fig. 3.26). In the region of weak absolute total overlap, the singlet ground state phase is found (marked with the two red bars) for both systems with all-equal effective coupling strengths ( $J_{\text{eff}}(1) = J_{\text{eff}}(2) = J_{\text{eff}}(3) = 1$ ) and systems with a reduced coupling strength ( $J_{\text{eff}}(1) = J_{\text{eff}}(3) = 1 > J_{\text{eff}}(2)$ ). According to the discussions above, this is the expected result.



What is interesting to see, however, is a rather sudden collapse of the energy difference of first excited and ground state ( $\Delta E_{0\leftrightarrow 1}$ ) at the left borders of the red bars, i.e.  $\theta_2 = 90^\circ$  and  $\theta_2 = 270^\circ$ , for  $J_{\text{eff}}(2) < 1$ . In fact, these data belong to scenario 3b) (which is why they are marked with blue circles). However, the transition to case 3b) is steady, but the steps of  $\theta_2$  are chosen too large to resolve this behavior.

Another, yet not clearly answered question is, how the absolute total overlap behaves in a singlet ground state phase. Two options are possible: Either  $|\Omega_{\text{tot}}|$  increases after the transition to the singlet ground state phase has occurred (just as  $\Delta E_{0\leftrightarrow 1}$  usually does, see for example Fig. 3.20 for case 2b)), or  $|\Omega_{\text{tot}}|$  remains low. Fig. 3.26 indicates, that the second option is valid. One can thus conclude, that the singlet ground state phase is always connected to a weak total overlap.

While one Fermi electron opens up the opportunity for either singlet or triplet ground state phases, no ground state phase crossovers were found for  $1 < n_F < 2G_F - 1$ . If  $n_F = 2$ , the ground state is a doublet, independent of  $|\Omega_{\text{tot}}|$  or effective coupling strengths. With three Fermi electrons, all impurities are screened, forming a singlet, which is also stable for any orbital configuration.

To sum up scenario 3a), one finds a very close relation to case 2b), where behavior apart from central-spin model physics is found if  $n_F = 1$ . This is not surprising, as case 2b) must be regarded as a limiting case of scenario 3a). It is found, that the overlap of the three Fermi orbitals is a fundamental quantity, where low total overlap is connected to a singlet ground state, while strong overlap returns triplet ground states. Moreover, the crossover between singlet and triplet ground states is not affected by the effective coupling strengths  $J_{\text{eff}}$ . Ground states apart from those expected from the central-spin model occur, however, only for one Fermi electron.

### Scenario 3b)

The results found for case 3a) are very similar to what has been found for scenario 2b). Since cases 2b) and 2c) are also closely related, an analogous connection might be found for cases 3a) and 3b). The latter scenario is defined by three coupling Fermi orbitals without any linear dependence, but two orbitals must have vanishing overlap. The difference to case 2c) is, that there is no linear dependence, resulting in  $\mathcal{L}_{\text{c.o.}} = 3$ . However, scenario 2c) is somehow a limiting case of scenario 3b), and thus its physics should be similar.

Indeed, the first data points for case 3b) with  $n_F = 1$ , presented in Fig. 3.26, show, that the ground state is nondegenerate. This is what has been found for scenario 2c) as well.

For a more profound analysis of case 3b), Fig. 3.27(a) shows the total overlap  $|\Omega_{\text{tot}}|$  as a stereographic projection, where orbitals  $\mathbf{U}_1$  and  $\mathbf{U}_2$  are orthogonal within the  $x$ - $z$ -plane. Note, however, that due to rotational symmetry, the presented data cover all angle combinations leading to scenario 3b). One immediately sees, that  $|\Omega_{\text{tot}}| < 1.5$ , and calculations even show, that  $|\Omega_{\text{tot}}| < \sqrt{2}$ . This is of importance, as  $\sqrt{2}$  is the maximum value the absolute total overlap can take within case 2c). Since case 3b) is also restricted to  $|\Omega_{\text{tot}}| \leq \sqrt{2}$ , it is not surprising, that for  $n_F = 1$  only nondegenerate ground states (i.e. singlets) - just like in case 2c) - are found.

In order to underpin the results, the energy of the ground state,  $E_0$ , as well as of the first excited state ( $E_1$ ) are presented in Fig. 3.27(b). For  $\rho \lesssim 2$  (i.e.  $\phi_2 \gtrsim 0^\circ$  and  $\phi_2 \lesssim 180^\circ$ ), the total overlap is close to its maximum value, but the singlet ground state energy is clearly below  $E_1$ . With decreasing  $\rho$ ,  $|\Delta E_{0\leftrightarrow 1}| = |E_0 - E_1|$  decreases as well, indicating a

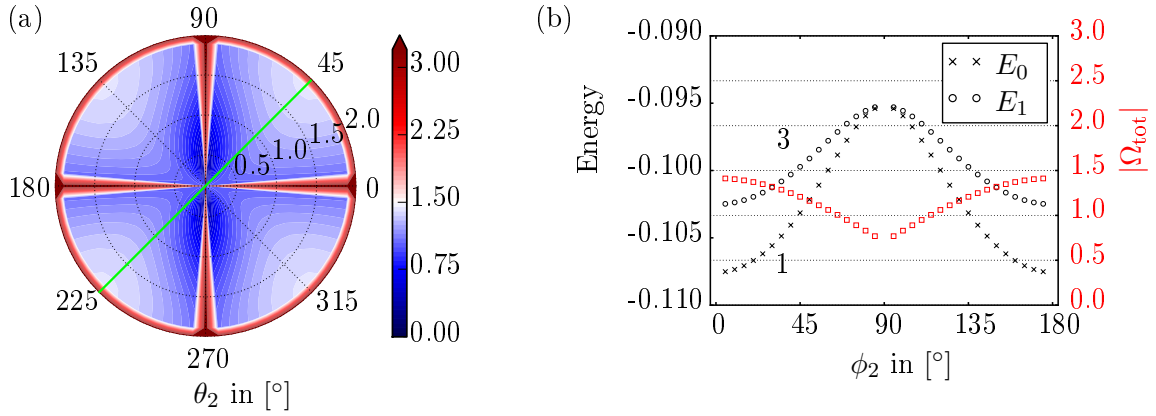


Figure 3.27.: Exemplary data for scenario 3b) with  $n_F = 1$ : (a) Total overlap  $|\Omega_{\text{tot}}|$  shown as a stereographic projection (see Fig. 3.24 for details) of the right semi-sphere spanned by orbital vector  $\mathbf{U}_3$ , which is described by polar angle  $\theta_2$  and azimuthal angle  $\phi_2$ . The latter transforms via Eq. (3.47) to  $\rho$ , which is written at the inner circles (0.5, ..., 2.0). Orbital  $\mathbf{U}_2$  is fixed at  $\theta_1 = 90^\circ$ . Dark red values belong to other overlapping scenarios. The green line shows where data of (b) is found. (b) Ground state ( $E_0$ ) and first excited energy ( $E_1$ ) dependent on  $\phi_2$ , together with the corresponding total overlap  $|\Omega_{\text{tot}}|$ . Angles  $\phi_2 > 90^\circ$  are equivalent to  $\theta_2 = 225^\circ$  from (a). Data for  $\phi_2 = 90^\circ$  is left out as this is case 3d). Numbers 1 and 3 represent the degeneracy of the energy levels.

transition of the singlet ground state at  $\rho = 0$  ( $\phi_2 = 90^\circ$ ). However, the singlet energies are unambiguously below the triplet energies over the entire range of  $\phi_2$ , proving that the ground state is nondegenerate. Numerical calculations show, that this statement holds true for the entire range of  $\theta_2$ , being thus in good agreement with former discussions of case 2c) and results obtained by investigation of the absolute total overlap.

Just like in cases 2a) - 2d), as well as in case 3a), the ground state is a doublet if two Fermi electrons occupy the three coupling Fermi orbitals. For  $n_F = 3$ , each Fermi orbital becomes singly occupied, fully screening the three impurity spins, which results in a singlet ground state. Contrary to  $n_F = 1$ , this is central-spin model behavior.

The calculations discussed above were performed with equal effective coupling strengths  $J_{\text{eff}}(1) = J_{\text{eff}}(2) = J_{\text{eff}}(3) = 1$ . Discussions about tuning the effective coupling strengths are neglected, as previous results of the very similar cases 2b), 2c), and 3a) have shown, that there is no influence on the ground state degeneracy. Numerical results, which are not presented here, are in accordance with this statement. Note, however, that  $J_{\text{eff}}$  can surely affect the degeneracy of the ground state energy, but completely decoupled orbitals (as in cases 2d), 3c) and 3d)) are required.

### Case 3c)

While scenario 3b) requires two coupling orbitals to be orthogonal to each other, case 3c) is defined by having one coupling Fermi orbital that is orthogonal to both others (see the overview in Fig. 3.15). Thus, one Fermi orbital is completely separated from the others. Case 3c) is thus a combination of a very simple central-spin model, consisting of one coupling Fermi orbital and its coupled impurity spin, and a case B)-part, known from the two-impurity spins discussions (see Subsec. 3.5.2 and the summarizing overview in Tab. 3.1).

As explained above, the ground state's degeneracy of scenarios with completely decoupled Fermi orbitals might be dependent on the relation among effective coupling strengths. For case 3c), there is a  $J_{\text{eff}}$ -dependent competition about whether the Fermi electron(s) occupy the single coupling Fermi orbital (hereafter referred to as the "singlet-forming" orbital), or rather the two overlapping Fermi orbitals.

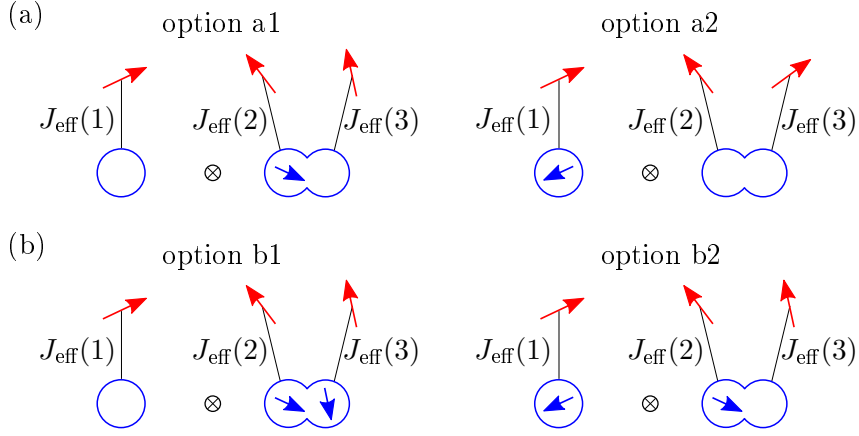


Figure 3.28.: Most favorable Fermi electron occupation possibilities for case 3c) with (a) one Fermi electron, or (b) two Fermi electrons (blue arrow(s)). The single orbital on the left is referred to as the "singlet-forming" orbital.

For  $n_F = 1$ , Fig. 3.28(a) shows the two possibilities of where the Fermi electron can be located. Whether it is option a1 or a2 depends on  $J_{\text{eff}}$ . As has been seen in the very similar case 2d) (see for example Figs. 3.22 and 3.23), option a1 will most likely be preferred, but if  $J_{\text{eff}}(1) > J_{\text{eff}}(2), J_{\text{eff}}(3)$ , then option a2 can be more favorable. It is rather a coincidence, that the ground state degeneracy is four in either case. For option a1, one impurity spin of the singlet-forming orbital is uncoupled, while the  $k_F$ -electron forms a doublet with the two remaining spins, thus giving the fourfold degeneracy. On the other hand, option a2 shows a clear singlet formation, and two free spins remain, also giving the degeneracy of four.

With two Fermi electrons, options b1 and b2 as shown in Fig. 3.28(b) are most favorable. The first option gives a doublet ground state due to the free spin, while both Fermi electrons occupy the overlapping Fermi orbitals, forming a singlet. The second option also gives a doublet, because a singlet is formed and combined with a doublet (which is case B) with  $n_F = 1$ , known from systems with two impurity spins).

Although the calculation of interimpurity correlations provided information about which option is found for a given combination of effective coupling strengths, it does not seem necessary to elaborate this in detail, since the crossover between options a1 and a2, as well as b1 and b2 will be similar to case 2d).

### No overlap of coupling Fermi orbitals - Case 3d)

As the last possible scenario of how coupling Fermi orbitals can overlap, the limiting case of no overlap (case 3d), see Fig. 3.15) will be discussed in the following. The three coupling Fermi orbitals build up a very simple central-spin model each, where a single impurity spin couples to a single Fermi orbital. Therefore, empty (and doubly) occupied orbitals leave the corresponding spin uncoupled, while singly occupied coupling orbitals form necessarily a singlet since the impurity spin aligns antiparallel ( $J_{\text{eff}} > 0$ ) to the Fermi electrons' spin. It goes without saying, that all interimpurity correlations are zero, as correlations cannot be mediated due to the missing of orbital overlap.

Although this particular case is easy to understand, it shows a huge diversity of ground state degeneracies that come with different relations among effective coupling strengths  $J_{\text{eff}}$ . It is a three-impurity extension of the previously discussed scenario C) (see Subsec. 3.5.3 and the summarizing overview in Tab. 3.1).

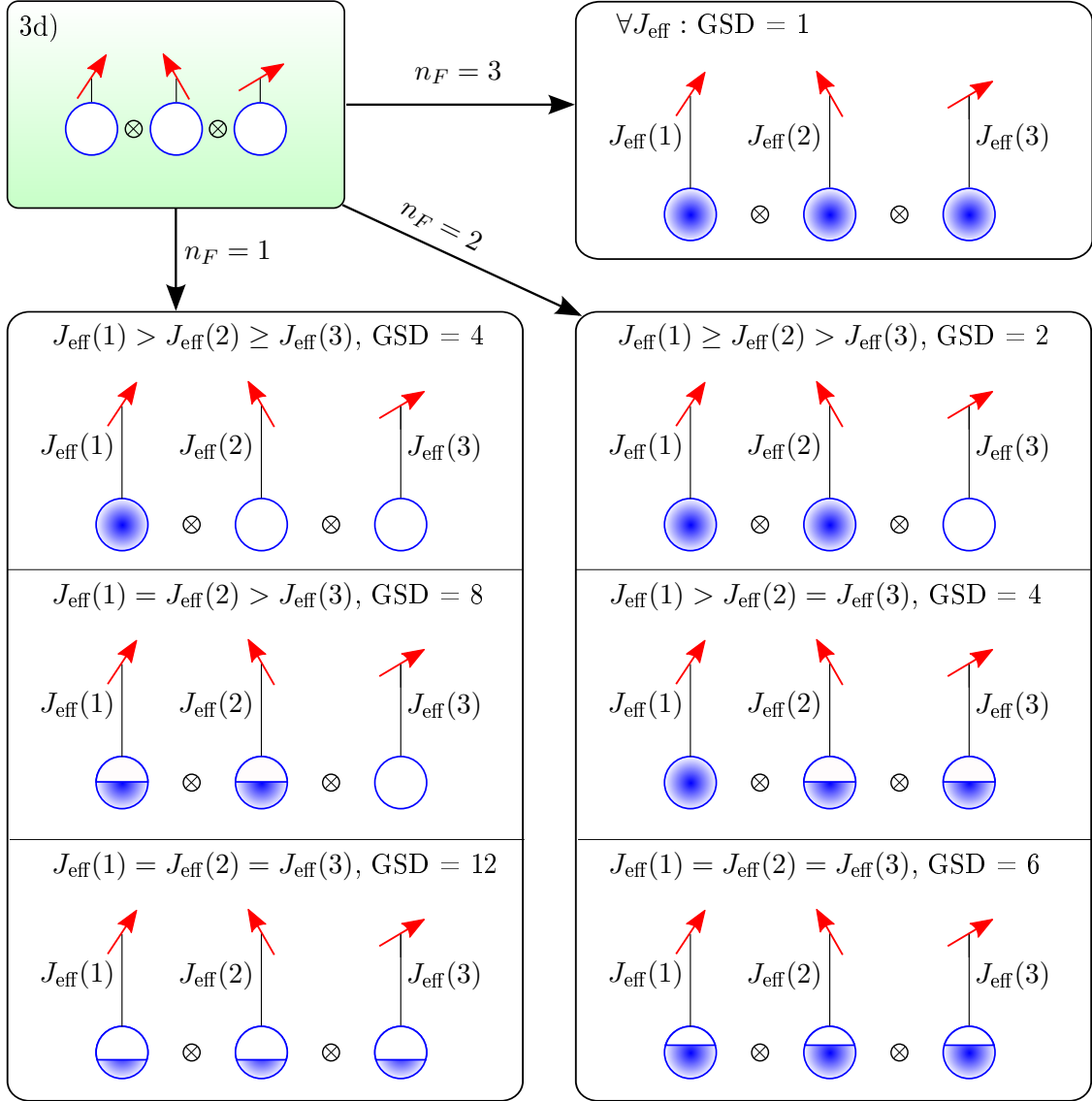


Figure 3.29.: Possible ground state degeneracies (GSD) of scenario 3d), dependent on the number of Fermi electrons  $n_F$  and effective coupling strengths  $J_{\text{eff}}$  between coupling Fermi orbitals (blue circles) and impurity spins (red arrows). The blue filling of Fermi orbitals is a measure for single Fermi electron occupation probability, where no filling is equivalent to zero and full filling is 100%.

Starting with the discussion of one Fermi electron ( $n_F = 1$ ), one has to check how coupling strengths  $J_{\text{eff}}$  are related to one another. A simple rule is, that the Fermi electron occupies the Fermi orbital with the strongest effective coupling. If one coupling strength dominates, the  $k_F$ -electron occupies the corresponding orbital, forming a singlet with the impurity spin. Two impurity spins with weaker effective coupling remain uncoupled, each contributing with a factor of two to the total ground state degeneracy. This situation is shown in the upper part of the  $n_F = 1$ -box in Fig. 3.29.

If, however, two effective coupling strengths are equal and greater than the third (for example  $J_{\text{eff}}(1) = J_{\text{eff}}(2) > J_{\text{eff}}(3)$ ), the Fermi electron can occupy either the orbital connected to  $J_{\text{eff}}(1)$  (hereafter simply called "orbital 1"), or, with equal probability, the

Fermi orbital connected to  $J_{\text{eff}}(2)$  (likewise named "orbital 2"). If the  $k_F$ -electron occupies orbital 1, the ground state is fourfold degenerate due to two free spins. However, the Fermi electron can also occupy orbital 2, where the ground state is likewise fourfold degenerate. Since occupation of either orbital 1 or 2 is energetically indifferent, both ground state degeneracies add up to a total of eight (see middle part of the  $n_F = 1$ -box in Fig. 3.29).

Moreover, all effective coupling strengths could be equal. In this case, occupation of either of the three coupling Fermi orbitals is equally probable. Similar to the discussion above, three equally probable fourfold degenerate ground state configurations exist, which add up to a twelvefold degenerate ground state.

The argumentation is quite similar, if two Fermi electrons are present (see also the corresponding  $n_F = 2$ -box in Fig. 3.29). Assuming one or two effective coupling strengths to be greater than the third, i.e.  $J_{\text{eff}}(1) \geq J_{\text{eff}}(2) > J_{\text{eff}}(3)$ , then both Fermi electrons occupy the two orbitals with the strongest effective coupling strength, forming a singlet each. One impurity spin remains uncoupled, as its corresponding Fermi orbital is empty, leaving a doublet ground state.

If a situation like  $J_{\text{eff}}(1) > J_{\text{eff}}(2) = J_{\text{eff}}(3)$  occurs, one Fermi electron certainly occupies orbital 1, as the effective coupling  $J_{\text{eff}}(1)$  is the strongest. The second  $k_F$ -electron will occupy either of the two remaining orbitals, since the effective coupling strengths are equal. This gives two energetically equivalent doublet ground states, each doublet emerging from the free spin. In total, the ground state is thus fourfold degenerate.

It remains the case of equal effective coupling strengths. There are three energetically equivalent combinations of Fermi electron placement, where a single impurity spin remains unscreened in each case. The  $k_F$ -electrons are either in orbitals 1 and 2, 1 and 3, or 2 and 3. The free impurity spin's degeneracy times these three combinations gives a sixfold degenerate ground state.

For  $n_F = 3$ , the relations among effective coupling strengths become irrelevant. Each Fermi electron occupies a coupling Fermi orbital, as this reduces the internal energy the most. All  $k_F$ -electrons form singlets with the impurity spins, giving a nondegenerate total ground state.

### 3.6.3. Summary of the nine scenarios

Now that all possible scenarios of coupling Fermi orbital overlap have been discussed in detail, an overview with the results for three impurities is given in Tab. 3.2. It shows the ground state degeneracy for each case up to filling  $n_F = \mathcal{L}_{\text{c.o.}}$ , where  $\mathcal{L}_{\text{c.o.}}$  is the linear span of coupling orbitals. This information is sufficient to derive the ground state degeneracy for any  $k_F$ -electron filling  $n_F$ : Either particle-hole symmetry can be used (fillings  $n_F$  and  $2G_F - n_F$  are equivalent), which is independent of the total number of Fermi orbitals  $G_F$ , or one uses the factorization of the ground state degeneracy, if  $n_F > \mathcal{L}_{\text{c.o.}}$  and  $G_F > \mathcal{L}_{\text{c.o.}}$ . The first factor ("GSD( $\mathcal{L}_{\text{c.o.}}$ )") is the degeneracy resulting from occupation of coupling Fermi orbitals, while the second factor ("GSD(U)") comes from occupation of the uncoupled orbitals. This has already been discussed in Sec. 3.5.5, and corresponding Eqs. (3.37) and (3.38) derived there are valid for any amount of impurities.

The discussions above have covered many different scenarios of orbital overlap, which will be helpful to understand the results obtained from the effective model (3.28) with  $R = 3$  impurities for exemplary systems. In the next subsection, the focus lies on finding and checking the theoretically predicted situations in exemplary systems.

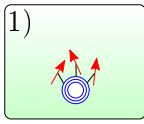
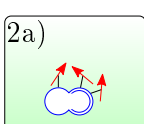
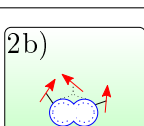
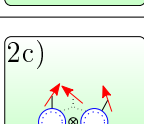
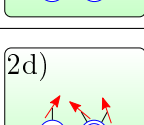
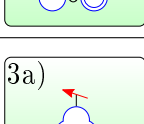
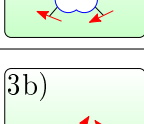
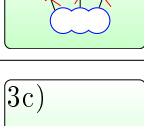
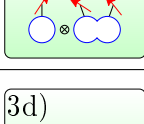
$n_F$ case	$n_F = 1$	$n_F = 2$	$n_F = 3$
1) 	<b>3</b> $\forall J_{\text{eff}}$	see Eqs. (3.37) and (3.38)	see Eqs. (3.37) and (3.38)
2a) 	<b>3</b> $\forall J_{\text{eff}}$ $\forall  \Omega_{\text{tot}} $	<b>2</b> $\forall J_{\text{eff}}$ $\forall  \Omega_{\text{tot}} $	see Eqs. (3.37) and (3.38)
2b) 	$\begin{cases} \mathbf{1} & , \text{ if }  \Omega_{\text{tot}}  \text{ weak} \\ \mathbf{3} & , \text{ if }  \Omega_{\text{tot}}  \text{ strong} \end{cases}$ $\forall J_{\text{eff}}$	<b>2</b> $\forall J_{\text{eff}}$ $\forall  \Omega_{\text{tot}} $	see Eqs. (3.37) and (3.38)
2c) 	<b>1</b> $\forall J_{\text{eff}}$ $\forall  \Omega_{\text{tot}} $	<b>2</b> $\forall J_{\text{eff}}$ $\forall  \Omega_{\text{tot}} $	see Eqs. (3.37) and (3.38)
2d) 	<b>4</b> $\forall J_{\text{eff}}$ $\forall  \Omega_{\text{tot}} $	<b>2</b> $\forall J_{\text{eff}}$ $\forall  \Omega_{\text{tot}} $	see Eqs. (3.37) and (3.38)
3a) 	$\begin{cases} \mathbf{1} & , \text{ if }  \Omega_{\text{tot}}  \text{ weak} \\ \mathbf{3} & , \text{ if }  \Omega_{\text{tot}}  \text{ strong} \end{cases}$ $\forall J_{\text{eff}}$	<b>2</b> $\forall J_{\text{eff}}$ $\forall  \Omega_{\text{tot}} $	<b>1</b> $\forall J_{\text{eff}}$ $\forall  \Omega_{\text{tot}} $
3b) 	<b>1</b> $\forall J_{\text{eff}}$ $\forall  \Omega_{\text{tot}} $	<b>2</b> $\forall J_{\text{eff}}$ $\forall  \Omega_{\text{tot}} $	<b>1</b> $\forall J_{\text{eff}}$ $\forall  \Omega_{\text{tot}} $
3c) 	<b>4</b> $\forall J_{\text{eff}}$ $\forall  \Omega_{\text{tot}} $	<b>2</b> $\forall J_{\text{eff}}$ $\forall  \Omega_{\text{tot}} $	<b>1</b> $\forall J_{\text{eff}}$ $\forall  \Omega_{\text{tot}} $
3d) 	$\begin{cases} \mathbf{4}, J_{\text{eff}}(1) > J_{\text{eff}}(2, 3) \\ \mathbf{8}, J_{\text{eff}}(1, 2) > J_{\text{eff}}(3) \\ \mathbf{12}, J_{\text{eff}}(1 = 2 = 3) \end{cases}$	$\begin{cases} \mathbf{2}, J_{\text{eff}}(1, 2) > J_{\text{eff}}(3) \\ \mathbf{4}, J_{\text{eff}}(1) > J_{\text{eff}}(2 = 3) \\ \mathbf{6}, J_{\text{eff}}(1 = 2 = 3) \end{cases}$	<b>1</b> $\forall J_{\text{eff}}$

Table 3.2.: Summary of the ground state degeneracy (bold number) dependent on the number of Fermi electrons ( $n_F$ ) for all possible overlap scenarios arising for systems with three impurities. The linear span of coupling orbitals ( $\mathcal{L}_{\text{c.o.}}$ ) is one for case 1), two for scenarios 2a) - 2d), and three for cases 3a) - 3d). For  $n_F > \mathcal{L}_{\text{c.o.}}$ , the ground state degeneracy can be derived by Eqs. (3.37) and (3.38). For systems with particle-hole symmetry,  $n_F$  is equivalent to  $2G_F - n_F$ . All results hold true  $\forall G_F$ .

### 3.6.4. Transferring the results to exemplary systems

#### Three impurities on an $8 \times 8$ -square lattice

An exemplary system, which is already known from the two-impurity analysis, is the  $8 \times 8$ -square lattice. Around half-filling, i.e. for  $n = 57, \dots, 72$  electrons, the degeneracy of the Fermi energy is eightfold ( $G_F = 8$ ), which is thus sufficiently large to (at least theoretically) find all scenarios presented in Fig. 3.15.

Placing the first two impurities on this lattice predetermines which scenarios will be found, because the corresponding coupling Fermi orbitals have a fixed relation (no, partial, or full overlap). The reader is reminded, that the Fermi orbitals come from diagonalization of the unperturbed system, therefore placing impurities only leads to selecting some of them as the coupling orbitals. As a consequence, fixing two impurities at certain lattice sites immediately excludes some of the overlapping scenarios (which is very interesting for experimental realizations). Placing the third impurity then leads to one of the nine cases discussed above.

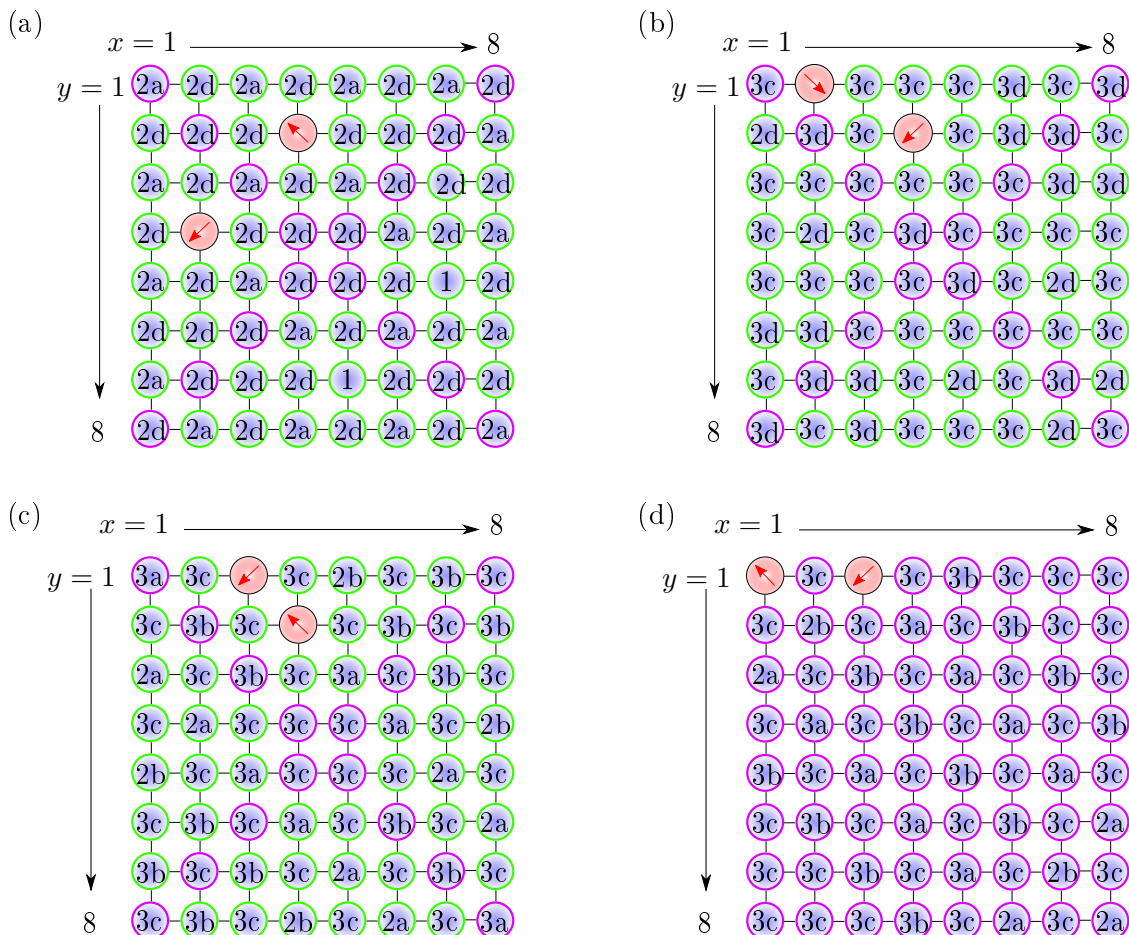


Figure 3.30.:  $8 \times 8$ -square lattice for  $n = 57$  electrons (i.e.  $n_F = 1$  and  $G_F = 8$ ) with open boundary conditions. For (a)-(d), two impurities are fixed at different sites (red bubbles with arrows), while the third is placed on the remaining lattice sites, giving a specific scenario which is labeled accordingly. For example, in (a) the first impurity is fixed at  $(2;4)$  and the second at  $(4;2)$ . If the third impurity is located at  $(1;7)$ , this geometry results in overlapping case 2a). In all subfigures, green circles around lattice sites represent cases where all three effective coupling strengths are equal, while purple borders indicate, that at least one effective coupling strength differs from the others.

To give an exemplary overview, Fig. 3.30 shows some impurity placement combinations, where two impurities are fixed and the third is placed on the remaining lattice sites.

Placing two impurities at sites (2;4) and (4;2), as done in Fig. 3.30(a), gives a case where two coupling Fermi orbitals are identical (fully overlapping). Therefore, only cases 1), 2a), and 2d) are possible realizations, which indeed were found. The calculated ground state degeneracy perfectly matches to the results found above (see summary in Tab. 3.2). For these three scenarios, the ground state degeneracies were predicted to be independent of the effective coupling strengths, which is in agreement with the numerical calculations (in Fig. 3.30, purple and green circles indicate that the effective coupling strengths are either different or equal).

If, however, at least one coupling Fermi orbital is orthogonal to both others, the effective coupling strengths come into play, determining in which Fermi orbital the Fermi electrons have their highest occupation probability. Corresponding scenarios are 2d), 3c), and 3d). Orbitals corresponding to sites (1;2) and (2;4) are obviously orthogonal, as can be seen in Fig. 3.30(b), thus giving an ideal basis to examine the named cases. Unfortunately, the influences of different effective coupling strengths do not change the ground state degeneracy for cases 2d) and 3c), as explicitly discussed above. Therefore, the focus will be on scenario 3d), where the relation among effective coupling strengths has direct influence on the ground state degeneracy (see Fig. 3.29 for detailed results).

3rd impurity site	$J_{\text{eff}}(1)$	$J_{\text{eff}}(2)$	$J_{\text{eff}}(3)$	ground state degeneracy
(1;6), (3;8), (6;1), (8;3)	0.011	0.011	0.011	12
(1;8), (8;1)	0.011	0.011	0.016	4
(2;2), (7;7)	0.011	0.011	0.016	4
(2;6), (3;7), (6;2), (7;3)	0.011	0.011	0.011	12
(2;7), (7;2)	0.011	0.011	0.016	4
(4;4), (5;5)	0.011	0.011	0.016	4

Table 3.3.: Effective coupling strengths and ground state degeneracy of all 3d)-scenarios shown in Fig. 3.30(b) with  $n_F = 1$ . Since first and second impurity are fixed at sites (1;2) and (2;4), their respective effective coupling strengths  $J_{\text{eff}}(1)$  and  $J_{\text{eff}}(2)$  do not change their values.

Tab. 3.3 gives an overview of the 16 sites, where the coupling Fermi orbital of the third impurity is orthogonal to the other two (orthogonal) coupling orbitals, thus resulting in case 3d).  $J_{\text{eff}}(1)$  and  $J_{\text{eff}}(2)$  are not dependent on the third impurity's location, which is why their values are fixed. Dependent on the placement of the third impurity, there are obviously only two sorts of Fermi orbitals, leading to values  $J_{\text{eff}}(3) = 0.011$  and  $J_{\text{eff}}(3) = 0.016$ . In the first case, all effective coupling strengths are equal, giving the twelvefold degenerate ground state, while in the latter case the Fermi orbital of the third impurity is clearly preferred for occupation by the only Fermi electron. As discussed above, this reduces the ground state degeneracy.

From the data presented in Tab. 3.3, one can easily find a scenario, where two effective coupling strengths are equal, but greater than the third ( $J_{\text{eff}}(1) = J_{\text{eff}}(2) > J_{\text{eff}}(3)$ ). Keeping the first impurity located at site (1;2), and placing the others at sites (1;8) and (2;2) provides such an example. The numerical calculation returns an eightfold degenerate ground state.

One can summarize, that all characteristics of case 3d) can be found in the  $8 \times 8$ -square lattice. The results found are in perfect agreement with the predictions made above. For comparison, the reader is referred to Fig. 3.29 and Tab. 3.2.



A great realization of partially overlapping orbitals is impurity placement at lattice sites (1;3) and (2;4), see Fig. 3.30(c), where scenarios 2a) - 2c) and 3a)- 3c) are expected to be found. As can immediately be seen, there is not a single lattice site, where the placement of the third impurity resulted in case 2c). Further search for this scenario within the  $8 \times 8$ -lattice has finished unsuccessful, no matter where the three impurities were placed. This, of course, does not deny the existence of scenario 2c), but its occurrence might generally be rather seldom. However, this is not surprising, as scenario 2c) can be seen as limiting case of scenario 3b).

Cases 2a), 3b), and 3c) as found in Fig. 3.30(c) show the expected ground state degeneracies, which are independent of the relation among effective coupling strengths. It is rather interesting to analyze cases 2b) and 3a), especially their absolute total overlap,  $|\Omega_{\text{tot}}|$ .

Starting with case 2b) shown in Fig. 3.30(c) resulting from the third impurity being placed at site (1;5), the absolute total overlap found is 1.5, and the ground state is a singlet. Due to symmetry, positions (4;8), (5;1), and (8;4) of the third impurity are physically equivalent. Placing the three impurities on sites (1;1), (1;3) and (7;7), as shown in Fig. 3.30(d), also gives a 2b)-case, where  $|\Omega_{\text{tot}}| \approx 1.48$ , and the ground state is also nondegenerate. These results fit to the former analysis of this case, where the reader is referred to Fig. 3.19, which shows the absolute total overlap for case 2b) in connection with singlet and triplet ground state phases. As often stated above, case 2b) is a scenario where the effective coupling strengths do not affect the ground state degeneracy. Indeed, the numerical calculations of the  $8 \times 8$ -lattice show, that the ground state is a singlet, independent of equal (Fig. 3.30(c)) or unequal (Fig. 3.30(d)) effective coupling strengths.

Although it would be nice to find impurity positions that lead to case 2b) with a triplet ground state, such a situation has not been found in the  $8 \times 8$ -lattice. The total overlap is always either 1.5 (if all  $J_{\text{eff}}$  are equal) or  $|\Omega_{\text{tot}}| \approx 1.48$  (at least one effective coupling strength differs from the others), which are the two overlap values discussed above. Accordingly, only nondegenerate ground states have been found.

While case 2b) is rather restricted due to requiring a linearly dependent Fermi orbital, scenario 3a) could show a greater variety of Fermi orbital overlap. To this end, the impurity constellations shown in Figs. 3.30(c) and (d), which result in case 3a), are analyzed. Very similar to what has been observed for case 2b), there are only two values the absolute overlap takes: For equal effective coupling strengths,  $|\Omega_{\text{tot}}| = 1.5$ , while  $|\Omega_{\text{tot}}| \approx 1.32$  if at least one effective coupling strength differs from the others. It is interesting, that these cases turn out to have triplet ground states, although  $|\Omega_{\text{tot}}|$  is either equal or even smaller than in case 2b). However,  $|\Omega_{\text{tot}}|$  is still in the regime, where nondegenerate ground states are expected, according to the former analysis (see for example  $|\Omega_{\text{tot}}|$  in Figs. 3.26 and 3.25).

For the  $8 \times 8$ -square lattice, certain impurity locations give case 3a) with  $|\Omega_{\text{tot}}| = 2$ , for example, if impurities are located at sites (2;7), (4;5), and (8;1). In these cases, the triplet ground state is found, which is again expected due to the large absolute total overlap. Cases with this rather large overlap all have in common, that the effective coupling strengths are equal.

### Square lattices of arbitrary size

The discussion of case 3d) has already shown, that there are just few "types" of Fermi orbitals, and finding only three different values for  $|\Omega_{\text{tot}}|$  in 3a)-cases underpins this assumption. A "type" of Fermi orbital  $U_{k_F}(i_r)$  is given by its weight, which is in close relation to the effective coupling strength  $J_{\text{eff}} = J \sum_g |U_{k_F g, i_r}|^2$  according to Eq. (3.29). Fig. 3.31(a) shows, that the  $8 \times 8$ -square lattice is indeed build up by just two different "types" of Fermi orbitals. This explains, why only very few different values of absolute total overlap in cases 2b) and 3a) were found. Moreover, scenarios with  $J_{\text{eff}}(1) > J_{\text{eff}}(2) > J_{\text{eff}}(3)$ , which would be interesting for case 3d) with two Fermi electrons, cannot be realized. Since the Fermi orbitals  $U_{k_F}(i_r)$  result from the unperturbed lattice, one can conclude that a variation of the lattice size gives hope to find more complex systems.

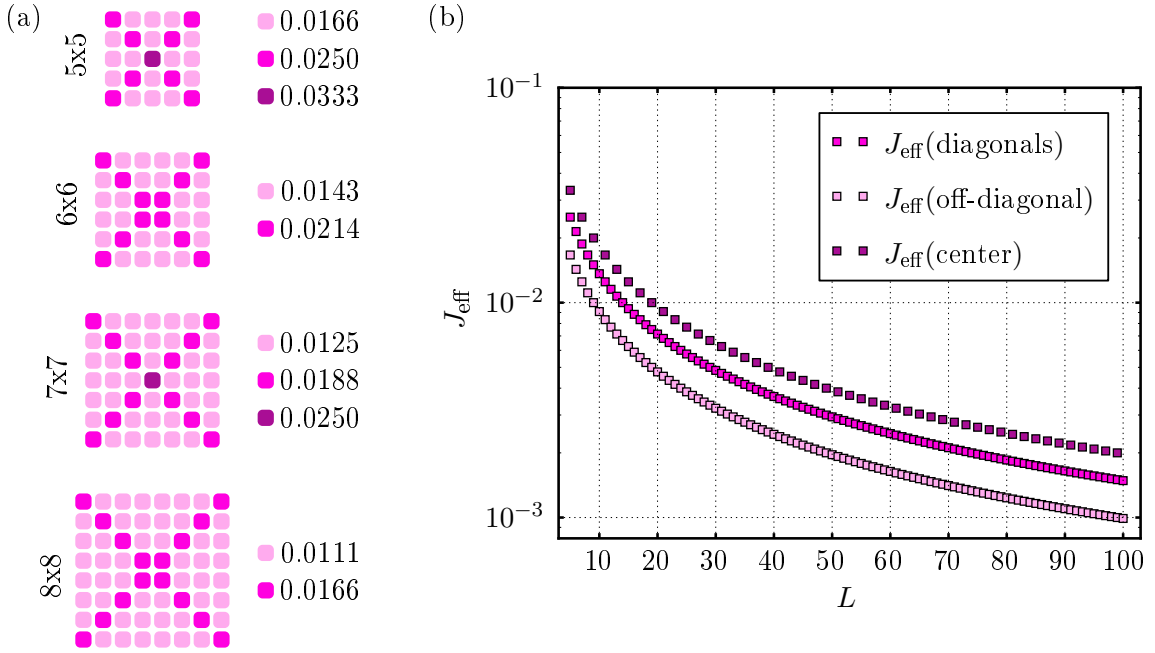


Figure 3.31.: (a) Effective coupling strength  $J_{\text{eff}}$  on each lattice site for systems of sizes  $L \times L$ , where  $L = 5, \dots, 8$ . (b) Effective coupling strengths of sites lying on the main diagonal ( $J_{\text{eff}}(\text{diagonals})$ ), on off-diagonal sites ( $J_{\text{eff}}(\text{off-diagonal})$ ), and (if  $L$  is odd) on the center site, plotted against lattice sizes  $L \times L$ , where  $L$  ranges from 5 to 100. The number of electrons is set to  $n = L^2$ , which ensures that the Fermi energy is the one of half-filling, which is the most degenerate one.

By varying the system size of the square lattice, one quickly explores a simple scheme: Every square lattice with even edge length  $L$  has only two differently weighted Fermi orbitals, i.e. only two different values of  $J_{\text{eff}}$  are found, where the greater values of  $J_{\text{eff}}$  are always found on the main diagonals. This scheme is also valid if  $L$  is odd, however, a third type of Fermi orbital comes into play, which is the one connected to the center site. This center orbital has the greatest weight, and its corresponding effective coupling strength  $J_{\text{eff}}(\text{center})$  is twice the strength of the off-diagonal couplings. For lattices with sizes  $L = 5, \dots, 8$ , this scheme is shown in Fig. 3.31(a).

With increasing lattice size, the effective coupling strengths decrease, which is clear, because orbitals  $U$  build up an orthonormal matrix. The greater the matrix dimension, the smaller its components to maintain the normalization. This can also be seen in Fig. 3.31(b), where the effective coupling strengths corresponding to the three types of orbital weights are plotted against the lattice size. To obtain comparable results, the electron filling was

chosen to  $n = L^2$  (half-filling), which ensures to get the most degenerate energy level (with degeneracy  $G_F = L$ ). Note, that for numerical applications  $n(L) = L(L - 1) + 1$  could be used, since it returns the same degenerate single-particle energy levels as  $n(L) = L^2$ , which is because the degeneracy of the Fermi energy levels corresponding to half-filling is  $G_F = L$  in every  $L \times L$ -square lattice.

The conclusion of the analysis above is, that only a handful of different Fermi orbitals exist, independent of the lattice dimension. For square lattices it is thus difficult, or maybe even impossible, to find all cases discussed with the toy model. This holds especially true for scenarios, where the absolute total overlap influences the final ground state degeneracy.

With the insights gained above, it is easy to "construct" certain cases. To this end, a simple notation is introduced: Orbitals resulting from lattice sites that are on the main diagonals of the square lattice are type "D", where the special case of the center orbital (in lattices with odd  $L$ ) is labeled "C". Off-diagonal orbitals are named "O"-type orbitals. For example, a "CDO"-combination is one impurity on the center site ("C"), one on a main diagonal site ("D") and one that is not placed on a site corresponding to the main diagonals ("O"). Of course, the order of the orbital types is arbitrary. Note, however, that a given orbital type combination is not strictly connected to a single case only. For example, "CDD" in a  $7 \times 7$ -lattice can be either case 2a), 2b), 3a), 3b), or 3c). The notation is supposed to distinguish between different orbital type combinations that all belong to the same scenario.

For case 2b), Tab. 3.4 shows combinations of different orbital types for the  $7 \times 7$ -square lattice. As one can see, there are only three orbital type combinations which include this scenario, for all of them the ground state is nondegenerate and the absolute overlap is around 1.50. This fits to the results presented above for the  $8 \times 8$ -lattice, where a "CDD"-case of course cannot be found, as this specific center orbital (type "C") is only present in lattices with odd  $L$ .

orbital type	exemplary impurity sites	$ \Omega_{\text{tot}} $	ground state degeneracy
"OOO"	(1;2), (1;4), (2;3)	1.50	1
"ODD"	(1;1), (1;3), (2;2)	1.48	1
"CDD"	(4;4), (1;1), (5;3)	1.49	1

Table 3.4.: Combination of orbital types in the  $7 \times 7$ -square lattice, which result in case 2b), with the corresponding absolute total overlap  $|\Omega_{\text{tot}}|$  and the found ground state degeneracy. Some combinations, like "OOD", do not result in case 2b) and are therefore not listed.

Equivalently to case 2b), results for scenario 3a) are shown in Tab. 3.5. There are more orbital combinations, each leading to a different absolute total overlap  $|\Omega_{\text{tot}}|$ . However, the ground state is always a triplet, even for the rather low overlap of orbital combination "ODD". Combining this result with the toy model analysis above, one can conclude that such a low value of  $|\Omega_{\text{tot}}|$  is in the crossover region between singlet and triplet ground states. The same holds true for  $|\Omega_{\text{tot}}| = 1.5$  in case 2b), where the rather large overlap could generate a triplet ground state (which, however, is not found).

The real importance of the results presented in Fig. 3.31 and Tabs. 3.4 and 3.5, is, that they can be in principle transferred to any square lattice of arbitrary size (although the finite-size regime should not be left, i.e. ensuring  $\Delta > 0$ ). For example, selecting a  $15 \times 15$ -lattice and placing impurities on sites (8;8), (1;1), and (7;9) gives an orbital combination "CDD", resulting in case 2b) with exactly the same absolute total overlap ( $|\Omega_{\text{tot}}| = 1.49$ ) as in the  $7 \times 7$ -lattice. This leads moreover to the conclusion, that (for  $n_F = 1$ ) every

orbital type	exemplary impurity sites	$ \Omega_{\text{tot}} $	ground state degeneracy
"OOO"	(1;2), (1;4), (2;5)	1.50	3
"OOD"	(1;1), (1;3), (2;4)	1.31	3
"ODD"	(1;1), (1;3), (3;5)	1.14	3
"DDD"	(1;1), (2;2), (3;3)	2.00	3
"CDD"	(4;4), (2;2), (3;3)	1.82	3

Table 3.5.: Combination of orbital types in the  $7 \times 7$ -square lattice, which result in case 3a), with the corresponding absolute total overlap  $|\Omega_{\text{tot}}|$  and the found ground state degeneracy. Other combinations, like "CDO", never result in case 3a) and are therefore not listed.

2b)-case has a singlet, and every 3a)-scenario has a triplet ground state, independent of the square lattice size.

Since all cases but 2b) and 3a) are independent of orbital overlap, the ground state degeneracy will not change if the lattice size is varied. Except for case 3d), where the individual effective coupling strengths are of importance, the ground state degeneracy of any three-impurity system is predetermined by the scenario resulting from impurity placement. This should be of great interest for experimental realizations.

For the discussions in the entire Subsec. 3.6.4, only the single Fermi electron cases have been regarded. As summarizing Tab. 3.2 shows,  $n_F > 1$  is not as interesting as  $n_F = 1$ , because ground state degeneracies are independent of the Fermi orbital's overlap. However, for case 3d) with  $n_F = 2$ , more than one ground state degeneracy can be found, dependent on  $J_{\text{eff}}$ . The analysis of different orbital types shows, that placing an impurity on each orbital type (i.e. "O", "D", and "C") results in having all three impurities coupled with different  $J_{\text{eff}}$ . With such a geometry, case 3d) with  $n_F = 2$  could be examined. One finds, however, that the center orbital is always overlapping with the orbitals on the main diagonals, which categorically excludes finding case 3d) with three different effective coupling strengths.

### 3.7. Short summary of results for two and three impurities

Summing up the analysis of the toy model, as well as the modeled systems with two and three impurities on square lattices, one finds that most of the overlapping scenarios can be realized. The ground state degeneracies found in calculations of square lattices fit to the ones predicted by the toy models. However, the toy models (especially for three impurities) cover parameter regimes, that are not found in calculations of the square lattice. The analysis of the orbital structure of square lattices shows, that some interesting quantities, such as the absolute total overlap or effective coupling strengths, are restricted to very few values, which is the reason why only some of the toy model's physics are found when placing impurities on a square lattice. The toy models, however, are great tools to understand the influences of orbital overlap and effective coupling strengths on ground state degeneracies and interimpurity correlations. This knowledge can be perfectly transferred to systems other than square lattices. Possibly in higher-dimensional systems, or in systems with a different lattice geometry, some of the missing cases (for example, the general 2c)-case, or case 2b) with a triplet ground state) could be found. Whatever orbital structure one would find there, for two and three impurities it has already been analyzed with the toy models. Therefore, classification and understanding of lattices with a geometry different than a square lattice will be rather simple as it is covered by the work presented here.

A great example is the on-resonant configuration presented in Sec. 3.1, i.e. two impurities coupled to neighboring sites of a ring. The geometry gives  $G_F = 2$ , and half-filling yields two Fermi electrons,  $n_F = 2$ . From the specific impurity placement, one gets a case C)-scenario (see Subsec. 3.5.3), which is that the impurity spins couple to a different Fermi orbital each, whereby the latter do not overlap. In the  $J \rightarrow 0$ -limit, one thus knows immediately, that the interimpurity spin-spin correlation  $\langle \mathbf{S}_1 \mathbf{S}_2 \rangle$  must vanish, while a perfect antiparallel alignment between impurity and substrate spin is found. Each impurity spin is thus totally screened, which can also be seen in the correlation function  $\langle \mathbf{S}_1 \mathbf{s}_{\text{tot}} \rangle = -3/4$ . This example shows, that the presented theory is powerful in predicting the correct ground state properties for  $J \rightarrow 0$ , just by knowledge of the Fermi orbitals.

Although the effective Hamiltonian, Eq. (3.28), takes the form of a central-spin model, one finds non-central-spin model behavior for specific scenarios of orbital overlap, which is, from the physical point of view, an astonishing result. Contrary to central-spin model physics, a spin-flip of an impurity spin is found, indicating an interimpurity coupling mechanism. Since the effective model results from first order perturbation theory, the non-central-spin model behavior cannot be ascribed to interaction of RKKY-type. Rather, it is a mechanism in first order of impurity-lattice coupling  $J$ . The analysis has shown, that this effect occurs only in certain parameter regimes, where a connection to the overlap of the unperturbed system's orbitals is found. However, the resulting nondegeneracy of the ground state can nevertheless be found in calculations of  $8 \times 8$ -square lattices. Since it has moreover been shown, that the found physics are basically independent of the lattice size, this spin-flip mechanism can be found in square lattices of any spatial extension.

Aside from these results, many insights were gained concerning the distribution of  $k_F$ -electrons over the Fermi orbitals. Thus, some scenarios seem to be easily transferable to lattices with much more impurities, for example, if the coupling orbitals for each impurity are identical, as in cases A) and 1), or if the overlap vanishes as in cases C) or 3d). Moreover, several scenarios can be "built" from few-impurity cases, like, for example, the three-impurity case 2d) which consists of a single-impurity case connected with two-impurity scenario A). A full classification of systems with more than three impurities, however, goes beyond the scope of this work, but the insights gained above are helpful to understand most scenarios arising for many-impurity systems. The "rules" for predicting the correct ground state of such systems are gathered in the next section.

### 3.8. Generalization to more than three impurities

It goes without saying, that adding more impurities to a system increases the amount of Fermi orbital overlap scenarios excessively. In detail, the case of  $R$  impurities is described by a toy model of  $R$  vectors. Using rotational symmetry of the problem, the first Fermi orbital can be described by a vector with one non-zero entry, the second Fermi orbital by a vector with two non-zero entries, and so on. The  $R$ th coupling Fermi orbital is thus a vector in  $R$ -dimensional Euclidean space. To describe each vector, one uses the  $n$ -spheres, which are the generalizations of the ordinary 2-sphere from 3-dimensional Euclidean space. The  $R$ th Fermi orbital vector is thus described by an  $(R - 1)$ -sphere, which requires a set of  $R - 1$  angles to be correctly represented. The total number of angles needed for a toy model which describes all overlap situations of a system with  $R$  impurities is therefore

$$n_{\triangleleft}(R) = \sum_{\hat{r}=1}^{R-1} (R - \hat{r}) . \quad (3.48)$$

Adding an impurity,  $R \rightarrow R + 1$ , increases  $n_{\triangleleft}(R)$  by  $R$ :

$$n_{\triangleleft}(R + 1) - n_{\triangleleft}(R) = R . \quad (3.49)$$

As  $n_{\triangleleft}(R)$  also gives the amount of overlaps (without double counting symmetric values, i.e.  $\Omega_{xy} = \Omega_{yx}$  is only one overlap), one immediately sees how rapidly the number of overlaps increases. While for the above discussed case of three impurities the number of overlaps is three, it increases by another three overlaps to a total of six overlaps for systems with four impurities. This sounds at first not too dramatic, but each overlap has three important values ( $0$ ,  $0 < |\Omega| < 1$ , and  $1$ ) that need a separate treatment each. A four-impurity system has therefore roughly  $3^3$ -times more overlapping scenarios than a three-impurity system. Although not all of these "new" options are physical, a huge amount of new scenarios still remains. Therefore, a classification, even if possible for a few more impurities, is rather pointless.

Nevertheless, some limiting cases can easily be generalized. A prime example is the scenario of full overlap, i.e. all coupling Fermi orbitals are identical. As this is the central-spin model, the ground state degeneracy is already known thanks to the Lieb-Mattis theorem [147]. One Fermi electron screens in total one out of  $R$  impurity spins, so that the remaining total spin is  $(R - 1)/2$ .

Another simple case is the missing overlap scenario (for two impurities named case C), for three impurities named case 3d)). The  $R$  coupling Fermi orbitals form  $R$  simple central-spin models with only one spin each. The occupation of the coupling Fermi orbitals follows the simple rule, that Fermi orbitals are being occupied according to their corresponding effective coupling strength, where strong  $J_{\text{eff}}$  favor Fermi electron occupation. A bunch of singlets is formed, and a possible ground state degeneracy comes from either remaining spins (if  $n_F < R$ ), or from distribution of  $k_F$ -electrons over uncoupled Fermi orbitals (if  $n_F > R$ ). Moreover, the ground state degeneracy will increase, if there are several energetically equivalent possibilities for Fermi electron occupation, leading to the same decrease of the system's internal energy. Despite the many options arising from possible combinations of effective coupling strengths, this case can be easily transferred to systems with a greater number of impurities. The difficulty is solely to find out all effective coupling strengths and to put them into the right order.

For systems where the single overlaps only take the values  $0$  and  $\pm 1$ , but not in between, predictions for  $R > 3$  are also possible. Such systems consist of several central-spin models, where the number of spins coupled to the "central" regions is determined by how many Fermi orbitals are identical. The occupation of Fermi orbitals follows the principle of minimizing the internal energy, which means that (partially) screening as many impurities as possible is favored. In such a scenario, however, the placement of Fermi electrons might not be obvious, because a competition between effective coupling strengths and screening multiple impurity spins might arise. This is closely related to case 2d), where this competition has been observed. In the end, interimpurity correlations help to understand, which effect dominates. Although the interplay of effective coupling strengths and screening can lead to many different ground state degeneracies, such scenarios are despite their complexity well understood, as it is still a combination of central-spin models only.

Sheer countless scenarios of orbital overlap are possible, if  $\Omega$  is not restricted to integer values only. It goes without saying, that a general recipe to correctly "guess" ground state degeneracies cannot be given, aside from the rules that have already been formulated in the discussions above. However, the results found within the previous sections of this work show, that following the rules is promising, as deviations have not been found so far. Therefore, a compendium of rules is listed below, which should be helpful to understand even complex scenarios resulting for many-impurity systems. Following these rules should help to classify and understand the physics of systems with more than three impurities.

1. **Maximal interaction with impurity spins.** Several partially screened impurity spins lower the internal energy usually more than one fully screened spin. Following this rule gives a helpful hint, where the Fermi electrons have their greatest occupation probability. The statement includes, that double occupation of Fermi orbitals is avoided if possible. Also, uncoupled Fermi orbitals are not occupied until all coupling Fermi orbitals are singly occupied.
2. **The stronger, the better.** The greater an effective coupling strength to a Fermi orbital is, the more likely is its occupation. This might be a competing effect to the first rule, especially if a  $k_F$ -electron can occupy either an orbital with few, strongly coupled spins, or one with many, but weakly coupled spins. In such a case, further research must be done (e.g. an analysis of interimpurity correlations).
3. **A real need for effective coupling strengths.** As long as the coupling Fermi orbitals are connected, a change in effective coupling strengths does not affect the contribution of these Fermi orbitals to the ground state degeneracy. Contrary, if a set of coupling Fermi orbitals is completely orthogonal to another set, then the effective coupling strength is needed to distinguish between favored orbitals according to the second rule. Examples for connected orbitals are cases 1), 2a), 2b), 3a), and 3b). In contrast, a clear separation of orbitals is found in cases 2c), 2d), 3c), and 3d).
4. **Increase of degeneracy due to equivalent situations.** It may occur, that some coupling Fermi orbitals are equivalent, i.e. where the same amount of impurity spins couples with the same effective coupling strengths to each of these Fermi orbitals. If there are not enough, or likewise too many Fermi electrons to singly occupy each of these equivalent Fermi orbitals, the ground state degeneracy increases by a factor, which is given by how many situations are physically equivalent. Case 3d) with equal effective coupling strengths is a prime example.
5. **The total overlap is a judge.** Even if it is clear, which orbitals are occupied by the Fermi electrons, some special cases have shown more than one stable ground state configuration dependent on the total overlap of the Fermi orbitals. This effect seems only to occur, if more than two Fermi orbitals overlap partially (cases 2b), 2c), 3a), and 3b)). If only one electron was present and the (absolute) total overlap was small, unexpected antiferromagnetic interimpurity correlations have been found. For strong overlap, the interimpurity correlations were ferromagnetic. For many-impurity systems, partially overlapping Fermi orbitals should be analyzed with this aspect in mind.
6. **Restriction to coupling Fermi orbitals.** Even if the degeneracy of a single particle energy level becomes large (in an  $L \times L$ -square lattice it is maximally  $L$ ), only as many Fermi orbitals as impurities given are relevant. By rotation of the orbital vectors one can build up a reduced Hilbert space, spanned only by coupling Fermi orbital vectors, while uncoupled Fermi orbitals are orthogonal to the former. Physics can be fully covered by examination of  $R$  orbitals.
7. **Dealing with large electron numbers  $n$ .** In fact, the interesting quantity is the number of Fermi electrons,  $n_F$ , as electrons with energy  $\varepsilon_k < \varepsilon_{k_F} = \varepsilon_F$  do not contribute. If all coupling Fermi orbitals are singly occupied, the remaining  $k_F$ -electrons distribute over all uncoupled Fermi orbitals. Fermi electrons on uncoupled orbitals contribute to the total ground state degeneracy with a factor given by Eq. (3.38). For numerical purposes, one can reduce calculations to only few Fermi electrons (usually  $n_F = R$ ) and multiply the resulting ground state degeneracy with the factor that represents the contribution of Fermi electrons on uncoupled orbitals to the ground state degeneracy.





## 4. Overscreening

### 4.1. A brief introduction to overscreening

Overscreening is a situation that occurs typically, if an impurity spin is connected by several coupling channels to the conduction electron system, and the number of participating electrons is greater than needed for a full screening of this spin [96]. Its physical relevance has shown up in the description of non-Fermi-liquid physics, as found in numerous actinide and rare-earth systems [99]. Since the latter are associated with heavy fermion physics, they are relevant for topological superconductors [38–40] and topological Kondo insulators [36, 41–44]. Moreover, in the currently very popular field of research on graphene, the peculiar physical properties of the latter seem to be associated with overscreening [148]. Furthermore, overscreening is a key mechanism in two-level systems of atom tunneling models in glassy materials [149–152].

The non-Fermi-liquid behavior has often been studied, both experimentally [153–156] and theoretically, especially in the one-impurity case [99, 157–160]. The theoretical results were quite successful using the multi-channel ("M-channel") Kondo model. The latter describes the coupling of an impurity spin to  $M$  degenerate conduction electron bands, thus yielding more than just the single channel known from the original Kondo model. In case of the two-channel Kondo model ("2CK"),

$$\mathcal{H}_{2CK} = J_1 \mathbf{s}_1 \mathbf{S} + J_2 \mathbf{s}_2 \mathbf{S} + \mathcal{H}_{\text{reservoirs}} , \quad (4.1)$$

the impurity spin  $\mathbf{S}$  is connected to two independent reservoirs, with coupling strengths  $J_{1,2}$ , respectively. If  $J_1 \neq J_2$ , the system is driven into the one-channel ground state associated with the stronger coupled reservoir, which, by the way, makes it difficult to observe the two-channel Kondo effect in experiments. If, however,  $J_1 = J_2$ , both reservoirs equally attempt to fully screen the impurity spin, which is not possible. This leads to partial screening of the impurity (overscreening) and an unstable configuration (the non-Fermi-liquid) arises [154]. Both the coupling strengths and the number of screening channels have obviously a strong influence on the low-energy physics, and will therefore be examined within the present work.

Despite of the research already done on overscreened impurities, a theoretical treatment within finite-size systems has only been done with conformal field theory techniques [97]. In the present work, overscreening in finite-size systems is examined by means of perturbation theory, similar to the framework established in Sec. 3.2. In the next section, the modified theory is presented. Numerical results, which are obtained by exact diagonalization of the effective Hamiltonian, are found in the sections thereafter. Some parts of the following sections have been established in collaboration with Y. Couzinié, and can be found in Ref. [161]. Overlap of the present work with this reference is cited accordingly.

## 4.2. Modified Hamiltonian

The model Hamiltonian (3.28) from Sec. 3.2.2 precludes overscreening, since each impurity spin is coupled to exactly one Fermi orbital. Overscreening, however, is the case of having several electronic channels available for screening of an impurity spin (see the characterization of under-, full, and overscreening in Fig. 1.2). Therefore, in order to get an overscreening situation, the crucial point is to get more than one coupling channel for each impurity spin.

The logical extension of the model presented in Sec. 3.2 is thus to allow for not only local, but also nonlocal impurity couplings. In the following, this is called a "generalized coupling". Note, that the channels obtained this way must not necessarily correspond to "independent reservoirs", as stated in the introduction above. Coupling an impurity to several independent subsystems is a rather artificial situation, which is often referred to as "forced" overscreening [161]. In the present work, a restriction to independent reservoirs is not wanted, as the focus lies on finding overscreening for a possibly realistic scenario, i.e. a single impurity interacting not only locally with the nanosubstrate.

The Hamiltonian describing  $R$  impurities, each coupling to all present electronic spins, is given by:

$$\mathcal{H}_1 = \sum_{r=1}^R \sum_{l=1}^L J_{li_r} \mathbf{s}_l \mathbf{S}_{i_r} , \quad (4.2)$$

whereby  $\mathbf{s}_l$  is the electronic spin at lattice site  $l$  and  $\mathbf{S}_{i_r}$  is the  $r$ th impurity, located at site  $i_r$ . The coupling strength is given by a matrix  $J_{li_r}$ . The total number of lattice sites is denoted by  $L$ .

Following the calculations from Sec. 3.2, a low-energy model can be obtained using perturbation theory, where the effective Hamiltonian  $\mathcal{H}^{\text{eff}}$  is likewise given via

$$\mathcal{H}^{\text{eff}} = P_0 \mathcal{H}_1 P_0 . \quad (4.3)$$

$P_0$  is the projection operator onto a  $\Gamma$ -fold degenerate  $N$ -particle ground state, see also Eq. (3.12). The results up to Eq. (3.16) can be transferred easily to the more general case presented here, giving

$$\mathcal{H}^{\text{eff}} = \frac{1}{2} \sum_{r=1}^R \sum_{g,g'}^G \sum_{\sigma,\sigma'}^{\uparrow,\downarrow} \sum_{l=1}^L J_{li_r} U_{k_F g,l} U_{l,k_F g'}^* \boldsymbol{\sigma}_{\sigma\sigma'} c_{k_F g\sigma}^\dagger c_{k_F g'\sigma'} P_0 \mathbf{S}_{i_r} . \quad (4.4)$$

Analogously to the effective Hamiltonian (3.16) derived in Sec. 3.2.2, Eq. (4.4) is rather unsuitable for vivid interpretations because the conduction electron system is described by delocalized spins. This issue can be solved by performing another transformation, but in contrast to the more specific case with local coupling only, the coupling matrix  $J_{li_r}$  and the sum over all lattice sites  $l$  must be included. Let  $M$  be the following  $G_F \times G_F$  matrix in  $g, g'$ , where  $G_F$  is the degeneracy of the Fermi energy level ( $G_F = G(k_F)$ ):

$$M_{gg'}(r) = \sum_{l=1}^L J_{li_r} U_{k_F g,l} U_{l,k_F g'}^* . \quad (4.5)$$

Using Eq. (3.17), one obtains two matrices, namely  $V_{hg}(r)$  and  $V_{g'h'}^*(r)$ , which can be used for  $r$ -dependent diagonalization of  $M$ :

$$\sum_{g,g'} V_{hg}(r) M_{gg'}(r) V_{g'h'}^*(r) = x_h(r) \delta_{hh'} . \quad (4.6)$$

In the equation above,  $x_h(r)$  is the  $h$ th of at most  $G_F$  non-zero eigenvalues. Since  $M$  is composed of  $L$  dyadic products, each weighted with a specific  $J_{i_r}$ , it is in general not possible to find an analytical expression for these eigenvalues. The eigenvalues  $x_h(r)$  represent the effective couplings of a single impurity spin (the  $r$ th impurity) to  $G_F$  (pairwise orthogonal) Fermi orbitals (which are indicated by  $h = 1, \dots, G_F$ ).

Gathering the results, one gets the effective low-energy Hamiltonian for generalized coupling:

$$\mathcal{H}^{\text{eff}} = \sum_{r=1}^R \sum_h^{G_F} x_h(r) \mathbf{s}_F(r) \mathbf{S}_{i_r} P_0, \quad (4.7)$$

where

$$\mathbf{s}_F(r) = \frac{1}{2} \sum_{\sigma, \sigma'} c_{k_F h \sigma}^\dagger \boldsymbol{\sigma}_{\sigma \sigma'} c_{k_F h \sigma'}. \quad (4.8)$$

Eq. (4.7) can be used to examine overscreening. A fundamental requirement is a degenerate Fermi energy level (i.e.  $G_F > 1$ ) and a minimum of two Fermi electrons ( $n_F > 1$ ).

### 4.3. Effective coupling strengths

This section is dedicated to get an impression of the relation between local and nonlocal coupling strengths. The analysis will be performed for a single impurity, clarifying how many coupling channels may arise. The understanding of this case is fundamental for a generalization to more than one impurity.

#### 4.3.1. Concept and interplay of local and nonlocal coupling

From a theoretical point of view, quantities such as the geometry, the locations of impurities, or the degeneracy of the Fermi energy level  $G_F$  are known. It remains the question, what happens if  $G_F$  takes large values (such as  $G_F = 8$  known from the  $8 \times 8$ -square lattices discussed in Chap. 3)? How many coupling channels are expected, and where do these channels come from? To answer these questions, one should take a more detailed look at the theory.

The number of coupling channels for a single impurity is given by the number of non-zero eigenvalues of matrix  $M$ , Eq. (4.5). Note, that  $M$  is a site-dependent object, meaning that matrix  $M$  for an impurity located at site  $i$  can (and in most cases will) be completely different from the matrix  $M$  corresponding to a different site  $j \neq i$ .

One can basically find two scenarios: Either the number of non-zero eigenvalues of  $M$  is smaller than  $G_F$  (see for example all but the lower right panel in Fig. 4.1), or it is equal to  $G_F$  (lower right panel in Fig. 4.1). In the first case, the impurity spin is not coupled to all  $G_F$  Fermi orbitals, giving rise to a distinction between "coupled" and "uncoupled" Fermi orbitals as has intensively been discussed in Chap. 3. In the second case, the impurity spin is coupled to all  $G_F$  Fermi orbitals.

Unfortunately, the number of coupling channels is a quantity which is not easily (if at all) accessible beforehand. One knows, however, that each summand  $J_{i_r} U_{k_F g, l} U_{l, k_F g'}^*$  in Eq. (4.5) contributes to the coupling channels. Assuming a large Fermi energy level degeneracy  $G_F$  and only local coupling, then  $M$  would be a  $G_F \times G_F$ -matrix consisting of a single dyadic product,  $M = J |U\rangle \langle U|$ . This matrix has obviously  $|U\rangle$  as an eigenvector (with the

only non-zero eigenvalue  $\langle U|U\rangle$ ) and one finds  $G_F - 1$  eigenvectors that are orthogonal to  $|U\rangle$  (see discussion in Sec. 3.2.2). This gives one coupling channel, as it was the case in Chap. 3. Introducing a next neighbor coupling adds - dependent on the geometry - at least one more dyadic product, which appears in the sum of matrix  $M$ , Eq. (4.5). Each of the dyadic products can be used to fix an eigenvalue, as was demonstrated in the case of local coupling only. It might happen, however, that the eigenvector of an additional dyadic product is linear dependent of an already known eigenvector. In the notation above, this would be the case if the dyadic product arising from next neighbor coupling also has eigenvector  $|U\rangle$ , which would solely renormalize the eigenvalue  $\langle U|U\rangle$  found from the local coupling contribution, and still  $G_F - 1$  eigenvalues are trivial. This is, however, usually not the case. On the other hand, the number of coupling contributions (local, next neighbor, ...) determines the number of dyadic products summed over in Eq. (4.5), and thus being the upper limit for the number of coupling channels.

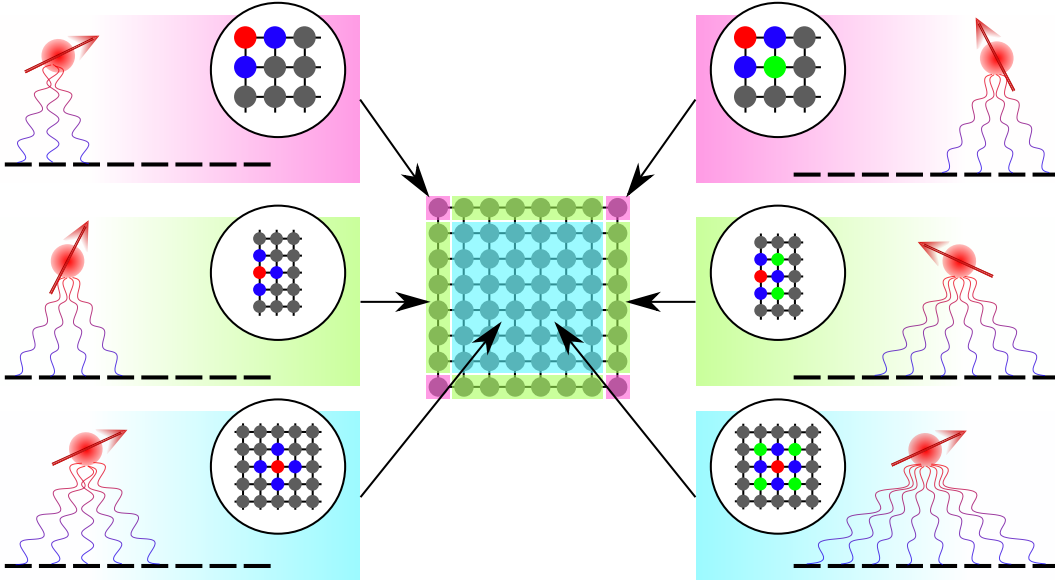


Figure 4.1.: Maximum amount of different coupling channels between a single impurity (red sphere with arrow) and  $G_F$  Fermi orbitals (black lines within the six panels), which arise in an  $8 \times 8$ -square lattice with open boundary conditions at around half-filling (ensuring  $G_F = 8$ ). The number of coupling channels varies with the location of the impurity: At the corner (pink boxes), at the edge (light green boxes), or in the center region (light blue boxes). The left panels show the maximum number of coupling channels for only local and next neighbor coupling, while next nearest neighbor coupling is additionally included in the right panels. The insets show a characteristic impurity location (red filled circles) and their couplings: local (red), next neighbor (blue), and next nearest neighbor coupling (green). For periodic boundary conditions, the light blue boxes provide the correct number of maximum coupling channels. Note in the lower right panel, that not all of the nine possible coupling channels emerge, as  $G_F = 8$ .

For a better understanding, a few examples may clarify the situation. An impurity coupled to site  $i$  of a one-dimensional ring with local and next neighbor coupling gives three dyadic products in matrix  $M$  (Eq. (4.5)), i.e. the local contribution at site  $i$ , and two next neighbor contributions at sites  $i \pm 1$ .  $G_F$  is usually fixed at two, but three "pieces of information" are available to characterize the eigenstates of  $M$ . This leads to two coupling channels, which is the maximum as  $G_F$  is the upper limit of possible channels. Including next nearest neighbor coupling would not change the number of coupling channels, as the maximum is already reached by the next neighbor contribution.

In a two-dimensional  $L \times L$ -square lattice with open boundary conditions, the degeneracy of the Fermi energy level around half-filling is  $L$ . Placing a single impurity at a corner site gives one coupling channel due to the local contribution, and two additional channels for next neighbor coupling. Placing the impurity at the edge, but not at a corner, would increase the number of possible channels to four (local plus three next neighbor couplings), while an impurity located somewhere in the middle of the lattice has a maximum of five coupling channels (local plus four next neighbor couplings). If  $L > 5$ , then the number of coupling channels is less than the number of available Fermi orbitals. However, if next nearest neighbor coupling is included as well, the number of coupling channels might become as large as  $G_F$ , and a coupling to each Fermi orbital would be included.

Fig. 4.1 shows a schematic example of an  $8 \times 8$ -square lattice with open boundary conditions. Dependent on the location of the impurity, the number of maximally possible coupling channels alters. Even for a fixed coupling range (for example local, next neighbors, and next nearest neighbors), it still depends on the impurity location, if it is coupled to all  $G_F$  Fermi orbitals or not. In addition, the number of coupling channels might decrease due to symmetries, which makes it hard to estimate the correct amount of channels. As a consequence, ground state properties (such as the degeneracy) become harder to predict, as the coupling channels help to understand how Fermi electrons distribute over the Fermi energy levels.

Summarizing this, the number of coupling channels is strongly dependent on the geometry of the system, i.e. the impurity placement, open or periodic boundary conditions, and the total electron filling which indicates the Fermi energy level and thus its degeneracy. The number of channels can be increased easily by adding nonlocal couplings beyond next neighbor coupling (such as next nearest, next next nearest neighbors, etc.). Due to its site dependence, the total number of coupling channels is not a fixed quantity. For an impurity spin at the corner of a square lattice there are less coupling channels than for an impurity located in the center of the same system. All these different options make a classification very difficult, even if only a single impurity is present. The complexity surely increases, if several impurities are connected to the host system.

### 4.3.2. Testing of the effective coupling-concept

The key idea formulated in the last subsection was, that each effective coupling constant belongs to a certain Fermi orbital. In the following, it will be checked if the results obtained by numerical calculations are in agreement with this idea.

#### Single impurity coupled to a ring

A simple example for testing is a ring, i.e. a one-dimensional chain with periodic boundary conditions, where the one-particle energy spectrum is twofold degenerate (except for the lowest energy level, and additionally the highest energy level in cases of even chain lengths). A single spin-1/2 impurity coupled to such a ring is sufficient to principally find overscreening. For this example, only local and next neighbor coupling shall be regarded, as depicted in Fig. 4.2(a). The effective low-energy model then contains two Fermi orbitals, to which the impurity spin is coupled with different strengths  $x_{1,2}$  (see Fig. 4.2(b)).

Fig. 4.2(c) shows the calculated effective coupling strengths  $x_{1,2}$  for both ferro- and antiferromagnetic local coupling  $J = \pm 0.1$ . A very important result is, that - except for  $J_{n,n} = 0$  - the restriction to next neighbor coupling is obviously sufficient to create two non-zero coupling channels between impurity spin and Fermi orbitals, being in agreement with the

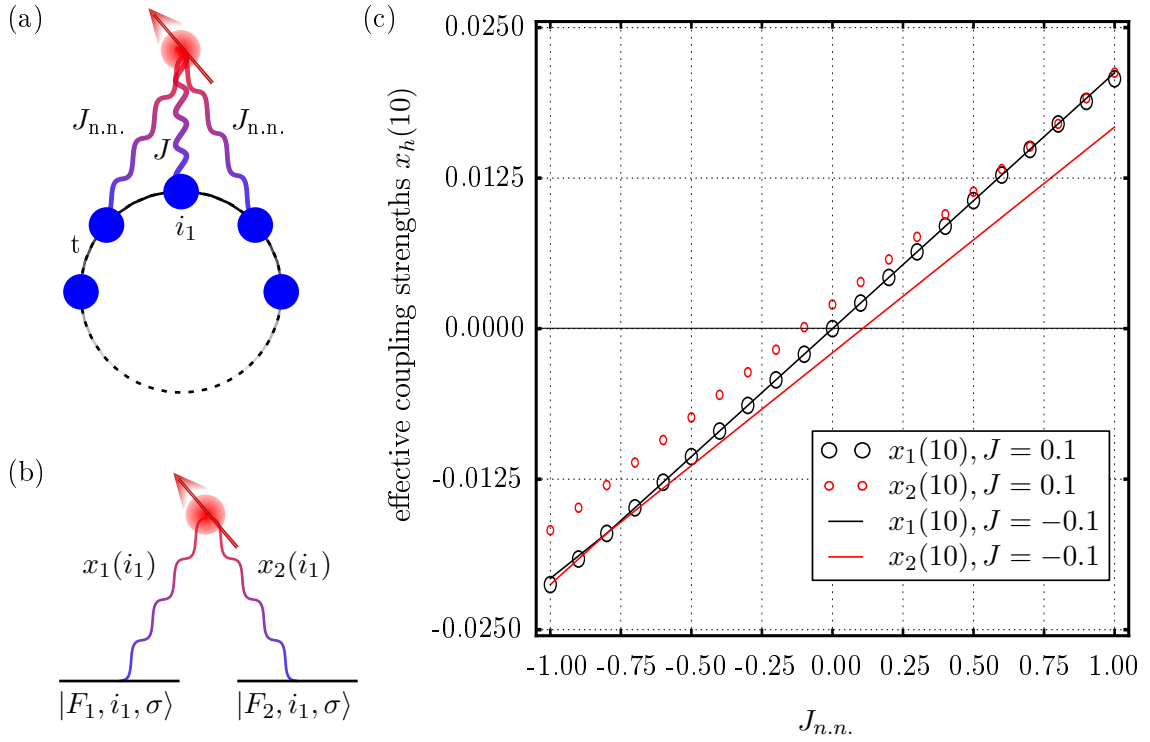


Figure 4.2.: (a) Ring with a single spin-1/2 impurity (red bubble with arrow, located at site  $i_1$ ) coupled locally with strength  $J$  and next neighbor-coupled with strength  $J_{n.n.}$ . Lattice sites with distance greater than one from the impurity, i.e. next next neighbor and beyond, are not coupled to the impurity, i.e. their coupling strength is set to zero. The conduction electrons may hop between neighboring sites with amplitude  $t$ . (b) Effective low-energy model: The impurity is coupled to two Fermi orbitals. The coupling strength is given by  $x_{1,2}$ , respectively. (c) Effective coupling strengths  $x_{1,2}$  between the single impurity and two Fermi orbitals, as modeled by (a) and (b). The local coupling is fixed at  $J = 0.1$  (red and black circles), and  $J = -0.1$  (red and black solid lines), while the next neighbor (n.n.) coupling is varied. The underlying geometry is a ring of  $L = 100$  sites, with the hopping fixed at  $t = 1$  and a filling of  $n = 51$  electrons. The only impurity is located at site  $i_1 = 10$ , which is due to periodicity an arbitrary choice. A similar figure is found in Ref. [161].

predictions made in the last subsection. Over the entire range, the effective couplings are of the same order, but not necessarily equal. This is an interesting aspect, because the deceptive symmetry in the original setup may suggest to find  $x_1 = x_2$ , especially in the regime where the nonlocal coupling strength dominates over the local coupling strength, i.e.  $|J_{n.n.}| > |J|$ . The data in Fig. 4.2(c) shows, that the effective couplings indeed approach one another, but only if local and nonlocal coupling are of the same type (both ferro- or antiferromagnetic). Calculations beyond  $J_{n.n.} > t$  are not trustworthy due to the validity range of the perturbation theory, but the tendency is that the effective coupling strengths do not merge asymptotically, but rather split up again (see also Ref. [161]). Moreover, from the data presented in Fig. 4.2(c), one finds the eigenvalues to linearly depend on  $J_{n.n.}$  (assuming a fixed local coupling  $J$ ). The explanation is, that each eigenvalue corresponds to one Fermi orbital, and, as the Fermi orbitals have in general a different weight each, the slopes of the functions  $x_1(J_{n.n.})$  and  $x_2(J_{n.n.})$  are different, where the local contribution  $J$  determines the ordinate (at  $J_{n.n.} = 0$ ) and therewith also the intersection of the eigenvalue functions.

To put this into a more theoretical context, the effective couplings are only then equal (i.e. the eigenvalues are degenerate), if the (usually symmetric) matrix  $M$ , see Eq. (4.5), has vanishing off-diagonal elements and the components  $M_{gg}$  are independent of index  $g$ . Due to the different weights  $U$ , this is in general not the case. Although the original system suggests a symmetry, the lattice sites are not symmetric with respect to the weights  $U$ . Therefore, there is no reason to expect a symmetry in the effective coupling strengths, not even if the local coupling  $J$  vanishes.

A specific point is  $J_{\text{n.n.}} = 0$ , which reproduces the theory presented in Sec. 3.2.2. The effective coupling  $x_1$  (black circles and black solid line in Fig. 4.2(c)) vanishes at this point, proving that the impurity spin is solely coupled to one Fermi orbital. At this point,  $x_2$  becomes equivalent with  $J_{\text{eff}}$  from the corresponding local coupling model from Sec. 3.2.2.

From the data presented in Fig. 4.2(c) one might conclude, that the effective couplings are one-to-one assigned to the real-space couplings (local and next neighbor), making  $x_1$  (black circles and black solid line) the effective coupling arising from next neighbor coupling  $J_{\text{n.n.}}$ , and  $x_2$  (red circles and red solid line) belonging to the local coupling  $J$ . It turns out, that this statement holds true in particular cases (see also the example of a square lattice in Fig. 4.6), but cannot be correct in general. One gets a simple example to show the opposite by adding the next nearest neighbor coupling to the ring system currently discussed. There are at most two coupling channels (limited due to  $G_F = 2$ ), the first arising from local coupling and the second from next neighbor coupling. The next nearest neighbor coupling, however, cannot create a new coupling channel, and thus necessarily affects at least one, but maybe even both coupling channels initially assigned to local and next neighbor coupling. Therefore, the concept that each longer-distant coupling creates a new channel, can in general not be correct.

Another glance should be taken on the sign of the effective couplings, as this distinguishes between ferro- and antiferromagnetic correlations. For  $|J_{\text{n.n.}}| > |J|$  in Fig. 4.2(c), the nonlocal coupling dominates over the local contribution, and thus the sign of the effective couplings is determined by  $J_{\text{n.n.}}$ . This leads to effectively ferromagnetic couplings ( $x_{1,2} < 0$ ) for  $J_{\text{n.n.}} \lesssim -0.1$ , while both effective coupling constants are antiferromagnetic for  $J_{\text{n.n.}} > 0$ . An interesting regime is found in between, where  $-0.1 < J_{\text{n.n.}} < 0$ . Within this realm, one of the effective couplings is positive (i.e. antiferromagnetic), while the other is ferromagnetic (negative sign). While the ferromagnetic regime is not of primary interest, the antiferromagnetic and the "mixed coupling" realms will be in the focus of the analysis presented below.

According to the results of Chap. 3, a single Fermi electron would occupy the Fermi orbital which is coupled the strongest to the impurity spin. For both the ferromagnetic and the antiferromagnetic realm, one should not be able to "spot" the occupied Fermi orbital, because the ground state is expected to be a singlet (antiferromagnetic regime) or a triplet (ferromagnetic regime), no matter which of the two orbitals is being occupied. In the mixed coupling region, however, the total spin of the ground state  $S_{\text{tot}}$  reveals, whether the Fermi electron occupies the ferromagnetically coupled orbital (giving  $S_{\text{tot}} = 1$  due to the triplet), or the antiferromagnetically coupled one (being the singlet ground state with  $S_{\text{tot}} = 0$ ).

Fig. 4.3 helps to answer this question. As can be seen, in the ferromagnetic phase (I), where both effective couplings  $x_{1,2} < 0$ , the ground state energy  $E_0$  is threefold degenerate, thus giving the expected triplet. The antiferromagnetic phase (III) shows according to the expectations for  $x_{1,2} > 0$  a nondegenerate ground state energy, which results in singlet formation. In the mixed coupling regime (II), there is a crossover between  $-0.08 < J_{\text{n.n.}} < -0.07$ , where the threefold degenerate ground state energy splits up into

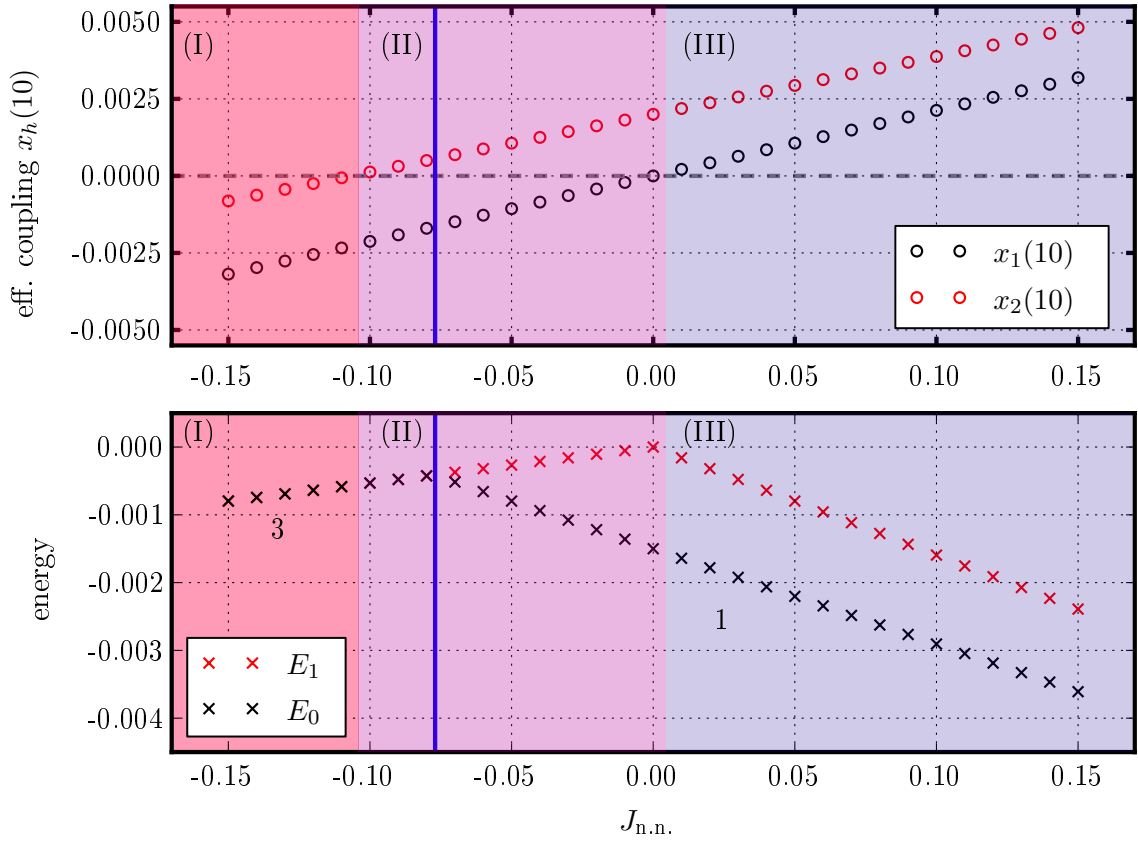


Figure 4.3.: Effective couplings  $x_{1,2}$  (upper panel) and lowest lying energy levels (lower panel) in dependence of the next neighbor coupling  $J_{n,n}$  for a ring with  $L = 100$  sites, a filling of  $N = 51$  electrons (i.e.  $n_F = 1$  and  $G_F = 2$ ), and an impurity spin with  $S = 1/2$  coupled to the nanosubstrate at lattice site 10 with fixed antiferromagnetic local coupling of value  $J = 0.1$  (see also Fig. 4.2). The upper panel is a more detailed view of the data presented in Fig. 4.2(c). In the lower panel, numbers 1 and 3 label the degeneracy of the ground state energy  $E_0$  (black crosses). Left of the blue line, only  $E_0$  is plotted. In both panels, ferromagnetic (I), mixed coupling (II), and antiferromagnetic (III) phases are highlighted. The vertical blue lines indicate the crossover between the singlet and the triplet ground state. A similar figure with slightly different parameters is found in Ref. [161].

a nondegenerate part (black crosses in the lower panel) and excited energy states (red crosses). In conclusion, below the critical value of  $J_{n,n}$  (which is roughly at  $-0.077$ ), the single Fermi electron occupies Fermi orbital  $|F_1, i_1 = 10, \sigma\rangle$ , and above of this critical value Fermi orbital  $|F_2, i_1 = 10, \sigma\rangle$  is being occupied.

The transition between the two occupation possibilities is obviously fluent. It remains the question, if the specific crossover point can be explained. Indeed an analytical solution is possible, since this is a simple two-spin problem. Let

$$\mathcal{H}_{sS} = \hat{J} \mathbf{s} \cdot \mathbf{S} \quad (4.9)$$

be the two-spin Hamiltonian, where the spins  $\mathbf{s}$  and  $\mathbf{S}$  are half-integer ( $S = 1/2$ ), and are coupled via  $\hat{J}$ . If the ground state is a triplet, then the internal energy is  $\langle \mathcal{H}_{sS} \rangle_{\text{triplet}} = \hat{J}/4$ . On the other hand, a singlet ground state gives  $\langle \mathcal{H}_{sS} \rangle_{\text{singlet}} = -3\hat{J}/4$  (see, for example, Ref. [161]). As  $x_1$  is the ferromagnetic (triplet-forming) effective coupling strength and  $x_2$  the (singlet-forming) antiferromagnetic coupling strength within the mixed coupling regime, there is a competition between the triplet ground state giving a ground state energy of



$x_1/4$ , and the singlet that pins the ground state energy to  $-3x_2/4$ . The crossover between singlet and triplet ground state thus occurs at  $x_1/x_2 = -3$ . If the ratio  $x_1/x_2 > -3$ , the system has a singlet ground state, below it is in the triplet ground state. Inserting the values of the effective coupling strengths from Fig. 4.3 into this relation gives the phase transition at exactly the marked point, thus perfectly matching with the calculated ground state energies and corresponding degeneracy.

The main conclusion from this analysis is, that the idea of assigning the effective couplings  $x_1$  and  $x_2$  to a specific Fermi orbital each (as depicted in Fig. 4.2(b)) is accurate. Moreover, a fluent phase transition between singlet and triplet ground state has been found in the very interesting mixed coupling regime. This includes, that triplet ground states can be found, even if the antiferromagnetic local coupling is stronger than the ferromagnetic nonlocal coupling, i.e.  $|J| > |J_{n.n.}|$ . According to the found ground states, the impurity is either not screened (triplet ground states), or fully screened (singlet ground states). With increasing number of Fermi electrons, the two coupling channels can be used to possibly find an overscreened regime, which is discussed below in Sec. 4.4. Before focusing on overscreening scenarios, the coupling strengths in two-dimensional systems will be analyzed.

## Square lattices

While the above discussed ring is limited to a twice degenerate Fermi energy level, the number of Fermi orbitals may be much larger in higher dimensional systems. A prototype example are  $L \times L$ -square lattices, which have an  $L$ -fold degenerate Fermi energy level (for  $L \geq 5$ ) at around half-filling. The theory predicts to have a various amount of maximally possible coupling channels, which strongly depends on the location of the impurity (as shown in Fig. 4.1).

Moreover, the number of coupling channels is affected by the range of the coupling, i.e. how many nonlocal couplings are taken into account. Although the real-space coupling does not translate one-to-one to the effective couplings, there is still a proportionality. In addition, it is important to realize, that the number of channels might decrease due to symmetries in the system.

An  $8 \times 8$ -square lattice at around half-filling (implying  $G_F = 8$ ) is used for testing. A single impurity located on a specific site of this lattice has then a fixed number of coupling channels, which is the value written on the corresponding lattice site in Fig. 4.4. From Subfig. (a), which shows the case of local and next neighbor coupling, as well as from Subfig. (b), showing local, next neighbor, and next nearest neighbor calculations, one can see that the maximum amount of coupling channels is often not achieved (orange colored lattice sites). On the other hand, the inclusion of longer-ranged couplings (Subfig. (b)) leads at least on most edge sites, and on all corners to the maximum amount of possible coupling channels. One could therefore surely expect to create the maximum amount of coupling channels by consideration of even longer-ranged couplings (beyond next nearest neighbor coupling).

The question, why at certain lattice sites the number of coupling channels does not take its maximally possible value is not simply answered. The most reasonable explanation is the highly symmetric form of the lattice geometry, which makes matrix  $M$  from Eq. (4.5) real and symmetric. As the eigenvalues of  $M$  are the effective couplings (and therewith the number of non-zero eigenvalues gives the number of coupling channels), this symmetry seems to be responsible for a reduction of the maximum amount of available coupling channels.

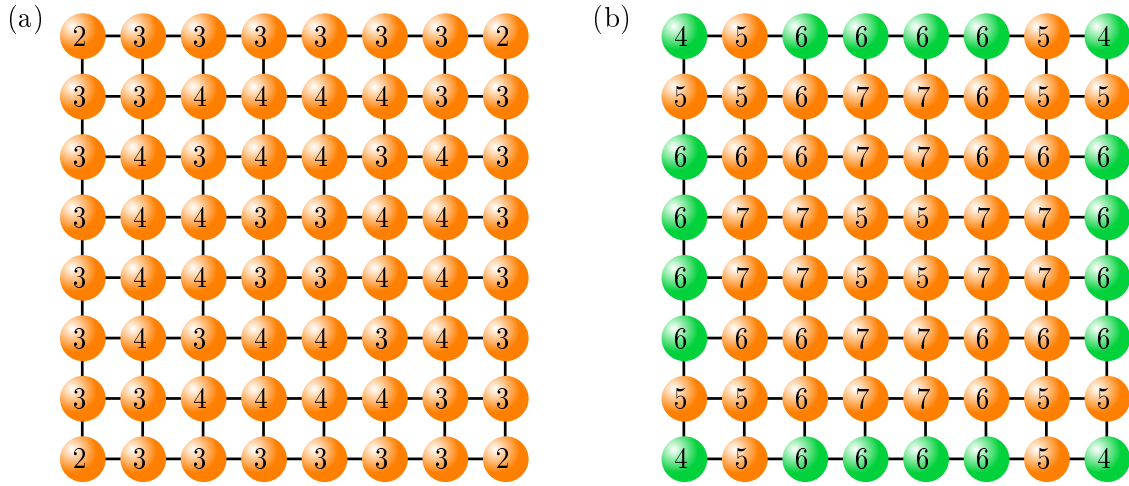


Figure 4.4.: A single impurity coupled to an  $8 \times 8$ -square lattice. Dependent on the location of the impurity, a different number of coupling channels (black number on the corresponding lattice site) is found. For example, an impurity located at site (2;2) in (a) has three coupling channels, and in (b) it has five. In Fig. (a), local ( $J = 0.1$ ) and next neighbor couplings ( $J_{n,n.} = 0.08$ ) are used, while in (b) additionally to these couplings also next nearest neighbor coupling of strength  $J_{n,n.n.} = 0.04$  has been included. If the maximum number of coupling channels according to Fig. 4.1 is reached, the lattice site is colored green, otherwise orange. In both figures, the electron filling is set to  $n = 57$  to ensure  $G_F = 8$ , and open boundary conditions are implemented.

This is underpinned by the following modification: By introducing an asymmetry in the nonlocal couplings, i.e. each coupling to a neighboring (and, optionally, next neighboring) site is modified by an anisotropy factor, one can ensure that all couplings (in real-space) are of different strength. Although this guarantees to have effectively different lattice site weights  $U$ , the number of coupling channels does not change at all. One can see both numerically and theoretically, that matrix  $M$  remains symmetric and real, despite of the implemented strong anisotropy of the couplings. One can conclude, that it is not the weight of the specific lattice sites that is responsible for the decreased number of coupling channels found, but rather the symmetry of  $M$  that reduces the amount of channels.

In order to find the maximum number of coupling channels, one could think of varying the size of the square lattice. This would change the lattice site weights  $U$ , but surely would not break the symmetry of matrix  $M$ . A reduction of the lattice size with a fixed set of coupling range (for example up to next nearest neighbors) should finally lead to the maximum amount of channels, as the latter are limited to maximally the number of Fermi orbitals  $G_F$ , which decreases with decreasing lattice extension. Another option is to change the shape of the nanostructure, from quadratic to rectangles of different spatial extensions. Of course, many other lattice geometries are also possible, but an analysis goes beyond the scope of the present work. Instead, the insights gained from the analysis above will be used to examine configurations that allow for overscreening. This is done in the following section.

## 4.4. Examples of overscreened impurities

In the last section, the focus lied on the analysis of the effective coupling strengths, which is helpful in understanding more complex systems and provides valuable information when searching for overscreening scenarios. In this section, examples are presented where overscreening is clearly found.

### 4.4.1. Overscreening in a ring

The above already considered system - a single spin-1/2 impurity coupled both locally and nonlocally (next neighbors) to a ring of  $L = 100$  sites - contained a single Fermi electron, which precludes overscreening due to the lack of necessary screening channels. This drawback can easily be fixed by increasing the amount of electrons from  $N = 51$  to  $N = 52$ , as this is a filling where two Fermi electrons are present, thus in total contributing with two screening channels.

The ferromagnetic phase is not of interest, since both Fermi electrons align parallel to the impurity spin, forming a fourfold degenerate ground state. Both numerical and analytical calculations (especially in Ref. [161]) prove this statement to be correct. The focus lies therefore on the mixed coupling and antiferromagnetic regime. Although the eigenvalues (and thus the effective couplings) remain unchanged after increasing the electron number, the  $J_{n,n}$ -dependent transition between ferro- and antiferromagnetic ground state in the mixed coupling regime is shifted. An analytical solution to the corresponding three-spin problem would deliver the critical crossover value, but since the result would not be easily transferable to other configurations, it is not worth the effort. Instead, numerical calculations show a clear change of the ground state degeneracy, which corresponds to this phase transition. This should be sufficient for the purposes of this analysis. For the given system, the critical  $J_{n,n}$  is found to be roughly between  $-0.11$  and  $-0.1$ , coinciding with the boundary between pure ferromagnetic and mixed coupling realm. Moreover, the critical value is in great agreement with the calculation of Ref. [161].

The two Fermi electrons distribute over the  $G_F = 2$  Fermi orbitals, forming an orbital spin  $\mathbf{s}_{k_F,h}$  each. In Fig. 4.5(a), the correlation function between the impurity spin  $\mathbf{S}_{10}$  and the orbital spin of the  $h$ th Fermi orbital are shown in dependence of the next neighbor coupling strength  $J_{n,n}$ . The ferromagnetic regime (I) shows that both orbital spins couple ferromagnetically to the impurity, which is expected since both effective couplings  $x_{1,2}$  are ferromagnetic. The ground state (see Fig. 4.5(b)) is accordingly fourfold degenerate.

At the crossover between ferromagnetic and mixed coupling regime (blue vertical line), the correlation  $\langle \mathbf{S}_{10} \mathbf{s}_{k_F,2} \rangle$  jumps from 0.25 to roughly  $-0.5$ , as the effective coupling  $x_2$  changes its sign from negative (ferromagnetic) to positive (antiferromagnetic). With increasing next neighbor coupling strength  $J_{n,n}$ , the effective ferromagnetic coupling ( $x_1$ ) decreases while the strength of the effective antiferromagnetic coupling ( $x_2$ ) increases. This shows up in the correlation functions as well, up to the point where the ferromagnetic coupling vanishes ( $x_1 = 0$  at  $J_{n,n} = 0$ ). This is exactly the local coupling case, where only one Fermi orbital is connected to the impurity. The only remaining coupling,  $x_2$ , is antiferromagnetic, so that impurity spin and the spin of orbital  $h = 2$  form a perfect singlet. Accordingly, the correlation function  $\langle \mathbf{S}_{10} \mathbf{s}_{k_F,2} \rangle$  takes its minimum value of  $-3/4$ , while the other one vanishes. The point  $J_{n,n} = 0$  thus represents the full screening situation, where the uncoupled Fermi electron has the freedom of spin, which leads to the twofold degenerate ground state at this point.

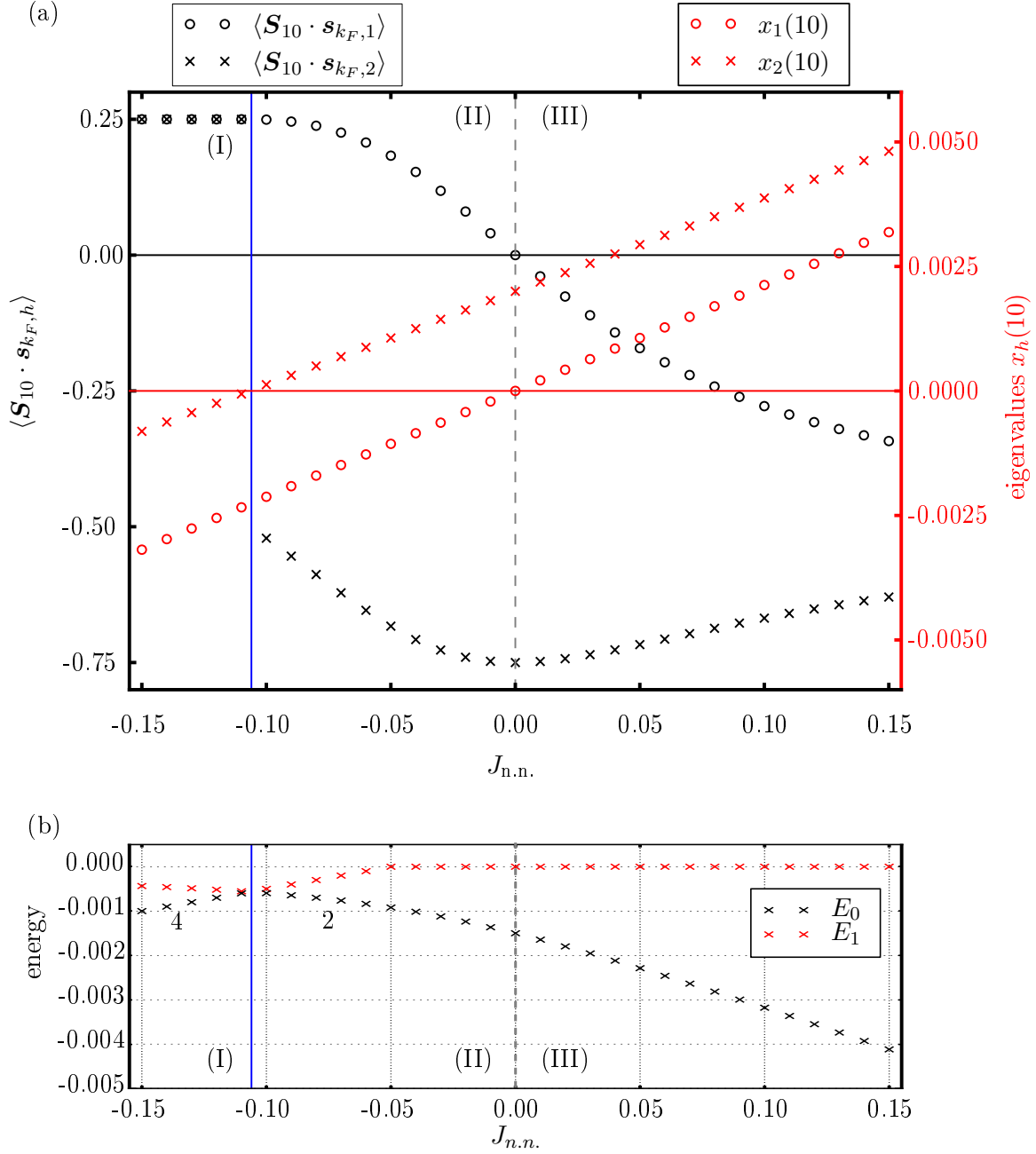


Figure 4.5.: A single impurity coupled locally and nonlocally (next neighbors) to a ring of  $L = 100$  sites. The filling is fixed at  $n = 52$ , ensuring to have two Fermi electrons. The impurity is located at lattice site  $i_1 = 10$ . In (a), the correlation functions (black data points) of impurity spin  $\mathbf{S}_{10}$  and the spin  $\mathbf{s}_{k_F, h}$  of the  $h$ th Fermi orbital are plotted against the next neighbor coupling  $J_{n,n}$ , while the local coupling is fixed at  $J = 0.1$ . Red data points represent the corresponding effective couplings  $x_{h=1,2}$ . Solid red and black lines mark the zero point for both the effective couplings (red) and the spin correlations (black). The blue vertical line separates ferromagnetic (I) from mixed coupling regime (II), and the dashed gray line at  $J_{n,n} = 0$  marks the crossover from the latter to the antiferromagnetic realm (III). In (b), the ground state ( $E_0$ ) and first excited ( $E_1$ ) energy are shown, where the numbers "4" and "2" represent the degeneracy of the lowest lying energy level.

In the mixed coupling regime, the effective couplings have opposite sign, thus the screening of the impurity is hampered. Therefore, this is a rather underscreened regime. Contrary, in the antiferromagnetic realm (III), both effective coupling strengths support the screening of the impurity by the present Fermi electrons. There are more screening channels available than needed for screening the spin-1/2 of the impurity, which is why this is the overscreened regime. Note, moreover, that both correlation functions merge asymptotically for  $J_{n,n.} \gg J$  in phase (III), showing that both Fermi electrons participate equivalently in the screening process.

The results shown here match well with the data presented in Ref. [161]. It is, however, yet unanswered, if the more complex interplay of coupling channels in higher dimensional systems can be understood as well. The next section is dedicated to address this question.

#### 4.4.2. Overscreening in square lattices

Contrary to one-dimensional systems, the degeneracy of the Fermi energy level can take large values in higher-dimensional systems. An above often discussed system is the  $8 \times 8$ -square lattice at around half-filling ( $n \geq 57$ ), where the Fermi energy level is eightfold degenerate. This immediately implies, that eight Fermi orbitals are found. One can learn from Fig. 4.4, that there is no situation, in which there are also eight coupling channels, but it already became clear, that the number of channels can be increased by inclusion of next nearest neighbor coupling (in real-space). The differences between local and next neighbor coupling, compared to local, next neighbor, and next nearest neighbor coupling, are in the focus of this analysis.

Let the (only) impurity  $\mathbf{S}_1$  be located at site (2;2), which is the one close to the upper left corner. For local and next neighbor coupling, there are three channels to be found, while five channels arise when next nearest neighbor coupling is also included (see Fig. 4.4). The first step is to figure out, which sign and what strength the effective couplings have. Figs. 4.6(a) and (b) show the effective coupling strengths in the most interesting regime (apart from the shown values, the sign of the effective couplings does not change any more and the trends simply continue).

Starting with the case, where only local and next neighbor coupling is regarded (Fig. 4.6(a)): There is a set of effective couplings, which is independent of the value of  $J_{n,n.}$  (black squares). These effective couplings obviously correspond to the local coupling contribution. Red data points are associated with the next neighbor coupling, which is also why the couplings vanish at  $J_{n,n.} = 0$ . Moreover, there is a special point ( $J_{n,n.} = 0.05$ ), where the couplings  $x_1$  and  $x_2$  are of equal strength.

Looking at the correlation functions between the impurity spin and the Fermi orbitals, Fig. 4.6(c), one has to distinguish between different fillings. For  $n = 57$ , i.e. the single Fermi electron case, there is (except for  $J_{n,n.} = 0.05$ ) only a single nonvanishing correlation, which takes the value  $\langle \mathbf{S}_1 \mathbf{s}_{k_F,1} \rangle = -3/4$ . From three possible coupling channels, the antiferromagnetic channel (corresponding to effective coupling  $x_1$ ) dominates, thus the Fermi electron fully screens the impurity spin. Accordingly, a nondegenerate ground state energy is found (see Fig. 4.6(e)).

However, at  $J_{n,n.} = 0.05$ , there are two equal effective coupling strengths, making the occupation of two different Fermi orbitals equally probable. The degeneracy of the ground state consequently rises to two, while the spin-orbital correlation  $\langle \mathbf{S}_1 \mathbf{s}_{k_F,1} \rangle$  decreases to  $-3/8$ , and a correlation to a second orbital ( $\langle \mathbf{S}_1 \mathbf{s}_{k_F,2} \rangle$ ) appears, taking the same value as the first correlation function due to the equal orbitals' occupation probabilities.

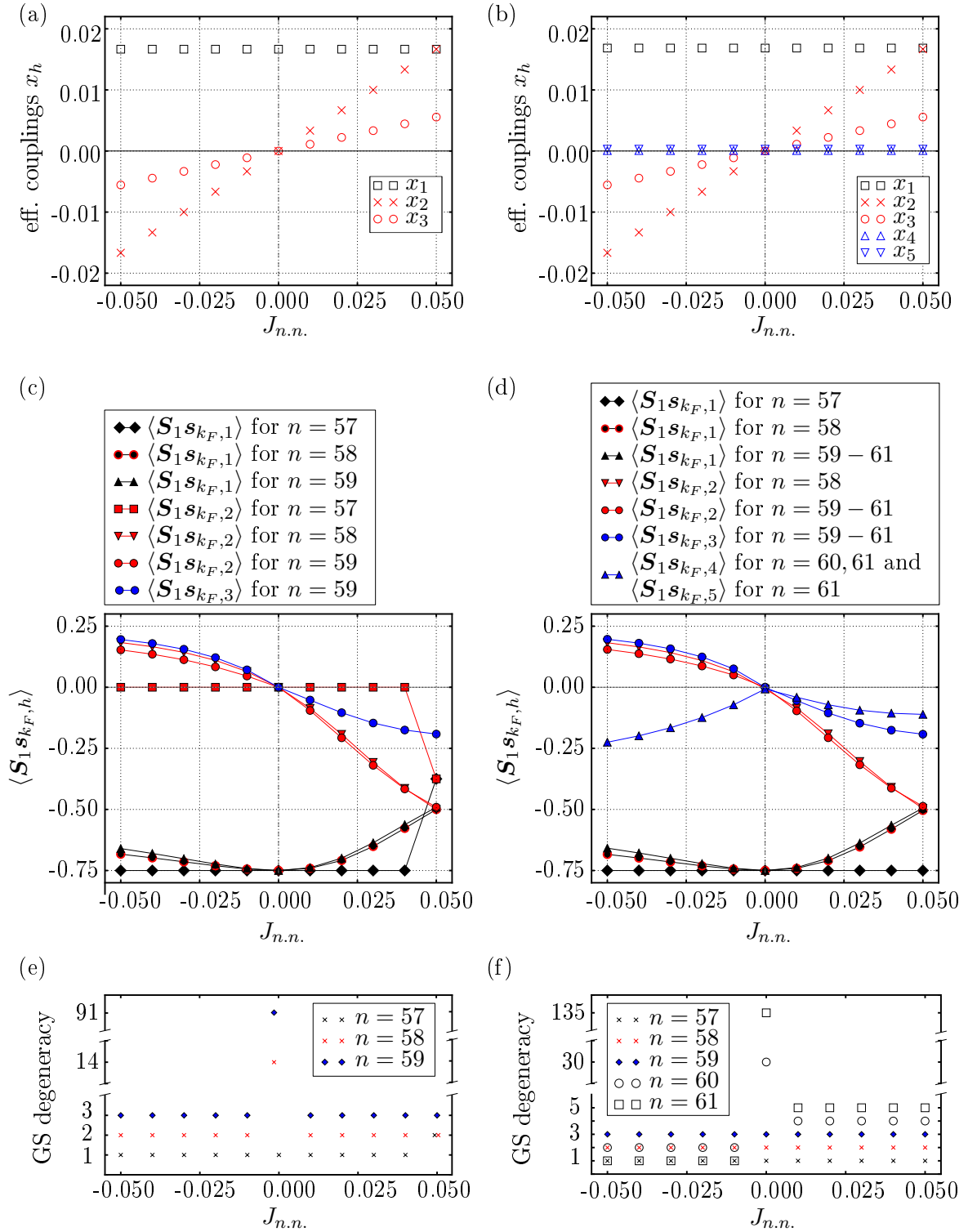


Figure 4.6.: For an  $8 \times 8$ -square lattice (open boundaries,  $n \geq 57 \rightarrow G_F = 8$ ) with a single spin-1/2 impurity coupled at site (2;2), the effective coupling strengths ((a), (b)), the correlations between impurity spin and Fermi orbitals ((c), (d)), and the degeneracy of the ground state ("GS", (e) and (f)) are plotted against the next neighbor coupling strength  $J_{n,n.}$ . In all plots, the local coupling  $J = 0.1$ . In the left panels, the next nearest neighbor coupling is set to zero, while in the right panels it is fixed at  $J_{n,n.n.} = 0.001$ . In (c) and (d), spin correlations which are zero (for example for all uncoupled orbitals) are not shown. In (e), the ground state degeneracy is twofold for both  $n = 57$  and  $n = 58$  at  $J_{n,n.} = 0.05$ , but the two corresponding data points were manually shifted to avoid full overlap, which would make one of the points disappear.

Inclusion of a second Fermi electron, which is the case for  $n = 58$ , brings a second effective coupling into play. The effective couplings compete, leading to a decrease of the correlation functions. For  $J_{n,n.} < 0$ , the impurity is underscreened, while it is overscreened for  $J_{n,n.} > 0$ . Therefore, effectively a spin-1/2 remains free, leading to the twofold degenerate ground state. At vanishing  $J_{n,n.}$ , there is only a single coupling channel, but two Fermi electrons. One of the latter is used for (fully) screening the impurity spin, while the other distributes over seven (spin-degenerate) uncoupled orbitals, giving a ground state degeneracy of  $\binom{7+2}{1} = 14$ .

The case of three Fermi electrons ( $n = 59$ ) can be understood similarly. As  $x_3$  is the weakest of the three effective coupling strengths, the influences of the third Fermi electron are weak as well. The spin-orbital correlations of the first two Fermi electrons vary only a bit, and the correlation of the third Fermi electron with the impurity spin is accordingly weak. Only the ground state degeneracy at  $J_{n,n.} = 0$  increases enormously, as there are two free Fermi electrons, raising the degeneracy to  $\binom{14}{2} = 91$ , see Fig. 4.6(e). In the regimes  $J_{n,n.} \neq 0$ , the three Fermi electrons all couple to the impurity spin, forming in total a triplet ground state. This can be understood as follows: For  $J_{n,n.} \ll 0$  the ferromagnetic coupling channels dominate, thus impurity spin and two Fermi electron spins are aligned parallel. The third Fermi electron is, however, aligned antiparallel to the impurity, thus the host's net magnetization is 1/2. As the total spin of the nanosubstrate is ferromagnetically correlated with the impurity spin, a triplet is formed (see left image of Fig. 4.7(a)).

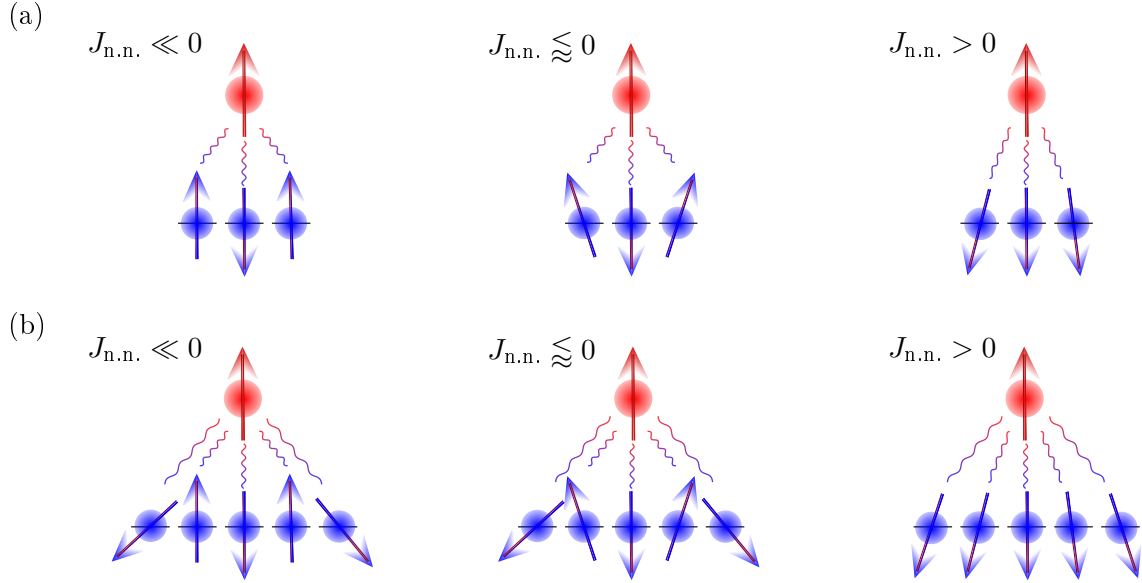


Figure 4.7.: Different ground state configurations explaining the degeneracy from Figs. 4.6(e,f). Results without (a) and with (b) next nearest neighbor coupling are shown in three different coupling regimes. In (a), three Fermi electrons ( $n = 59$ ) are considered, while five ( $n = 61$ ) are taken into account in (b).

For weak, but ferromagnetic next neighbor couplings, the dominating coupling is between impurity spin and the antiferromagnetically coupled orbital (following the notation above, this would be orbital  $h = 1$  with  $x_1$  being the effective coupling). The two weakly ferromagnetic coupled Fermi electrons are still connected to the impurity, thus an indirect exchange occurs, ensuring a parallel alignment of these two Fermi electrons (see middle image of Fig. 4.7(a)). This is again a triplet, which gives the threefold degenerate ground state energy.

The antiferromagnetic case ( $J_{n,n.} > 0$ ) can be understood as a central-spin model, where the impurity acts as the central part coupled antiferromagnetically to the "sublattice" of

Fermi electrons. According to the Lieb–Mattis theorem [147], the net spin is  $S = 1$ , being the found triplet ground state (right image of Fig. 4.7(a)).

So far, the case of local and next neighbor coupling is understood. The situation becomes more complex, when next nearest neighbor coupling is also taken into account. Two more coupling channels arise (see Fig. 4.6(b)), which, however, are weak compared to the already known ones. One should note, that the specific point  $J_{n,n.} = 0.05$  is from a numerical point of view not degenerate (contrary to what has been observed in (a)), since a new, and very small energy scale (i.e.  $J_{n,n.n.}$ ) comes into play, which leads to a fine splitting of the eigenvalues. One could clearly speak of a quasi-degeneracy though, but especially in Figs. 4.6(d) and (f) the data is treated as nondegenerate. The interpretation, if considered this case as degenerate, is however similar to the case of  $J_{n,n.} = 0.05$  discussed above.

Due to the weak effective coupling strengths  $x_{4,5}$ , the qualitative behavior of the spin-orbital correlations for  $n = 57, 58, 59$  is very similar to the case of only local and next neighbor coupling. If more than three Fermi electrons are in the system, i.e. for  $n = 60$  ( $n_F = 4$ ) and  $n = 61$  ( $n_F = 5$ ), the first three spin-orbital correlation functions  $\langle \mathbf{S}_1 \mathbf{s}_{k_F, \{1,2,3\}} \rangle$  remain unchanged, while one ( $n = 60$ ) or two ( $n = 61$ ) new correlation functions show up as expected, see Fig. 4.6(d). Since the effective couplings  $x_4$  and  $x_5$  are of similar order, the correlation functions are almost identical. The fact, that  $J_{n,n.n.}$  is chosen antiferromagnetically, can perfectly be seen in the negative values of  $\langle \mathbf{S}_1 \mathbf{s}_{k_F, \{4,5\}} \rangle$ . However, the minimum value of  $-3/4$  is not reached, showing that the contribution of the fourth and fifth Fermi electron to the screening process is smaller than the contribution from stronger coupled orbitals.

Except for  $J_{n,n.} = 0.05$ , the ground state degeneracy for  $n = 57 - 59$  electrons is equivalent to the values obtained without next nearest neighbor coupling, see Fig. 4.6(f). As discussed above, the ground state for  $n = 57$  remains a singlet at  $J = 0.05$ , because the effective couplings  $x_1$  and  $x_2$  are not degenerate anymore (but they are quasi-degenerate). What is interesting, however, is a clear change of the ground state for fillings  $n = 60, 61$  around  $J_{n,n.} = 0$ . In the regime of ferromagnetic next neighbor coupling,  $J_{n,n.} < 0$ , some screening channels cancel out, leading to a doublet ( $n = 60$ ) or a singlet ( $n = 61$ ) ground state. The latter configuration is shown on the left side of Fig. 4.7(b). Different from the case with three Fermi electrons, the host's magnetization is antiferromagnetically correlated to the impurity spin, thus a singlet ground state is formed rather than the triplet observed for  $n = 59$ . This holds also true for weak ferromagnetic coupling, even if the correlation between impurity spin and the Fermi orbital coupled with strength  $x_1$  dominates. The weakly coupled Fermi orbitals have in total a vanishing magnetization, which is the reason a nondegenerate ground state is found. The case of all antiferromagnetic couplings (right image of Fig. 4.7(b)) can be considered as a central-spin model as already discussed above, with a quintet ground state as expected from the Lieb–Mattis theorem [147]. Note, that the latter case is a highly overscreened situation, while ferromagnetic next neighbor couplings lead to full screening of the impurity spin.

A specific point is again  $J_{n,n.} = 0$ , where the vanishing of the next neighbor coupling reduces the number of coupling channels from five to three, thus for  $n = 57 - 59$  the three (all antiferromagnetic) coupling channels are served by a Fermi electron each, leading to overscreening of the impurity. Filling the system with more electrons gives free Fermi electrons, which distribute over the uncoupled Fermi orbitals. The threefold degenerate impurity–Fermi electron construct times the binomial  $\binom{10}{1}$  for  $n_F = 4$ , or  $\binom{10}{2}$  for  $n_F = 5$ , yields the given ground state degeneracies of 30, and 135, respectively. Further increase of the electron number simply gives more free Fermi electrons that distribute over uncoupled orbitals, very similar to the results presented in Chap. 3.

The results and discussions presented here characterize the physics of single impurities coupled to square lattices. Varying the impurity position on the lattice will surely have



enormous influences on coupling strengths and the number of coupling channels, but insights other than the ones presented above are not expected. The interesting interplay of different coupling strengths shows fascinating physics, such as strongly underscreened, fully screened, and overscreened regimes.



## 5. Applicability to quasi-degenerate systems

Real materials are usually not available without crystallographic defects, which could be, for example, locally slightly different lattice constants, as possibly induced by impurities [162], or missing lattice sites (so-called vacancies) [163]. While in perfect lattices (without any defects) symmetries bring up degeneracies in the energy spectra, lattice defects break such symmetries. As a consequence, the degeneracy of the eigenenergy spectrum vanishes because the energy levels split up. Is the splitting small compared to the distance of neighboring energy levels, one calls this the quasi-degenerate case.

Apart from the crystallographic structure, physical effects can be the reason for the breaking of symmetry. As an example, spin-orbit coupling, and also valley mixing, destroy the degeneracy of energy levels in carbon nanotubes [164, 165]. Moreover, magnetic fields, as well as relativistic corrections are known to induce energy level splittings, be it in substrates, molecules, or single atoms, where these effects are associated with fine and hyperfine structure splitting. A consideration of slightly split energy levels is therefore of interest for nanosystem physics.

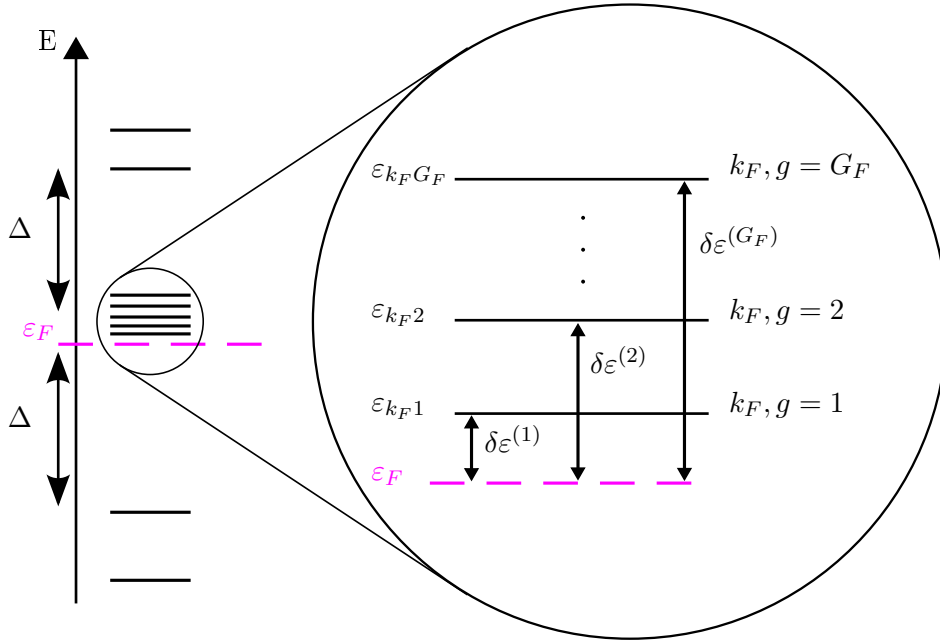


Figure 5.1.: Exemplaric energy dispersion (left) of a system with a quasi-degenerate energy level multiplet (zoomed view on the right). The pink reference level ( $\varepsilon_F$ ) is used to define an energy distance  $\delta\varepsilon^{(g)}$  for  $g = 1, \dots, G_F$  energy levels belonging to the quasi-degenerate multiplet. The indices " $k_F$ " indicate that the Fermi energy level lies within the multiplet.

The question to address here is, whether the theories presented in Chaps. 3 and 4 are applicable to the more realistic quasi-degenerate systems. This requires to introduce a new energy scale,  $\delta\varepsilon^{(g)}$ , which is the energy difference between an energy level of the quasi-degenerate multiplet and a (maybe even virtual) reference energy level (see schematic

Fig. 5.1). As the latter can be chosen freely, the reference level can be set at the energy corresponding to the Fermi energy level of a degenerate system.

Remembering the energy discussion from Sec. 3.2.2, the temperature must be small compared to the inter-level spacing  $\Delta$ , in order to avoid electronic exchange between multiplets, as the latter are not covered by first order perturbation theory. For the same reason, the splitting of a degenerate energy level (forming the quasi-degenerate multiplet) should not be too large, giving  $\delta\varepsilon^{(G_F)} \ll \Delta$ , where  $\delta\varepsilon^{(G_F)}$  can be seen as the energy range of the associated multiplet.

The idea of transferring results from degenerate to quasi-degenerate systems is build on regarding the multiplet energy levels as degenerate levels. Therefore, thermal electronic excitations within the multiplet are welcome, as this allows for equally probable Fermi electron occupation of any of the multiplet levels. In case of  $T = 0$ , the model reduces to a nondegenerate system, which is well covered by the above presented theories. At the end of the day, the temperature is solely restricted to be smaller than the inter-multiplet distance, i.e.  $T \ll \Delta$ .

To account for the finite system size, the coupling strength  $J$  should be weaker than  $J_\Delta$ , which leads according to Eqs. (3.9) and (3.11) to  $J \lesssim -1/\ln \Delta$ . Within these parameter regimes, the first order perturbation theory remains valid. The next question is, if and how the theory must be modified for quasi-degenerate systems.

First off, the close-lying energy levels are the reason why Schrödinger's perturbation theory fails for quasi-degenerate systems [166]. Brillouin-Wigner perturbation theory (see Appendix A and Refs. [166, 167]), instead, is applicable in two different ways. The first is to apply higher order perturbation theory, which includes electronic excitation processes between all energy levels. A second possibility is to take only higher order excitations around the quasi-degenerate multiplet into account. The latter idea benefits of fewer terms to deal with, and even allows to treat the quasi-degenerate problem within a slightly modified first order perturbation theory. The upcoming paragraphs are meant to develop the theoretical framework for the last-mentioned case.

In the degenerate case, the degenerate energy levels at the Fermi energy were labeled  $\varepsilon_{k_F g} = \varepsilon_F$ . For the quasi-degenerate case the notation remains the same, but  $\varepsilon_F$  is now only an energy to refer to, without any energy levels. Instead, the formerly  $G_F$  degenerate levels split up, each with a custom energy  $\varepsilon_{k_F g}$  given by

$$\varepsilon_{k_F g} = \varepsilon_F + \delta\varepsilon^{(g)} , \quad (5.1)$$

gathering them in a multiplet, as depicted in Fig. 5.1.

Let  $\mathcal{H}_0^{\text{qdeg}}$  be the Hamiltonian of noninteracting conduction electrons of a quasi-degenerate system:

$$\begin{aligned} \mathcal{H}_0^{\text{qdeg}} &= \sum_{k,g,\sigma} \varepsilon_{kg} c_{kg\sigma}^\dagger c_{kg\sigma} \\ &\quad \neq k_F \\ &= \sum_{k,g,\sigma} \varepsilon_{kg} c_{kg\sigma}^\dagger c_{kg\sigma} + \sum_{g\sigma} \varepsilon_{k_F g} c_{k_F g\sigma}^\dagger c_{k_F g\sigma} . \end{aligned} \quad (5.2)$$

In the last step, the energies of the relevant multiplet were extracted from the sum over  $k$ . Expanding Eq. (5.2) by adding a zero of the form

$$0 = \sum_{g,\sigma} \varepsilon_F c_{k_F g\sigma}^\dagger c_{k_F g\sigma} - \sum_{g,\sigma} \varepsilon_F c_{k_F g\sigma}^\dagger c_{k_F g\sigma} , \quad (5.3)$$

whereby the two summands represent each a set of  $G_F$ -fold degenerate energy levels with energy  $\varepsilon_F$ , one retrieves a Hamiltonian of  $N$  noninteracting conduction electrons of a degenerate system  $\mathcal{H}_0^{\text{deg}}$ ,

$$\mathcal{H}_0^{\text{deg}} := \sum_{k,g,\sigma}^{\neq k_F} \varepsilon_{kg} c_{kg\sigma}^\dagger c_{kg\sigma} + \sum_{g,\sigma}^{G_F} \varepsilon_F c_{k_F g \sigma}^\dagger c_{k_F g \sigma} , \quad (5.4)$$

as well as a term representing the multiplet of interest,  $\Delta\mathcal{H}$ :

$$\Delta\mathcal{H} = \sum_{g\sigma} (\varepsilon_{k_F g} - \varepsilon_F) c_{k_F g \sigma}^\dagger c_{k_F g \sigma} = \sum_{g\sigma} \delta\varepsilon^{(g)} c_{k_F g \sigma}^\dagger c_{k_F g \sigma} = \sum_g \delta\varepsilon^{(g)} n_{k_F g} . \quad (5.5)$$

Up to this point, only a reformulation of the quasi-degenerate "free" Hamiltonian  $\mathcal{H}_0^{\text{qdeg}}$  has been done, resulting in

$$\mathcal{H}_0^{\text{qdeg}} = \mathcal{H}_0^{\text{deg}} + \Delta\mathcal{H} . \quad (5.6)$$

The idea behind this procedure is to map  $\mathcal{H}_0^{\text{qdeg}}$  onto a degenerate Hamiltonian, to which conventional Brillouin–Wigner perturbation theory can be applied [166]. Moreover, the quasi-degenerate multiplet labeled  $\Delta\mathcal{H}$  is extracted from the "free" Hamiltonian and can be treated as part of the perturbation. Using Eq. (5.6), the full Hamiltonian  $\mathcal{H}$  of a quasi-degenerate system, consisting of a "free" Hamiltonian  $\mathcal{H}_0^{\text{qdeg}}$  and a perturbation  $V_J$ , can thus be rewritten as the "free" Hamiltonian of a degenerate system,  $\mathcal{H}_0^{\text{deg}}$ , plus a renormalized perturbation  $\tilde{\mathcal{H}}_1 = V_J + \Delta\mathcal{H}$ :

$$\mathcal{H} = \mathcal{H}_0^{\text{qdeg}} + V_J = \mathcal{H}_0^{\text{deg}} + \Delta\mathcal{H} + V_J = \mathcal{H}_0^{\text{deg}} + \tilde{\mathcal{H}}_1 . \quad (5.7)$$

With the last form of  $\mathcal{H}$ , one can apply the Brillouin–Wigner perturbation theory just as discussed in Appendix A.

As the focus of this work lies on linear-in- $J$  perturbation theory, the energy corrections up to first order are of interest. According to Appendix A, Eq. (A.16), and similar to Eq. (3.13), one gets the following effective Hamiltonian for the quasi-degenerate case with perturbation  $\tilde{\mathcal{H}}_1$ :

$$\mathcal{H}_{\text{eff}}^{\text{qdeg}} = E^{\text{FS}} + P_0 \tilde{\mathcal{H}}_1 P_0 = E^{\text{FS}} + P_0 (V_J + \Delta\mathcal{H}) P_0 . \quad (5.8)$$

As discussed above for the degenerate case, the energy contribution of the Fermi sea  $E^{\text{FS}}$  is in the following neglected. The effective Hamiltonians of degenerate and quasi-degenerate systems only differ by  $P_0 \Delta\mathcal{H} P_0$ . This term hosts a temperature dependence in  $n_{k_F g}$ , which is responsible for the number of quasi-degenerate energy levels that need to be included. Therefore, in the extreme case of  $T = 0$ , the quasi-degenerate system is completely equivalent to a nondegenerate one, and thus properties such as the ground state degeneracy differ significantly from the degenerate system's physics. If  $\delta\varepsilon^{(G_F)} < T \ll \Delta$ , all energy levels can be occupied leading to the same amount of available energy levels as in the degenerate case. Therefore, quasi-degenerate and degenerate systems are equal in this realm.

In between, i.e.  $T < \delta\varepsilon^{(G_F)}$ , only fewer energy levels are available for Fermi electron occupation, which is comparable to a degenerate system without the full degeneracy  $G_F$ . In such cases, physics might change drastically: Reduction of  $G_F$  leads to fewer uncoupled orbitals, thus free Fermi electrons have less orbitals to occupy, which leads to a decrease of the system's total ground state spin. Moreover, the number of coupling orbitals could decrease, which leads to either different coupling scenarios (as examined in Chap. 3), or decreases the number of coupling channels (changing the results obtained for overscreened systems, see Chap. 4). It is, however, dependent on many factors, if quasi-degenerate systems differ from their degenerate counterparts. A great example is a case 1)-scenario

(review Fig. 3.15) with a single Fermi electron. A decrease of  $G_F$  would change neither the ground state degeneracy, nor the overlap of orbitals, and thus physics remained the same. However, for a different filling (more than one Fermi electron), the decrease of available orbitals indeed changes the physical properties.

Summing this up, quasi-degenerate systems may show the same physical properties as associated degenerate systems, if the temperature allows for inclusion of all  $G_F$  quasi-degenerate energy levels, but is also small enough to avoid interference with other energy levels ( $T \ll \Delta$ ). If the temperature is small compared to the intra-multiplet level splitting, the physics will most probably change due to the decrease of available orbitals (i.e. a decrease of  $G_F$ ). This change is strongly dependent on the system parameters, such as geometry and filling. For  $T \rightarrow 0$ , a crossover to a nondegenerate scenario must occur. The characteristics of this transition strongly depend on the system's properties.

Nevertheless, even for a decreased degeneracy parameter  $G_F$ , the theories presented in Chaps. 3 and 4 are fully applicable to quasi-degenerate systems in the regime  $T \ll \Delta$ . The only difficulty is to find the number of participating energy levels (i.e. the "new" degeneracy parameter  $G_F$ ). With this parameter, the theories can be used as above.

# 6. Summary and outlook

## 6.1. Summary of the work

In the present work, magnetic impurities coupled to non-magnetic, metallic hosts of finite size - so-called Kondo boxes - have been in the focus. The confined host systems (i.e. the nanosubstrates, such as the cyclopentadiene ligands of metallocenes, [105]) have, contrary to bulk systems, discrete one-particle energy spectra, which brings an energy gap  $\Delta$  between neighboring energy levels into play. This gap is relevant for the "finite-size Kondo effect", which is the screening of the magnetic impurities' spins by Fermi electrons below a critical temperature, called Kondo temperature  $T_K$ .

For some selected situations, the finite-size Kondo effect has been studied before: In an initial publication of Thimm et al [110], a single impurity has been analyzed in a confined system. Later, valuable insights were gained by Schwabe et al [86, 87], who placed a second impurity into the host, examining not only the finite-size Kondo effect, but also the interplay between the impurity spins, namely observing the RKKY exchange mechanism. In a subsequent paper [131], it was shown that specific placement of the impurities may lead to quantum localization, exhibiting interesting physics such as the inverse indirect magnetic exchange ("IIME")-mechanism [119].

These previous results, which are summarized within Chap. 2 of the present work, all have one thing in common: The one-particle energy spectra of the nanosubstrates are non-degenerate. However, artificially constructed nanosystems (such as rings, square lattices, etc.), or molecules (such as the metallocenes) often have several intrinsic symmetries (e.g. rotational or mirror symmetries). If the symmetry group is non-abelian, the one-particle energy spectra become degenerate. As a direct consequence, not only one, but multiple Fermi electrons might be available for screening of one or more magnetic impurities.

Not much has yet been known about the physics of such nanosystems with degenerate Fermi energy level. Are the impurity spins over-, under-, or fully screened? Which role do number and location of the impurities play? What happens, if impurities are coupled with either equal or unequal coupling strengths? How does a particular choice of the nanosubstrate and its electron filling influence the results? What is the total spin of the nanostructure, and how is it influenced by the former aspects? By means of first order perturbation theory, valid for weak coupling strengths in the limit of zero temperature, these questions were answered in the present work. Theoretical results are checked by numerical calculations by means of exact diagonalization of the effective Hamiltonian.

Within Chap. 3 of this work, the theoretical treatment of degenerate energy levels has been performed by extension of the perturbative approach to the Kondo box model. An effective model is obtained, where a set of  $G_F$  delocalized electronic orbitals is associated with each impurity spin, with  $G_F$  being the degeneracy of the Fermi energy level. Within this set of  $G_F$  orbitals, the impurity spin couples to only one orbital, forming a "central-spin" model.

While this situation can be understood easily for a single impurity, the physics becomes very complex if a second impurity is involved. The relevant parts, i.e. the "coupling Fermi

orbitals" of each set, might be in one out of three possible scenarios: They either overlap fully, partially, or do not overlap at all. Adding a third impurity increases this diversity, resulting in nine different scenarios of possible coupling Fermi orbital overlap. Within the present work, it has been elaborated that the placement of impurities determines the scenario found. Most scenarios show central-spin model behavior, which is parallel alignment of spins belonging to the same "sublattice", and antiparallel alignment between the sublattices. Here, one sublattice consists of Fermi electrons in their delocalized orbitals, and the second sublattice is built up by impurity spins. However, some scenarios show surprising differences from this behavior, because an antiferromagnetic alignment of impurity spins has been found. This leads to the conclusion that an indirect interimpurity coupling in first-order of the coupling constant occurs. A deeper analysis of this phenomenon has shown, that such behavior can be traced back to the total overlap of coupling Fermi orbitals.

To fully examine the possible coupling scenarios, toy models, which describe each coupling Fermi orbital by means of a vector, were introduced. Since the length of these vectors is directly associated with an effective coupling strength, the influences of both equally and unequally strong coupled impurity spins were analyzed. Dependent on the scenario, the effective couplings can have either none, or very strong influence on the ground state, since the coupling may determine the "priority" of which impurity must be screened "most importantly".

Due to the full description of each overlap scenario by means of the toy models, basically any host-lattice geometry can be understood. Whatever geometry a nanosubstrate has, following the mathematical transformations presented in this work gives a complete overview of the coupling Fermi orbitals. For up to three impurities, their relation among each other has been classified here, giving important information about the expected ground state degeneracy. The toy model predictions were tested on several exemplary systems (usually  $8 \times 8$ -square lattices), with the result, that most of the predicted scenarios can be realized in simple host geometries, and theoretical expectations are correct. Gathering all insights gained, general rules are presented that help to understand the physics, if more than three impurities are present.

It can be ascribed to the model of Chap. 3, which assumes impurity spins to be coupled only locally to the lattice, that under- and full screening of impurity spins is found, but overscreening is completely precluded. As the latter is of great interest, especially for systems that show non-Fermi-liquid behavior, the previous theory is modified by inclusion of nonlocal coupling, i.e. impurity spins couple not only locally, but also to neighboring and next neighboring lattice sites. As a result, each impurity spin couples to more than one Fermi orbital within its corresponding set of  $G_F$  Fermi orbitals. A basic understanding of these newly arising coupling channels has been given within Chap. 4 of the present work. For the case of a single impurity, examples of overscreening were found and examined. One finds, that the contributions of local and nonlocal coupling can be clearly identified in these systems, although such assignments are not of general character. Another interesting results is, that especially in the tested  $8 \times 8$ -square lattice, the theoretically predicted number of maximally available coupling channels is usually not reached. The reason for this effect is most likely to be connected to symmetries in the mathematical structure.

Last but not least, the question is answered, if, and how the theory presented in this work can be applied to systems with a quasi-degenerate one-particle energy spectrum. Crystallographic defects, but also other physical effects can lead to symmetry breaking and thus to a splitting of the originally degenerate Fermi energy level. At zero temperature, such systems must in principle be treated as systems with nondegenerate one-particle energy spectra, which is a simple limiting case included in the present approach. If, however, the



level splitting is small as compared to the temperature  $T$ , one can still use (degenerate) perturbation theory, since the quasi-degenerate case becomes essentially equivalent to the degenerate case in this limit. With increasing temperature, simply more and more levels must be taken into account, which is analogous to successively increasing the energy level degeneracy  $G_F$ . As the role of this parameter was studied in detail, transferring results to the quasi-degenerate case is easily possible.

Besides the fascinating physics found, a deep understanding for multiple impurities embedded in a confined nanostructure is gained. With the models introduced, simple tools to examine the interplay of host geometry, impurity placement, and electron fillings are given. It is also worth mentioning, that the theory bears great advantages for numerical simulation, since the Hilbert space of the host material states is comparably small, as all but the few Fermi electron states can be disregarded. This in principle allows to model lattices with several million sites, or likewise nanostructures with many impurities coupled to the latter, making the presented theory and its extensions powerful tools for the examination of Kondo boxes.

## 6.2. Outlook

The results presented in this work give many insights into Kondo box physics, where especially the influences of the nanostructure's geometry, the electronic filling of the nanosubstrate, and both location and coupling of multiple impurities to the host were analyzed in detail. Some aspects, however, could not be paid attention to. In the following, possibilities for further research are named, and briefly analyzed.

Using the presented theory, a first step could be to analyze the screening competition between multiple impurities and Fermi electrons in systems allowing for overscreening, and checking the results against the local-coupling cases of Chap. 3. In the next step, impurity spins with spin quantum numbers  $S > 1/2$  could be in the focus of both systems with local and generalized coupling. This could be of interest, e.g., in the context of  $CoH_x$  complexes acting as impurities, where the number of bonded hydrogen atoms can be used to manipulate the total spin of the complex (spin-1 for  $x = 1$  and spin-1/2 for  $x = 2$ ) [168–170], for  $Co$ -atoms on either  $Cu_2N$  or  $h-BN/Rh(111)$ , where the  $Co$ -atoms have an effective spin of 3/2 (see Refs. [170, 171] and references therein), or for large-spin impurities such as  $Tm$  [149]. Furthermore, a possible screening competition between multiple impurities with different spin quantum numbers and Fermi electrons could be examined. It seems moreover possible that results are influenced by different effective coupling strengths, which are characteristic of the nanosubstrate, but not dependent on the impurity's spin. This aspect becomes even more interesting in overscreened scenarios, where multiple screening channels of different strengths are available. Using this, access to multi-channel Kondo physics is provided, e.g. as found when iron impurities are deposited in gold, which can be described by a spin-3/2 three-channel Kondo model [172, 173]. Progress in this direction bears the huge advantage, that the theory presented in this work does not require any formal changes.

As this work has its focus on the so-called on-resonant cases, i.e. scenarios where the Fermi energy levels are partially occupied, the case of fully occupied levels (off-resonant situation) has only been touched when summarizing previous theoretical achievements. In order to deal with such off-resonant scenarios, the theory presented in this work must be extended to second order perturbation theory in  $J$ . Although this seems not to be impossible, the second order perturbation theory is much more difficult to apply. However, if successful, one is able to analyze interimpurity interactions, which are expected to compete with the finite-size Kondo effect as shown in detail in Refs. [86, 87].

Especially for comparison with real experiments, including the coupling of the nanostructure to a bath is a topic of high priority. This is, because quantum dots and nanowires, which build up the nanosubstrates of the systems presented in this work, are often connected to leads, or are confined in cavities. Therefore, an interaction with the environment takes place. As the previous work from Ref. [86] has shown, this can lead to a breakdown of the finite-size Kondo effect. One can therefore expect, that the coupling to a bulk system with continuous energy spectrum competes with the effects described in the present work.

Last but not least, experimental testing of the theories presented would be desirable. Possible realizations are artificially constructed nanosubstrates containing magnetic adatoms, whereby an insulating spacer separates the nanosystem from the bulk substrate. The experimental challenges would be to ensure the nanostructures' isolation and to create the artificial lattice plus adatom (possibly using STM). Assuming the first condition can be realized (e.g. as it is the case for  $CoH_x$  on  $h-BN/Rh(111)$ , where  $h-BN$  decouples the  $CoH_x$  complex from the underlying  $Rh(111)$  metal [171]), one would still have to deal with the construction of a perfect nanostructure, including equal distances between all nanosubstrate atoms and the perfect placement of impurities. Since all of these aspects seem hard to be realized, one would rather adjust the parameters of the theory: Firstly, an imperfect lattice leads to very individual hoppings  $t_{ij}$  between sites  $i$  and  $j$ , invalidating the assumption  $t_{ij} = t$  for all next neighboring atoms. Secondly, for impurities not placed directly on top of a nanosubstrate atom (for example if placed in between, on so-called hollow lattice sites), a local coupling is not well defined, thus the coupling to all close lying sites should be regarded. Although the presented theories are indeed tailored to address these modifications, the main issue is to get experimental access to all the required parameters.

Instead of artificially constructing a playground to test the theory, one could focus on existing, and maybe even already investigated systems such as metallocene molecules [105]. The latter consist of cyclopentadiene ligands, which are connected by a metallic atom. The ligands (i.e. the host) bear several intrinsic symmetries (rotation, mirror, etc.), providing a degenerate one-particle energy spectrum. Discretization of the latter is due to the confinement of the geometry also given. However, it is first necessary to obtain the one-particle energy spectrum of the ligands. As the atomic orbitals of the ligands are not just simply  $s$ -orbitals (which would justify the usage of the tight-binding approximation), firstly the theory must be extended to include multiple atomic orbitals. Moreover, the energy spectrum of the ligands will most likely be affected by the pure presence of the metallic atom, due to physical effects such as crystal field splitting. It would thus be necessary to extract impurity influences, which are not of spin-spin interaction type. Gathering these in form of an effective potential, one could possibly obtain a renormalized free Hamiltonian representing the ligands, which can be used to apply the presented theory. Note, that this is everything but an easy task, which most likely must be performed individually for each nanostructure. However, with knowledge of the free Hamiltonian and experimentally observed quantities such as the coupling strengths, one should be able to describe the physics of such nanostructures by means of the (probably slightly modified) theories presented here.

The possible extensions listed above have without doubt a great potential for discovering fascinating physics, especially if several aspects are combined. The present work gives a solid basis for further research on impurity-doped nanosystems, bringing theory and experiments closer together.

# A. Brillouin–Wigner perturbation theory for degenerate systems

The central point of perturbation theory is the decomposition of a given Hamiltonian  $\mathcal{H}$  into an unperturbed part  $\mathcal{H}_0$ , which can be solved exactly, and a perturbation  $\mathcal{H}_1$  [166, 167]. The latter should be small with respect to  $\mathcal{H}_0$ . The key formula is

$$\mathcal{H} = \mathcal{H}_0 + \lambda \mathcal{H}_1 , \quad (\text{A.1})$$

where  $\lambda \in [0; 1]$  is an adjustable parameter.

The unperturbed Hamiltonian  $\mathcal{H}_0$  has discrete eigenvalues  $E_n^{(0)}$  and orthonormal eigenstates  $|n\rangle^{(0)}$ :

$$\mathcal{H}_0 |n\rangle^{(0)} = E_n^{(0)} |n\rangle^{(0)} . \quad (\text{A.2})$$

In Brillouin-Wigner perturbation theory [167], one defines a projector  $P_n$  and its complement  $Q_n$  for each unperturbed eigenstate:

$$P_n = |n\rangle^{(0)} \langle n| \quad \text{and} \quad Q_n = \mathbb{1} - P_n = \sum_{m \neq n} P_m . \quad (\text{A.3})$$

From the spectral representation of  $\mathcal{H}_0$ ,

$$\mathcal{H}_0 = \sum_n E_n^{(0)} P_n , \quad (\text{A.4})$$

it results immediately

$$[\mathcal{H}_0, Q_n]_- = 0 . \quad (\text{A.5})$$

Using the stationary Schrödinger equation for the full Hamiltonian,

$$\mathcal{H} |n\rangle = E_n |n\rangle , \quad (\text{A.6})$$

and inserting Eq. (A.1), yields

$$(E_n - \mathcal{H}_0) |n\rangle = \lambda \mathcal{H}_1 |n\rangle . \quad (\text{A.7})$$

Left-multiplying the above equation with  $Q_n$  and recalling Eq. (A.5), one gets

$$Q_n |n\rangle = \lambda R_n \mathcal{H}_1 |n\rangle , \quad (\text{A.8})$$

where

$$R_n = Q_n (E_n - \mathcal{H}_0)^{-1} = (E_n - \mathcal{H}_0)^{-1} Q_n = \sum_{m \neq n} \frac{P_m}{E_n - E_m^{(0)}} . \quad (\text{A.9})$$

In order to get the eigenstate corrections to the full problem, one rewrites  $|n\rangle$  using the common convention  ${}^{(0)} \langle n | n \rangle = 1$ , as well as Eq. (A.3):

$$|n\rangle = (P_n + Q_n) |n\rangle = |n\rangle^{(0)} \langle n | n \rangle + \lambda R_n \mathcal{H}_1 |n\rangle = |n\rangle^{(0)} + \lambda R_n \mathcal{H}_1 |n\rangle . \quad (\text{A.10})$$

The equation above allows a recursive calculation of the eigenstate with corrections up to arbitrary order of  $\lambda$ . One finds

$$\text{order } \lambda^0: \quad |n\rangle = |n\rangle^{(0)} , \quad (\text{A.11})$$

$$\text{order } \lambda^1: \quad |n\rangle = |n\rangle^{(0)} + \lambda R_n \mathcal{H}_1 |n\rangle^{(0)} , \quad (\text{A.12})$$

$$\text{order } \lambda^2: \quad |n\rangle = |n\rangle^{(0)} + \lambda R_n \mathcal{H}_1 |n\rangle^{(0)} + (\lambda R_n \mathcal{H}_1)^2 |n\rangle^{(0)} , \quad (\text{A.13})$$

$$\vdots$$

$$\text{full solution:} \quad |n\rangle = \sum_{j=0}^{\infty} (\lambda R_n \mathcal{H}_1)^j |n\rangle^{(0)} . \quad (\text{A.14})$$

With these eigenkets, one gets a representation for the energies  $E_n$  of the full problem by left–multiplication of  ${}^{(0)}\langle n|$  to Eq. (A.7):

$$E_n = E_n^{(0)} + {}^{(0)}\langle n| \lambda H_1 |n\rangle , \quad (\text{A.15})$$

where again  ${}^{(0)}\langle n| n\rangle = 1$  has been used. Substituting  $|\psi_n\rangle$  as given by Eq. (A.14) into the equation above, one gets the following form for the energies of the full problem:

$$\begin{aligned} E_n = & E_n^{(0)} + {}^{(0)}\langle n| \lambda \mathcal{H}_1 |n\rangle^{(0)} + \lambda^2 \sum_{m_1 \neq n} \frac{{}^{(0)}\langle n| \mathcal{H}_1 |m_1\rangle \langle m_1| \mathcal{H}_1 |n\rangle^{(0)}}{E_n - E_{m_1}^{(0)}} + \dots \\ & \dots + \lambda^{j+1} \sum_{m_1 \neq n} \sum_{m_2 \neq n} \dots \sum_{m_j \neq n} \frac{{}^{(0)}\langle n| \mathcal{H}_1 |m_1\rangle \langle m_1| \mathcal{H}_1 |m_2\rangle \dots \langle m_j| \mathcal{H}_1 |n\rangle^{(0)}}{(E_n - E_{m_1}^{(0)}) (E_n - E_{m_2}^{(0)}) \dots (E_n - E_{m_j}^{(0)})} + \dots \end{aligned} \quad (\text{A.16})$$

With Eq. (A.16), a given Hamiltonian can be approximated up to wanted order. For the purpose of this work, first order is sufficient, but the latter equation gives the framework to extend the theories to higher orders.

## B. Hilbert space dimension

For an understanding of the physics predicted by analytically developed theories, one usually cannot avoid a numerical treatment. However, even for systems with a finite number of states (such as the case for nanostructures), standard computers fail to solve a full Hamiltonian within an acceptable amount of calculation time. Despite of hoping for the advent of supercomputers, one is thus interested in theories that keep numerical computation effort on a low level. In this context, it is helpful if the modeled Hamiltonian is of low Hilbert space dimension  $\dim H$ .

Here, the Hilbert space dimension of the effective low-energy model is examined, showing the efficiency of the models proposed in this work. Several parameters define the space of possible states: The number of impurities, their spin quantum numbers, the number of Fermi electrons, and the number of sites the latter can distribute over. To keep the discussion simple, the impurities are assumed to carry a spin-1/2. For an amount of  $R$  impurities,  $2^R$  states arise due to the impurities' spin degeneracy. Regarding the conduction electrons, of which there are as many as  $n_F$ , they distribute over  $2G_F$  Fermi orbitals, respecting their spin degeneracy. Ensuring Pauli's exclusion principle, one thus gets  $\binom{2G_F}{n_F}$  possible configurations, i.e. basis states.

For numerical purposes, it is often necessary to sort these states according to their total magnetization  $M^z \in \left[-\frac{R+n_F}{2}; +\frac{R+n_F}{2}\right]$ . Let  $\lambda$  be the number of Fermi electrons with spin orientation " $\downarrow$ ", and  $\Lambda$  the total number of particles (Fermi electrons and impurity spins) with spin orientation " $\downarrow$ ". In terms of the maximal magnetization,  $M_{\max}^z = \frac{R+n_F}{2}$ , where  $n_F$ ,  $R$ , and  $G_F$  are kept constant, one can then write

$$\Lambda = M_{\max}^z - M^z = \frac{R + n_F}{2} - M^z, \quad (\text{B.1})$$

with  $\Lambda \in [0, R + n_F]$ . Using this, the dimension of the Hilbert space corresponding to a given magnetization  $M^z$  reads

$$\dim H|_{M^z} = \sum_{\lambda=\max(0, n_F-G_F, \Lambda-R)}^{\min(G_F, \Lambda, n_F)} \binom{R}{\Lambda - \lambda} \binom{G_F}{n_F - \lambda} \binom{G_F}{\lambda}. \quad (\text{B.2})$$

The first binomial represents possible impurity alignments, the second stands for the number of Fermi electrons with spin orientation " $\uparrow$ ", while the third binomial gives the number of  $k_F$ -electrons with spin orientation " $\downarrow$ ". The lower boundary of the summation is at least zero, since a negative number of spin- $\downarrow$  Fermi electrons is not physical. To realize a given magnetization, it might be necessary to have at least some spin- $\downarrow$  Fermi electrons (the best example is  $M^z = -\frac{R+n_F}{2}$ ), which is why the lower boundary is not simply zero. Likewise, the upper boundary is restricted, as only  $G_F$  Fermi electrons can be of spin- $\downarrow$  type ( $\min(G_F, \dots)$ ), while not more than  $\Lambda$  particles are present ( $\min(\dots, \Lambda, \dots)$ ). Moreover, the number of spin- $\downarrow$  Fermi electrons must be at most the number of present Fermi electrons ( $\min(\dots, n_F)$ ).

Using Eq. (B.2), one can calculate the dimension of all subspaces of  $H$ . The largest one is, dependent on the number of Fermi electrons and impurity spins, either  $M^z = 0$ , or

$M^z = \pm 1/2$ . Three impurities, embedded in an  $8 \times 8$ -square lattice with open boundary conditions and a total filling of 59 electrons can be taken as a great example to show the numerical advantages of the perturbative approach. Breaking down the given information, one obtains from  $n = 59$ , that  $G_F = 8$  (see Fig. 3.6 in the main text), and  $n_F = 3$ . With  $R = 3$  and  $M^z = 0$ , one gets  $\Lambda = 3$  (see Eq. (B.1)). According to Eq. (B.2), the dimension of the  $M^z = 0$ -subspace is

$$\dim H|_{M^z=0} = \sum_{\lambda=0}^3 \binom{R}{\Lambda - \lambda} \binom{G_F}{n_F - \lambda} \binom{G_F}{\lambda} = \sum_{\lambda=0}^3 \binom{3}{3 - \lambda} \binom{8}{3 - \lambda} \binom{8}{\lambda} = 1456 . \quad (\text{B.3})$$

The Hamilton matrix, which must be diagonalized, has thus  $(\dim H)^2 \lesssim 2.12 \cdot 10^6$  entries.

When solving the full problem (for example, by exact diagonalization of the full Hamilton matrix), the total Hilbert space has a dimension of  $2^R \cdot \binom{2 \cdot L^2}{n}$ , which is for the  $8 \times 8$ -square lattice ( $L = 8$ ) with three spin-1/2 impurities and  $n = 59$  electrons a total of roughly  $1.3 \cdot 10^{38}$  states. The  $M^z = 0$ -subspace has roughly  $1.73 \cdot 10^{37}$  states, so that the Hamiltonian in matrix form has about  $3 \cdot 10^{74}$  entries. To (exactly) diagonalize the latter is beyond the scope of every computing power.

This example visualizes, how difficult an exact solution by numerical means is, and underlines the power of efficient theories for numerical purposes. Regarding computational performance, one can conclude that the theory presented in this work is very efficient.

# References

- [1] K.-D. Schotte, *Die Geschichte des Magnetismus*, (2004) [http://users.physik.fu-berlin.de/~schotte/MAGNET/Wolfram\\_Mag\\_1.pdf](http://users.physik.fu-berlin.de/~schotte/MAGNET/Wolfram_Mag_1.pdf) (visited on 01/02/2017).
- [2] H.-J. Van Leeuwen, *J. Phys. Radium* **2**, 361 (1921).
- [3] W. J. de Haas, J. de Boer, and G. J. van den Berg, *Physica* **1**, 1115 (1934).
- [4] J. Friedel, *The London, Edinburgh, and Dublin Philosophical Magazine and Journal of Science* **43**, 153 (1952).
- [5] J. Friedel, *Canadian Journal of Physics* **34**, 1190 (1956).
- [6] J. Friedel, *Il Nuovo Cimento* (1955-1965) **7**, 287 (1958).
- [7] B. T. Matthias, M. Peter, H. J. Williams, A. M. Clogston, E. Corenzwit, and R. C. Sherwood, *Phys. Rev. Lett.* **5**, 542 (1960).
- [8] B. T. Matthias, H. Suhl, and E. Corenzwit, *Phys. Rev. Lett.* **1**, 92 (1958).
- [9] R. M. Bozorth, B. T. Matthias, H. Suhl, E. Corenzwit, and D. D. Davis, *Phys. Rev.* **115**, 1595 (1959).
- [10] B. T. Matthias and E. Corenzwit, *Phys. Rev.* **100**, 626 (1955).
- [11] A. Hewson, *The kondo problem to heavy fermions* (Cambridge University Press, New York, N.Y., 1993).
- [12] P. W. Anderson, *Phys. Rev.* **124**, 41 (1961).
- [13] J. Kondo, *Progress of Theoretical Physics* **32**, 37 (1964).
- [14] M. P. Sarachik, E. Corenzwit, and L. D. Longinotti, *Phys. Rev.* **135**, A1041 (1964).
- [15] C. Zener, *Phys. Rev.* **81**, 440 (1951).
- [16] P. W. Anderson, *Journal of Physics C: Solid State Physics* **3**, 2436 (1970).
- [17] K. G. Wilson, *Rev. Mod. Phys.* **47**, 773 (1975).
- [18] H. Bethe, *Zeitschrift für Physik* **71**, 205 (1931).
- [19] N. Andrei, *Phys. Rev. Lett.* **45**, 379 (1980).
- [20] P. B. Wiegmann, *Journal of Physics C: Solid State Physics* **14**, 1463 (1981).
- [21] P. Wiegmann, *Physics Letters A* **80**, 163 (1980).
- [22] N. Kawakami and A. Okiji, *Physics Letters A* **86**, 483 (1981).
- [23] K. M. Stadler, A. K. Mitchell, J. von Delft, and A. Weichselbaum, *Phys. Rev. B* **93**, 235101 (2016).
- [24] A. A. Zvyagin, *Phys. Rev. B* **66**, 174430 (2002).
- [25] L. Kouwenhoven and L. Glazman, *Physics World* **14**, 33 (2001).
- [26] K. Andres, J. E. Graebner, and H. R. Ott, *Phys. Rev. Lett.* **35**, 1779 (1975).
- [27] F. Steglich, J. Aarts, C. D. Bredl, W. Lieke, D. Meschede, W. Franz, and H. Schäfer, *Phys. Rev. Lett.* **43**, 1892 (1979).
- [28] H. v. Löhneysen, T. Pietrus, G. Portisch, H. G. Schlager, A. Schröder, M. Sieck, and T. Trappmann, *Phys. Rev. Lett.* **72**, 3262 (1994).

- 
- [29] N. D. Mathur, F. M. Grosche, S. R. Julian, I. R. Walker, D. M. Freye, R. K. W. Haselwimmer, and G. G. Lonzarich, *Nature* **394**, 39 (1998).
- [30] M. S. Torikachvili, S. Jia, E. D. Mun, S. T. Hannahs, R. C. Black, W. K. Neils, D. Martien, S. L. Bud'ko, and P. C. Canfield, *Proceedings of the National Academy of Sciences* **104**, 9960 (2007).
- [31] J. J. Joyce, A. J. Arko, J. Lawrence, P. C. Canfield, Z. Fisk, R. J. Bartlett, and J. D. Thompson, *Phys. Rev. Lett.* **68**, 236 (1992).
- [32] P. C. Canfield, J. D. Thompson, W. P. Beyermann, A. Lacerda, M. F. Hundley, E. Peterson, Z. Fisk, and H. R. Ott, *Journal of Applied Physics* **70**, 5800 (1991).
- [33] H. Suderow, S. Vieira, J. D. Strand, S. Bud'ko, and P. C. Canfield, *Phys. Rev. B* **69**, 060504 (2004).
- [34] M. A. Tanatar, J. Paglione, S. Nakatsuji, D. G. Hawthorn, E. Boaknin, R. W. Hill, F. Ronning, M. Sutherland, L. Taillefer, C. Petrovic, P. C. Canfield, and Z. Fisk, *Phys. Rev. Lett.* **95**, 067002 (2005).
- [35] M. B. Salamon, N. Cornell, M. Jaime, F. F. Balakirev, A. Zakhidov, J. Huang, and H. Wang, *Scientific Reports* **6**, Article, 21469 EP (2016).
- [36] O. Erten, P. Ghaemi, and P. Coleman, *Phys. Rev. Lett.* **116**, 046403 (2016).
- [37] S.-i. Kimura, H. Takao, J. Kawabata, Y. Yamada, and T. Takabatake, *Journal of the Physical Society of Japan* **85**, 123705 (2016).
- [38] A. Altland and R. Egger, *Phys. Rev. Lett.* **110**, 196401 (2013).
- [39] B. Béri and N. R. Cooper, *Phys. Rev. Lett.* **109**, 156803 (2012).
- [40] A. Altland, B. Béri, R. Egger, and A. M. Tsvelik, *Phys. Rev. Lett.* **113**, 076401 (2014).
- [41] M. Dzero, J. Xia, V. Galitski, and P. Coleman, *Annual Review of Condensed Matter Physics* **7**, 249 (2016).
- [42] L. Jiao, S. Rößler, D. J. Kim, L. H. Tjeng, Z. Fisk, F. Steglich, and S. Wirth, *Nature Communications* **7**, Article, 13762 EP (2016).
- [43] L. Isaev, G. Ortiz, and I. Vekhter, *Phys. Rev. B* **92**, 205423 (2015).
- [44] K. T. Law, C. Y. Seng, P. A. Lee, and T. K. Ng, *Phys. Rev. B* **81**, 041305 (2010).
- [45] D. M. Eigler and E. K. Schweizer, *Nature* **344**, 524 (1990).
- [46] E. J. Heller, M. F. Crommie, C. P. Lutz, and D. M. Eigler, *Nature* **369**, 464 (1994).
- [47] H. C. Manoharan, C. P. Lutz, and D. M. Eigler, *Nature* **403**, 512 (2000).
- [48] J. Li, W.-D. Schneider, R. Berndt, and B. Delley, *Phys. Rev. Lett.* **80**, 2893 (1998).
- [49] W. Chen, V. Madhavan, T. Jamneala, and M. F. Crommie, *Phys. Rev. Lett.* **80**, 1469 (1998).
- [50] H. T. Dang, M. dos Santos Dias, A. Liebsch, and S. Lounis, *Phys. Rev. B* **93**, 115123 (2016).
- [51] J. Bork, Y.-h. Zhang, L. Diekhoner, L. Borda, P. Simon, J. Kroha, P. Wahl, and K. Kern, *Nat Phys* **7**, 901 (2011).
- [52] D. Goldhaber-Gordon, H. Shtrikman, D. Mahalu, D. Abusch-Magder, U. Meirav, and M. A. Kastner, *Nature* **391**, 156 (1998).
- [53] S. M. Cronenwett, T. H. Oosterkamp, and L. P. Kouwenhoven, *Science* **281**, 540 (1998).
- [54] J. Schmid, J. Weis, K. Eberl, and K. v. Klitzing, *Physica B Condensed Matter* **256**, 182 (1998).



- 
- [55] F. Simmel, R. H. Blick, J. P. Kotthaus, W. Wegscheider, and M. Bichler, *Phys. Rev. Lett.* **83**, 804 (1999).
- [56] J. Nygard, D. H. Cobden, and P. E. Lindelof, *Nature* **408**, 342 (2000).
- [57] A. Hofmann, V. F. Maisi, C. Gold, T. Krähenmann, C. Rössler, J. Basset, P. Märki, C. Reichl, W. Wegscheider, K. Ensslin, and T. Ihn, *Phys. Rev. Lett.* **117**, 206803 (2016).
- [58] A. W. Heine, D. Tutuc, G. Zwicknagl, and R. J. Haug, *Phys. Rev. Lett.* **116**, 096802 (2016).
- [59] S. Bock, A. Liliashvili, and T. Gasenzer, *Phys. Rev. B* **94**, 045108 (2016).
- [60] M. Koga, M. Matsumoto, and H. Kusunose, *Journal of the Physical Society of Japan* **81**, 123703 (2012).
- [61] M. Koga, M. Matsumoto, and H. Kusunose, *Journal of the Physical Society of Japan* **85**, 063702 (2016).
- [62] A. Golub, I. Kuzmenko, and Y. Avishai, *Phys. Rev. Lett.* **107**, 176802 (2011).
- [63] M. Lee, J. S. Lim, and R. López, *Phys. Rev. B* **87**, 241402 (2013).
- [64] M. Cheng, M. Becker, B. Bauer, and R. M. Lutchyn, *Phys. Rev. X* **4**, 031051 (2014).
- [65] Z. Gao and W.-J. Gong, *Phys. Rev. B* **94**, 104506 (2016).
- [66] L. Li, Z. Cao, T.-F. Fang, H.-G. Luo, and W.-Q. Chen, *Phys. Rev. B* **94**, 165144 (2016).
- [67] R. Zhang, D. Zhang, Y. Cheng, W. Chen, P. Zhang, and H. Zhai, *Phys. Rev. A* **93**, 043601 (2016).
- [68] K. Hattori, K. Itakura, S. Ozaki, and S. Yasui, *Phys. Rev. D* **92**, 065003 (2015).
- [69] T. Kanazawa and S. Uchino, *Phys. Rev. D* **94**, 114005 (2016).
- [70] I. Affleck, *Acta Phys. Polon.* **B26**, 1869 (1995), arXiv:cond-mat/9512099.
- [71] P. Fröjdh and H. Johannesson, *Phys. Rev. B* **53**, 3211 (1996).
- [72] J. Erdmenger, M. Flory, C. Hoyos, M.-N. Newrzella, A. O'Bannon, and J. M. S. Wu, *Fortschritte der Physik* **64**, 322 (2016).
- [73] J.-H. Sun, D.-H. Xu, F.-C. Zhang, and Y. Zhou, *Phys. Rev. B* **92**, 195124 (2015).
- [74] T. Yanagisawa, *Journal of Physics: Conference Series* **603**, 012014 (2015).
- [75] A. K. Mitchell and L. Fritz, *Phys. Rev. B* **92**, 121109 (2015).
- [76] L. Fritz and M. Vojta, *Reports on Progress in Physics* **76**, 032501 (2013).
- [77] D. Withoff and E. Fradkin, *Phys. Rev. Lett.* **64**, 1835 (1990).
- [78] K. Dhochak, R. Shankar, and V. Tripathi, *Phys. Rev. Lett.* **105**, 117201 (2010).
- [79] S. D. Das, K. Dhochak, and V. Tripathi, *Phys. Rev. B* **94**, 024411 (2016).
- [80] K. Matveev, *Journal of Experimental and Theoretical Physics* **72**, 892 (1990).
- [81] K. A. Matveev, *Phys. Rev. B* **51**, 1743 (1995).
- [82] H. Kusunose, *Journal of the Physical Society of Japan* **85**, 113701 (2016).
- [83] G. Yoo, J. Park, S.-S. B. Lee, and H.-S. Sim, *Phys. Rev. Lett.* **113**, 236601 (2014).
- [84] N. E. Sluchanko, *Low Temperature Physics* **41**, 544 (2015).
- [85] A. Wong, S. E. Ulloa, N. Sandler, and K. Ingersent, *Phys. Rev. B* **93**, 075148 (2016).
- [86] A. Schwabe, D. Gütersloh, and M. Potthoff, *Phys. Rev. Lett.* **109**, 257202 (2012).
- [87] A. Schwabe, "From the kondo box problem to the physics of the kondo-lattice box", Dissertation (Institut für Theoretische Physik, Universität Hamburg, 2013).

- 
- [88] I. Hagymási, J. Sólyom, and Ö. Legeza, *Phys. Rev. B* **92**, 035108 (2015).
- [89] A. Georges, L. de' Medici, and J. Mravlje, *Annual Review of Condensed Matter Physics* **4**, 137 (2013).
- [90] M. Vojta, R. Bulla, and P. Wölfle, *The European Physical Journal Special Topics* **224**, 1127 (2015).
- [91] I. Affleck, (2010).
- [92] V. Barzykin and I. Affleck, *Phys. Rev. Lett.* **76**, 4959 (1996).
- [93] A. K. Mitchell, M. Becker, and R. Bulla, *Phys. Rev. B* **84**, 115120 (2011).
- [94] C. Yang and A. E. Feiguin, *Phys. Rev. B* **95**, 115106 (2017).
- [95] A. Schwabe, M. Hänsel, M. Potthoff, and A. K. Mitchell, *Phys. Rev. B* **92**, 155104 (2015).
- [96] Nozières, Ph. and Blandin, A., *J. Phys. France* **41**, 193 (1980).
- [97] A. M. Sengupta and Y. B. Kim, *Phys. Rev. B* **54**, 14918 (1996).
- [98] I. Kuzmenko, T. Kuzmenko, Y. Avishai, and G. B. Jo, (2017), arXiv:1611.08673v4 [cond-mat.quant-gas].
- [99] V. Y. Irkhin, *The European Physical Journal B* **89**, 117 (2016).
- [100] D. Gatteschi, R. Sessoli, and J. Villain, *Molecular nanomagnets*, Vol. 5 (Oxford University Press on Demand, 2006).
- [101] I. Žutić, J. Fabian, and S. Das Sarma, *Rev. Mod. Phys.* **76**, 323 (2004).
- [102] L. Bogani and W. Wernsdorfer, *Nat Mater* **7**, 179 (2008).
- [103] D. C. Ralph, C. T. Black, and M. Tinkham, *Phys. Rev. Lett.* **74**, 3241 (1995).
- [104] D. C. Ralph, C. T. Black, and M. Tinkham, *Phys. Rev. Lett.* **78**, 4087 (1997).
- [105] C. H. Booth, M. D. Walter, M. Daniel, W. W. Lukens, and R. A. Andersen, *Phys. Rev. Lett.* **95**, 267202 (2005).
- [106] T. Zapata, N. Bennett, V. Struzhkin, Y. Fei, F. Jelezko, J. Biskupek, U. Kaiser, R. Reuter, J. Wrachtrup, F. Al Ghannam, and P. Hemmer, (2017), arXiv:1702.06854.
- [107] T. W. Odom, J.-L. Huang, C. L. Cheung, and C. M. Lieber, *Science* **290**, 1549 (2000).
- [108] Y. Bomze, I. Borzenets, H. Mebrahtu, A. Makarovski, H. U. Baranger, and G. Finkelstein, *Phys. Rev. B* **82**, 161411 (2010).
- [109] W. Shao-Quan, W. Shun-Jin, S. Wei-Li, and Y. Wan-Lun, *Chinese Physics* **13**, 510 (2004).
- [110] W. B. Thimm, J. Kroha, and J. von Delft, *Phys. Rev. Lett.* **82**, 2143 (1999).
- [111] R. K. Kaul, G. Zaránd, S. Chandrasekharan, D. Ullmo, and H. U. Baranger, *Phys. Rev. Lett.* **96**, 176802 (2006).
- [112] P. Simon and I. Affleck, *Phys. Rev. Lett.* **89**, 206602 (2002).
- [113] P. S. Cornaglia and C. A. Balseiro, *Phys. Rev. B* **66**, 115303 (2002).
- [114] P. S. Cornaglia and C. A. Balseiro, *Phys. Rev. B* **66**, 174404 (2002).
- [115] Y. Luo, C. Verdozzi, and N. Kioussis, *Phys. Rev. B* **71**, 033304 (2005).
- [116] T. Hand, J. Kroha, and H. Monien, *Phys. Rev. Lett.* **97**, 136604 (2006).
- [117] S. Galkin, C. A. Balseiro, and M. Avignon, *The European Physical Journal B - Condensed Matter and Complex Systems* **38**, 519 (2004).
- [118] G. Chiappe and A. A. Aligia, *Phys. Rev. B* **66**, 075421 (2002).
- [119] A. Schwabe, I. Titvinidze, and M. Potthoff, *Phys. Rev. B* **88**, 121107 (2013).

- 
- [120] A. M. Calle, M. Pacheco, G. B. Martins, V. M. Apel, G. A. Lara, and P. A. Orellana, *Journal of Physics: Condensed Matter* **29**, 135301 (2017).
- [121] J. A. Andrade, D. J. García, and P. S. Cornaglia, *Phys. Rev. B* **92**, 165416 (2015).
- [122] P. P. Baruselli, R. Requist, M. Fabrizio, and E. Tosatti, *Phys. Rev. Lett.* **111**, 047201 (2013).
- [123] G. Binnig, H. Rohrer, C. Gerber, and E. Weibel, *Phys. Rev. Lett.* **49**, 57 (1982).
- [124] A. Bezryadin, C. Dekker, and G. Schmid, *Applied Physics Letters* **71**, 1273 (1997).
- [125] D. L. Klein, R. Roth, A. K. L. Lim, A. P. Alivisatos, and P. L. McEuen, *Nature* **389**, 699 (1997).
- [126] P. Schlottmann, *Phys. Rev. B* **65**, 024420 (2001).
- [127] P. Schlottmann, *Phys. Rev. B* **65**, 024431 (2001).
- [128] P. Schlottmann, *Phys. Rev. B* **65**, 174407 (2002).
- [129] G. Franzese, R. Raimondi, and R. Fazio, *EPL (Europhysics Letters)* **62**, 264 (2003).
- [130] R. Bedrich, S. Burdin, and M. Hentschel, *Phys. Rev. B* **81**, 174406 (2010).
- [131] A. Schwabe, M. Hänsel, and M. Potthoff, *Phys. Rev. A* **90**, 033615 (2014).
- [132] L. Ansari, G. Fagas, J.-P. Colinge, and J. C. Greer, *Nano Letters* **12**, 2222 (2012).
- [133] N. J. Craig, J. M. Taylor, E. A. Lester, C. M. Marcus, M. P. Hanson, and A. C. Gossard, *Science* **304**, 565 (2004).
- [134] L. Zhou, J. Wiebe, S. Lounis, E. Vedmedenko, F. Meier, S. Blugel, P. H. Dederichs, and R. Wiesendanger, *Nat Phys* **6**, 187 (2010).
- [135] N. Néel, R. Berndt, J. Kröger, T. O. Wehling, A. I. Lichtenstein, and M. I. Katsnelson, *Phys. Rev. Lett.* **107**, 106804 (2011).
- [136] M. A. Ruderman and C. Kittel, *Phys. Rev.* **96**, 99 (1954).
- [137] T. Kasuya, *Progress of Theoretical Physics* **16**, 45 (1956).
- [138] K. Yosida, *Phys. Rev.* **106**, 893 (1957).
- [139] S. Doniach, *Physica B+C* **91**, 231 (1977).
- [140] R. Jullien, J. Fields, and S. Doniach, *Phys. Rev. Lett.* **38**, 1500 (1977).
- [141] A. K. Mitchell, P. G. Derry, and D. E. Logan, *Phys. Rev. B* **91**, 235127 (2015).
- [142] A. Allerdt, C. A. Büsser, G. B. Martins, and A. E. Feiguin, *Phys. Rev. B* **91**, 085101 (2015).
- [143] J. R. Schrieffer and P. A. Wolff, *Phys. Rev.* **149**, 491 (1966).
- [144] S. R. White, *Phys. Rev. Lett.* **69**, 2863 (1992).
- [145] U. Schollwöck, *Annals of Physics* **326**, January 2011 Special Issue, 96 (2011).
- [146] R. Bulla, T. A. Costi, and T. Pruschke, *Rev. Mod. Phys.* **80**, 395 (2008).
- [147] E. Lieb and D. Mattis, *Journal of Mathematical Physics* **3**, 749 (1962).
- [148] M. Kharitonov and G. Kotliar, *Phys. Rev. B* **88**, 201103 (2013).
- [149] P. Kómár, *Multichannel kondo model*, (2012) [http://isites.harvard.edu/fs/docs/icb.topic1191951.files/Peter\\_Komar\\_Multichannel\\_Kondo\\_print.pdf](http://isites.harvard.edu/fs/docs/icb.topic1191951.files/Peter_Komar_Multichannel_Kondo_print.pdf) (visited on 03/03/2017).
- [150] W. F. Brinkman, R. C. Dynes, and J. M. Rowell, *Journal of Applied Physics* **41**, 1915 (1970).
- [151] N. S. Wingreen, B. L. Altshuler, and Y. Meir, *Phys. Rev. Lett.* **75**, 769 (1995).
- [152] I. Affleck and A. W. W. Ludwig, *Phys. Rev. B* **48**, 7297 (1993).

- [153] B. Andraka and A. M. Tsvelik, *Phys. Rev. Lett.* **67**, 2886 (1991).
- [154] R. M. Potok, I. G. Rau, H. Shtrikman, Y. Oreg, and D. Goldhaber-Gordon, *Nature* **446**, 167 (2007).
- [155] S.-S. Yeh and J.-J. Lin, *Phys. Rev. B* **79**, 012411 (2009).
- [156] L. J. Zhu, S. H. Nie, P. Xiong, P. Schlottmann, and J. H. Zhao, *Nature Communications* **7**, Article, 10817 (2016).
- [157] P. Coleman, L. B. Ioffe, and A. M. Tsvelik, *Phys. Rev. B* **52**, 6611 (1995).
- [158] J. Gan, N. Andrei, and P. Coleman, *Phys. Rev. Lett.* **70**, 686 (1993).
- [159] D. L. Cox and A. Zawadowski, *Advances in Physics* **47**, 599 (1998).
- [160] O. Parcollet, A. Georges, G. Kotliar, and A. Sengupta, *Phys. Rev. B* **58**, 3794 (1998).
- [161] Y. Couzinié, “Multi-channel kondo effect in finite lattices”, Bachelor thesis (Institut für Theoretische Physik, Universität Hamburg, 2016).
- [162] S. Takeno, *Progress of Theoretical Physics* **25**, 102 (1961).
- [163] S. Li, M. S. Sellers, C. Basaran, A. J. Schultz, and D. A. Kofke, *Int J Mol Sci* **10**, 2798 (2009).
- [164] J. S. Lim, M.-S. Choi, M. Y. Choi, R. López, and R. Aguado, *Phys. Rev. B* **74**, 205119 (2006).
- [165] D. Mantelli, C. P. Moca, G. Zaránd, and M. Grifoni, *Physica E: Low-dimensional Systems and Nanostructures* **77**, 180 (2016).
- [166] L. E. Picasso, L. Bracci, and E. d’Emilio, “Perturbation theory in quantum mechanics”, in *Mathematics of complexity and dynamical systems*, edited by R. A. Meyers (Springer New York, New York, NY, 2011), pp. 1351–1375.
- [167] W. Nolting, *Grundkurs Theoretische Physik 7*, Grundkurs Theoretische Physik (Springer, 2005).
- [168] P. P. Baruselli, M. Fabrizio, and E. Tosatti, (2017), arXiv:1703.06057 [cond-mat].
- [169] J. J. Parks, A. R. Champagne, T. A. Costi, W. W. Shum, A. N. Pasupathy, E. Neuscamman, S. Flores-Torres, P. S. Cornaglia, A. A. Aligia, C. A. Balseiro, G. K.-L. Chan, H. D. Abruña, and D. C. Ralph, *Science* **328**, 1370 (2010).
- [170] P. Jacobson, M. Muenks, G. Laskin, O. O. Brovko, V. S. Stepanyuk, M. Ternes, and K. Kern, (2016), arXiv:1609.00612 [cond-mat.mes-hall].
- [171] M. Ternes, *Progress in Surface Science* **92**, 83 (2017).
- [172] T. A. Costi, L. Bergqvist, A. Weichselbaum, J. von Delft, T. Micklitz, A. Rosch, P. Mavropoulos, P. H. Dederichs, F. Mallet, L. Saminadayar, and C. Bäuerle, *Phys. Rev. Lett.* **102**, 056802 (2009).
- [173] M. Hanl, A. Weichselbaum, T. A. Costi, F. Mallet, L. Saminadayar, C. Bäuerle, and J. von Delft, *Phys. Rev. B* **88**, 075146 (2013).

# List of publications and author contributions

- **Cooperation of different exchange mechanisms in confined magnetic systems**

Andrej Schwabe, Mirek Hänsel, and Michael Potthoff

Physical Review A **90**, 033615 - published 15 September 2014

The content of this work is discussed in Chap. 2.

This author has performed numerical calculations using DMRG, and contributed to the discussions of the effective low-energy models.

- **Screening mechanisms in magnetic nanostructures**

Andrej Schwabe, Mirek Hänsel, Michael Potthoff, and Andrew K. Mitchell

Physical Review B **92**, 155104 - published 2 October 2015

The content of this work is discussed in Chap. 3.

This author has developed the theoretical framework of the effective low-energy model, performed numerical calculations, and contributed to the analysis and preparation of the manuscript.



# Eidesstattliche Erklärung

## Declaration on oath

Hiermit erkläre ich an Eides statt, dass ich die vorliegende Dissertationsschrift selbst verfasst und keine anderen als die angegebenen Quellen und Hilfsmittel benutzt habe.

I hereby declare, on oath, that I have written the present dissertation by my own and have not used other than the acknowledged resources and aids.

Hamburg, July 13, 2017

Mirek Hänsel





# Danksagung

An dieser Stelle möchte ich mich ganz herzlich bei all den Menschen bedanken, die mich auf dem Weg zur Promotion begleitet haben.

Auf wissenschaftlicher Seite gilt der Dank den vielen (auch ehemaligen) Mitgliedern der Arbeitsgruppe, allen voran Michael Potthoff, der als Betreuer immer ein offenes Ohr und Zeit für fruchtbare Diskussionen hatte. Seine Ratschläge und Anregungen haben geholfen, die komplexe Physik kritisch zu hinterfragen und dem Forschungsvorhaben ein solides Konzept zu verleihen.

Namentlich erwähnen möchte ich meinen Bürokollegen Matthias Peschke, mit dem ich nicht nur über Fachliches, sondern auch über jedes andere Thema reden konnte. Ein Zugewinn an interessanten Informationen war bei fast jedem Gespräch garantiert.

Den ehemaligen Mitgliedern Andrej Schwabe und Irakli Titvinidze sei für ihr Engagement und für viele hilfreiche Tipps in meiner Einarbeitungsphase gedankt.

Selbstverständlich gilt der Dank auch den anderen Kollegen, sei es für fachliche Ratschläge oder einfach nur für die willkommene Ablenkung von der Physik in der Mittagspause.

Nicht minder wichtig ist der Dank, den ich meiner gesamten Familie aussprechen möchte. Die Unterstützung von allen Seiten, insbesondere auch das Verständnis für mitunter lange Arbeitsabende im Institut und die für die Physik geopfertenen Wochenenden sind von unschätzbarem Wert bei einem Großprojekt wie der Promotion.